Hybrid modeling technique for nonlinear 2D electromagnetic problems

Citation for published version (APA):
Bao, J. (2019). *Hybrid modeling technique for nonlinear 2D electromagnetic problems: towards a design framework for variable flux reluctance machines*. [Phd Thesis 1 (Research TU/e / Graduation TU/e), Electrical Engineering]. Technische Universiteit Eindhoven.

Document status and date:
Published: 18/06/2019

Document Version:
Publisher's PDF, also known as Version of Record (includes final page, issue and volume numbers)

Please check the document version of this publication:

• A submitted manuscript is the version of the article upon submission and before peer-review. There can be important differences between the submitted version and the official published version of record. People interested in the research are advised to contact the author for the final version of the publication, or visit the DOI to the publisher's website.
• The final author version and the galley proof are versions of the publication after peer review.
• The final published version features the final layout of the paper including the volume, issue and page numbers.

Link to publication

General rights
Copyright and moral rights for the publications made accessible in the public portal are retained by the authors and/or other copyright owners and it is a condition of accessing publications that users recognise and abide by the legal requirements associated with these rights.

- Users may download and print one copy of any publication from the public portal for the purpose of private study or research.
- You may not further distribute the material or use it for any profit-making activity or commercial gain
- You may freely distribute the URL identifying the publication in the public portal.

If the publication is distributed under the terms of Article 25fa of the Dutch Copyright Act, indicated by the "Taverne" license above, please follow below link for the End User Agreement:

www.tue.nl/taverne

Take down policy
If you believe that this document breaches copyright please contact us at:

openaccess@tue.nl

providing details and we will investigate your claim.

Download date: 17. Nov. 2023

Hybrid Modeling Technique for Nonlinear 2D Electromagnetic Problems

Towards a Design Framework for Variable Flux Reluctance Machines

PROEFSCHRIFT

ter verkrijging van de graad van doctor aan de Technische Universiteit
Eindhoven, op gezag van de rector magnificus prof.dr.ir. F.P.T. Baaijens, voor
een commissie aangewezen door het College voor Promoties, in het openbaar te
verdedigen op dinsdag 18 juni 2019 om 11:00 uur

door

Jing Bao

geboren te Hangzhou, China

Dit proefschrift is goedgekeurd door de promotoren en de samenstelling van de promotiecommissie is als volgt:

voorzitter:	prof.dr.ir. P.H.N. de With	
promotor:	prof.dr. E.A. Lomonova MSc	
copromotor:	dr.ir. B.L.J. Gysen	
leden:	dr. G. Pellegrino	(Politecnico di Torino)
	dr. S.T. Lundmark	(Chalmers University of Technology)
	prof.dr.ing. A.J.M. Pemen	
	prof.dr. Y. Amara	(Université du Havre)
adviseur:	dr.ir. R.L.J. Sprangers	(Punch Powertrain)

Het onderzoek of ontwerp dat in dit proefschrift wordt beschreven is uitgevoerd in overeenstemming met de TU/e Gedragscode Wetenschapsbeoefening.

Hybrid Modeling Technique for Nonlinear 2D Electromagnetic Problems

Towards a Design Framework for Variable Flux Reluctance Machines

---

J. Bao

This research is part of the Impuls I program, supported by TU/e HTSC, Punch Powertrain nv, Belgium, and Prodrive Technologies B.V., The Netherlands.

Copyright © J. Bao, 2019. All right reserved. No part of this thesis may be reproduced or distributed in any form or by any means, or stored in a database or retrieval system, without the prior written permission of the author.

A catalogue record is available from the Eindhoven University of Technology Library. ISBN: 978-90-386-4797-5

Summary

Hybrid Modeling Technique for Nonlinear 2D Electromagnetic Problems

Towards a Design Framework for
Variable Flux Reluctance Machines

The electric machine is a vital component in the powertrain of electric vehicles that demands for low cost, robust structure, high speed, high torque density, etc. Due to the concerns about possible price fluctuation and shortages in the supply of the permanent magnets (PMs), the car manufacturers have been developing methods for reducing rare-earth materials used in the vehicles. Hence, the reluctance machines, designed to be independent (or less dependent) of the PMs, are gaining more and more attention. This thesis researches the variable flux reluctance machines (VFRM), which due to their cheap and robust rare-earth-free structures, are considered to be a promising candidate for automotive applications. The VFRM is a relatively new class of electric machine that consists of a stator with both field and armature windings and a salient rotor. The machine electromagnetic behavior is complex, since the requirement of high torque and power densities within a small volume leads the machine to a working condition at saturation.

To accurately estimate the performance, numerical methods are often applied such as finite element modeling (FEM), which are time-consuming especially for initial sizing and topology selection, and hence, the development of an alternative solution is required. Aiming at reducing computation effort as well as accurate modeling of the machine performance, a two-dimensional (2D) hybrid modeling technique is developed in the first part of the thesis. This novel computation technique combines two analytical modeling methods, spatial-harmonic-based Fourier modeling and mesh-based magnetic equivalent circuit (MEC), into one framework. Such combination inherits the merit of Fourier modeling which is fast and accurate, and the characteristic of MEC which allows for the modeling of magnetic saturation. To make the developed method applicable to a wide class of linear/rotary/tubular, PM/reluctance electrical machines, the computation framework is extended to the Cartesian, polar and axisymmetric coordinate systems with generalized expressions. In Chapter 2, the mathematical formulation including saturation and motion is established, and is verified for benchmark problems in each of the coordinate system, proving its applicability to a broad class of electromagnetic actuators and machines.

The modeling technique is further applied to a saturated VFRM in Chapter 3, which demonstrates the methods for machine performance analysis. Based on the magnetic field in the airgap, the mean torque, torque waveform and torque ripple are derived. The flux linkage, back-emf and nonlinear incremental inductance including slot leakage are obtained. The iron losses are calculated using the instantaneous magnetic field, and a fast prediction of the ac copper loss is developed. The aforementioned machine quantities show a good agreement with 2D nonlinear FEM, and the obtained accuracy is sufficient for modeling and design purposes. The simulation methods are applicable for other types of machines.

The second part of this thesis provides the physical understanding, design considerations, optimization and realization of the VFRMs. To obtain an intensive understanding of the machine working principle due to its multi-excited topology, the torque production mechanism and torque components are investigated in Chapter 4. Different topologies of the VFRMs are analyzed and are compared on the aspects of winding factors, flux linkage and torque. Based on the comparison results, the design rules for the selection of pole numbers and winding configuration are provided.

Due to its salient structure, the VFRM suffers from relatively large torque ripples. In Chapter 5, the torque ripples are analyzed and minimized based on the derived inductance and torque equations. Various torque ripple reduction methods using the rotor skewing, rotor teeth non-uniformity, and harmonic injection, are discussed with the verified effectiveness for both non-saturated and saturated situations. Additionally, based on the nature of multi-excitation in VFRMs (that the field current, armature current and commutation angle are all controllable), the torque-speed characteristic, power factor and enhancement of the flux-weakening capability are discussed.

The design principles from aforementioned analysis are implemented on a VFRM in Chapter 6 for an indirect drive in the 48 V mild hybrid system, which requires the continuous power of 5 kW, maximum power of 10 kW, peak torque of 45 Nm and maximum speed of 18 krpm. With a strict limitation on machine outer dimensions, the machine geometry is optimized towards maximizing the efficiency, whilst the winding design is performed towards maximizing the filling factor and minimizing the ac copper loss. Furthermore, a prototype of the developed design for the 48 V mild hybrid system is realized and presented in Chapter 7. The predicted machine performance is verified by measurements on the motor/generator test bench.

To conclude, this thesis presents a fast and accurate hybrid modeling technique, where the nonlinear phenomena of the soft-magnetic materials is taken into account. This computation methodology is suitable for the analysis of nonlinear 2D electromagnetic problems and the design of different classes of electric machines. On the other hand, this thesis treats the detailed analysis of VFRMs with the established design framework. A design is accomplished for the 48 V mild hybrid system with the experimental verification that validates the predicted results.

Contents

Summary v

List of symbols xiii

1 Introduction 1
1.1 History of the electric vehicle 2
1.2 Mild hybrid system 2
1.3 Electrical machines in powertrains 3
1.3.1 DC machine 4
1.3.2 Induction machine 4
1.3.3 Permanent magnet synchronous machine 4
1.3.4 Synchronous brushed machine 4
1.3.5 Reluctance machine 5
1.4 Electromagnetic modeling 6
1.5 Research objectives 9

I Hybrid modeling technique 11

2 Generalized formulation 13
2.1 Introduction 14
2.2 Assumptions 15
2.3 Division in regions 16
2.4 Modeling of Fourier regions 17
2.5 Modeling of MEC regions 18
2.5.1 Meshing method 18
2.5.2 Constitution of MEC elements 19
2.5.3 Magnetic reluctances 20
2.5.4 Permanent magnet related magnetomotive force 24
2.5.5 Current related magnetomotive force 25
2.5.6 Magnetic field within MEC elements 31
2.5.7 Elements at the boundaries of MEC regions 32
2.6 Boundary conditions 33
2.6.1 Continuous boundary conditions between Fourier and MEC regions 35
2.6.2 Continuous boundary conditions between Fourier regions 40

- 2.6.3 Dirichlet/Neumann boundary conditions 41
- 2.7 Motion 43
  - 2.7.1 Motion-integrated tangential boundary conditions 43
  - 2.7.2 Motion-integrated normal boundary conditions 46
- 2.8 Modeling of nonlinear magnetic materials 47
- 2.9 Finite element verification 49
  - 2.9.1 Cartesian coordinate system 50
  - 2.9.2 Polar coordinate system 52
  - 2.9.3 Axisymmetric coordinate system 54
  - 2.9.4 Simulation parameters 57
- 2.10 Summary and conclusions 61

3 Modeling of variable flux reluctance machines **63**
- 3.1 Introduction 64
- 3.2 Geometry of the benchmark machine: 12/10 VFRM 64
- 3.3 Application of the hybrid analytical modeling 66
  - 3.3.1 Division in regions 66
  - 3.3.2 Meshing of MEC regions 67
  - 3.3.3 Current related magnetomotive force 68
  - 3.3.4 Boundary conditions 71
  - 3.3.5 Matrix formulation 72
  - 3.3.6 Numerical implementation 72
- 3.4 Magnetic flux density 74
- 3.5 Torque 75
- 3.6 Flux linkage, back-emf and phase voltage 77
- 3.7 Inductance 81
- 3.8 Losses 84
  - 3.8.1 Iron losses 85
  - 3.8.2 Copper losses 86
- 3.9 Efficiency and power factor 94
- 3.10 Summary and conclusions 94

II Variable flux reluctance machines 97

4 Topologies and configurations **99**
- 4.1 Introduction 100
- 4.2 Operating principles 100
  - 4.2.1 Electric energy 100
  - 4.2.2 Magnetic energy 101
  - 4.2.3 Electromagnetic torque 104
- 4.3 Winding factor 112
  - 4.3.1 Pole combinations 113
  - 4.3.2 Winding configurations 114
  - 4.3.3 Distribution factor 114
  - 4.3.4 Harmonic cancellation of distribution factor 121
  - 4.3.5 Pitch factor 125

4.4 Influence of the number of rotor poles 126
4.5 Unbalanced magnetic pull 130
4.6 Selection of stator and rotor poles 131
4.7 Summary and conclusions 132

5 Design considerations 133
5.1 Introduction 134
5.2 Torque ripple minimization 134
    5.2.1 Rotor skewing 135
    5.2.2 Rotor teeth non-uniformity 140
    5.2.3 Harmonic current injection 143
5.3 Field weakening capability 149
    5.3.1 DQ-reference frame 149
    5.3.2 Torque-speed characteristic 152
5.4 Power factor 158
5.5 Scaling of outer dimensions 159
5.6 Summary and conclusions 163

6 Design for mild hybrid system 165
6.1 Introduction 166
6.2 Machine requirements 166
6.3 Selection of the soft magnetic material 167
6.4 Initial sizing 167
    6.4.1 Outer dimensions 167
    6.4.2 Split ratio 169
    6.4.3 Stator and rotor tooth widths 170
6.5 Optimization 170
    6.5.1 Objective 170
    6.5.2 Algorithm 171
    6.5.3 Stator geometry adjustment 174
    6.5.4 3D effect 174
6.6 Winding design 177
    6.6.1 Coil connections 177
    6.6.2 Coil design 179
    6.6.3 Integrated-coil topology 183
6.7 Final design 187
6.8 Summary and conclusions 189

7 Experimental verification 191
7.1 Introduction 192
7.2 Realization of the prototype 192
7.3 Test setup 192
7.4 Resistances and inductances 196
7.5 Back-emf waveform 198
7.6 Torque-current performance 201
7.7 Thermal evaluation 206

7.8 Summary and conclusions 208

III Closing 209

8 Conclusions and recommendations 211
8.1 Conclusions of Part I 212
8.1.1 Generalized hybrid analytical modeling technique 212
8.1.2 Modeling of variable flux reluctance machines 213
8.2 Conclusions of Part II 214
8.2.1 Topologies and configurations of variable flux reluctance machines 214
8.2.2 Design considerations 215
8.2.3 Design of the VFRM for 48 V mild hybrid system 216
8.2.4 Experimental verification 216
8.3 Thesis contributions 217
8.4 Recommendations 218

A Magnetic field solutions in Fourier regions 221

B Distribution of magnetomotive force in *q*- or *pq*-directions 225

C Distribution factor and pitch factor of VFRMs 231

Bibliography 235

Acknowledgements 247

Curriculum Vitae 249

List of symbols

Symbol	Quantity	Unit
α_{ri}	Rotor tooth inner arc	deg or rad
α_{ro}	Rotor tooth outer arc	deg or rad
α_{si}	Stator tooth inner arc	deg or rad
α_{so}	Stator tooth outer arc	deg or rad
Δ_θ	Rotation angle (electrical)	deg or rad
D_{so}	Stator outer diameter	m
D_{si}	Stator inner diameter	m
D_{ro}	Rotor outer diameter	m
D_{ri}	Rotor inner diameter	m
η	Efficiency	-
Λ	Flux linkage	Wb
$\Lambda_{fcoil,1}$	Fundamental flux linkage of a single ac coil	Wb
$\phi_{q\pm}$	Flux flows in the positive/negative q-directions	Wb
$\phi_{p\pm}$	Flux flows in the positive/negative p-directions	Wb
$\mathcal{F}$	Magnetomotive force	A
$\hat{\mathcal{F}}_{ac}$	Peak magnetomotive force of the armature winding	A
$\mathcal{F}_{dc}$	Magnetomotive force of the field winding	A
$\mathcal{F}_{p\pm}$	Magnetomotive force in the positive/negative p-direction	A
$\mathcal{F}_{q\pm}$	Magnetomotive force in the positive/negative q-direction	A
μ_0	Permeability of vacuum ($4\pi\times10^{-7}$)	H/m
μ_r	Relative permeability	-
μ_r^k	Relative permeability of element k	-
$\vec{A}$	Magnetic vector potential	Wb/m
$\vec{B}$	Magnetic flux density vector	T
F	Force	N
$\vec{H}$	Magnetic field strength vector	A/m
h_c	Heat transfer coefficient	W/Km^2
h_{sy}	Stator yoke height	m
h_{ry}	Rotor yoke height	m
$\vec{J}$	Current density vector	A/m^2
J_{eddy}	Eddy current density	A/m^2
ρ	Copper resistivity	$\Omega \cdot m$

σ	Copper conductivity	S/m
m	Number of phases	-
$\vec{M}$	Magnetization vector	A/m
$\vec{M}_p$	Magnetization vector in the p-direction	A/m
$\vec{M}_q$	Magnetization vector in the q-direction	A/m
k_d	Distribution factor	-
k_p	Pitch factor	-
k_f	Filling factor	-
l_l	Length in the l-direction	m
l_p	Length in the p-direction	m
l_q	Length in the q-direction	m
L	Number of elements in one layer	-
L_{sk}	Stack length	m
L_{ff}	Self inductance of the field winding	H
M_{fph}	Mutual inductance between the field winding and armature windings	H
L_{fph}	Self inductance of the armature windings	H
M_{fph}	Mutual inductance of the armature windings	H
N_{ac}	Number of turns per ac coil	-
N_{dc}	Number of turns per dc coil	-
N_h	Total number of harmonics	-
ψ	Magnetic scalar potential	A
p	General coordinate	m
$P_{cu,d}$	Dc copper loss	W
$P_{cu,a}$	Ac copper loss	W
PF	Power factor	-
p_{Fe}	Iron loss density	W/kg
p_{hys}	Hysteresis loss density	W/kg
p_{eddy}	Eddy current loss density	W/kg
p_{exc}	Excess loss density	W/kg
P_s	Number of the stator poles	-
P_r	Number of the rotor poles	-
q	General coordinate	m or rad
r_b	Bottom radius of the MEC element	m
r_t	Top radius of the MEC element	m
$\Re_p\pm$	Magnetic reluctance in the positive/negative p-direction	H^{-1}
$\Re_q\pm$	Magnetic reluctance in the positive/negative q-direction	H^{-1}
$\mathcal{S}_f$	Scaling factor in hybrid analytical modeling	-
S_{pl}/S_{ql}	Cross section of a MEC element in pl-/ql- plane	m^2
SR	Split ratio	-
T_{em}	Electromagnetic torque	Nm
$\bar{T}_{em}$	Mean value of the electromagnetic torque	Nm
T_{rip}	Torque ripple	Nm
T_{ff}	Torque induced by the self inductance of the field winding	Nm
$T_{f,ph}$	Torque induced by the mutual inductances between	Nm

	the field winding and armature windings	
$T_{l,ph}$	Torque induced by the self inductances of the armature windings	Nm
$T_{m,ph}$	Torque induced by the mutual inductances of the armature windings	Nm
$\mathbb{T}$	Maxwell stress tensor	T^2
W_c	Co-energy	J
W_{ele}	Electric energy	J
W_{mag}	Magnetic energy	J
τ_{per}	Width of periodicity	m or rad
$X_{sf,a}$	Axial scaling factor	-
$X_{sf,r}$	Radial scaling factor	-

Abbreviation	Description
2D	Two-dimensional
3D	Three-dimensional
ac	Alternating current
dc	Direct current
emf	Electromotive force
EV	Electric vehicle
HEV	Hybrid electric vehicle
FEM	Finite element modeling
mmf	Magnetomotive force
MEC	Magnetic equivalent circuit
HAM	Hybrid analytical modeling
PM	Permanent magnet
PMSM	Permanent magnet synchronous machine
RMS	Root mean square
SRM	Switched reluctance machine
UMP	Unbalanced magnetic pull
VFRM	Variable flux reluctance machine

Chapter 1

Introduction

1.1 History of the electric vehicle

The first electric vehicle appeared in the 19^{th} century. Innovators in Hungary, the Netherlands and the United States began with the concept of a battery-powered vehicle and created some of the first small-scale electric cars. Up to the second half of the 19^{th} century, French and English inventors already built some of the first practical electric cars [116, 122].

By the beginning of the 20^{th} century, electric cars accounted for around a third of the vehicles on the road, e.g., in the year 1900, about 4200 automobiles were on the road, out of which 38% were electric, 22% were gasoline powered, and 40% were steam powered [101]. However, due to the low gas price and the massive facilities of gas stations, electric vehicles disappeared by 1935.

The next resurge of electric vehicles (EVs) began in the late 1960s, attributed to the development of power electronics. The increasing price and shortage of gasoline maintained the interest [104]. However, the vehicles produced at that moment were still not comparable to gasoline-powered cars.

Experiencing rise and fall, the soar of the EVs finally happened in the end of the 20^{th} century. Toyota Prius, the first mass-produced hybrid electric vehicle (HEV), was released in Japan in 1997; and Tesla, the electric car that could go more than 200 miles on a single charge, was planned and announced in 2006. The success in technology shows the potential for a more sustainable future [122] and spurred other automakers to look for more efficient, more powerful and more intelligent solutions for EVs.

1.2 Mild hybrid system

Stepped into the 21^{st} century, there is continuously pressure coming from the government and the public to reduce vehicle exhaust emissions. To protect the environment, stringent regulations are proposed, e.g., European Union's target that to reduce CO_2 emission to 95 g/km by 2021. In fact, powertrain electrification is more and more considered as a feasible alternative to purely improve the internal combustion engine efficiency.

During the evolution of EVs and HEVs, hybrid powertrain with regenerative recovery ability is recognized as one of the most effective methods to reduce CO_2 emissions [13, 43, 84, 86]. A subsidiary electrical system operating at 48 V can offer the advantages from hybridization to achieve fuel consumption benefit without the complexity associated with full hybrid electric vehicles [79]. Moreover, such a 48 V mild hybrid system provides the possibility to supply relatively high output power for electrical compressors [63], power steering, etc., which is limited by the current 12 V electrical systems in conventional internal combustion automobiles.

(a)

(b)

Figure 1.1: Pictures of (a) Prius [121], and (b) Tesla roadster [120].

Table 1.1: Machine types in some representative EVs [104].

EV	Machine type	Released year
Tesla Model 3	Permanent magnet machine	2017
Tesla Model S	Induction machine	2012
Renault ZOE	Synchronous brushed machine	2011
Nissan Leaf	Permanent magnet machine	2010
NICE Mega City	DC machine	2006

1.3 Electrical machines in powertrains

The electrical machine, the main component in the powertrains, provides traction power by converting the electric energy from the battery into mechanical energy. There are many considerations for the design of electrical machines in EVs and HEVs, and one of the key choices is the machine type. Variety of machine types are investigated for automotive applications in the literature [3, 22, 28] and some are already commercially available. The types in the market include the DC machine, induction machine, permanent magnet machine and synchronous brushed machine. Additionally, another type, the reluctance machine, has been proposed but has not yet been commercially released in EVs. In Table 1.1, some of the commercially available EVs are listed with their respective machine types [104].

1.3.1 DC machine

The DC machine was the preferred option in variable-speed operation applications before the development of advanced power electronics, because of their well-established technology, reliability, low cost and simple control. However, the development of solid-state power semiconductors makes it increasingly practical and more beneficial to use other AC machines instead of DC machines in traction applications, mainly due to their disadvantages of low power density, costly maintenance of the coal brushes and low efficiency [104, 130].

1.3.2 Induction machine

As the most mature technology amongst various brushless motor drives, the induction machine is considered as a potential candidate for the electric propulsion of EVs and HEVs. They were already widely used in famous EV models, owing to their simple structure, reliability, ruggedness, low maintenance and low cost. However, induction machines still face a number of drawbacks, including lower efficiency, lower power factor, etc., in comparison with permanent magnet synchronous machines [101, 104, 130].

1.3.3 Permanent magnet synchronous machine

The permanent magnet synchronous machines are widely used in automotive propulsion because of their high efficiency, high torque, high power density and ease of control [44, 91, 92]. Apart from these merits, the constant power region of permanent magnet machines is limited by their relatively low field weakening capability. Conventionally, d-axis armature current is introduced to counteract the permanent magnet flux linkage. However, the machine is not efficient at high speed due to the d-axis current, and the speed range may still be inadequate due to the inverter limitations in terms of current and voltage ratings. Additionally, a large d-axis current may result in the risk of permanent magnet (PM) demagnetization, and magnets with a large coercivity have to be considered to avoid demagnetization during field weakening [41, 101, 124, 128, 130].

1.3.4 Synchronous brushed machine

In a synchronous brushed machine, the magnetic field is generated by the coils in the rotor that are connected to a voltage source through a slip ring. The main advantage of this machine is the ability to vary the magnetic flux linkage induced by the field current in the rotor, which eases high-speed operation at constant power region [31]. Additionally, the rotor is robust compared to permanent magnet machines, and the temperature is only limited by the conductor insulation. However, the magnetizing current in the rotor contributes to extra losses, and hence, efficiency is sacrificed in the constant torque region. Moreover, reliability and maintenance of the mechanical slip ring is not preferred, hence, brushless methods of transferring power to the rotor field winding are being developed [50, 80, 104, 107].

1.3.5 Reluctance machine

Expecting an increasing production of EVs and HEVs, car manufacturers have been developing methods for reducing rare-earth materials used in vehicles [23, 51, 102], due to the concerns about possible price fluctuation and shortages in supply in the future. Hence, reluctance machines, designed to be independent (or less dependent) of the PMs, are gaining more and more attention [65]. There are many types of reluctance machines, including the synchronous reluctance machine, the switched reluctance machine, the multi-excited reluctance machine, etc.

The synchronous reluctance machine has the stator similar to induction machine, while the rotor is designed to maximize the saliency ratio [111]. One of the disadvantages of this machine is the low power factor, and in the literature it is proposed to add a small amount of PM in the rotor for improvement [26, 87]. However, the risk of PM demagnetization (especially using low-energy PMs) limits the maximum stator current. Another major concern is the speed, the ribs and bridge areas of the rotor would fail because of the high centrifugal forces [21].

The switched reluctance machine has the advantage of a simple structure, tolerance of hostile operating environments, large constant-power range, large overload capacity and reduced price [25, 100]. However, the machine suffers from large torque ripples, high acoustic noise, complex control (e.g., torque sharing functions) [67], requirement of large dc-link capacitor and unconventional power electronic circuit that has to excite phases subsequently.

To overcome the shortcomings of switched reluctance machines, three-phase multi-excited reluctance machines are proposed [7, 115, 123]. For dc-excited types, there are both field winding and armature windings located in the stator [97, 114]. Compared to switched reluctance machines, they are improved in the aspects of torque ripple and power electronic circuit, because sinusoidal excitation is implemented for the armature current and the utilization of a commercial three-phase inverter can be considered [129]. Compared to the permanent magnet synchronous machine, it benefits from the controllable flux linkage of field winding that can enhance the speed extension capability. However, an additional circuit for the controllable field current is needed.

Amongst various types of dc-excited reluctance machines, the variable flux reluctance machine is a relatively novel type in the literature. Different from the dc-excited flux switching machine with a relatively complex winding configuration, the variable flux reluctance machine has concentrated windings, which is beneficial to reduce the end winding length and to obtain a higher filling factor, and is also relatively simple to manufacture. Due to the aforementioned merits, this thesis considers the variable flux reluctance machine for further research.

1.4 Electromagnetic modeling

Since power density and efficiency need to be optimized within a given volume and thermal constraints [81], accurate and fast modeling of the electromagnetic performance is of major importance in electrical machine design. To obtain an accurate magnetic field distribution for different types of machines, especially for machines that operate under saturated conditions such as reluctance machines, numerical models are commonly used. The geometries are discretized in finite mesh elements. Each of the element is an independent region of the domain where field equations are defined. The field variables are often interpolated using a first or second order polynomial. The finite element method (FEM) is powerful but time-consuming, since the mesh density is an essential condition for the accuracy of solutions. To reduce the computation time, development of analytical and semi-analytical modeling techniques is desirable [20, 52, 60].

For structures with periodicity, Fourier modeling is particularly interesting since it is fast and accurate [36, 83]. The Maxwell equations are solved in terms of the magnetic vector potential and the field solutions are written in the form of a Fourier series [59]. The limitation of this method is the inability to take circumferential variations of magnetic permeability into account [53, 54]. Although in [109, 110], the inclusion of finite permeable soft-magnetic material is successfully realized by expressing the permeability distribution in a region as a Fourier series, the computation of magnetic nonlinearity is not yet reported. Moreover, geometric details with high-permeable materials are still difficult.

To consider nonlinear material behavior, the magnetic equivalent circuit (MEC), that incorporates the magnetic nonlinearity with an iterative solver, seems to be a suitable method [72, 96, 105, 113]. However, it is difficult to construct flux paths to accurately obtain field and torque solutions, and a prior knowledge of the flux distribution is necessary. This limits the application of MEC to the electrical machine that has a flux density distribution strongly dependent on movement or the machine that has significant leakage flux. In [119], an automated design method using MEC is introduced for a flux switching machine. Several MEC modules are predefined and are assembled correspondingly for different moving positions. Although the workload involved in adapting the flux path is reduced, the coarse construction of flux tubes still limits the accuracy, as well as the flexibility of this method.

To further reduce the effort of constructing the flux paths as well as to increase the accuracy, mesh-based MEC (also called mesh-based reluctance network) is investigated [4, 14, 38]. Due to the adequate mesh, the accuracy is significantly improved compared to the conventional MEC, however, the dense mesh network all over the domain reduces the advantage of computation time.

To combine the merits of fast computation from Fourier modeling and the capability of including nonlinearity from mesh-based MEC, a hybrid analytical modeling technique (HAM) is considered in this thesis and is further developed. In this method, the regions with linear magnetic materials are modeled using Fourier modeling, while regions with nonlinear materials are modeled using MEC [1, 69, 88–90]. Between coupled Fourier and MEC regions, the boundary conditions of continuous magnetic field is ensured, which leads to a set of linear equations that solves the unknowns of the field solution.

A brief comparison between the HAM and FEM is summarized in Table 1.2. The number of mesh elements in the HAM is significantly smaller than in the FEM since regions with homogeneous permeability are not meshed. Additionally, for FEM softwares, e.g., Altair Flux2D, second order element that describes behavior by quadratic equations is commonly adopted, which further increases nodal unknowns. On the other hand, the force/torque calculation of airgap region in the HAM considers the direct semi-analytical solutions of Maxwell's equations, which is given by a typical number of harmonic order of 10^2; while the FEM uses the virtual work method that takes the solution for the total meshed geometry.

Suitable modeling techniques are diverse for different problems, and often a trade-off between accuracy and computation time has to be made. Considering the calculation of machine quantities like force/torque and inductance that are related to magnetostatic problems, the HAM, as an alternative to FEM, provides a fast tool for research and development of a wide class of electrical machines.

Table 1.2: Comparison between HAM and FEM.

HAM	FEM
Mesh	
- Mesh elements in regions where nonlinear material exists 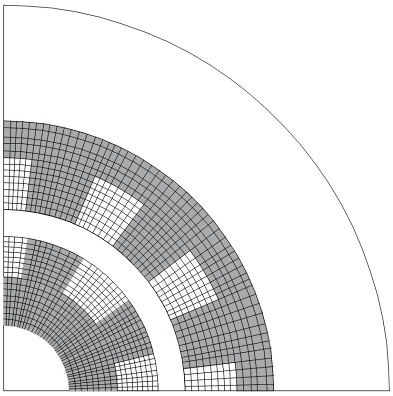	- Mesh elements in entire geometric domain 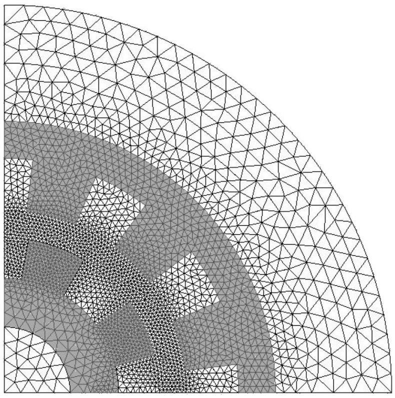
Node	
- Single potential node in element center 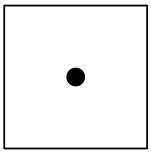	- Second order element: 6 nodes 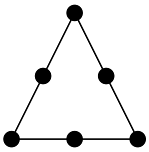
Force/Torque calculation	
- Maxwell stress tensor method - F or $T = \sum_{n=1}^{N_h} f(a_n, b_n, c_n, d_n)$ - Typical order of N_h: 10^2	- Virtual work method - $\begin{cases} F \text{ or } T = \dfrac{\partial W_c}{\partial q} \\ W = \sum_{e=1}^{N_e} \int_{V_e} \left[\int_0^H B_e dH_e \right] dV_e \end{cases}$ - Typical order of N_e: 10^5

Notes:
* The mesh takes a quarter of a 12/8 switched reluctance machine as the example;
* F and T are force and torque, respectively, N_h is the harmonic order, and a_n, b_n, c_n and d_n are Fourier coefficients of field solutions;
* W_c is the co-energy, q is the displacement, B is the magnetic flux density, H is the magnetic field strength, N_e is the total number of finite elements and V_e is the volume of 'e' [17].

1.5 Research objectives

The research objectives of the thesis are summarized in this section. There are mainly two parts of the objectives:

Part I: Establish a generalized modeling framework and methodology that offers accurate and relatively fast prediction for nonlinear 2D electromagnetic problems.

The sub-objectives and the thesis outline of this part are listed as the following:

1.1 *Extension of the 2D hybrid analytical modeling technique to predict the electromagnetic field in Cartesian, polar and axisymmetric coordinate systems for a wide class of permanent magnet and reluctance machines:*
    - *Incorporate the nonlinear magnetic materials;*
    - *Construct the position-dependent boundary conditions that allow free motion without re-meshing;*
    - *Incorporate the description of geometric details.*

    Chapter 2 presents the generalized hybrid analytical modeling technique for the calculation of the magnetic field distribution in nonlinear 2D electromagnetic problems. The mathematical formulations are introduced. The solution and accuracy are discussed based on a set of benchmark examples in each of the considered coordinate systems which are verified with FEM.

1.2 *Accurate prediction of machine quantities using the hybrid analytical modeling technique.*
    The hybrid analytical modeling technique is applied to a variable flux reluctance machine in Chapter 3. It provides accurate predictions for the magnetic field distribution (in the entire geometric domain), torque, torque ripple, flux linkage, electromotive force, incremental inductances, iron losses, eddy current, and ac copper losses.

Part II: Establish the design framework for the variable flux reluctance machines, and realize a design for automotive 48 V mild hybrid system.

The sub-objectives and the thesis outline of this part are listed as the following:

2.1 *Description of the operating principle and design considerations of variable flux reluctance machines:*
    - *Obtain a physical insight of torque production mechanism;*
    - *Understand the influences of machine topologies and configurations on the performance, and provide suggestions for optimum design selection;*

- *Investigate methods for torque ripple reduction and speed extension enhancement.*

Chapter 4 derives the torque equation of the variable flux reluctance machine based upon the variations in inductances to identify the various torque production mechanisms. The selection of machine topology is investigated based on the analysis of winding factor, influence of the number of rotor poles and magnetic pull.

In Chapter 5, design considerations towards minimizing the torque ripples and widening the speed range are given, which brings more insight in the relationship of machine parameters and performances. The sources of torque ripples are analyzed, and ripples are minimized by machine geometry adjustment and harmonic injection. The influence of field current and armature current on the torque-speed characteristic is given. The field weakening capability is discussed and the means for improvement with proper current arrangement is provided.

2.2 *Experimental verification on a prototype design for 48 V mild hybrid system.* The prototype design of a variable flux reluctance machine for the 48 V mild hybrid system is presented in chapter 6. The realization of the prototype is presented in chapter 7 together with the measurement results, which verify the predicted performances.

Part I

Hybrid modeling technique

Chapter 2

Generalized formulation

Part of the content in this chapter is published in:

J. Bao, B.L.J. Gysen and E.A. Lomonova, 'Hybrid Analytical Modeling of Saturated Linear and Rotary Electrical Machines: Integration of Fourier Modeling and Magnetic Equivalent Circuits', *IEEE Transactions on Magnetics*, Vol. 54, No. 11, pp. 1-5, 2018.

2.1 Introduction

As the base for deriving machine performances, calculation of the magnetic field is of major importance in the design process of electrical machines. To obtain accurate magnetic field distribution for many different types of machines, especially for devices with nonlinear magnetic materials, finite element method is commonly used, which is powerful but time-consuming.

As a relatively fast and accurate alternative to finite element method, the hybrid analytical modeling that integrates Fourier modeling and MEC is discussed in this chapter for the mathematical formulation. In the last decade, some papers have been published related to this technique. In [69, 88–90], the mesh-based MEC is only connected to one side of the Fourier modeling. A promising result of the magnetic field is provided in the airgap in [89] for a linear PM structure, and cogging force/torque is precisely estimated in [90] for various electromagnetic structures. Furthermore, material nonlinearity is shortly discussed in [90]. The cogging force for PM machines with different slot geometries is calculated, where saturation is considered in the stator using Newton-Raphson method. In [95], bidirectional coupling on both sides of the MEC regions are applied, achieving excellent matching of flux density in the overall structure with linear material properties. In this chapter, saturation incorporated with bi-directional coupled HAM (Fourier coupled on both sides of the MEC region), is extensively presented and validated. The fixed-point iteration method is provided for nonlinear magnetic material, which gives physical insight especially in the inductance calculation and is more robust than Newton-Raphson method [40, 47].

Additionally, in [89], the method of including motion is mentioned. Minimum displacement step is set corresponding to the dimension of mesh elements, and meanwhile the source vector is modified. However, the dependence of the moving step on the mesh element is not convenient in some circumstances, especially when the mesh size varies in the direction of motion. Therefore, it is proposed in this chapter to directly integrate the movement into the boundary conditions that allows free movement of MEC regions without re-constructing the mesh network.

Above all, this chapter presents the HAM in a generalized manner for the application in Cartesian, polar and axisymmetric coordinate systems. The content first focuses on the model formulation and description of magnetic sources, followed by the motion-integrated boundary conditions. Afterwards, the modeling of nonlinear material is introduced, including the formulation of magnetic properties in MEC elements and the iterative algorithm for saturation. In the end, validation of the HAM is performed by the comparison with FEM for benchmark examples in the considered three coordinate systems.

Table 2.1: Notation for coordinate systems.

Coordinate system	Cartesian	Polar	Axisymmetric	General
Normal	y	r	r	p
Tangential	x	θ	z	q
Longitudinal	z	z	θ	l

2.2 Assumptions

Before applying the hybrid analytical modeling technique, the following assumptions are made:

1. The problem is described in a 2D coordinate system;
2. Source terms (coils/permanent magnet) are invariant in the longitudinal direction;
3. Only isotropic material properties are used;
4. The problem is quasi static.

All electromagnetic devices have three-dimensional (3D) geometries. To use a two-dimensional (2D) modeling technique, the geometry should be invariant in one of the directions, or the variation is negligible. This assumption is valid in many circumstances for electric machines: for rotary machines that have relatively long axial length compared to its radius, 3D effects are often negligible; for tubular actuators, the axisymmetric geometry inherently leads to a 2D problem.

The modeled geometry inhibits periodicity, and only one period is considered in HAM. To present the diverse applicability of the HAM, it is applied to the geometries in three different 2D coordinate systems, i.e., Cartesian (x, y), polar (r, θ) and axisymmetric (r, z). In this thesis, periodicities are respectively applied in the x-, θ-, and z-directions. For generality of the explanations in the following content, the normal direction is referred as the p-direction, the tangential (periodicity) direction is referred as the q-direction, while the longitudinal (invariant) direction is referred as the l-direction. A summary of the notation for coordinate systems is listed in Table 2.1.

2.3 Division in regions

As explained in section 2.2, periodicities are applied in the x-, θ- and z-directions in Cartesian, polar and axisymmetric coordinate systems, therefore, regions are divided in the y-, r- and r-directions, respectively. The regions in this thesis are equally sized with the periodic boundaries, and the magnetic permeability in the geometry determines the division of regions. Fourier modeling is suitable for the regions with homogeneous permeability. For regions with varying permeability, they are modeled using meshed MEC, that allows to have unique permeability in each mesh element and hence, is capable to take non-homogeneous permeability into account.

One exception is the permanent magnets positioned in non-ferromagnetic materials or air. If the permeability of the permanent magnet is close to unity, it is possible to assign this as a Fourier region. The other exception is the current-carrying coil bundles in a slot. They usually do not spread over the full periodic boundaries, instead of introducing mode matching as in [54, 106], the presence of coils implies a MEC region in this thesis.

As a summary of the rule:

- All regions share the same periodic boundaries;
- The division of regions depends on the variation of magnetic permeability and presence of permanent magnets or coils.

An example is given for illustration with the geometry shown in Fig. 2.1(a). The geometry in the example is divided into five regions. The permanent magnets are buried in iron and the permeability changes significantly from ferromagnetic material to PM, hence, the permanent magnets and their adjacent iron are described by a MEC region that is indicated as ‘Region II: MEC region’ in the figure. Meanwhile, the presence of coils implies a new MEC region, indicated as ‘Region IV: MEC region’. On the other hand, the airgap, the air regions above the coils and beneath the PMs are all described as Fourier regions. However, if air surrounds the permanent magnets instead of iron, the PM array can be modeled as a Fourier region as shown in Fig. 2.1(b) with the label of ‘Region II: Fourier region’.

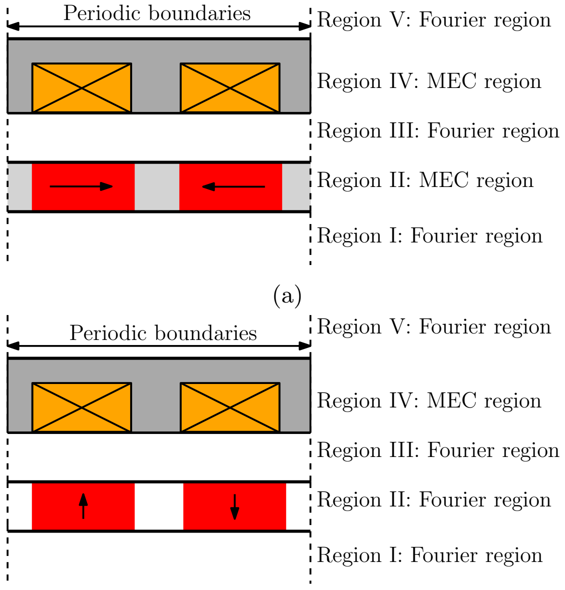
Periodic boundaries
Region V: Fourier region
Region IV: MEC region
Region III: Fourier region
Region II: MEC region
Region I: Fourier region
Periodic boundaries
Region V: Fourier region
Region IV: MEC region
Region III: Fourier region
Region II: Fourier region
Region I: Fourier region

(a)

(b)

Figure 2.1: The illustration of region division for two benchmark linear actuators.

2.4 Modeling of Fourier regions

For magnetostatic problem, the Maxwell equations are written as,

$$\nabla \times \vec{H} = \vec{J}, \tag{2.1}$$

$$\nabla \cdot \vec{B} = 0. \tag{2.2}$$

Since the divergence of $\vec{B}$ is zero as described in equation (2.2), the field $\vec{B}$ can be written as the rotation of the magnetic vector field, $\vec{A}$,

$$\vec{B} = \nabla \times \vec{A}. \tag{2.3}$$

Additionally, the magnetic flux density $\vec{B}$ is related to the magnetic field strength $\vec{H}$ by the constitution relation,

$$\vec{B} = \mu_0 \left(\mu_r \vec{H} + \vec{M}_0 \right), \tag{2.4}$$

where $\vec{M}_0$ represents the magnetization vector of a permanent magnet. Substituting equations (2.3) and (2.4) into equation (2.1) gives,

$$\nabla^2 \vec{A} = -\mu_0 \left(\nabla \times \vec{M}_0 \right) - \mu_0 \mu_r \vec{J}. \tag{2.5}$$

As mentioned in section 2.3, the presence of current density, $\vec{J}$, indicates a MEC region, hence, the expressions of $\vec{J}$ are omitted for Fourier regions. In 2D geometries, the magnetization vector has both p- and $q-$ components, therefore, only the l-component of the magnetic vector potential exists. The Poisson equation, (2.5), reduces to a single equation in each coordinate system and is given by the following,

Cartesian:

$$\frac{\partial^2 A_l}{\partial p^2} + \frac{\partial^2 A_l}{\partial q^2} = -\mu_0 \left(\frac{\partial M_p}{\partial q} - \frac{\partial M_q}{\partial p} \right), \tag{2.6}$$

Polar:

$$\frac{1}{p} \frac{\partial}{\partial p} p \frac{\partial A_l}{\partial p} + \frac{1}{p^2} \frac{\partial^2 A_l}{\partial q^2} = -\mu_0 \left[\frac{1}{p} \frac{\partial \left(p M_q \right)}{\partial p} - \frac{1}{p} \frac{\partial M_p}{\partial q} \right], \tag{2.7}$$

Axisymmetric:

$$\frac{1}{p} \frac{\partial}{\partial p} p \frac{\partial A_l}{\partial p} + \frac{\partial^2 A_l}{\partial q^2} - \frac{1}{p^2} A_l = -\mu_0 \left(\frac{\partial M_p}{\partial q} - \frac{\partial M_q}{\partial p} \right). \tag{2.8}$$

The solutions of equations (2.6)-(2.8) are given in Appendix A.

2.5 Modeling of MEC regions

The MEC regions are meshed to accurately obtain the magnetic field in both p- and q-directions. In contrast to Fourier regions that formulate the magnetostatic problem in the terms of magnetic vector potential, the magnetic field in the MEC regions is formed by the scalar potential in the center node of each mesh element. This section explains the meshing principle used in this thesis, the constitution of mesh elements, and the expression of magnetic fields within the MEC regions.

2.5.1 Meshing method

It is feasible to implement conformal or non-conformal meshing in the MEC regions. For a conformal meshing, there is always matching of vertices at the edge of two adjacent mesh elements. The advantage is that no interpolation is required at a conformal interface. In Fig. 2.2(a), an example of the conformal meshing is illustrated. As can be seen, all the vertices of one mesh element matches with corresponding vertices in one of the surrounding elements. In contrast, Fig. 2.2(b) shows an example of the non-conformal meshing, where partial matching of edges exists at the interface, e.g., between element k_1 and k_2. Such arrangement is able to provide more flexibility in mesh density. However, to simplify the implementation, only conformal meshing is discussed in this thesis. Although the number of elements in each layer is constrained to be the same, conformal meshing still provides the freedom of variation in both widths and heights, and is possible to make denser mesh where is needed, as shown in Fig. 2.2(c).

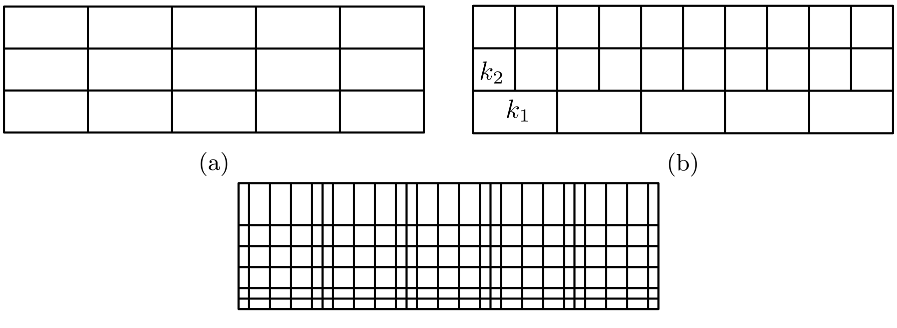

(a) (b)

(c)

Figure 2.2: (a) An example of the conformal meshing, (b) an example of the non-conformal meshing, and (c) an example of the conformal meshing with varying heights and widths.

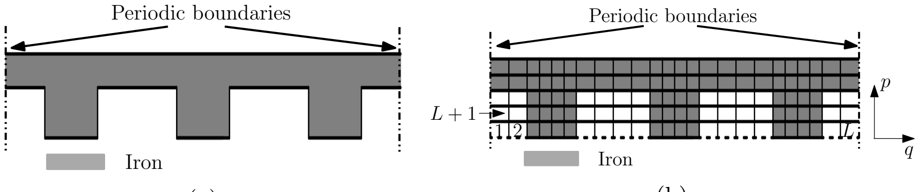

(a) (b)

Figure 2.3: (a) An example of a geometry with permeability variation, and (b) the schematic graph of meshing for the geometry in Fig. 2.3(a).

On the other hand, the mesh is formed such that the material boundaries coincide with the mesh element edges [93]. An example is given in Fig. 2.3(a) where the geometry has ferromagnetic material, and the schematic graph of the meshing is shown in Fig. 2.3(b). As illustrated, the mesh guarantees that each MEC element contains homogeneous material.

For explanation in the subsequent content, the mesh elements are numbered following the rule that ascends first in the q-direction and afterwards in the p-direction as illustrated in Fig. 2.3(b). Suppose that there are L elements in the first layer, the second layer starts at $(L+1)$ correspondingly, and the numbers of element are the same in all the layers of a region due to the conformal meshing.

2.5.2 Constitution of MEC elements

The mesh shapes are quadrilateral in this thesis, such that the reluctances and sources are naturally decomposed in normal and tangential directions for 2D geometries. In the geometric center of each element, a potential node, ψ, is defined, and it forms the unknown matrix of the MEC region. To solve the values of ψ, each MEC element should contain the information of reluctances and magnetic sources as shown in Fig. 2.4, where 'k' in the superscript denotes the number-

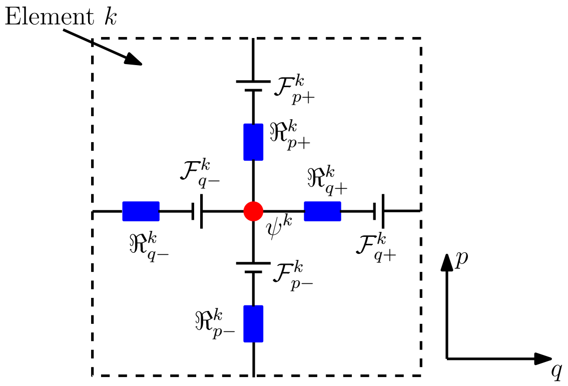

Figure 2.4: Reluctances and *mmf* sources of the element k.

ing of the element. In both positive and negative pq-directions, a reluctance and magnetic source are assumed. The reluctance is determined by the dimensions and permeability. The magnetic source is described by the magnetomotive force (mmf). The derivation is divided into three categories, i.e., PM related, current related and saturation related, which is repectively explained in sections 2.5.4, 2.5.5 and 2.8.

2.5.3 Magnetic reluctances

As depicted in Fig. 2.4, reluctances are assumed from the potential node to each of the edges. To be more specific, $\Re^k_{q-}$, $\Re^k_{q+}$, $\Re^k_{p-}$ and $\Re^k_{p+}$ are defined to cover the space from the potential node to the edges in $-q$-, $+q$-, $-p$- and $+p$-directions, respectively. As examples, the reluctances are given for several commonly used shapes, i.e., rectangular shape in the Cartesian coordinate system, circular sector shape in the polar coordinate system, and rectangular shape in the axisymmetric coordinate system.

Rectangular-shaped element in the Cartesian coordinate system

Assume the rectangular MEC element in the Cartesian coordinate system is with the width of l^k_q in q-direction, length of l^k_p in p-direction and depth of l^k_l in l-direction. In Fig. 2.5(a), it illustrates the flux tubes assumed for the q-direction, where each of the flux tube covers half of the element in the q-direction with the cross section in the pl-plane. The corresponding reluctances, $\Re^k_{q-}$ and $\Re^k_{q+}$, both have a length of $l^k_q/2$ and a cross section S^k_{pl} equals to $l^k_p l^k_l$. The expression of the reluctances is therefore [93],

$$\Re^k_{q-} = \Re^k_{q+} = \frac{l^k_q}{2\mu_0\mu^k_r S^k_{pl}} = \frac{l^k_q}{2\mu_0\mu^k_r l^k_p l^k_l}, \tag{2.9}$$

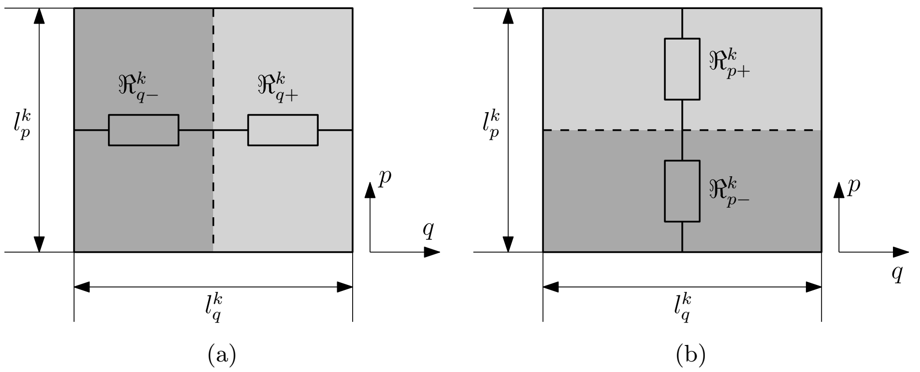

(a) (b)

Figure 2.5: The MEC element with a rectangular shape in the Cartesian coordinate system: flux tubes and reluctances (a) in the q-direction, and (b) in the p-direction.

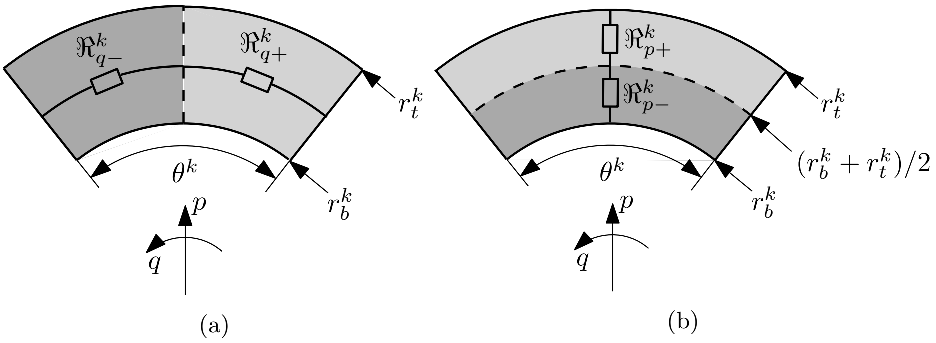

(a) (b)

Figure 2.6: The MEC element with a circular sector shape in the polar coordinate system: flux tubes and reluctances (a) in the q-direction, and (b) in the p-direction.

where μ_r^k is the relatively permeability. Similar to the reluctances in the q-direction, two flux tubes are assumed for the p-direction as well, that are shown in Fig. 2.5(b). The reluctances, $\Re_{p-}^k$ and $\Re_{p+}^k$, both have a length of $l_p^k/2$ and a cross section of S_{ql}^k equals to $l_q^k l_l^k$, hence, the reluctances are given as,

$$\Re_{p-}^k = \Re_{p+}^k = \frac{l_p^k}{2\mu_0\mu_r^k S_{ql}^k} = \frac{l_p^k}{2\mu_0\mu_r^k l_q^k l_l^k}. \tag{2.10}$$

Circular-sector-shaped element in the polar coordinate system

Figure 2.6 shows the circular-sector-shaped element in the polar coordinate system, where the angle remains the same, θ^k, along the p-direction. The radius at the bottom and top of the element is r_b^k and r_t^k, respectively, and the depth in the l-direction is l_l^k. In Fig. 2.6(a), it illustrates the flux tubes assumed for the

q-direction, each of the flux tubes cover half of the element in the q-direction. Therefore, the values of $\Re^k_{q-}$ and $\Re^k_{q+}$ are equal, and the expression is,

$$\Re^k_{q-} = \Re^k_{q+} = \frac{\theta^k}{2\mu_0\mu_r^k l_l^k \ln\left(\frac{r_t^k}{r_b^k}\right)}. \tag{2.11}$$

For the flux tube in the p-direction, the element is divided by an arc with the radius of the mean value of r_t^k and r_b^k, as illustrated in Fig. 2.6(b). Since the radii are different in the top and bottom flux tubes, the analytical expressions of $\Re^k_{p-}$ and $\Re^k_{p+}$ are not the same, given as

$$R^k_{p+} = \frac{1}{\mu_0\mu_r^k\theta^k l_l^k}\ln\left(\frac{2r_t^k}{r_t^k + r_b^k}\right), \tag{2.12}$$

$$R^k_{p-} = \frac{1}{\mu_0\mu_r^k\theta^k l_l^k}\ln\left(\frac{r_t^k + r_b^k}{2r_b^k}\right). \tag{2.13}$$

However, if the difference between r_b^k and r_t^k is small, $\Re^k_{p-}$ and $\Re^k_{p+}$ are almost equal.

Rectangular-shaped element in the axisymmetric coordinate system

In Fig. 2.7(a) and (b), the cross section of an element in 2D view for the axisymmetric coordinate system is illustrated, which is similar to the one in the Cartesian coordinate system. However, if consider such an element in 3D view as shown in Fig. 2.7(c), S^k_{pl} is actually the circumferential surface of a cylinder for $\Re^k_{q-}$ and $\Re^k_{q+}$. The expression is consequently,

$$R^k_{q-} = R^k_{q+} = \frac{\frac{l_q^k}{2}}{\mu_0\mu_r^k\left(2\pi\frac{r_t + r_b}{2}\right)(r_t - r_b)} = \frac{l_q^k}{2\mu_0\mu_r^k\pi\left(r_t^2 - r_b^2\right)}. \tag{2.14}$$

For the p-direction, the length in the l-direction are different in the top and bottom flux tubes, therefore, $\Re^k_{p-}$ and $\Re^k_{p+}$ are different, and are described as,

$$R^k_{p+} = \frac{1}{2\mu_0\mu_r^k\pi l_q^k}\ln\left(\frac{2r_t^k}{r_t^k + r_b^k}\right), \tag{2.15}$$

$$R^k_{p-} = \frac{1}{2\mu_0\mu_r^k\pi l_q^k}\ln\left(\frac{r_t^k + r_b^k}{2r_b^k}\right). \tag{2.16}$$

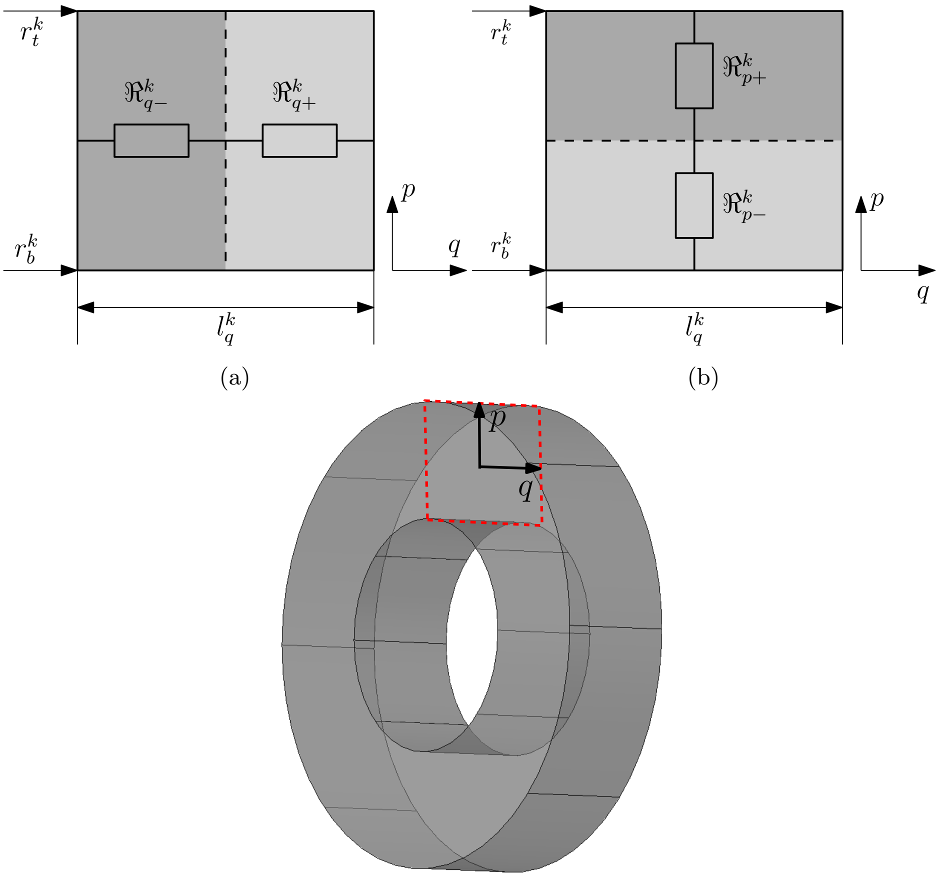
r_t^k
$\Re_{q-}^k$
$\Re_{q+}^k$
r_b^k
p
q
l_q^k
r_t^k
$\Re_{p+}^k$
$\Re_{p-}^k$
r_b^k
p
q
l_q^k
p
q

(a) (b)

(c)

Figure 2.7: The MEC element with a rectangular shape in the axisymmetric coordinate system: (a) flux tubes and reluctances in the q-direction, (b) flux tubes and reluctances in the p-direction, and (c) the cross section of an element in 3D view.

Irregular-shaped element

If the element shapes are not defined by the aforementioned regular shapes, the reluctances should be calculated by the general equations,

$$\Re^k_{q-} = \frac{1}{\mu_0 \mu_r} \int\limits_{l^k_{q-}} \frac{1}{S^k_{pl}(q)} dq, \tag{2.17}$$

$$\Re^k_{q+} = \frac{1}{\mu_0 \mu_r} \int\limits_{l^k_{q+}} \frac{1}{S^k_{pl}(q)} dq, \tag{2.18}$$

$$\Re^k_{p-} = \frac{1}{\mu_0 \mu_r} \int\limits_{l^k_{p-}} \frac{1}{S^k_{ql}(p)} dp, \tag{2.19}$$

$$\Re^k_{p+} = \frac{1}{\mu_0 \mu_r} \int\limits_{l^k_{p+}} \frac{1}{S^k_{ql}(p)} dp. \tag{2.20}$$

2.5.4 Permanent magnet related magnetomotive force

The mmf is used to describe the magnetic sources in the MEC region. In this subsection, the permanent magnet related mmf source is derived. By using the proper meshing algorithm, the description of the MEC element is limited to either PM presence or PM absence, and the PM related mmf only exists in the elements where the permanent magnet is located. The value of the mmf is defined by the magnetization and element size. Since the field is described in pq-directions, the magnetization has to be decomposed into pq-directions as well. The expression of the mmf is,

$$\mathcal{F}^k_{p-} = \frac{\vec{M}^k_p l^k_{p-}}{\mu^k_r}, \tag{2.21}$$

$$\mathcal{F}^k_{p+} = \frac{\vec{M}^k_p l^k_{p+}}{\mu^k_r}, \tag{2.22}$$

$$\mathcal{F}^k_{q-} = \frac{\vec{M}^k_q l^k_{q-}}{\mu^k_r}, \tag{2.23}$$

$$\mathcal{F}^k_{q+} = \frac{\vec{M}^k_q l^k_{q+}}{\mu^k_r}, \tag{2.24}$$

where μ_r^k takes the exact value of the PM relatively permeability. As the potential of a MEC element is defined to locate at the geometric center, it is often,

$$l_{p-}^k = l_{p+}^k = \frac{l_p^k}{2}, \tag{2.25}$$

$$l_{q-}^k = l_{q+}^k = \frac{l_q^k}{2}, \tag{2.26}$$

and if this holds, $\mathcal{F}_{p-}^k = \mathcal{F}_{p+}^k$ and $\mathcal{F}_{q-}^k = \mathcal{F}_{q+}^k$.

2.5.5 Current related magnetomotive force

Unlike the PM related magnetomotive force that only exists in the elements where physically the PM is present, the current related magnetomotive force forms contours within and outside the coil regions, and the distribution of mmfs has to guarantee the fulfillment of Ampere's law for any arbitrary contours. There are several arrangements that can meet this law. In [89], the q-directional current related mmf is introduced for the situation of homogeneous current density within one slot. In this section, it is extended to two current densities within one slot, which is applicable for more situations, e.g., switched reluctance machines, flux switching machines, variable flux reluctance machines, etc. Three distribution methods are introduced, i.e., mmf in merely the p-direction, in merely the q-direction, and in both pq-directions. Since the derivation of these methods are similar, herewith only the first one is elaborated in this subsection, and the latter two are introduced in Appendix B.

mmf in p-direction for the Cartesian coordinate system

For the method of distributing mmfs in merely the p-direction, the derivation starts from a simple topology with a single coil bundle in one slot in the Cartesian coordinate system, as shown in Fig. 2.8(a), where the coil has a width of w_c and a height of h_c. Two typical contours are used to explain the arrangement of mmf values, in which contour (1) encloses the whole coil region and contour (2) encloses part of the coil. Based on Ampere's law, the summation of the mmf in contour (1) should satisfy

$$\sum mmf_{(1)} = JS_c, \tag{2.27}$$

where S_c is the slot area that equals to $w_c h_c$. Assume the mmf sources for contour (1) concentrate in two columns of elements within the height of h_c in the teeth as shown in Fig. 2.8(b). It indicates that the summation of mmf in the left and right tooth should equal to $JS_c/2$ and $-JS_c/2$, respectively, where the sign '-' implies an actual mmf opposite to the pre-defined direction.

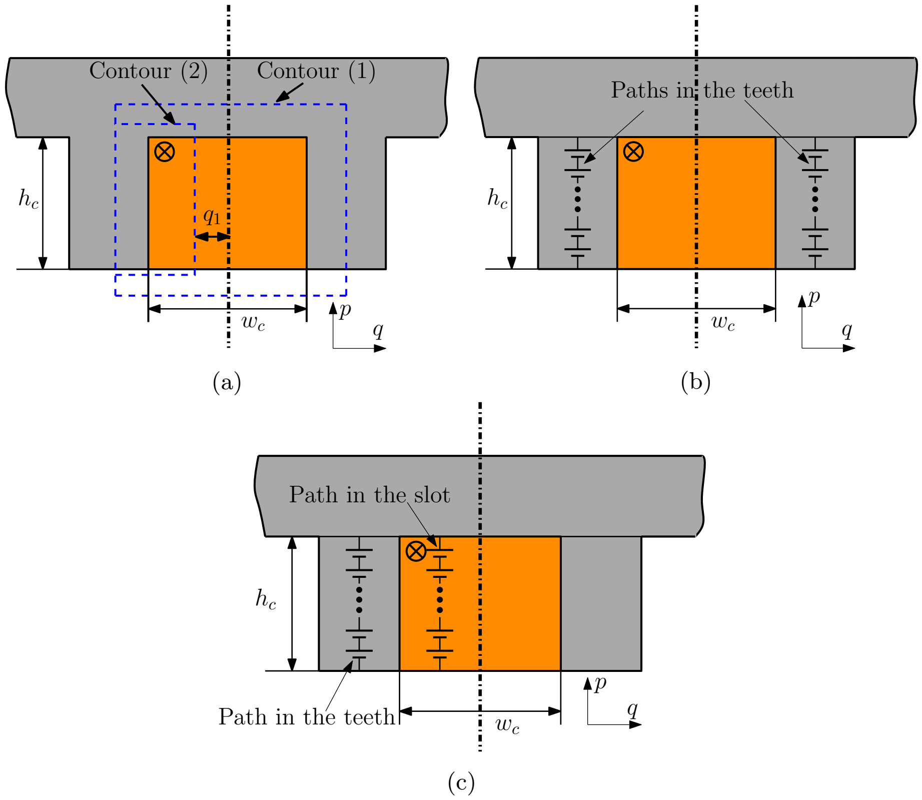
Contour (2)
Contour (1)
h_c
q_1
w_c
p
q
(a)
Paths in the teeth
h_c
w_c
p
q
(b)
Path in the slot
h_c
Path in the teeth
w_c
p
q
(c)

Figure 2.8: (a) Topology of a single coil in one slot and two representative contours, (b) distribution of mmfs for paths of contour (1) in the teeth, and (c) distribution of mmfs for paths of contour (2) in the tooth and slot.

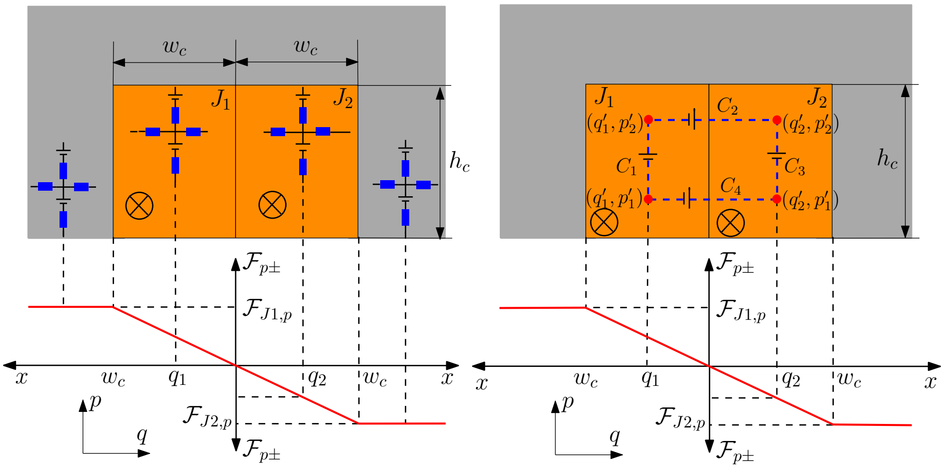
w_c
w_c
J_1
J_2
h_c
$\mathcal{F}_{p\pm}$
$\mathcal{F}_{J1,p}$
x
w_c
q_1
q_2
w_c
x
p
q
$\mathcal{F}_{J2,p}$
$\mathcal{F}_{p\pm}$
J_1
C_2
J_2
(q_1', p_2')
(q_2', p_2')
C_1
C_3
C_4
(q_1', p_1')
(q_2', p_1')
h_c
$\mathcal{F}_{p\pm}$
$\mathcal{F}_{J1,p}$
x
w_c
q_1
q_2
w_c
x
p
q
$\mathcal{F}_{J2,p}$
$\mathcal{F}_{p\pm}$

(a) (b)

Figure 2.9: Illustration of the mmf distribution: (a) for the topology of two coils in one slot ($\mathcal{F}_{J_1,p} = J_1 w_c h_c$ and $\mathcal{F}_{J_2,p} = J_2 w_c h_c$), and (b) the path that partially encloses both coils.

On the other hand, the summation of the mmf sources in contour (2) should satisfy

$$\sum mmf_{(2)} = \left(\frac{1}{2} - \frac{q_1}{w_c}\right) JS_c, \tag{2.28}$$

where q_1 is the distance between the slot centerline and the edge of contour (2) in the slot. Assume the mmf sources for contour (2) are distributed in the teeth and slot within the height of h_c, as shown in Fig. 2.8(c). As derived for contour (1), the summation of the mmfs in the tooth equals to $JS_c/2$, consequently, the summation of mmfs in the slot has to be $\frac{q_1}{w_c} JS_c$ to satisfy equation (2.28). This indicates that the mmf in the slot is linear to the value of q_1 defined in Fig. 2.8. For example, if a path lies in the slot for $q_1 = 0.25w_c$, a quarter of the coil is enclosed, summation of mmfs at the path should be $0.25J_cS_c$. As such, the rule comes that the distribution of mmf has a dependence on the element location, showing a linear relationship to the q-coordinate of the element until reaching the slot edges.

Additionally, to obtain the mmf for a single element, the dimension of the element itself has to be considered as well. Therefore, the mmf is given as

$$\mathcal{F}^k_{p\pm} = \frac{l^k_{p\pm}}{h_c} \cdot JS_c \tag{2.29}$$

when located in the tooth, and is,

$$F^k_{p\pm} = \frac{l^k_{p\pm}}{h_c} \cdot \frac{q_1}{w_c} JS_c \tag{2.30}$$

Table 2.2: Distribution of the current related *mmf* sources in the p-direction for the example in Fig. 2.9(a).

Location	$\mathcal{F}^k_{p\pm}$ for J_1	$\mathcal{F}^k_{q\pm}$ for J_1	$\mathcal{F}^k_{p\pm}$ for J_2	$\mathcal{F}^k_{q\pm}$ for J_2
Tooth	$\frac{l^k_{p\pm}}{h_c}\mathcal{F}_{J1,p}$	0	$-\frac{l^k_{p\pm}}{h_c}\mathcal{F}_{J2,p}$	0
Slot	$\frac{q^k}{w_c}\frac{l^k_{p\pm}}{h_c}\mathcal{F}_{1,p}$	0	$-\frac{q^k}{w_c}\frac{l^k_{p\pm}}{h_c}\mathcal{F}_{2,p}$	0

Notes: q^k is the q-coordinate of element k, $\mathcal{F}_{J_1,p} = J_1 w_c h_c$ and $\mathcal{F}_{J_2,p} = J_2 w_c h_c$.

when located in the slot.

The aforementioned concept is applied to the topology of two coils in one slot. Figure 2.9(a) shows the coils positioned in the slot with two different current densities, J_1 and J_2. The *mmf* representing the left coil is arranged in the left tooth and left half of the slot, while the *mmf* for the right coil is arranged in the right tooth and slot, respectively. Having the origin at the center line of the slot, the distribution of the *mmf* is illustrated in Fig. 2.9(a). The *mmf*s in the left and right teeth are linear to $J_1 S_c$ and $-J_2 S_c$, respectively, while in the slot, the *mmf*s are also linear to the value of q-coordinate. Taking into account the element sizes, the obtained *mmf* values are listed in Table 2.2.

A contour shown in Fig. 2.9(b), that partially encloses two coils simultaneously, is used to verify the above results. The contour is defined by four vertices with the coordinates of (q'_1, p'_1), (q'_1, p'_2), (q'_2, p'_1) and (q'_2, p'_2), marked as the red dots in the figure. The *mmf* of the four edges are calculated as:

$$mmf_{C_1} = \frac{q'_1}{w_c} J_1 w_c h_c \int_{p'_1}^{p'_2} d\left(\frac{l^k_{p\pm}}{h_c}\right) = q'_1 J_1 \left(p'_2 - p'_1\right), \tag{2.31}$$

$$mmf_{C_2} = 0, \tag{2.32}$$

$$mmf_{C_3} = -\frac{q'_2}{w_c} J_2 w_c h_c \int_{p'_1}^{p'_2} d\left(\frac{l^k_{p\pm}}{h_c}\right) = -q'_2 J_2 \left(p'_2 - p'_1\right), \tag{2.33}$$

$$mmf_{C_4} = 0. \tag{2.34}$$

The total *mmf* is therefore, $mmf_{C_1} + mmf_{C_2} - mmf_{C_3} - mmf_{C_4} = q'_1 J_1 \left(p'_2 - p'_1\right) + q'_2 J_2 \left(p'_2 - p'_1\right)$, which exactly equals to the current enclosed by this contour, stating the fulfillment of Ampere's law.

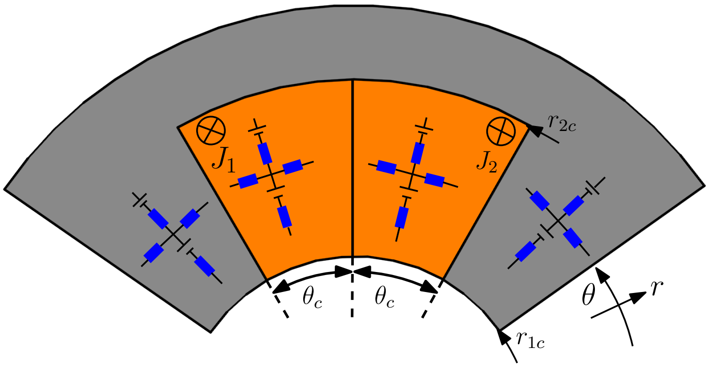

(a)

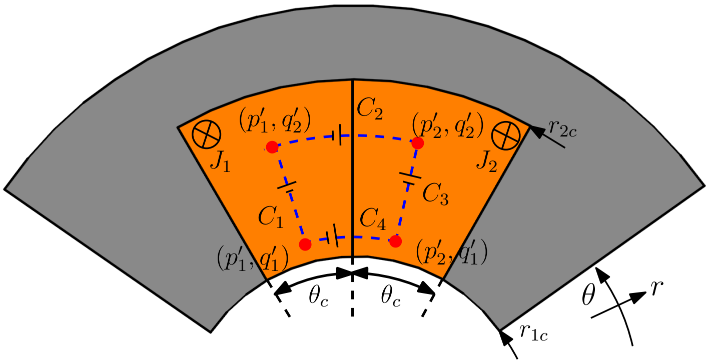

(b)

Figure 2.10: (a) Topology of two coils in one slot, and (b) the path that partially encloses both coils.

mmf in the p-direction for the axisymmetric coordinate system

Since the 2D view of the region in the axisymmetric coordinate system is similar as in the Cartesian coordinate system, the expression of the mmf is the same as the Cartesian coordinate system.

mmf in the p-direction for the polar coordinate system

For the polar coordinate system, the surface area of coil regions follows $\int d(qp^2)$, instead of $\int d(pq)$ for the Cartesian coordinate system. The integration, $\int d(qp^2)$, shows a linear relationship with q-coordinate and a quadratically linear relationship with p-coordinate, which is reflected by the element location and element size, respectively. This rule is explained by the geometry of two coils in a slot as shown in Fig. 2.10(a). Assume that the slot is with an angle of $2\theta_c$, an inner and outer radius of r_{1c} and r_{2c}, respectively, the distribution of mmfs is summarized

Table 2.3: Distribution of current related mmf sources in the p-direction for the example in Fig. 2.10(a).

Pos.	$\mathcal{F}_{p+}^k$ for J_1	$\mathcal{F}_{p-}^k$ for J_1	$\mathcal{F}_{q\pm}^k$ for J_1
Tooth	$\frac{(r_t^k)^2-(r_m^k)^2}{r_{2c}^2-r_{1c}^2}\mathcal{F}_{J1,p}$	$\frac{(r_m^k)^2-(r_b^k)^2}{r_{2c}^2-r_{1c}^2}\mathcal{F}_{J1,p}$	0
Slot	$\frac{q^k}{\theta_c}\frac{(r_t^k)^2-(r_m^k)^2}{r_{2c}^2-r_{1c}^2}\mathcal{F}_{1,p}$	$\frac{q^k}{\theta_c}\frac{(r_m^k)^2-(r_b^k)^2}{r_{2c}^2-r_{1c}^2}\mathcal{F}_{1,p}$	0
Pos.	$\mathcal{F}_{p+}^k$ for J_2	$\mathcal{F}_{p-}^k$ for J_2	$\mathcal{F}_{q\pm}^k$ for J_2
Tooth	$-\frac{(r_t^k)^2-(r_m^k)^2}{r_{2c}^2-r_{1c}^2}\mathcal{F}_{J2,p}$	$-\frac{(r_m^k)^2-(r_b^k)^2}{r_{2c}^2-r_{1c}^2}\mathcal{F}_{J2,p}$	0
Slot	$-\frac{q^k}{\theta_c}\frac{(r_t^k)^2-(r_m^k)^2}{r_{2c}^2-r_{1c}^2}\mathcal{F}_{2,p}$	$-\frac{q^k}{\theta_c}\frac{(r_m^k)^2-(r_b^k)^2}{r_{2c}^2-r_{1c}^2}\mathcal{F}_{2,p}$	0

Notes: $\mathcal{F}_{1,p} = J_1\pi[(r_{2c})^2-(r_{1c})]^2\theta_c$, $\mathcal{F}_{2,p} = J_2\pi[(r_{2c})^2-(r_{1c})]^2\theta_c$, r_t^k and r_b^k is, respectively, the top and bottom radius of element k, and $r_m^k = (r_t^k + r_b^k)/2$.

in Table 2.3. As listed, the values of $\mathcal{F}_{p-}^k$ and $\mathcal{F}_{p+}^k$ are different since the upper and bottom halves of an element are not symmetric as explained in section 2.5.3. To verify the results, a path shown in Fig. 2.10(b) that partially encloses both coils is considered. The mmfs of the four edges are calculated as:

$$mmf_{C_1} = q_1' J_1\pi \int_{p_1'}^{p_2'} d\left(\left(r_t^k\right)^2 - \left(r_b^k\right)^2\right) = q_1' J_1\pi \left[\left(p_2'\right)^2 - \left(p_1'\right)^2\right], \tag{2.35}$$

$$mmf_{C_2} = 0, \tag{2.36}$$

$$mmf_{C_3} = -q_2' J_2\pi \int_{p_1'}^{p_2'} d\left(\left(r_t^k\right)^2 - \left(r_b^k\right)^2\right) = -q_2' J_2\pi \left[\left(p_2'\right)^2 - \left(p_1'\right)^2\right], \tag{2.37}$$

$$mmf_{C_4} = 0. \tag{2.38}$$

As such, the total magnetomotive force is, $mmf_{C_1} + mmf_{C_2} - mmf_{C_3} - mmf_{C_4} = q_1' J_1\pi \left[\left(p_2'\right)^2 - \left(p_1'\right)^2\right] + q_2' J_2\pi \left[\left(p_2'\right)^2 - \left(p_1'\right)^2\right]$, which exactly equals to the enclosed current.

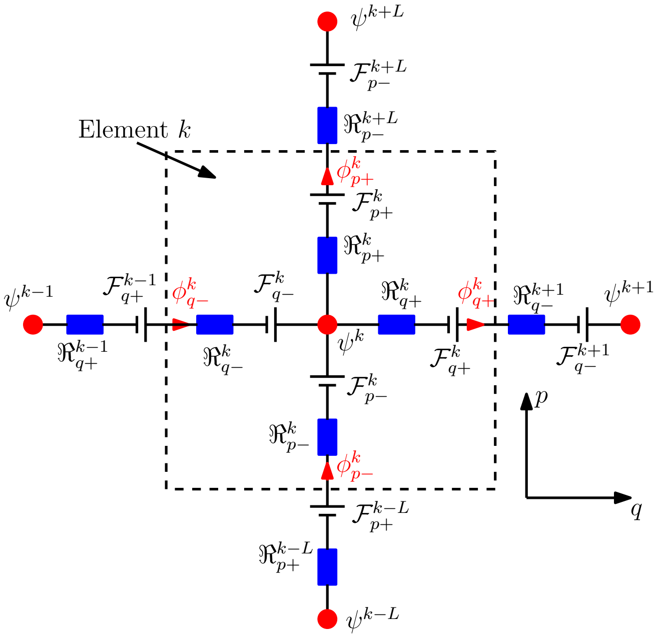
ψ^{k+L}
$\mathcal{F}^{k+L}_{p-}$
$\Re^{k+L}_{p-}$
Element k
ϕ^k_{p+}
$\mathcal{F}^k_{p+}$
$\Re^k_{p+}$
ψ^{k-1}
$\mathcal{F}^{k-1}_{q+}$
ϕ^k_{q-}
$\mathcal{F}^k_{q-}$
$\Re^k_{q+}$
ϕ^k_{q+}
$\Re^{k+1}_{q-}$
ψ^{k+1}
$\Re^{k-1}_{q+}$
$\Re^k_{q-}$
ψ^k
$\mathcal{F}^k_{q+}$
$\mathcal{F}^{k+1}_{q-}$
$\mathcal{F}^k_{p-}$
p
$\Re^k_{p-}$
ϕ^k_{p-}
$\mathcal{F}^{k-L}_{p+}$
q
$\Re^{k-L}_{p+}$
ψ^{k-L}

Figure 2.11: Coupling of the MEC elements.

2.5.6 Magnetic field within MEC elements

After obtaining the reluctances and magnetomotive forces, the magnetostatic problem in MEC regions is derived using the magnetic scalar potential. As mentioned in section 2.5.2, each MEC element has a potential node in the geometric center. According to the Kirchoff's law, the flux goes into the node should be equal to the flux goes out. Assume the fluxes are predefined with the directions shown in Fig. 2.11, the conservation of flux gives,

$$\phi^k_{q-} + \phi^k_{p-} - \phi^k_{p+} - \phi^k_{q+} = 0. \tag{2.39}$$

To obtain the fluxes in equation (2.39), the coupling among MEC elements has to be considered. For an element that is not at the boundaries of an MEC region, it is connected to four adjacent elements that are respectively in the $-q$, $+q$, $-p$ and $+p$-directions, as shown in Fig. 2.11. Assume there are L elements in each layer, the four adjacent elements are consequently numbered as $k-1$, $k+1$, $k-L$ and $k+L$, respectively. As a result, the fluxes in equation (2.39) are defined by the potential of element k and its four surroundings, that gives,

$$\phi_{p-}^{k} = \frac{\psi^{k-L} - \psi^{k} + \mathcal{F}_{p+}^{k-L} + \mathcal{F}_{p-}^{k}}{\Re_{p+}^{k-L} + \Re_{p-}^{k}}, \tag{2.40}$$

$$\phi_{p+}^{k} = \frac{\psi^{k} - \psi^{k+L} + \mathcal{F}_{p+}^{k} + \mathcal{F}_{p-}^{k+L}}{\Re_{p+}^{k} + \Re_{p-}^{k+L}}, \tag{2.41}$$

$$\phi_{q-}^{k} = \frac{\psi^{k-1} - \psi^{k} + \mathcal{F}_{q+}^{k-1} + \mathcal{F}_{q-}^{k}}{\Re_{q+}^{k-1} + \Re_{q-}^{k}}, \tag{2.42}$$

$$\phi_{q+}^{k} = \frac{\psi^{k} - \psi^{k+1} + \mathcal{F}_{q+}^{k} + \mathcal{F}_{q-}^{k+1}}{\Re_{q+}^{k} + \Re_{q-}^{k+1}}, \tag{2.43}$$

where ψ^{k-L}, ψ^{k+L}, ψ^{k-1} and ψ^{k+1} represent the potentials of element $k-L$, $k+L$, $k-1$ and $k+1$, respectively, and $\mathcal{F}_{p\pm}^{k-L}$, $\mathcal{F}_{p\pm}^{k+L}$, $\mathcal{F}_{p\pm}^{k-1}$, $\mathcal{F}_{p\pm}^{k+1}$, $\mathcal{F}_{q\pm}^{k-L}$, $\mathcal{F}_{q\pm}^{k+L}$, $\mathcal{F}_{q\pm}^{k-1}$ and $\mathcal{F}_{q\pm}^{k+1}$ represent the magnetomotive forces of elements $k-L$, $k+L$, $k-1$ and $k+1$ in $\pm p$- and $\pm q$-directions, respectively.

With the obtained fluxes within an element, the magnetic flux density is calculated by taking the mean values from the positive and negative directions, given as,

$$B_{q}^{k} = \frac{\phi_{q-}^{k} + \phi_{q+}^{k}}{2S_{pl}^{k}}, \tag{2.44}$$

$$B_{p}^{k} = \frac{\phi_{p-}^{k} + \phi_{p+}^{k}}{2S_{ql}^{k}}. \tag{2.45}$$

If S_{pl}^{k} or S_{ql}^{k} varies along the p- or q-directions, the linear interpolation is performed.

2.5.7 Elements at the boundaries of MEC regions

Periodicity is used to describe the magnetic field for the elements at the periodic boundaries of an MEC region. Elements located in the first column next to the periodic boundaries, illustrated in dark gray in Fig. 2.12, are coupled to the last column next to the periodic boundaries that are illustrated in light gray in Fig. 2.12. This means, for element k that lies in the first column, the according element $k-1$ is assumed to locate in the last column, with the actual numbering as $k+L-1$. Similarly, for element k that lies in the last column, the according element $k+1$ locates in the first column, with the actual numbering as $k-L+1$. Such relationship is summarized as,

$$k-1 \rightarrow k+L-1, \qquad (k \text{ in the first column}), \tag{2.46}$$

$$k+1 \rightarrow k-L+1, \qquad (k \text{ in the last column}), \tag{2.47}$$

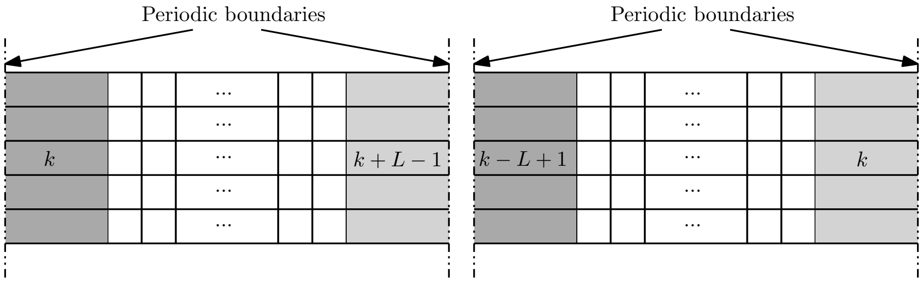

(a) (b)

Figure 2.12: Illustration of element k located (a) in the first column next to the periodic boundaries, and (b) in the last column next to the periodic boundaries.

As a result, equations (2.42)-(2.43) become,

$$\phi_{q-}^{k} = \frac{\psi^{k+L-1} - \psi^{k} + \mathcal{F}_{q+}^{k+L-1} + \mathcal{F}_{q-}^{k}}{\Re_{q+}^{k+L-1} + \Re_{q-}^{k}}, \qquad (k \text{ in the first column}), \tag{2.48}$$

$$\phi_{q+}^{k} = \frac{\psi^{k} - \psi^{k-L+1} + \mathcal{F}_{q+}^{k} + \mathcal{F}_{q-}^{k-L+1}}{\Re_{q+}^{k} + \Re_{q-}^{k-L+1}}, \qquad (k \text{ in the last column}). \tag{2.49}$$

On the other hand, if an element lies in the bottom layer of an MEC region, there is no element $k-L$ lies beneath, instead, the value of ϕ_{p-}^{k} is obtained by the flux density in the Fourier region below. Similarly, if an element lies in the top layer of an MEC region, the value of ϕ_{p+}^{k} is defined by the flux density in the Fourier region above. The detailed explanation is given in section 2.6.1.

2.6 Boundary conditions

The equations of the magnetic field within the regions are introduced in previous sections. To solve the unknowns in the MEC and Fourier regions, boundary conditions should be satisfied in both normal and tangential directions. For coupled regions, the condition of continuous magnetic field has to be satisfied, while for the boundaries at the edge of the domain, Neumann or Dirichlet boundary conditions are applied. For illustration, the boundary conditions are defined for the two examples in Fig. 2.1, as presented in Fig. 2.13.

In this section, the equations of the following boundary conditions are discussed for the assumption that all the regions adopt the same coordinate system:

- Continuity between Fourier and MEC regions;
- Continuity between Fourier regions;

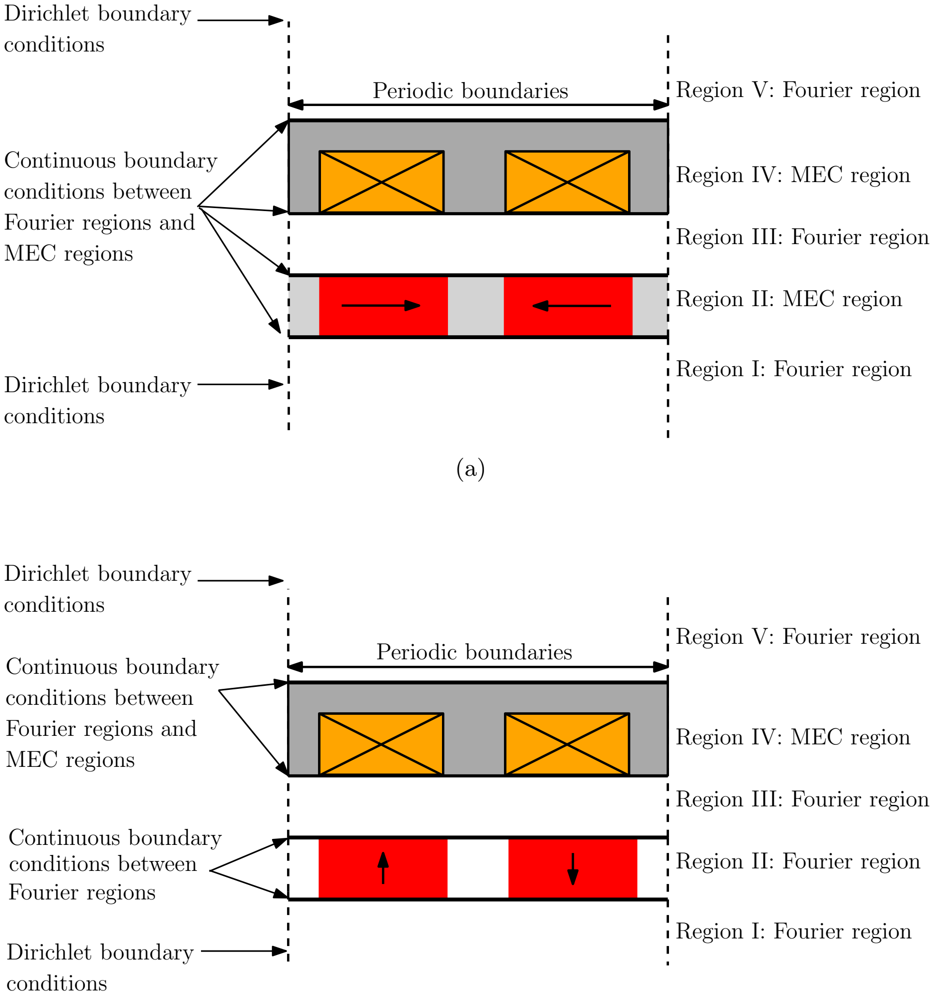
Dirichlet boundary conditions
Periodic boundaries
Region V: Fourier region
Continuous boundary conditions between Fourier regions and MEC regions
Region IV: MEC region
Region III: Fourier region
Region II: MEC region
Region I: Fourier region
Dirichlet boundary conditions
Dirichlet boundary conditions
Periodic boundaries
Region V: Fourier region
Continuous boundary conditions between Fourier regions and MEC regions
Region IV: MEC region
Region III: Fourier region
Continuous boundary conditions between Fourier regions
Region II: Fourier region
Region I: Fourier region
Dirichlet boundary conditions

(a)

(b)

Figure 2.13: The illustration of boundary conditions for two benchmark linear actuators.

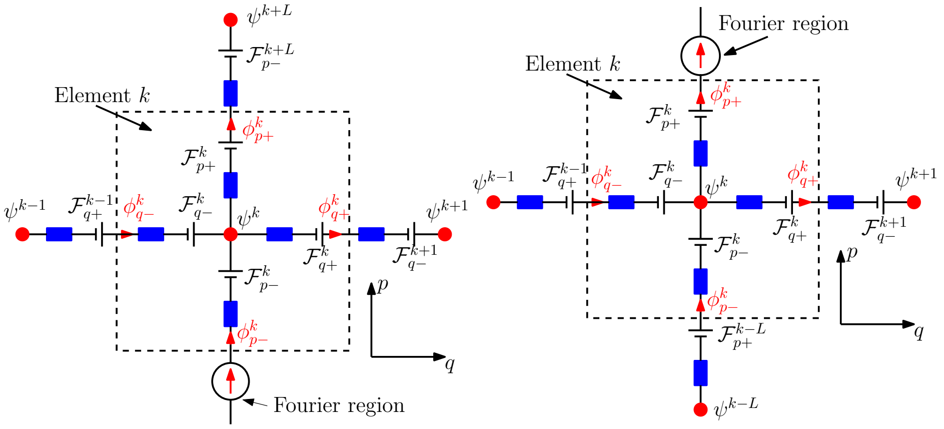
ψ^{k+L}
$\mathcal{F}_{p-}^{k+L}$
Element k
ϕ_{p+}^{k}
$\mathcal{F}_{p+}^{k}$
ψ^{k-1}
$\mathcal{F}_{q+}^{k-1}$
ϕ_{q-}^{k}
$\mathcal{F}_{q-}^{k}$
ψ^{k}
ϕ_{q+}^{k}
ψ^{k+1}
$\mathcal{F}_{q+}^{k}$
$\mathcal{F}_{q-}^{k+1}$
$\mathcal{F}_{p-}^{k}$
ϕ_{p-}^{k}
p
q
Fourier region
Fourier region
Element k
ϕ_{p+}^{k}
$\mathcal{F}_{p+}^{k}$
ψ^{k-1}
$\mathcal{F}_{q+}^{k-1}$
ϕ_{q-}^{k}
$\mathcal{F}_{q-}^{k}$
ψ^{k}
ϕ_{q+}^{k}
ψ^{k+1}
$\mathcal{F}_{q+}^{k}$
$\mathcal{F}_{q-}^{k+1}$
$\mathcal{F}_{p-}^{k}$
ϕ_{p-}^{k}
$\mathcal{F}_{p+}^{k-L}$
ψ^{k-L}
p
q

(a) (b)

Figure 2.14: Flux from the Fourier region for the MEC elements (a) in the bottom layer, and (b) in the top layer.

- Dirichlet/Neumann boundary condition of Fourier or MEC regions;

2.6.1 Continuous boundary conditions between Fourier and MEC regions

The magnetic field in Fourier regions and MEC regions are expressed in spatial frequency and space domains, respectively. The field continuity are ensured by equating normal magnetic flux density and tangential magnetic field strength.

Continuity of normal magnetic flux density

For the elements at the bottom or top boundaries of a MEC region, there are no adjacent elements connected below or above, hence, the coupling among MEC elements that are given by equations (2.40)-(2.41) is not valid directly due to the lack of ψ^{k-L} and ψ^{k+L}, respectively. Consequently, it is not possible to derive ϕ_{p-}^{k} or ϕ_{p+}^{k} directly to form the flux conservation described in equation (2.39). However, on the other side, the coupling with Fourier regions provides the extra flux sources that can be used to describe the inward or outward flux for a MEC element. To show this more intuitively, the flux sources from Fourier regions are illustrated in Fig. 2.14. For the MEC elements in the bottom layer, the inward flux is defined by the magnetic flux of the Fourier region below, while for the MEC elements in the top layer, the top outward flux is defined by the Fourier region above.

The magnetic flux from the Fourier region is obtained from the magnetic flux density and the corresponding surface area. For an element at the bottom or top layer, the Fourier region provides a magnetic flux as,

$$\phi_{p-}^{k} = \oint_{S} B_{p}^{FA_b}(q, h_b) dS_{ql}^{k}, \quad (k \in \mathbb{Z} : k \in [1, L]), \tag{2.50}$$

$$\phi_{p+}^{k} = \oint_{S} B_{p}^{FA_t}(q, h_b) dS_{ql}^{k}, \quad (k \in \mathbb{Z} : k \in [K - L + 1, K]), \tag{2.51}$$

where h_b is the p-coordinate where the coupling between Fourier and MEC regions appears, FA_b and FA_t indicate the Fourier region below or above the MEC region, L is the number of elements in one layer, and K is the total number of elements in the region. As such, the MEC elements are numbered within the interval of [1, L] for the bottom layer and are within [$K - L + 1$, K] for the top layer.

Assume q_1^k and q_0^k are the q-coordinates of the left and right edges for MEC-element k at the coupling interface, equations (2.50)-(2.51) can be rewritten as, Cartesian:

$$\begin{aligned} \phi_{p-}^{k} &= l_l^k \int_{q_0^k}^{q_1^k} B_{p}^{FA_b}(q, h_b) dq, \quad (k \in \mathbb{Z} : k \in [1, L]), \\ \phi_{p+}^{k} &= l_l^k \int_{q_0^k}^{q_1^k} B_{p}^{FA_t}(q, h_b) dq, \quad (k \in \mathbb{Z} : k \in [K - L + 1, K]), \end{aligned} \tag{2.52}$$

polar:

$$\phi_{p-}^{k} = l_l^k h_b \int_{q_0^k}^{q_1^k} B_{p}^{FA_b}(q, h_b) dq, \quad (k \in \mathbb{Z} : k \in [1, L]), \tag{2.53}$$

$$\phi_{p+}^{k} = l_l^k h_b \int_{q_0^k}^{q_1^k} B_{p}^{FA_t}(q, h_b) dq, \quad (k \in \mathbb{Z} : k \in [K - L + 1, K]), \tag{2.54}$$

axisymmetric:

$$\begin{aligned} \phi_{p-}^{k} &= 2\pi h_b \int_{q_0^k}^{q_1^k} B_{p}^{FA_b}(q, h_b) dq, \quad (k \in \mathbb{Z} : k \in [1, L]), \\ \phi_{p+}^{k} &= 2\pi h_b \int_{q_0^k}^{q_1^k} B_{p}^{FA_t}(q, h_b) dq, \quad (k \in \mathbb{Z} : k \in [K - L + 1, K]). \end{aligned} \tag{2.55}$$

Substituting $B_p^{FA_b}$ and $B_p^{FA_t}$ in equations (2.52)-(2.55) by the expression of the flux density in the Fourier region that is given by equation (A.13) in Appendix

A, the magnetic flux is evaluated as,

$$\phi_{p-}^{k} = \sum_{n=0}^{N_h} \left\{ -\frac{1}{\omega_n} \left[\cos\left(\omega_n q_1^k\right) - \cos\left(\omega_n q_0^k\right) \right] B_{psn}^{FA_b}(h_b) \mathcal{L}_l^k \right.$$
$$\left. + \frac{1}{\omega_n} \left[\sin\left(\omega_n q_1^k\right) - \sin\left(\omega_n q_0^k\right) \right] B_{pcn}^{FA_b}(h_b) \mathcal{L}_l^k \right\}, \quad (k \in \mathbb{Z} : k \in [1, L]), \tag{2.56}$$

$$\phi_{p+}^{k} = \sum_{n=0}^{N_h} \left\{ -\frac{1}{\omega_n} \left[\cos\left(\omega_n q_1^k\right) - \cos\left(\omega_n q_0^k\right) \right] B_{psn}^{FA_t}(h_b) \mathcal{L}_l^k \right.$$
$$\left. + \frac{1}{\omega_n} \left[\sin\left(\omega_n q_1^k\right) - \sin\left(\omega_n q_0^k\right) \right] B_{pcn}^{FA_t}(h_b) \mathcal{L}_l^k \right\}, \tag{2.57}$$
$$(k \in \mathbb{Z} : k \in [K - L + 1, K]),$$

where $\mathcal{L}_l^k$ is defined as,

$$\mathcal{L}_l^k = \begin{cases} l_l^k, & \text{Cartesian,} \\ h_b l_l^k, & \text{polar,} \\ 2\pi h_b, & \text{axisymmetric.} \end{cases} \tag{2.58}$$

After defining the inward and outward magnetic flux from the Fourier region, the continuity of normal magnetic flux density is realized by substituting ϕ_{p-}^{k} or ϕ_{p+}^{k} into the flux conservation equation, this gives,

$$\phi_{q-}^{k} - \phi_{q+}^{k} - \phi_{p+}^{k} + \sum_{n=0}^{N_h} \left\{ -\frac{1}{\omega_n} \left[\cos\left(\omega_n q_1^k\right) - \cos\left(\omega_n q_0^k\right) \right] B_{psn}^{FA_b}(h_b) \mathcal{L}_l^k \right.$$
$$\left. + \frac{1}{\omega_n} \left[\sin\left(\omega_n q_1^k\right) - \sin\left(\omega_n q_0^k\right) \right] B_{pcn}^{FA_b}(h_b) \mathcal{L}_l^k \right\} = 0, \quad (k \in \mathbb{Z} : k \in [1, L]), \tag{2.59}$$

$$\phi_{q-}^{k} - \phi_{q+}^{k} + \phi_{p-}^{k} - \sum_{n=0}^{N_h} \left\{ -\frac{1}{\omega_n} \left[\cos\left(\omega_n q_1^k\right) - \cos\left(\omega_n q_0^k\right) \right] B_{psn}^{FA_t}(h_b) \mathcal{L}_l^k \right.$$
$$\left. + \frac{1}{\omega_n} \left[\sin\left(\omega_n q_1^k\right) - \sin\left(\omega_n q_0^k\right) \right] B_{pcn}^{FA_t}(h_b) \mathcal{L}_l^k \right\} = 0,$$
$$(k \in \mathbb{Z} : k \in [K - L + 1, K]). \tag{2.60}$$

Continuity of tangential magnetic field strength

Different from the boundary condition of normal continuity that converts the magnetic field in the Fourier region into the space domain, the continuity in the tangential direction is realized by converting the magnetic field strength in the MEC region into the spatial frequency domain.

It is, first, assumed that the q-directional magnetic flux density and magnetization remains constant within a MEC element, such that the value at the top or bottom edge of an element equals to the value at the center. Accordingly, the q-directional magnetic field strength at the element edges is represented by the value at the center as well.

Using the constitutive relation equation (2.4), the magnetic field strength for element k, H_q^k, can be written in terms of the value of B_q^k, giving,

$$H_q^k = \frac{1}{\mu_0 \mu_r^k} B_q^k - \frac{1}{\mu_r^k} M_q^k. \tag{2.61}$$

Substituting the expression of B_q^k by equation (2.44), H_q^k is converted to,

$$H_q^k = \frac{\phi_{q-}^k + \phi_{q+}^k}{2\mu_0 \mu_r^k S_{pl}^k} - \frac{1}{\mu_r^k} M_q^k. \tag{2.62}$$

The values of H_q^k in the bottom or top MEC layers should be converted into spatial frequency domain with the same harmonic orders as in the Fourier region. Since H_q^k is assumed to be constant within each element, the waveform of magnetic field strength is actually staircase-shaped in a layer. Therefore, the conversion is derived as,

$$\begin{aligned} H_{qsn}^{MEC} &= \frac{2}{\tau_{per}} \int_0^{\tau_{per}} H_q^k \sin(\omega_n q) dq = \frac{2}{\tau_{per}} \sum_k \int_{q_0^k}^{q_1^k} H_q^k \sin(\omega_n q)\, dq, \\ &= -\frac{2}{\omega_n \tau_{per}} \sum_k H_q^k \left[\cos\left(\omega_n q_1^k\right) - \cos\left(\omega_n q_0^k\right)\right], \quad (n \in \mathbb{Z} : n \in [1, N_h]), \end{aligned} \tag{2.63}$$

$$\begin{aligned} H_{qcn}^{MEC} &= \frac{2}{\tau_{per}} \int_0^{\tau_{per}} H_q^k \cos(\omega_n q) dq = \frac{2}{\tau_{per}} \sum_k \int_{q_0^k}^{q_1^k} H_q^k \cos(\omega_n q)\, dq \\ &= \frac{2}{\omega_n \tau_{per}} \sum_k H_q^k \left[\sin\left(\omega_n q_1^k\right) - \sin\left(\omega_n q_0^k\right)\right], \quad (n \in \mathbb{Z} : n \in [1, N_h]), \end{aligned} \tag{2.64}$$

where τ_{per} is the width of periodicity. The obtained H_{qsn}^{MEC} and H_{qcn}^{MEC} should be kept equal to all the corresponding harmonics of the magnetic field strength in

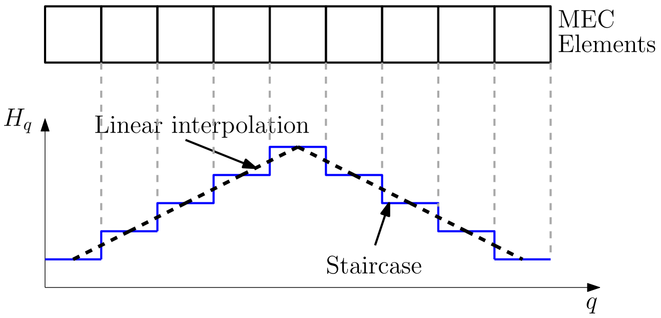

Figure 2.15: Two methods, i.e., staircase shaped and linear interpolation, for expressing H field in the q-direction.

the Fourier region. By substituting equation (2.62) into equations (2.63)-(2.64), this gives,

$$\begin{aligned}&\frac{1}{\mu_r^{FA_b}\mu_0}B_{qsn}^{FA_b} - \frac{1}{\mu_r^{FA_b}}M_{qsn}^{FA_b} = -\frac{2}{\omega_n\tau_{per}}\sum_{k=1}^{L}\left(\frac{\phi_{q-}^k+\phi_{q+}^k}{2\mu_0\mu_r^k S_{pl}^k} - \frac{1}{\mu_r^k}M_q^k\right)\\ &\left[\cos\left(\omega_n q_1^k\right)-\cos\left(\omega_n q_0^k\right)\right], \quad (n\in\mathbb{Z}: n\in[1,N_h]),\end{aligned} \tag{2.65}$$

$$\begin{aligned}&\frac{1}{\mu_r^{FA_b}\mu_0}B_{qcn}^{FA_b} - \frac{1}{\mu_r^{FA_b}}M_{qcn}^{FA_b} = \frac{2}{\omega_n\tau_{per}}\sum_{k=1}^{L}\left(\frac{\phi_{q-}^k+\phi_{q+}^k}{2\mu_0\mu_r^k S_{pl}^k} - \frac{1}{\mu_r^k}M_q^k\right)\\ &\left[\sin\left(\omega_n q_1^k\right)-\sin\left(\omega_n q_0^k\right)\right], \quad (n\in\mathbb{Z}: n\in[1,N_h]),\end{aligned} \tag{2.66}$$

for the bottom layer, and

$$\begin{aligned}&\frac{1}{\mu_r^{FA_t}\mu_0}B_{qsn}^{FA_t} - \frac{1}{\mu_r^{FA_t}}M_{qsn}^{FA_t} = -\frac{2}{\omega_n\tau_{per}}\sum_{k=K-L+1}^{K}\left(\frac{\phi_{q-}^k+\phi_{q+}^k}{2\mu_0\mu_r^k S_{pl}^k} - \frac{1}{\mu_r^k}M_q^k\right)\\ &\left[\cos\left(\omega_n q_1^k\right)-\cos\left(\omega_n q_0^k\right)\right], \quad (n\in\mathbb{Z}: n\in[1,N_h]),\end{aligned} \tag{2.67}$$

$$\begin{aligned}&\frac{1}{\mu_r^{FA_t}\mu_0}B_{qcn}^{FA_t} - \frac{1}{\mu_r^{FA_t}}M_{qcn}^{FA_t} = \frac{2}{\omega_n\tau_{per}}\sum_{k=K-L+1}^{K}\left(\frac{\phi_{q-}^k+\phi_{q+}^k}{2\mu_0\mu_r^k S_{pl}^k} - \frac{1}{\mu_r^k}M_q^k\right)\\ &\left[\sin\left(\omega_n q_1^k\right)-\sin\left(\omega_n q_0^k\right)\right], \quad (n\in\mathbb{Z}: n\in[1,N_h]),\end{aligned} \tag{2.68}$$

for the top layer, where ϕ_{q-}^k and ϕ_{q+}^k are evaluated by equations (2.42)-(2.43).

In addition to defining a staircase-shaped magnetic field strength, it is possible to use linear interpolation, the difference is shown in Fig. 2.15. The magnetic field strength with the linear interpolation is written as,

$$
\begin{aligned}
&H_q^k(q) = \left(\frac{H_q^k - H_q^{k-1}}{\dfrac{q_1^k - q_0^{k-1}}{2}} \right) \left(q - \frac{q_0^{k-1} + q_1^{k-1}}{2} \right) + H_q^{k-1}, \\
&\left(q \in \mathbb{R} : q \in \left[q_0^k, \frac{q_0^k + q_1^k}{2} \right] \right),
\end{aligned}
\tag{2.69}
$$

$$
\begin{aligned}
&H_q^k(q) = \left(\frac{H_q^{k+1} - H_q^k}{\dfrac{q_1^{k+1} - q_0^k}{2}} \right) \left(q - \frac{q_0^k + q_1^k}{2} \right) + H_q^k, \\
&\left(q \in \mathbb{R} : q \in \left[\frac{q_0^k + q_1^k}{2}, q_1^k \right] \right).
\end{aligned}
\tag{2.70}
$$

instead of equation (2.62). For MEC regions with adequate elements, the results of using these two methods are close.

2.6.2 Continuous boundary conditions between Fourier regions

Between two Fourier regions, continuity of the normal magnetic flux density and tangential magnetic field strength gives,

$$B_p^{\mathrm{i}}\left(h_b, q\right) = B_p^{\mathrm{i}+1}\left(h_b, q\right), \quad (q \in \mathbb{R} : q \in [0, \tau_{per}]), \tag{2.71}$$

$$H_q^{\mathrm{i}}\left(h_b, q\right) = H_q^{\mathrm{i}+1}\left(h_b, q\right), \quad (q \in \mathbb{R} : q \in [0, \tau_{per}]), \tag{2.72}$$

where h_b is the p-coordinate of the boundary, and i and $\mathrm{i}+1$ imply two adjacent Fourier regions. Using the constitutive relation described in equation (2.4), the magnetic field strength in equation (2.72) is written in terms of the magnetic flux density,

$$
\begin{aligned}
&\frac{1}{\mu_0 \mu_r^{\mathrm{i}}} B_q^{\mathrm{i}}\left(h_b, q\right) - \frac{1}{\mu_r^{\mathrm{i}}} M_q^{\mathrm{i}}\left(h_b, q\right) \\
&= \frac{1}{\mu_0 \mu_r^{\mathrm{i}+1}} B_q^{\mathrm{i}+1}\left(h_b, q\right) - \frac{1}{\mu_r^{\mathrm{i}+1}} M_q^{\mathrm{i}+1}\left(h_b, q\right), \quad (q \in \mathbb{R} : q \in [0, \tau_{per}]).
\end{aligned}
\tag{2.73}
$$

Since the magnetic field in Fourier regions is formulated in the spatial frequency domain, and adjacent Fourier regions are assumed to have the same spatial frequencies, the continuity defined by equations (2.71) and (2.73) implies equating the coefficients for both sine and cosine functions. Hence, equation (2.71) is converted to,

$$B_{psn}^{\mathrm{i}}(h_b) = B_{psn}^{\mathrm{i}+1}(h_b), \quad (n \in \mathbb{Z} : n \in [1, N_h]), \tag{2.74}$$

$$B_{pcn}^{\mathrm{i}}(h_b) = B_{pcn}^{\mathrm{i}+1}(h_b), \quad (n \in \mathbb{Z} : n \in [1, N_h]), \tag{2.75}$$

and equation (2.73) is converted to,

$$\begin{aligned}
&\frac{1}{\mu_0\mu_r^{\mathrm{i}}}B_{qsn}^{\mathrm{i}}\left(h_b\right)-\frac{1}{\mu_r^{\mathrm{i}}}M_{qsn}^{\mathrm{i}}\left(h_b\right)\\
&=\frac{1}{\mu_0\mu_r^{\mathrm{i}+1}}B_{qsn}^{\mathrm{i}+1}\left(h_b\right)-\frac{1}{\mu_r^{\mathrm{i}+1}}M_{qsn}^{\mathrm{i}+1}\left(h_b\right),\quad (n\in\mathbb{Z}:n\in[1,N_h]),
\end{aligned}\tag{2.76}$$

$$\begin{aligned}
&\frac{1}{\mu_0\mu_r^{\mathrm{i}}}B_{qcn}^{\mathrm{i}}\left(h_b\right)-\frac{1}{\mu_r^{\mathrm{i}}}M_{qcn}^{\mathrm{i}}\left(h_b\right)\\
&=\frac{1}{\mu_0\mu_r^{\mathrm{i}+1}}B_{qcn}^{\mathrm{i}+1}\left(h_b\right)-\frac{1}{\mu_r^{\mathrm{i}+1}}M_{qcn}^{\mathrm{i}+1}\left(h_b\right),\quad (n\in\mathbb{Z}:n\in[1,N_h]).
\end{aligned}\tag{2.77}$$

2.6.3 Dirichlet/Neumann boundary conditions

In addition to the continuity that applies at the interface of regions, the noncontinuous boundary conditions are applied at the edges of the geometric domain, which implies that the magnetic field vanishes to zero or only tangential field exists. The implementation of noncontinuous boundary conditions are different for Fourier and MEC regions, and are explained separately in the subsequent content.

Fourier regions

For a Fourier region with a boundary located at the edge of a geometric domain, e.g. $p \to \infty$, the magnetic field vanishes to zero, also known as the Dirichlet boundary condition. Under this circumstance, both the flux density in p- and q-directions are zero, which gives,

$$B_p^{\mathrm{i}}=0,\tag{2.78}$$

$$B_q^{\mathrm{i}}=0.\tag{2.79}$$

Equations (2.78)-(2.79) imply that the sum of the Fourier series is zero at $p \to \infty$, which can be interpreted that the coefficients for sine and cosine functions are all zero for all harmonics, this gives,

$$B_{psn}^{\mathrm{i}}\big|_{p\to\infty}=0,\quad (n\in\mathbb{Z}:n\in[1,N_h]),\tag{2.80}$$

$$B_{pcn}^{\mathrm{i}}\big|_{p\to\infty}=0,\quad (n\in\mathbb{Z}:n\in[1,N_h]),\tag{2.81}$$

$$B_{qsn}^{\mathrm{i}}\big|_{p\to\infty}=0,\quad (n\in\mathbb{Z}:n\in[1,N_h]),\tag{2.82}$$

$$B_{qcn}^{\mathrm{i}}\big|_{p\to\infty}=0,\quad (n\in\mathbb{Z}:n\in[1,N_h]).\tag{2.83}$$

Another type of non-continuous boundary condition that can be applied at the edge of Fourier regions is the Neumann boundary condition, i.e., the tangential

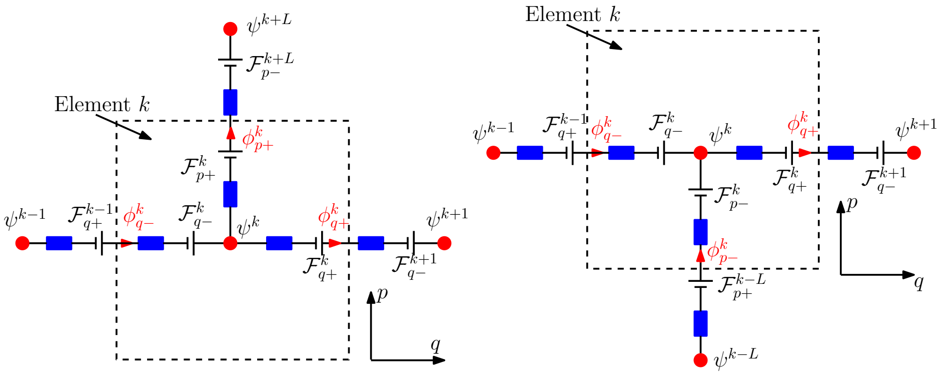
ψ^{k+L}
$\mathcal{F}_{p-}^{k+L}$
Element k
ϕ_{p+}^{k}
$\mathcal{F}_{p+}^{k}$
ψ^{k-1}
$\mathcal{F}_{q+}^{k-1}$
ϕ_{q-}^{k}
$\mathcal{F}_{q-}^{k}$
ψ^{k}
ϕ_{q+}^{k}
ψ^{k+1}
$\mathcal{F}_{q+}^{k}$
$\mathcal{F}_{q-}^{k+1}$
p
q
Element k
ψ^{k-1}
$\mathcal{F}_{q+}^{k-1}$
ϕ_{q-}^{k}
$\mathcal{F}_{q-}^{k}$
ψ^{k}
ϕ_{q+}^{k}
ψ^{k+1}
$\mathcal{F}_{p-}^{k}$
$\mathcal{F}_{q+}^{k}$
$\mathcal{F}_{q-}^{k+1}$
p
ϕ_{p-}^{k}
$\mathcal{F}_{p+}^{k-L}$
q
ψ^{k-L}

(a) (b)

Figure 2.16: Noncontinuous boundary conditions for elements located at (a) the bottom of the geometric domain, and (b) the top of the geometric domain.

magnetic field strength is zero. Using the constitutive relation equation in (2.4), this gives,

$$B_q^{\mathrm{i}} - \mu_0 M_q^{\mathrm{i}} = 0. \tag{2.84}$$

Similarly, equation (2.84) is interpreted that all the sine and cosine terms are zero, which means,

$$B_{qsn}^{\mathrm{i}}(h_b) - \mu_0 M_{qsn}^{\mathrm{i}}(h_b) = 0, \quad (n \in \mathbb{Z} : n \in [1, N_h]), \tag{2.85}$$

$$B_{qcn}^{\mathrm{i}}(h_b) - \mu_0 M_{qcn}^{\mathrm{i}}(h_b) = 0, \quad (n \in \mathbb{Z} : n \in [1, N_h]). \tag{2.86}$$

MEC regions

For a MEC region, it is not feasible to physically have an edge that is approaching $p \to \infty$, since it results in a MEC region with an infinite number of elements. However, the zero-flux boundary condition implies that the flux is reserved within the domain and no flux flows outside the region, therefore, a Neumann boundary condition can be applied instead. Consequently, no flux exits in positive or negative p-directions for the top or bottom layer, respectively, as illustrated in Fig. 2.16. Using the flux conservation, the following relationship is indicated,

$$\phi_{q-}^{k} - \phi_{p+}^{k} - \phi_{q+}^{k} = 0, \quad (k \in \mathbb{Z} : k \in [1, L]), \tag{2.87}$$

$$\phi_{q-}^{k} + \phi_{p-}^{k} - \phi_{q+}^{k} = 0, \quad (k \in \mathbb{Z} : k \in [K - L + 1, K]). \tag{2.88}$$

Similarly, the zero-flux boundary condition for the positive or negative q-directions are,

$$\phi_{q-}^{k} + \phi_{p-}^{k} - \phi_{p+}^{k} = 0, \tag{2.89}$$

$$\phi_{p-}^{k} - \phi_{p+}^{k} - \phi_{q+}^{k} = 0. \tag{2.90}$$

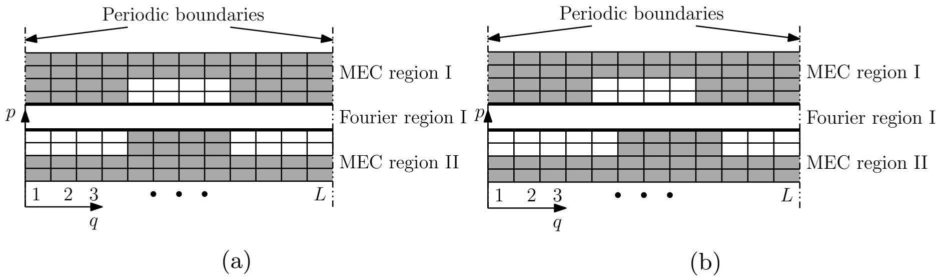

Figure 2.17: The schematic graph of a geometry (a) without displacement, and (b) with a displacement of one element width.

2.7 Motion

This section illustrates the modeling of relative motion that can occur between Fourier and MEC regions, which is a common situation in the modeling of electric machines. For example, in a rotary machine, the rotation leads to a q-directional displacement between the rotor (MEC region) and the airgap (Fourier region). Generally, any motion in 2D modeling can be decomposed respectively by movements in p- and q-directions. The modeling of motion in the p-direction is realized by varying the value of p-coordinate of the coupling interface, i.e., h_b in the boundary conditions. The modeling of motion in the q-direction is explained in the following.

2.7.1 Motion-integrated tangential boundary conditions

There are generally two methods to model the q-directional movement:

- Circulate the column of MEC elements while the mathematical expression of the boundary condition in section 2.6.1 is not changed;
- Integrate motion into the boundary conditions while the network of MEC elements remains the same.

An example is used to illustrate the principle of the first method in Fig. 2.17, where two MEC regions are at the top and bottom of a Fourier region, respectively. The initial position is shown in Fig. 2.17(a), and in Fig. 2.17(b) MEC region II moves in the positive q-direction with one element width. It is equivalent to the situation that the reluctance network of MEC region II circulates one column to the right, i.e., column 1, 2, $\cdots$, $L-1$, L in Fig. 2.17(a) is translated to column 2, 3, $\cdots$, L, 1 in Fig. 2.17(b). The drawback of this method lies in the limitation of moving distance, due to the link between displacement and element size, that the allowable motion has to be multiple of the mesh size.

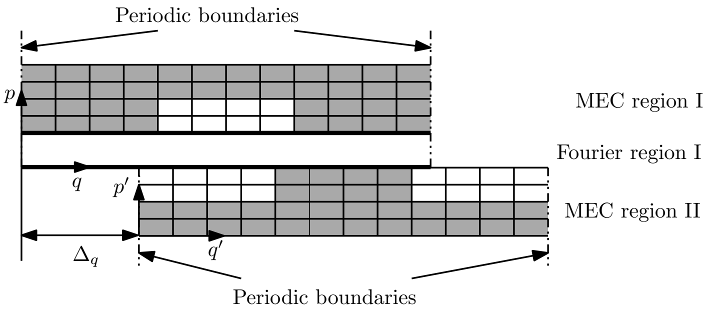

Figure 2.18: The schematic graph of a geometry modeled in stator and mover coordinate systems, which have a displacement of Δ_q in between.

The second method directly integrates the motion into the boundary conditions. The aim is to allow free movement of MEC regions in the q-direction without reconstructing the MEC network. To achieve this goal, static and moving geometries are separately modeled in stator and mover coordinate systems, while the former coordinate system is defined as fixed in space and the latter one moves in the q-direction. Still using the previous example, MEC region I and Fourier region I are now modeled in the stator coordinate system, while MEC region II is modeled in the mover coordinate system as illustrated in Fig. 2.18. The origins of the two coordinate systems are displaced with a distance of Δ_q. For the generality of the explanations in the following content, the terms in the stator coordinates are written with 's' in the subscript and are written with 'm' for the mover coordinates.

For the tangential continuous boundary condition, the consistency of magnetic field strength should be applied to the sets of Fourier coefficients in the same coordinate system [6]. As Fourier region I and MEC region II adopt different coordinate systems, the conversion of Fourier series from stator to mover coordinate system for Fourier region I is required. The following steps are taken:

1. The magnetic field strength of MEC region II is expressed as sine and cosine Fourier series, $H_{qsn,m}^{MEC_{\mathrm{II}}}$ and $H_{qcn,m}^{MEC_{\mathrm{II}}}$, in the mover coordinate system by using equations (2.63)-(2.64).

2. Fourier terms for Fourier region I are converted from the stator coordinate system to the mover coordinate system using the relationship of $q = q' + \Delta_q$. It means for a point that is located at q' in the mover coordinate system, the corresponding position is $(q' + \Delta_q)$ in the stator coordinate system. As a result, the value of magnetic field strength of Fourier region I is able to be described as,

$$H_{q,s}^{FA_{\mathrm{I}}} = \sum_{n=1}^{N_h} \left[H_{qsn,s}^{FA_{\mathrm{I}}} \sin\left(\omega_n \left(q' + \Delta_q\right)\right) + H_{qcn,s}^{FA_{\mathrm{I}}} \cos\left(\omega_n \left(q' + \Delta_q\right)\right) \right], \quad (2.91)$$

in the stator coordinate system, and is

$$H_{q,m}^{FA_{\mathrm{I}}} = \sum_{n=1}^{N_h} \left[H_{qsn,m}^{FA_I} \sin\left(\omega_n q'\right) + H_{qcn,m}^{FA_I} \cos\left(\omega_n q'\right) \right], \tag{2.92}$$

in the mover coordinate system. The value of magnetic field strength should be the same regardless the coordinate systems. This leads to,

$$\begin{aligned} &\sum_{n=1}^{N_h} \left[H_{qsn,s}^{FA_{\mathrm{I}}} \sin\left(\omega_n \left(q' + \Delta_q\right)\right) + H_{qcn,s}^{FA_{\mathrm{I}}} \cos\left(\omega_n \left(q' + \Delta_q\right)\right) \right] \\ &= \sum_{n=1}^{N_h} \left[H_{qsn,m}^{FA_{\mathrm{I}}} \sin\left(\omega_n q'\right) + H_{qcn,m}^{FA_{\mathrm{I}}} \cos\left(\omega_n q'\right) \right]. \end{aligned} \tag{2.93}$$

By equating every harmonic, equation (2.93) becomes,

$$\begin{aligned} &H_{qsn,s}^{FA_{\mathrm{I}}} \sin\left(\omega_n \left(q' + \Delta_q\right)\right) + H_{qcn,s}^{FA_{\mathrm{I}}} \cos\left(\omega_n \left(q' + \Delta_q\right)\right) \\ &= H_{qsn,m}^{FA_{\mathrm{I}}} \sin\left(\omega_n q'\right) + H_{qcn,m}^{FA_{\mathrm{I}}} \cos\left(\omega_n q'\right), \quad \left(n \in \mathbb{Z} : n \in [1, N_h]\right). \end{aligned} \tag{2.94}$$

Since equation (2.94) is valid for any arbitrary q', the following sets of equations are derived,

$$H_{qsn,m}^{FA_{\mathrm{I}}} = H_{qsn,s}^{FA_{\mathrm{I}}} \cos\left(\omega_n \Delta_q\right) - H_{qcn,s}^{FA_{\mathrm{I}}} \sin\left(\omega_n \Delta_q\right), \tag{2.95}$$

$$H_{qcn,m}^{FA_{\mathrm{I}}} = H_{qsn,s}^{FA_{\mathrm{I}}} \sin\left(\omega_n \Delta_q\right) + H_{qcn,s}^{FA_{\mathrm{I}}} \cos\left(\omega_n \Delta_q\right). \tag{2.96}$$

3. Equality is ensured for the magnetic field strength for Fourier region I and MEC region II in the mover coordinate system,

$$H_{qsn,m}^{FA_{\mathrm{I}}} = H_{qsn,m}^{MEC_{\mathrm{II}}}, \tag{2.97}$$

$$H_{qcn,m}^{FA_{\mathrm{I}}} = H_{qcn,m}^{MEC_{\mathrm{II}}}. \tag{2.98}$$

By using the above three steps, the tangential boundary conditions in section 2.6.1 are converted to:

$$\begin{aligned} &\left(\frac{1}{\mu_r^{FA_t} \mu_0} B_{qsn}^{FA_t} - \frac{1}{\mu_r^{FA_t}} M_{qsn}^{FA_t} \right) \cos\left(\omega_n \Delta_q\right) - \left(\frac{1}{\mu_r^{FA_t} \mu_0} B_{qcn}^{FA_t} - \frac{1}{\mu_r^{FA_t}} M_{qcn}^{FA_t} \right) \\ &\sin\left(\omega_n \Delta_q\right) = -\frac{2}{\omega_n \tau_{per}} \sum_{k=K-L+1}^{K} \left(\frac{\phi_{q-}^k + \phi_{q+}^k}{2\mu_0 \mu_r S_{pl}^k} - \frac{1}{\mu_r^k} M_q^k \right) \left[\cos\left(\omega_n q_1^k\right) - \cos\left(\omega_n q_0^k\right) \right], \\ &\left(n \in \mathbb{N} : n \in [1, N_h]\right), \end{aligned} \tag{2.99}$$

$$\begin{aligned} &\left(\frac{1}{\mu_r^{FA_t} \mu_0} B_{qsn}^{FA_t} - \frac{1}{\mu_r^{FA_t}} M_{qsn}^{FA_t} \right) \sin\left(\omega_n \Delta_q\right) + \left(\frac{1}{\mu_r^{FA_t} \mu_0} B_{qcn}^{FA_t} - \frac{1}{\mu_r^{FA_t}} M_{qcn}^{FA_t} \right) \\ &\cos\left(\omega_n \Delta_q\right) = \frac{2}{\omega_n \tau_{per}} \sum_{k=K-L+1}^{K} \left(\frac{\phi_{q-}^k + \phi_{q+}^k}{2\mu_0 \mu_r S_{pl}^k} - \frac{1}{\mu_r^k} M_q^k \right) \left[\sin\left(\omega_n q_1^k\right) - \sin\left(\omega_n q_0^k\right) \right], \\ &\left(n \in \mathbb{N} : n \in [1, N_h]\right), \end{aligned}$$

(2.100)

for the MEC region located below the Fourier region, and are

$$\begin{aligned}&\left(\frac{1}{\mu_r^{FA_b}\mu_0}B_{qsn}^{FA_b} - \frac{1}{\mu_r^{FA_b}}M_{qsn}^{FA_b}\right)\cos\left(\omega_n\Delta_q\right) - \left(\frac{1}{\mu_r^{FA_b}\mu_0}B_{qcn}^{FA_b} - \frac{1}{\mu_r^{FA_b}}M_{qcn}^{FA_b}\right)\\ &\sin\left(\omega_n\Delta_q\right) = -\frac{2}{\omega_n\tau_{per}}\sum_{k=1}^{L}\left(\frac{\phi_{q-}^k+\phi_{q+}^k}{2\mu_0\mu_r S_{pl}^k} - \frac{1}{\mu_r^k}M_q^k\right)\left[\cos\left(\omega_n q_1^k\right) - \cos\left(\omega_n q_0^k\right)\right],\\ &(n\in\mathbb{N}: n\in[1,N_h]),\end{aligned} \tag{2.101}$$

$$\begin{aligned}&\left(\frac{1}{\mu_r^{FA_b}\mu_0}B_{qsn}^{FA_b} - \frac{1}{\mu_r^{FA_b}}M_{qsn}^{FA_b}\right)\sin\left(\omega_n\Delta_q\right) + \left(\frac{1}{\mu_r^{FA_b}\mu_0}B_{qcn}^{FA_b} - \frac{1}{\mu_r^{FA_b}}M_{qcn}^{FA_b}\right)\\ &\cos\left(\omega_n\Delta_q\right) = \frac{2}{\omega_n\tau_{per}}\sum_{k=1}^{L}\left(\frac{\phi_{q-}^k+\phi_{q+}^k}{2\mu_0\mu_r S_{pl}^k} - \frac{1}{\mu_r^k}M_q^k\right)\left[\sin\left(\omega_n q_1^k\right) - \sin\left(\omega_n q_0^k\right)\right],\\ &(n\in\mathbb{N}: n\in[1,N_h]).\end{aligned} \tag{2.102}$$

for the MEC region located at the top of the Fourier region.

2.7.2 Motion-integrated normal boundary conditions

For element k, assuming the left and right edges are located at q_0^k and q_1^k in the mover coordinate system, the corresponding edges are $(q_0^k+\Delta_q)$ and $(q_1^k+\Delta_q)$ in the stator coordinate system. Flux flows from or to the Fourier region becomes,

$$\phi_{p-}^k = \int_{q_0^k+\Delta_q}^{q_1^k+\Delta_q} B_p^{FA_b}(q,h_b)\mathcal{L}_l^k dq, \tag{2.103}$$

$$\phi_{p+}^k = \int_{q_0^k+\Delta_q}^{q_1^k+\Delta_q} B_p^{FA_t}(q,h_b)\mathcal{L}_l^k dq. \tag{2.104}$$

Consequently, the normal boundary conditions, equations (2.59)-(2.60), are rewritten as,

$$\begin{aligned}&\phi_{q-}^k - \phi_{q+}^k - \phi_{p+}^k + \sum_{n=0}^{N_h}\left\{-\frac{1}{\omega_n}\left[\cos\left(\omega_n\left(q_1^k+\Delta_q\right)\right) - \cos\left(\omega_n\left(q_0^k+\Delta_q\right)\right)\right]\right.\\ &\left.B_{psn}^{FA_b}(h_b)\mathcal{L}_l^k + \frac{1}{\omega_n}\left[\sin\left(\omega_n\left(q_1^k+\Delta_q\right)\right) - \sin\left(\omega_n\left(q_0^k+\Delta_q\right)\right)\right]B_{pcn}^{FA_b}(h_b)\mathcal{L}_l^k\right\}\\ &= 0, \quad (k\in\mathbb{Z}: k\in[1,L]),\end{aligned} \tag{2.105}$$

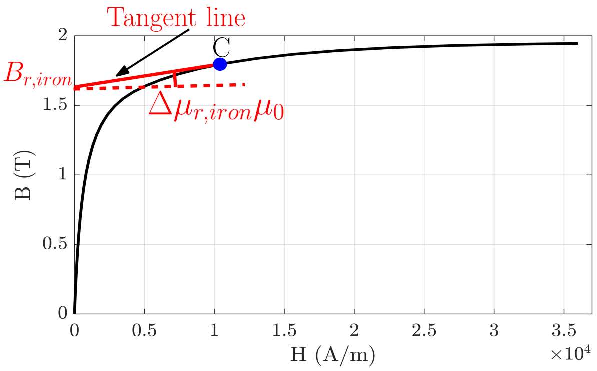

Figure 2.19: *B*-*H* curve of the iron.

$$\phi_{q-}^{k} - \phi_{q+}^{k} + \phi_{p-}^{k} - \sum_{n=0}^{N_h} \left\{ -\frac{1}{\omega_n} \left[\cos\left(\omega_n \left(q_1^k + \Delta_q\right)\right) - \cos\left(\omega_n \left(q_0^k + \Delta_q\right)\right)\right] \right.$$
$$\left. B_{psn}^{FA_t}(h_b)\mathcal{L}_l^k + \frac{1}{\omega_n} \left[\sin\left(\omega_n \left(q_1^k + \Delta_q\right)\right) - \sin\left(\omega_n \left(q_0^k + \Delta_q\right)\right)\right] B_{pcn}^{FA_t}(h_b)\mathcal{L}_l^k \right\}$$
$$= 0, \quad (k \in \mathbb{Z} : k \in [K - L + 1, K]). \tag{2.106}$$

2.8 Modeling of nonlinear magnetic materials

The modeling of nonlinear materials is introduced in this section, and the goal is to:

- Integrate the nonlinear *B*-*H* relationship into the expression of reluctances and *mmf* sources of MEC elements;
- Use an iterative algorithm to identify the actual operating point on the *B*-*H* curve.

Assume the soft magnetic material follows a nonlinear *B*-*H* curve that is shown in Fig. 2.19. For a random working point C, the expression of the *B*-*H* relationship can be locally linearized by a tangent line. By using the constitutive relation, this gives,

$$H_C = \frac{B_C}{\mu_0 \Delta\mu_{r,iron}} - \frac{1}{\Delta\mu_{r,iron}} \frac{B_{r,iron}}{\mu_0}, \tag{2.107}$$

where $\Delta\mu_{r,iron}$ is the incremental relative permeability defined by the slope of the tangent line, and $B_{r,iron}$ is the remanent magnetic flux density defined by the intercept. The term '$B_{r,iron}/\mu_0$' in this equation is possible to be analogous to the magnetization of a permanent magnet [12].

The orientation of such 'magnetization' is decomposed into pq-directions. Taking into account the fact that the 'magnetization' is positively correlated to the flux density (the higher the flux density, the higher the value of $B_{r,iron}$), the Pythagorean theorem is used for the decomposition, which derives,

$$\vec{M}_{p,iron} = \frac{B_p}{\sqrt{B_p^2 + B_q^2}} \frac{B_{r,iron}}{\mu_0} \vec{p}, \tag{2.108}$$

$$\vec{M}_{q,iron} = \frac{B_q}{\sqrt{B_p^2 + B_q^2}} \frac{B_{r,iron}}{\mu_0} \vec{q}. \tag{2.109}$$

This indicates that apart from the permanent magnet and current, the nonlinear *B-H* curve adds another mmf source to MEC elements. The values of the 'magnetization' in equations (2.108)-(2.109) are substituted into equations (2.21)-(2.24) to derive the corresponding magnetomotive force, resulting in the following expressions,

$$\mathcal{F}_{p-}^k = \frac{\vec{M}_{p,iron}^k l_{p-}^k}{\Delta\mu_{r,iron}^k}, \tag{2.110}$$

$$\mathcal{F}_{p+}^k = \frac{\vec{M}_{p,iron}^k l_{p+}^k}{\Delta\mu_{r,iron}^k}, \tag{2.111}$$

$$\mathcal{F}_{q-}^k = \frac{\vec{M}_{q,iron}^k l_{q-}^k}{\Delta\mu_{r,iron}^k}, \tag{2.112}$$

$$\mathcal{F}_{q+}^k = \frac{\vec{M}_{q,iron}^k l_{q+}^k}{\Delta\mu_{r,iron}^k}. \tag{2.113}$$

Additionally, the value of $\Delta\mu_{r,iron}^k$ is used as the relatively permeability in the formulation of reluctances.

The saturation problem is solved iteratively using the flowchart as shown in Fig. 2.20. First, the model is solved with initial values of $\Delta\mu_{r,iron}$ and $B_{r,iron}$, which are assumed for un-saturated iron, e.g., $\Delta\mu_{r,iron} = 2000$ and $B_{r,iron} = 0$. In each iterative step, the reluctances and mmfs have to be re-calculated using the updated $\Delta\mu_{r,iron}$, $\vec{M}_{p,iron}$ and $\vec{M}_{q,iron}$. Values of B_p and B_q are derived by solving the boundary conditions with the newly defined MEC elements. Afterwards, $\Delta\mu_{r,iron}$, $\vec{M}_{p,iron}$ and $\vec{M}_{q,iron}$ are updated corresponding to the newly obtained B_p and B_q. Various global convergence conditions are applicable, e.g., difference of force or torque between two adjacent iterative steps is smaller than a certain level, and this is set to be 0.2% in this thesis.

As an alternative, Newton Ralphson method, which is based on a first-order Taylor expansion of the residual, is able to allow quadratic convergence to the solution.

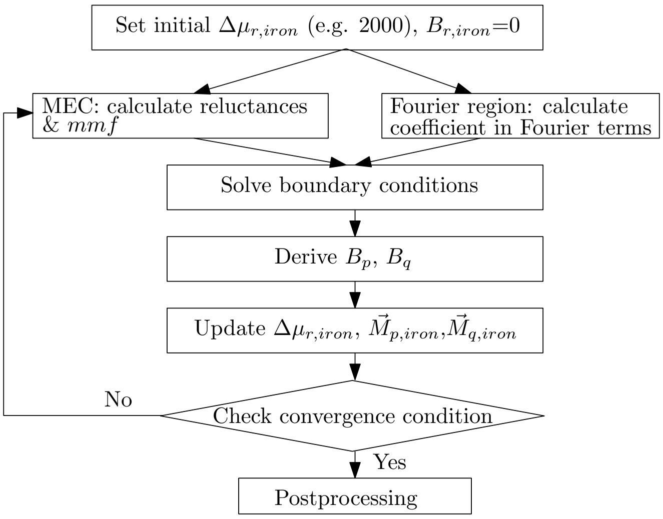
Set initial $\Delta\mu_{r,iron}$ (e.g. 2000), $B_{r,iron}$=0
MEC: calculate reluctances & mmf
Fourier region: calculate coefficient in Fourier terms
Solve boundary conditions
Derive B_p, B_q
Update $\Delta\mu_{r,iron}$, $\vec{M}_{p,iron}$,$\vec{M}_{q,iron}$
No
Check convergence condition
Yes
Postprocessing

Figure 2.20: Flowchart of the HAM to include saturation.

This method can further accelerate the convergence, and is valuable for transient analysis [47].

2.9 Finite element verification

To verify the hybrid analytical modeling technique, it is applied to three benchmark examples in Matlab for the three coordinate systems. The first example considers a non-periodic E-core structure in the Cartesian coordinate system and shows how the non-periodic geometry is converted into a periodic problem in the HAM. The second example considers a 12/8 (stator/rotor pole ratio) switched reluctance machine (SRM) in the polar coordinate system with displacement. This verifies the incorporation of motion in the HAM. The third example models a tubular permanent magnet machine (TPMA) in the axisymmetric coordinate system that has both the excitation of permanent magnet and current. All three examples use the soft magnetic material that has the nonlinear *B*-*H* curve shown in Fig. 2.19.

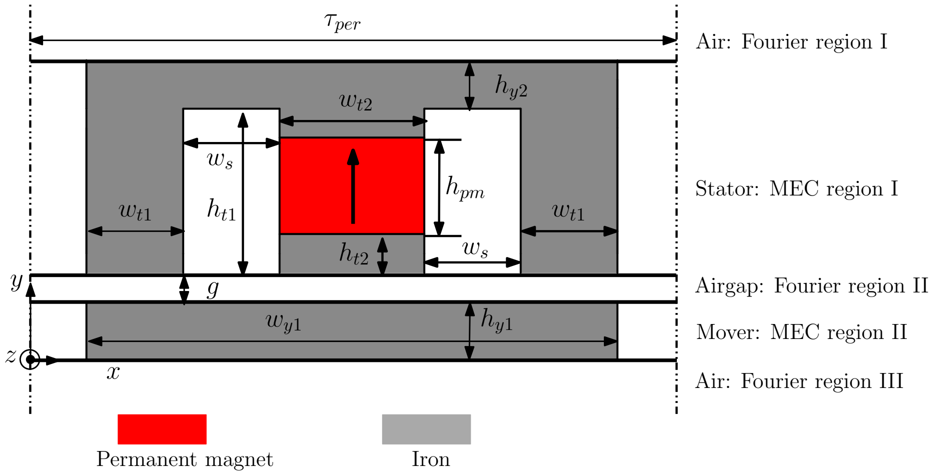

Figure 2.21: Geometry of the benchmark example in the Cartesian coordinate system.

2.9.1 Cartesian coordinate system

The HAM is aiming for periodic geometries, however, the modeling of a non-periodic geometry is still possible. One way is to apply Newmann boundary conditions at the q-directional borders of the geometry. A 2D non-periodic E-core reluctance actuator with permanent magnet shown in Fig. 2.21 is given as an example, and the dimensions are provided in Table 2.4.

MEC regions I and II are used to model the bottom and top iron parts, respectively. Fourier regions I-III are used for the air regions, where Fourier region II models the airgap, and I and III represent the top and bottom air regions until infinity.

Due to the fringing effect in the end of the airgap, sufficient air is included in the model on the left and right side of the actuator. It is assumed that at the left and right edges of the geometric domain, Neumann boundary conditions are applicable, i.e., $H_x = 0|_{x=0 \text{ or } \tau_{per}}$. This is realized by setting infinite reluctances in the $-x$- and $+x$-directions for the elements that are located next to the left and right edges, respectively.

The flux density distribution calculated by HAM is shown in Fig. 2.22(a), while the results obtained by FEM are shown in Fig. 2.22(b), as can be seen, the two figures show a very good agreement. For better comparison, the magnitude of the flux density is compared at every location for the FEM and HAM results, using,

$$|\Delta B| = |B_{FEM} - B_{HAM}| \,. \tag{2.114}$$

The distribution of $|\Delta B|$ is shown in Fig. 2.22(c). The overall discrepancy is small, and most of the remaining error concentrates at the corners of the teeth. The

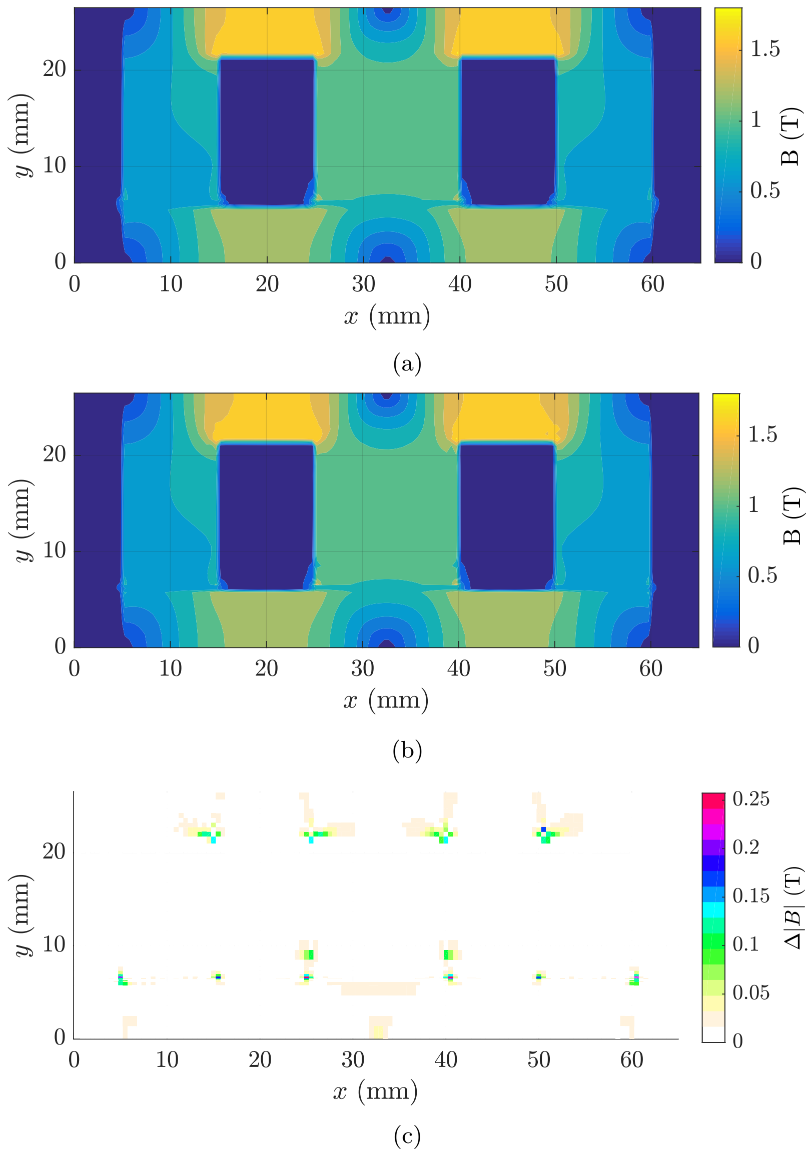

(a)

(b)

(c)

Figure 2.22: Magnetic flux density distribution for the E-core structure shown in Fig. 2.21: (a) magnitude obtained by HAM, (b) magnitude obtained by FEM, and (c) the difference of magnitude obtained by HAM and FEM.

Table 2.4: Dimensions and material properties of the benchmark example in the Cartesian coordinate system.

Parameter	Description	value	Unit
h_{pm}	height of PM	10	mm
h_{y1}	height of the bottom iron	6	mm
g	airgap length	0.5	mm
h_{t1}	height of the side teeth	15	mm
h_{t2}	height of the middle tooth	2	mm
h_{y2}	height of the top yoke	5	mm
w_{y1}	width of the bottom iron	55	mm
w_{t1}	width of the side tooth	10	mm
w_s	width of the slot	10	mm
w_{t2}	width of the middle tooth	15	mm
τ_{per}	total width	65	mm
l_{sk}	stack length	50	mm
B_{rem}	Remanence of PM	1.2	T
$\mu_{r,pm}$	Relative permeability of PM	1.05	-

agreement in flux density indicates that the representation of nonlinear material property in MEC regions as well as the iterative algorithm for saturation both function well.

2.9.2 Polar coordinate system

The second benchmark example is a 12/8 SRM in the polar coordinate system. Since the periodicity is 180°, half of the machine is modeled, as shown in Fig. 2.23. The stator and mover are modeled by meshed MEC, while the air regions and non-magnetic shaft are modeled as Fourier regions. The dimensions of the SRM are listed in Table 2.5. Notice that the inner and outer tooth arcs of the rotor, α_{ri} and α_{ro}, are not equal, such that the equations for the regular-shaped reluctances are not valid. Instead, equations (2.17)-(2.20) are used to calculate reluctances for the rotor.

The rotor position shown in Fig. 2.23 is the position corresponding to $\Delta_\theta = 0°$. To verify the motion-integrated boundary conditions, it is intended to apply the HAM to calculate the magnetic field when the rotor rotates 3° counterclockwise without remshing the MEC regions. The magnetic flux density distribution obtained by the HAM and FEM is respectively shown in Figs. 2.24(a) and (b), and as can be seen, the results of the two methods are in good agreement. For 'MEC region II' in the HAM, the angles of the MEC elements vary along each column of the mesh grid, since the rotor tooth arcs vary along the r-direction. However, in the post-processing of FEM, evenly-distributed grids are defined to export the results. The dimensions of the mesh grid in the HAM cannot be directly implemented

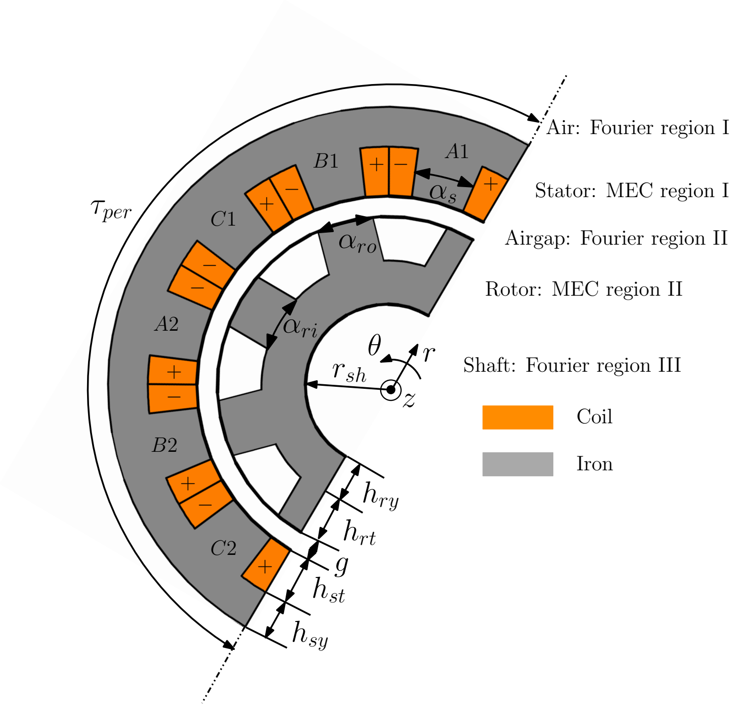
Air: Fourier region I
Stator: MEC region I
Airgap: Fourier region II
Rotor: MEC region II
Shaft: Fourier region III
Coil
Iron
τ_{per}
$A1$
$B1$
$C1$
$A2$
$B2$
$C2$
α_s
α_{ro}
α_{ri}
θ
r
z
r_{sh}
h_{ry}
h_{rt}
g
h_{st}
h_{sy}
+
−

Figure 2.23: Geometry of the benchmark example in the polar coordinate system.

Table 2.5: Dimensions and current densities of the benchmark example in the polar coordinate system.

Parameter	Description	value	Unit
r_{sh}	Shaft radius	20.5	mm
h_{ry}	Rotor yoke height	11	mm
h_{rt}	Rotor tooth height	14	mm
g	Airgap length	0.5	mm
h_{st}	Stator tooth height	14	mm
h_{sy}	Stator yoke height	10	mm
α_s	Stator tooth arc	16	deg.
α_{ro}	Rotor tooth outer arc	18	deg.
α_{ri}	Rotor tooth inner arc	26	deg.
τ_{per}	Width of periodicity	180	deg.
J_A	Current density of phase A	10	A/mm^2
J_B	Current density of phase B	0	A/mm^2
J_C	Current density of phase C	0	A/mm^2

Table 2.6: Dimensions, material properties and current densities of the benchmark example in the axisymmetric coordinate system.

Parameter	Description	value	Unit
h_{pm}	Height of PM	5	mm
g	Airgap length	0.5	mm
h_t	Height of stator teeth	3	mm
h_y	Height of stator yoke	2	mm
w_{pm}	Magnet width	15	mm
w_i	Iron width	15	mm
Δ_m	Mover position	4	mm
w_t	Stator teeth width	8	mm
w_s	Stator slot width	12	mm
τ_{per}	Width of periodicity	60	mm
B_{rem}	Remanence of PM	1.2	T
$\mu_{r,pm}$	Relative permeability of PM	1.05	-
J_A	Current density of phase A	0	A/mm^2
J_B	Current density of phase B	15	A/mm^2
J_C	Current density of phase C	-15	A/mm^2

in the FEM, hence, $|\Delta B|$ is not presented for this example. To further prove the accuracy of HAM, the flux density in the center of the airgap is shown in Fig. 2.24(c), and in overall, good agreement is visible. These results reveals the validity of the method for incorporating motion in the HAM as the rotor is rotated 3 degrees counterclockwise.

2.9.3 Axisymmetric coordinate system

The third example is a tubular permanent magnet actuator in the axisymmetric coordinate system. The machine topology is shown in Fig. 2.25 and the dimensions are listed in Table 2.6. In this example, magnetic sources of both permanent magnet and current exist. The magnitude of the flux density obtained by HAM, the magnitude obtained by FEM, and the difference between HAM and FEM is shown in Figs. 2.26(a), (b) and (c), respectively.

In general, an overall good agreement is observed in the flux density distribution, the error again are mainly located at the edges of the teeth. On the other hand, different methods of distributing current related mmf sources are used in the benchmark examples, the mmf for the switched reluctance machine is arranged merely in the q-direction, and for the tubular actuator, it is arranged in merely the p-direction. The match of results in both examples indicates that both methods are valid.

Furthermore, for a more detailed numerical comparison, the force/torque components obtained by HAM and FEM are compared, and the results are listed in

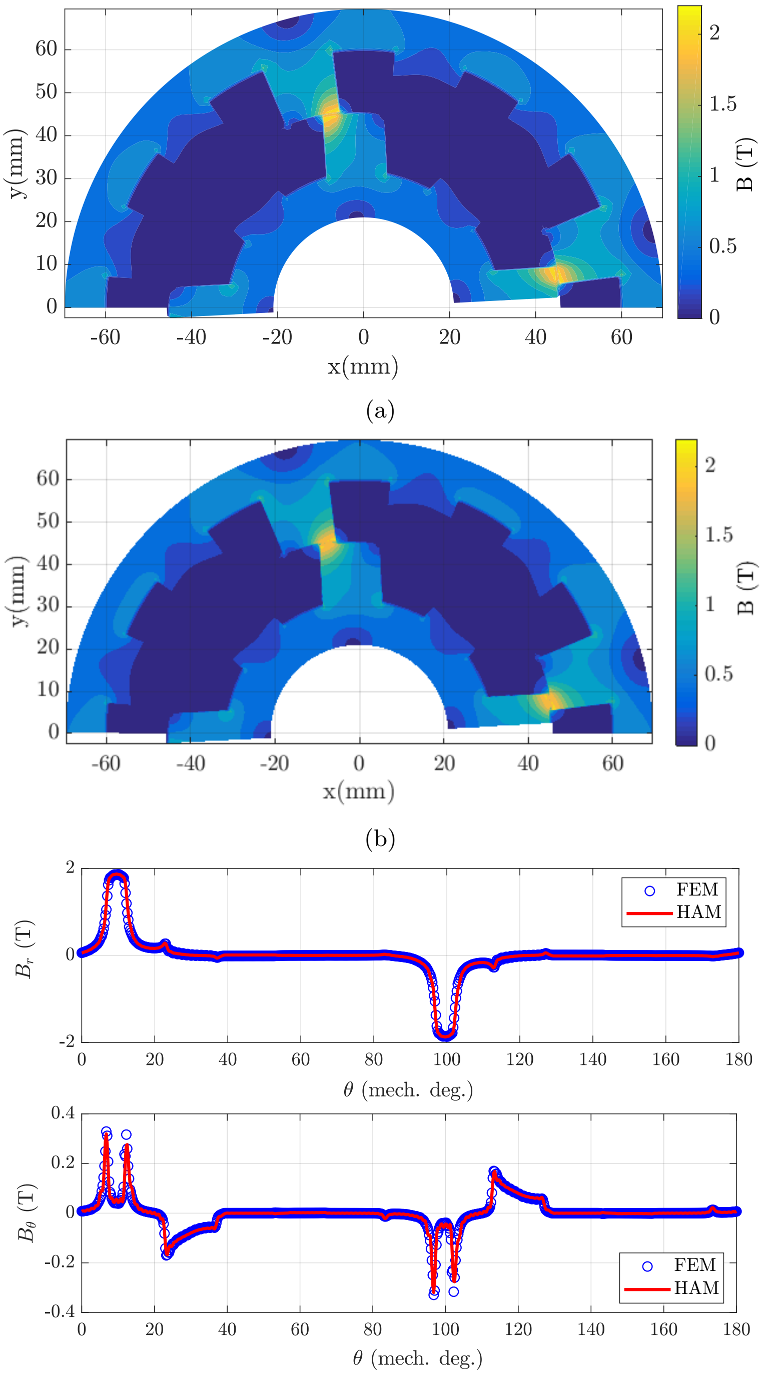

(a)

(b)

(c)

Figure 2.24: Magnetic flux density for the SRM: (a) the magnitude obtained by HAM, (b) the magnitude obtained by FEM, and (c) normal and tangential components in the center of the airgap.

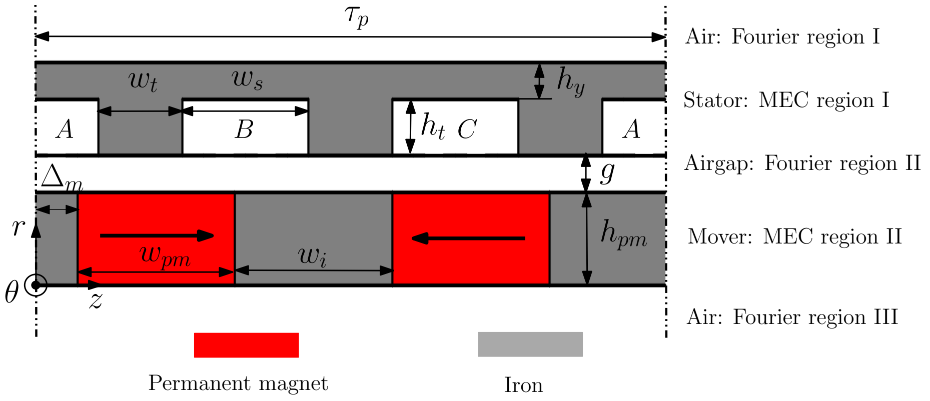
τ_p
w_t
w_s
h_y
A
B
h_t
C
A
g
Δ_m
r
w_{pm}
w_i
h_{pm}
θ
z
Air: Fourier region I
Stator: MEC region I
Airgap: Fourier region II
Mover: MEC region II
Air: Fourier region III
Permanent magnet
Iron

Figure 2.25: Geometry of the benchmark example in the axisymmetric coordinate system.

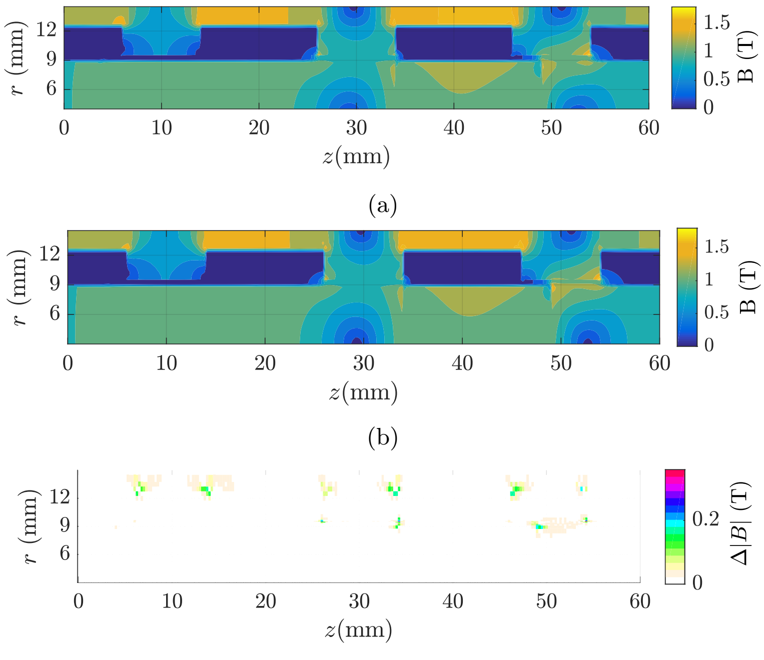

(a)

(b)

(c)

Figure 2.26: Magnetic flux density for the tubular permanent magnet actuator: (a) magnitude obtained by HAM, (b) magnitude obtained by FEM, and (c) the difference of magnitude obtained by HAM and FEM.

Table 2.7: The force/torque of the benchmark examples obtained by HAM and FEM.

	Cartesian: F_y (N)	Polar: T (Nm)	Axisymmetric: F_z (N)
HAM	460.42	13.47	9.90
FEM	465.25	13.63	9.85
Difference (%)	1.04	1.17	0.51

Table 2.8: Simulation parameters of the benchmark examples using HAM and FEM.

	Cartesian		Polar		Axisymmetric	
Parameters	HAM	FEM	HAM	FEA	HAM	FEA
N_h	10/65/10	-	10/90/10	-	10/130/10	-
Mesh nodes	4550	27001	9360	97961	5760	17074
Total	4890	30593	9760	97961	6320	17074

Note: The values of N_h are listed sequentially for Fourier region I/Fourier region II/Fourier region III for each benchmark example. For the benchmark examples in the polar and axisymmetric coordinate systems, two sets of Fourier series, a_n and c_n in equations (A.22)-(A.25), are omitted for Fourier region I, while b_n and d_n are omitted for Fourier region III, the reasons are given section 3.3.4.

Table 2.7. The difference are small for all the three benchmark examples.

If the model contains a lot of irregular-shaped geometric details for MEC regions, the calculation of the reluctance network is complicated and the accuracy is limited. Additionally, for the situations when flux density changes dramatically, the allocation of element size has to be carefully considered. For example, when stator and rotor teeth start to align in the SRM, the value of flux density varies significantly close to the vertex of the teeth, consequently, a relatively dense mesh is desired.

2.9.4 Simulation parameters

The results above are derived with the following simulation parameters given in Table 2.8, with respect to the harmonic orders and total number of elements. As can be seen, the total number of unknowns in HAM is much smaller than the number of mesh nodes in FEM. However, to ensure the accuracy of FEM results that perform as references, the FEM is densely meshed, even over-meshed than required, therefore, the comparison listed in Table 2.8 is not fair enough.

To compare the computation effort of these two methods more convincingly, the influence of unknowns or number of nodes is investigated. The forces in normal and tangential directions of the example in the Cartesian coordinate system, F_x and F_y, are used as indications. In FEM, normally two or three layers of mesh elements are included in the airgap to ensure the accuracy. Herein the reference mesh grid in FEM is obtained when the mesh size in the airgap is kept to half the airgap length, while in other parts, the mesh size is set to be 1 mm, as such, the reference grid has the number of mesh nodes at '30593'. To reduce this number, the element is gradually reduced in FEM while the airgap mesh size remains. In HAM, both the mesh density and the number of harmonic order increases, such that the value of unknowns finally reaches '23990'.

The relationship between the force components and the unknowns/mesh nodes is shown in Fig. 2.27. The variation of F_y is illustrated in percentage. However, the theoretic value of F_x is zero due to the symmetric geometry, hence, it is illustrated in 'Newton' instead of percentage. As can be seen, the variation of F_y and F_x are both higher in FEM than in HAM when the number of nodes is smaller than 1.5×10^4. This is attributed to the small mesh in the airgap of FEM, which not only contributes a lot of mesh nodes by itself, but also significantly limits the mesh size adjacent to it. Therefore, in order to reach the same level of nodes as in the HAM, the mesh size in the FEM increases tremendously away from the airgap, and consequently, some are even ill-shaped as shown in Fig. 2.28. Apart from the concerns about the number of nodes/unknowns, the sparsity of the matrix is another argument where the HAM brings the benefit. The meshed-MEC matrix that is built upon a single potential node within each element, is potentially sparser than the matrix of FEM that built with second-order triangular elements. As a result, less computational load is required for the sparse system of HAM.

Similar analysis is also performed for a longer airgap length, i.e., $g = 8$ mm, and the comparison results of F_x and F_y obtained by the HAM and FEM are shown in Fig. 2.29(a) and (b), respectively. The mesh size of the airgap in FEM can be relatively large in this situation, hence, does not constrain the mesh size near the airgap anymore. On the contrary, the shortcoming of conformal meshing, which forces the same number of mesh elements in the x-direction for all the mesh layers, is highlighted in the HAM for such a long airgap length. To reach a number of MEC elements as low as 2000, a coarse mesh has to be constructed near the airgap, which reduces the accuracy.

The above comparison shows the potential of HAM for less computational intensity for the geometry with a small airgap, which is normally the situation of electric machines. Such possibility of using less numbers of elements is beneficial for the initial sizing and optimization of the electric machine design. Moreover, as aforementioned, the current adopted conformal meshing limits the MEC size to some extent, hence, some parts of the structure are over-meshed, e.g., stator yoke in the model. If non-conformal meshing is implemented in the HAM, the essential number of MEC elements can be further reduced.

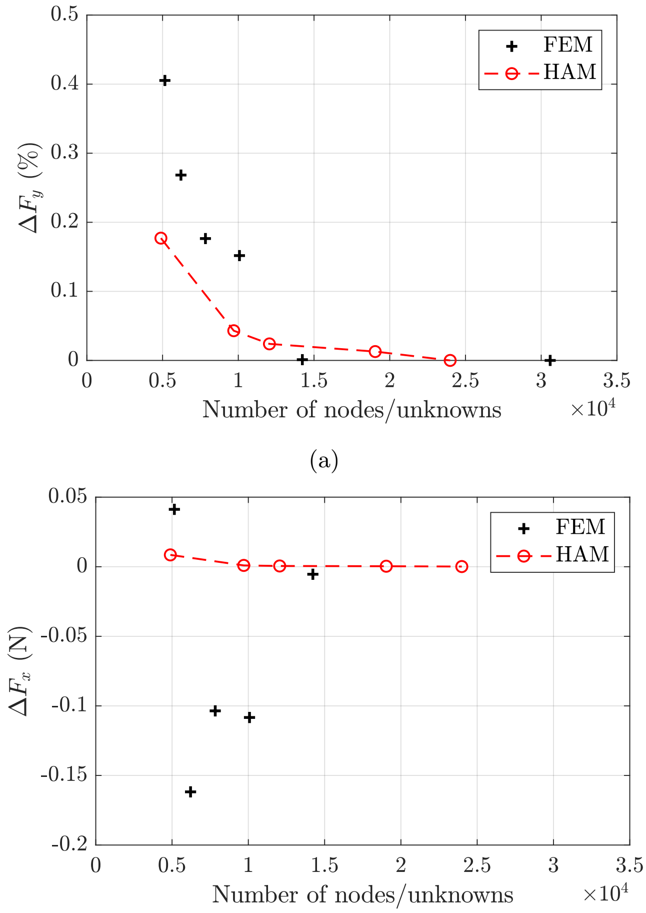

(a)

(b)

Figure 2.27: Airgap length is 0.5 mm: (a) variation of F_y in percentage regarding the nodes/unknowns in FEM/HAM, and (b) values of F_x in Newton regarding the number of nodes/unknowns in FEM/HAM.

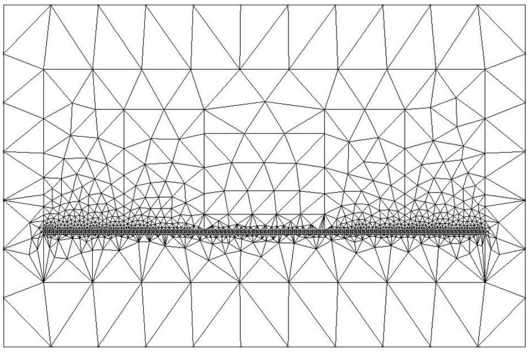

Figure 2.28: The FEM mesh grid for the E-core actuator with 0.5 mm airgap.

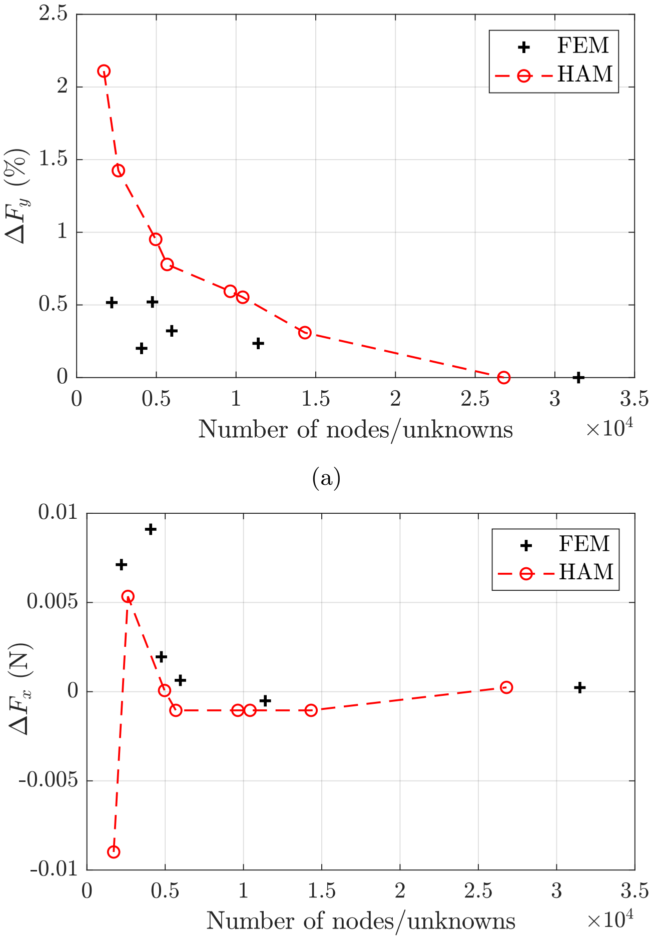

(a)

(b)

Figure 2.29: Airgap length is 8 mm: (a) variation of F_y in percentage regarding the nodes/unknowns in FEM/HAM, and (b) values of F_x in Newton regarding the number of nodes/unknowns in FEM/HAM.

2.10 Summary and conclusions

A 2D generalized hybrid analytical modeling technique is given for the derivation of flux density distribution, that is capable to include nonlinear magnetic material property. The model combines Fourier modeling, which is accurate and fast, with meshed magnetic equivalent circuits, which have unique permeability in mesh elements and therefore, can model local saturation.

Two-dimensional geometries are divided into regions in the normal direction, depending on the variation of magnetic permeability and presence of permanent magnets or coils. Generally, only regions with homogeneous permeability (or negligible variation of permeability) are modeled using Fourier modeling. The meshed MEC, on the other hand, is used for regions with nonlinear materials. Within each Fourier region, the magnetic field is derived by magnetostatic equation in terms of the magnetic vector potential. For each MEC region, the magnetic field is expressed by the scalar potential on the basis of reluctances and mmf sources of MEC elements, where the current related mmf sources is emphasized to fulfill the Ampere's law. As such, the magnetic field is given by sets of unknown coefficients, and the solution is derived by solving continuous and non-continuous boundary conditions. To avoid re-meshing caused by geometric movement, the motion is directly integrated in the boundary conditions that allows free movement in both normal and tangential directions. Furthermore, saturation is considered by applying locally linearized B-H relationship to each MEC element, as well as the iterative algorithms that updates the local B-H relationship each time.

The generalized HAM is applied to 2D geometries in Cartesian, polar and axisymmetric coordinate systems, and is verified with FEM on three benchmark problems in each of the coordinate systems. A very good agreement is obtained between FEM and HAM in all the examples, that indicates a promising application of HAM to a wide class of linear/rotary/tubular, PM/reluctance electric machines.

Chapter 3

Modeling of variable flux reluctance machines

Part of the content in this chapter is published in:

J. Bao, S. R. Aleksandrov, B. L. J. Gysen and E. A. Lomonova, ‘Analysis of variable flux reluctance machines using hybrid analytical modeling’, in Thirteenth International Conference on Ecological Vehicles and Renewable Energies (EVER), Monte-Carlo, 2018, pp. 1-7.

3.1 Introduction

With the derived magnetic flux density in Chapter 2, the next step is to apply the method to electrical machines to obtain machine quantities. In this chapter, the variable flux reluctance machine (VFRM) is used to show the methodology of using HAM to derive machine performances. The VFRM is an interesting candidate for automotive applications due to its low material cost, robustness and broad speed range, as explained in section 1.3.5.

This chapter starts with the geometry of the benchmark machine and its geometric details that are included in the modeling, followed by the application of the HAM. On the basis of flux density distribution, the calculation methods for the torque, flux linkage, back-emf, inductances and losses (iron loss and ac copper loss) are explained subsequently. The obtained results from the HAM are verified with 2D FEM.

3.2 Geometry of the benchmark machine: 12/10 VFRM

The variable flux reluctance machine is a PM-less machine. It has three-phase armature windings and an extra field winding both in the stator. Among different stator-pole/rotor-pole combinations, 12/10 VFRM is a good selection as is explained in Chapter 4. The geometry is shown in Fig. 3.1.

As the analyzed machine inhibits half periodicity in the θ-direction, the stator and rotor are bisected, and one half of them is studied. Half of the machine geometry can be divided into five parts, i.e.,

- The stator core, including a yoke and 6 teeth;
- The stator slots, contain 6 coils of the armature windings and field winding, respectively;
- The airgap between the stator and rotor;
- The rotor core, including a yoke, 4 complete teeth and 2 halved teeth;
- The nonmagnetic shaft.

The dimensions and geometric parameters for these parts are defined in Table 3.1.

Neither the stator or rotor teeth have any tooth tips. The inner and outer tooth arcs are different, indicating that the teeth and slot widths vary along the r-direction. Each complete slot contains four coil bundles including two dc coil

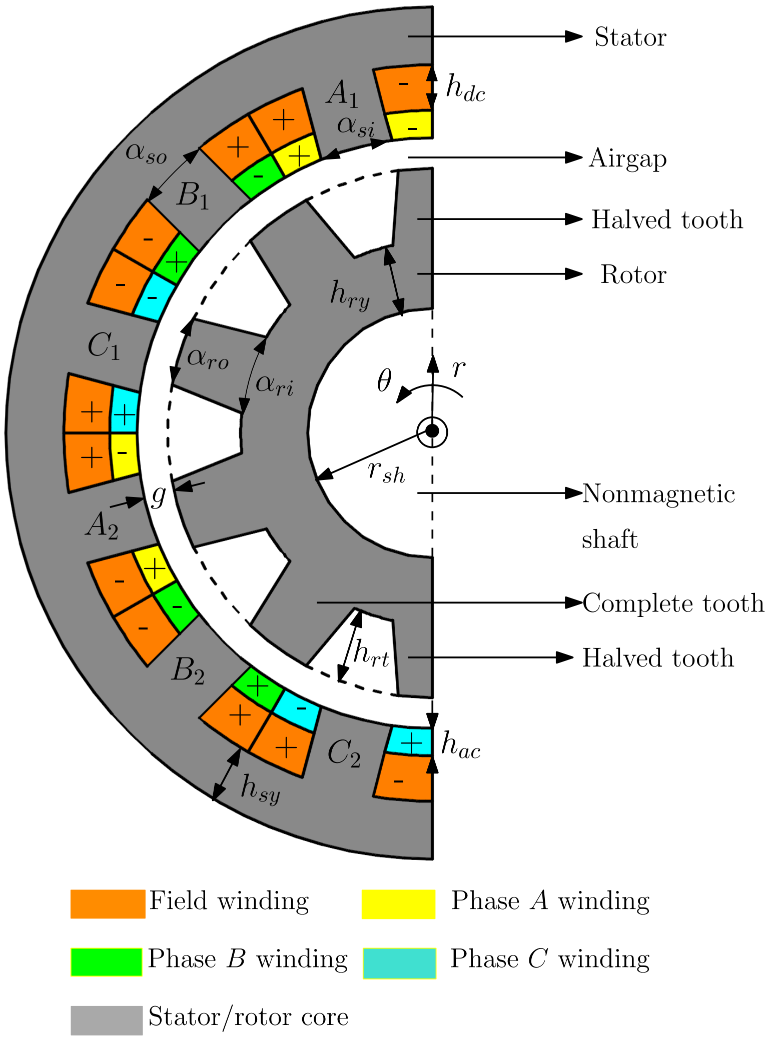
Stator
h_{dc}
A_1
α_{si}
α_{so}
B_1
Airgap
Halved tooth
Rotor
h_{ry}
C_1
α_{ro}
α_{ri}
θ
r
r_{sh}
g
A_2
Nonmagnetic shaft
Complete tooth
Halved tooth
h_{rt}
B_2
C_2
h_{ac}
h_{sy}
+
-
Field winding
Phase A winding
Phase B winding
Phase C winding
Stator/rotor core

Figure 3.1: Cross section of the 12/10 VFRM.

Table 3.1: Geometric parameters of the benchmark 12/10 VFRM.

Parameter	Description	value	unit
r_{sh}	Shaft radius	20.5	mm
h_{ry}	Rotor yoke height	11	mm
h_{rt}	Rotor teeth height	14	mm
g	Airgap length	0.5	mm
h_{ac}	Ac coil height	7	mm
h_{dc}	Dc coil height	7.5	mm
h_{sy}	Stator yoke height	9.5	mm
α_{si}	Stator tooth inner arc	15	deg.
α_{so}	Stator tooth outer arc	11.4	deg.
α_{ro}	Rotor tooth outer arc	14	deg.
α_{ri}	Rotor tooth inner arc	24	deg.
τ_{per}	Width of periodicity	180	deg.
L_{sk}	Stack length	87.5	mm
N_{ac}	Number of turns in single ac coil	^{*10}	-
N_{dc}	Number of turns in single dc coil	^{*10}	-
$J_{ac,rms}$	RMS current density of ac coils	^{*10}	A/mm^2
J_{dc}	Current density of dc coils	^{*10}	A/mm^2

Notes: * Current density of ac and dc coils varies when calculating torque, back-emf and inductance, which is specified in sections 3.5, 3.6 and 3.7. Number of turns, N_{ac} and N_{dc}, are varied in section 3.8.2.

bundles and two ac coil bundles from different phases. Both the field winding and armature windings are concentrated windings, and the predefined current flowing directions are indicated in Fig. 3.1. The ferromagnetic material follows the B-H curve shown in Fig. 2.19.

For the following content, it is defined that the rotation angle (in electrical degrees), Δ_θ, is referred as zero when the rotor tooth aligns with stator tooth A_2, and is considered as the starting position for one electric revolution.

3.3 Application of the hybrid analytical modeling

3.3.1 Division in regions

The geometry is divided into five regions as indicated in Fig. 3.2: the outer air, airgap and shaft are modeled by Fourier regions since μ_r is unity, while the stator and rotor are modeled using meshed MEC due to the non-homogeneous μ_r.

To model rotation, the outer air, stator and airgap are modeled using the stator coordinate system, while the rotor and shaft are modeled using the mover coordinate system. During rotation, displacement appears at the boundary between

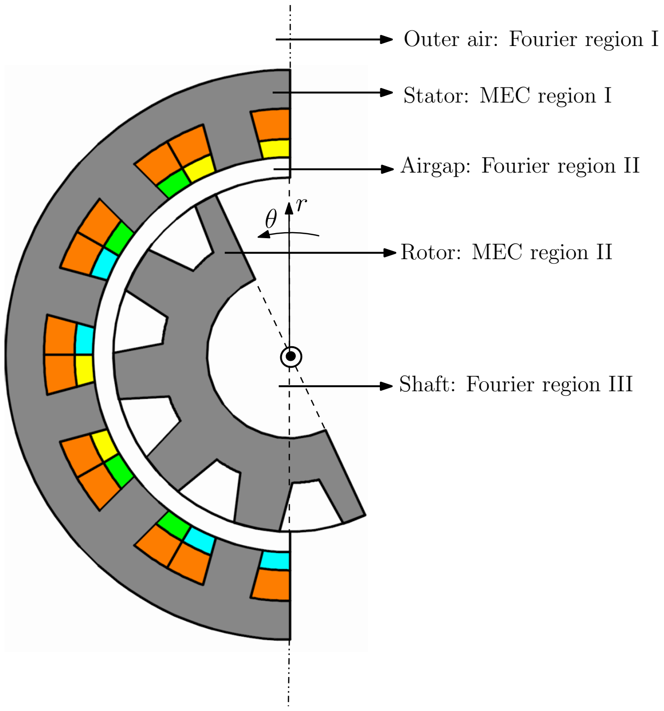
Outer air: Fourier region I
Stator: MEC region I
Airgap: Fourier region II
θ
r
Rotor: MEC region II
Shaft: Fourier region III

Figure 3.2: Region division of the 12/10 VFRM.

the airgap and rotor, i.e., Fourier region II and MEC region II.

3.3.2 Meshing of MEC regions

As explained in section 2.5.1, the mesh network is arranged such that material junctions coincide with the element edges. An example is shown in Fig. 3.3(a) that illustrates the schematic conformal meshing for a single stator pole. Notice that since the inner and outer tooth arcs are different in the stator and rotor, the angle of MEC element varies accordingly along the r-direction.

The mesh grid used in reality is denser than the schematic graph to guarantee the accuracy, and the actual mesh adopted is shown in Fig. 3.3(b). Due to the fact that the flux concentrates at the tooth vertices when the stator and rotor teeth start to align, the mesh size is relatively small at these positions, marked with red circles in the figure. Additionally, the mesh grid is set to be denser approaching the airgap.

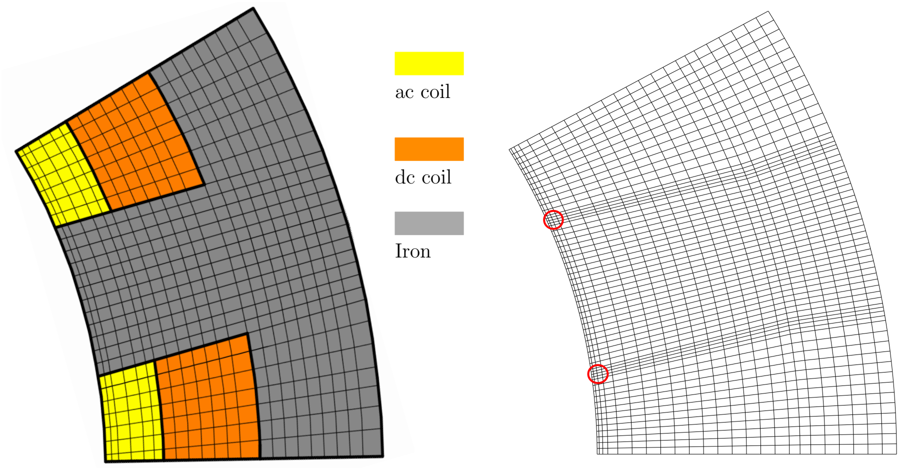

(a) (b)

Figure 3.3: (a) Schematic mesh grid for a single pole in the stator, and (b) the actual mesh grid used in the HAM.

3.3.3 Current related magnetomotive force

In Chapter 2, the rules for deriving current related magnetomotive forces are illustrated. To express the current sources of VFRMs, the method introduced in section 2.5.5 and Appendix B (with two current densities in a slot) have to be extended to allow for the situation with four current densities in a slot. This presents the ability of HAM to tackle with different winding configurations. Although only concentrated windings are introduced in this section, the technique can be easily adapted to distributed winding topologies by re-arranging the current density distribution among the coil regions.

The q-directional current related mmf sources are used in this section. The mmf is dependent on the location, and the summation of the magnetomotive forces on any q-directional path should equal to the current enclosed by the path. To explain the implementation of this rule in the VFRM, six categories of mmfs are discussed with the locations indicated in Fig 3.4(a) by the red dots. The locations are respectively:

- in the two ac coils;
- in the two dc coils;
- in the yoke above two dc coils.

First, the mmf sources in the ac coils are defined. Assume the element is located in ac coil I with the r-coordinate r^k. For an arc with radius r^k passing through,

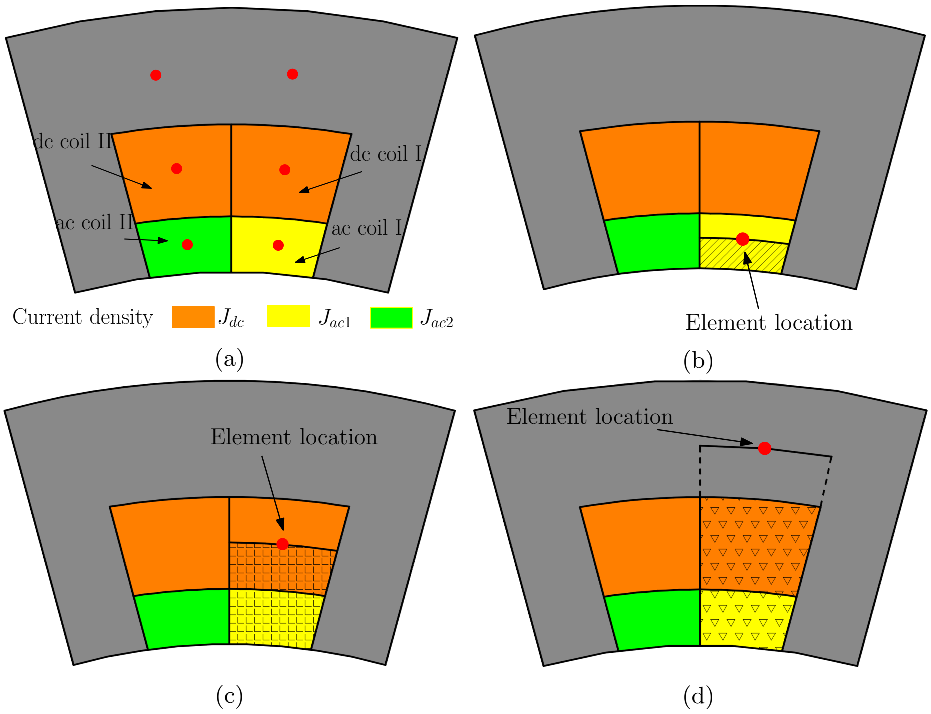
dc coil II
dc coil I
ac coil II
ac coil I
Current density
J_{dc}
J_{ac1}
J_{ac2}
(a)
Element location
(b)
Element location
(c)
Element location
(d)

Figure 3.4: (a) The locations of the six representative points of the q-directional mmfs, and the enclosed area when the element is located in (b) ac coil I, (c) dc coil I, and (d) the yoke, respectively.

together with slot edges, it forms a contour that encloses the coil area shown in Fig. 3.4(b) with slashes. Assuming the enclosed area is S_{ac,r^k}, the summation of mmfs along this arc should be equal to $J_{ac1}S_{ac,r^k}$. Apart from this enclosed area, the dimension of the element itself also has to be considered. Suppose the angle of the path at r^k is θ_{r^k}, the ratio between the width of element k and the path length is θ^k/θ_{r^k}. The mmf source of element k is therefore, $\theta^k/\theta_{r^k} \times J_{ac1}S_{ac,r^k}$. Considering the fact that there are mmf sources in both positive and negative q-directions, the expression of the mmf is therefore,

$$\mathcal{F}^k_{q\pm} = \frac{\theta^k}{2\theta_{r^k}} J_{ac1} S_{ac,r^k}. \tag{3.1}$$

Similarly, the expression of mmfs located in ac coil II are,

$$\mathcal{F}^k_{q\pm} = \frac{\theta^k}{2\theta_{r^k}} J_{ac2} S_{ac,r^k}. \tag{3.2}$$

It has to be mentioned that the current flowing direction is interpreted by the sign of the current density.

Second, the mmf in the dc coils is derived. For an element in dc coil I with radius r^k, again assume an arc passing through. It forms an area that includes the entire ac coil and part of the dc coil, illustrated as the area with small squares in Fig. 3.4(c). The expression of the mmf is therefore,

$$\mathcal{F}^k_{q\pm} = \frac{\theta^k}{2\theta_{r^k}} \left(J_{ac1} S_{ac} + J_{dc} S_{dc,r^k}\right), \tag{3.3}$$

where S_{ac} is the entire area of a single ac coil bundle and S_{dc,r^k} is the enclosed dc coil bundle area. The mmf in dc coil II is similarly written as,

$$\mathcal{F}^k_{q\pm} = \frac{\theta^k}{2\theta_{r^k}} \left(J_{ac2} S_{ac} + J_{dc} S_{dc,r^k}\right). \tag{3.4}$$

At last, for the element located in the yoke at radius r^k, both the ac and dc coil bundles are enclosed, which is presented by the area with small triangles in Fig 3.4(d). Hence, the expression of mmf in the yoke above dc coil I is,

$$F^k_{q\pm} = \frac{\theta^k}{2\theta_{r^k}} \left(J_{ac1} S_{ac} + J_{dc} S_{dc}\right), \tag{3.5}$$

where S_{dc} is the entire area of a single dc coil bundle. The mmf in the yoke above dc coil II is similarly written as,

$$F^k_{q\pm} = \frac{\theta^k}{2\theta_{r^k}} \left(J_{ac2} S_{ac} + J_{dc} S_{dc}\right). \tag{3.6}$$

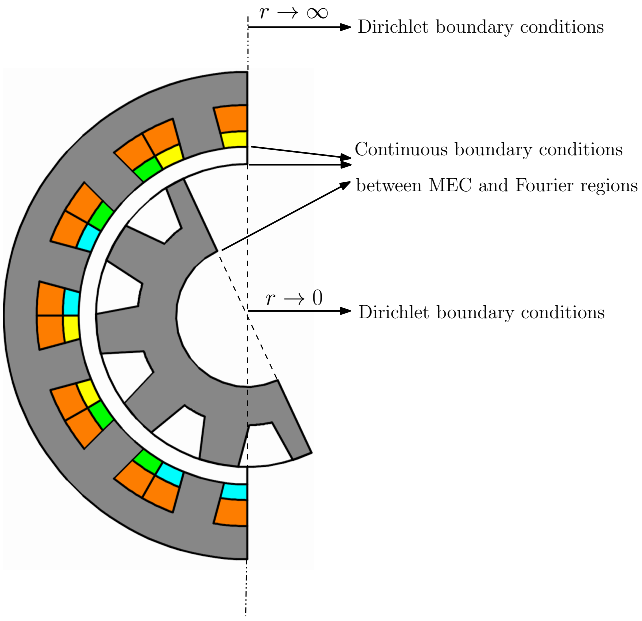
$r \to \infty$
Dirichlet boundary conditions
Continuous boundary conditions
between MEC and Fourier regions
$r \to 0$
Dirichlet boundary conditions

Figure 3.5: Boundary conditions of the 12/10 VFRM.

3.3.4 Boundary conditions

The boundary conditions are clarified in Fig. 3.5. Continuous boundary conditions are applied between Fourier and MEC regions. Since Fourier region II (airgap) and MEC region II (rotor) are defined in stator and mover coordinates, respectively, the coupling of their interface uses equations (2.99), (2.100) and (2.106). For other interfaces, the corresponding Fourier and MEC regions are defined in the same coordinate system, hence, equations (2.59)-(2.60) and equations (2.65)-(2.68) are applied.

Dirichlet boundary conditions are defined at $r \to \infty$ and $r \to 0$ for Fourier regions I (outer air region) and III (shaft). For r approaches to zero that happens in Fourier region III, the term $p^{-\omega_n - 1}$ in equations (A.22)-(A.25) in Appendix A goes to infinity, indicating that the Fourier coefficients b_n and d_n should be zero. Consequently, they are not included in the unknowns. Similarly, for $r \to \infty$ in Fourier region I, the term $p^{\omega_n - 1}$ reaches infinity, accordingly, a_n and c_n in equations (A.22)-(A.25) in Appendix A are zero and are excluded in the unknowns as well.

3.3.5 Matrix formulation

As explained in section 3.3.4, two sets of Fourier coefficients are omitted in Fourier regions I and III, respectively, hence, the unknown matrix of Fourier regions is given as,

$$\mathbf{X} = \left[\mathbf{b}^{\mathrm{I}}\ \mathbf{d}^{\mathrm{I}}\ \mathbf{a}^{\mathrm{II}}\ \mathbf{b}^{\mathrm{II}}\ \mathbf{c}^{\mathrm{II}}\ \mathbf{d}^{\mathrm{II}}\ \mathbf{a}^{\mathrm{III}}\ \mathbf{c}^{\mathrm{III}}\right]^{\mathrm{T}}, \tag{3.7}$$

where the superscript represents the numbering of the Fourier region. The vectors are the array of unknown coefficients that form with,

$$\begin{aligned}
&\mathbf{b}^{\mathrm{I}} = \left[b_1^{\mathrm{I}}\ b_2^{\mathrm{I}}\ \ldots\ b_{N_h}^{\mathrm{I}}\right],\\
&\mathbf{d}^{\mathrm{I}} = \left[d_1^{\mathrm{I}}\ d_2^{\mathrm{I}}\ \ldots\ d_{N_h}^{\mathrm{I}}\right],\\
&\ldots\\
&\mathbf{c}^{\mathrm{III}} = \left[c_1^{\mathrm{III}}\ c_2^{\mathrm{III}}\ \ldots\ c_{N_h}^{\mathrm{III}}\right].
\end{aligned} \tag{3.8}$$

The unknowns for the MEC regions are a vector of the scalar potentials, written as,

$$\boldsymbol{\Psi} = \left[\psi_{\mathbf{1}}\ \psi_{\mathbf{2}}\ \ldots\ \psi_{\mathbf{K}}\right]^{\mathrm{T}}. \tag{3.9}$$

The sets of boundary conditions lead to the matrix,

$$\begin{bmatrix} \mathbf{E_b} \\ \mathbf{E_{MEC}} \end{bmatrix} \begin{bmatrix} \mathbf{X} \\ \boldsymbol{\Psi} \end{bmatrix} = \begin{bmatrix} \mathbf{Y_b} \\ \mathbf{Y_{MEC}} \end{bmatrix}. \tag{3.10}$$

The matrix $\mathbf{E_b}$ provides the coefficients related to the unknowns in the boundary conditions between Fourier and MEC regions; while $\mathbf{E_{MEC}}$ provides the coefficients related to the unknowns in the flux conservation equation, equation (2.39), that provides the magnetic field within the MEC regions. The matrix $\mathbf{Y_b}$ describes the source terms in the boundary conditions between Fourier and MEC regions; while $\mathbf{Y_{MEC}}$ is for the source terms in equations (2.40)-(2.43).

3.3.6 Numerical implementation

The accuracy of the model is strongly related to the number of harmonics, and sufficient number of harmonics is essential to obtain accurate results. Especially for Fourier region II that models the airgap region, a high order of harmonics is generally preferred. However, the constants for Fourier coefficients, i.e., $p^{\omega_n - 1}$ and $p^{-\omega_n - 1}$, significantly increase as the order of harmonic increases for the situations of $p > 1$ and $p < 1$, respectively. As a consequence, matrix $\mathbf{E_b}$ is ill-conditioned, leading to an inaccurate result.

To allow adequate harmonic orders, proper scaling is applied. For Fourier modeling, it is realized by giving a normalization height p_0, since the expression of magnetic field in Fourier region shares the term of p^{ω_n-1} or $p^{-\omega_n-1}$ [52],

$$\frac{p^{\omega_n^k-1}}{p_0^{\omega_n^k-1}} = \left(\frac{p}{p_0}\right)^{\omega_n^k-1}, \tag{3.11}$$

$$\frac{p^{-\omega_n^k-1}}{p_0^{-\omega_n^k-1}} = \left(\frac{p}{p_0}\right)^{-\omega_n^k-1}. \tag{3.12}$$

For coupling between Fourier and MEC regions, the same scaling has to be applied simultaneously for these two types of regions. In the polar coordinate system, it is realized by scaling the entire geometric domain by the same scaling factor, $\mathcal{S}_f$, in the radial direction, that makes the median value of the airgap approaches the value of unity. As such, both the inner and outer airgap boundaries have a radius very close to unity.

For the VFRM with dimensions listed in Table 3.1, the scaling factor is selected by,

$$\mathcal{S}_f = \frac{1}{r_{sh} + h_{ry} + h_{rt} + 0.5g}. \tag{3.13}$$

As such, the values of $p^{-\omega_n-1}$ and p^{ω_n-1} are reduced to the magnitude of 10^{-2} or 10^2 at the airgap coupling interfaces with a harmonic order up to 180.

Theoretically, if the mesh network in the MEC region is scaled up by $\mathcal{S}_f$ in the r-direction, the values of l_p^k, l_q^k, S_{pl}^k and S_{ql}^k are all scaled by $\mathcal{S}_f$. This means that the reluctance values are not changed in the non-scaled and scaled geometries according to equations (2.17)-(2.20). To obtain the correct flux density distribution, the current related mmf has to be multiplied by $\mathcal{S}_f$ as well. As a result, the obtained flux is scaled by $\mathcal{S}_f$, and the resulting B_q^k and B_p^k in a scaled geometry remain the same as the non-scaled geometry based on equations (2.44)-(2.45).

As the flux density distribution is the same in the scaled and non-scaled geometries, the results can be directly used for deriving machine quantities, while if Fourier coefficients are needed, e.g., in torque calculation, they have to be scaled by $(\frac{1}{\mathcal{S}_f})^{\omega_n-1}$ or $(\frac{1}{\mathcal{S}_f})^{-\omega_n-1}$.

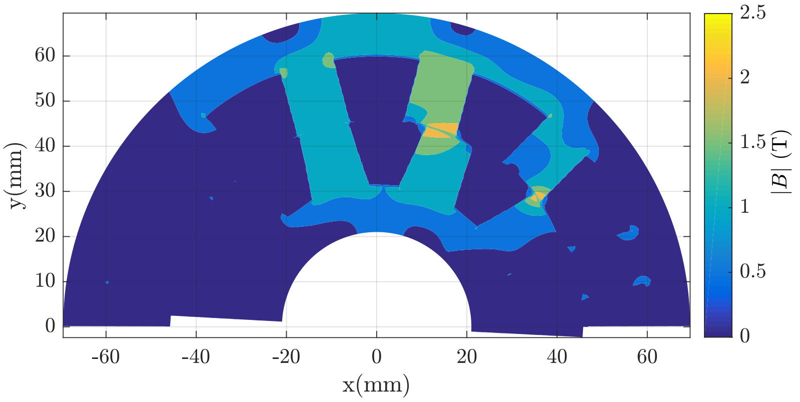

(a)

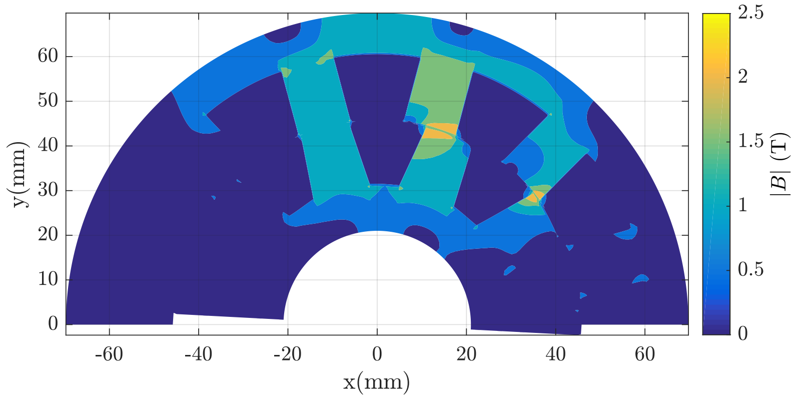

(b)

Figure 3.6: The distribution of the flux density magnitude, $|B|$, obtained by (a) HAM, and (b) FEM.

3.4 Magnetic flux density

As the basis for deriving machine performances, the flux density is presented in this section. Two-dimensional nonlinear FEM with the same material as HAM, is used as a reference to verify the results. The FEM is solved as a quasi-static problem for the calculation of almost all the machine quantities, except the ac copper loss.

The flux density distribution obtained by the HAM is shown in Fig. 3.6(a) for the rotation angle $\Delta_\theta = 0$. The results of FEM is shown in Fig. 3.6(b), an overall agreement between HAM and FEM is observed, including the area with magnetic saturation.

For a more intense comparison, the flux density in the center of the airgap is presented and compared in Fig. 3.7. The values of radial and circumferential components are presented in Fig. 3.7(a). As can be seen, an overall very good agreement is achieved. However, there are still remaining differences close to the teeth vertices, that is respectively about 0.15 T and 0.2 T in the radial and circumferential directions as shown in Fig. 3.7(b).

3.5 Torque

This section presents the derivation methods of the electromagnetic torque. It is possible to derive the torque in saturated VFRMs by using the virtual work method and the Maxwell stress tensor method. The virtual work method calculates the torque based on the concept of energy conversion [48, 85]. Theoretically, the instant electromagnetic torque can be calculated by,

$$T_{em} = \frac{\partial W_c\left(\theta\right)}{\partial \theta}, \tag{3.14}$$

where W_c is the co-energy in a system, defined as,

$$W_c = \int\limits_{V} \int\limits_{0}^{H} \left(\vec{B} d\vec{H}\right) dV. \tag{3.15}$$

Since the analytical expression of the magnetic field in ferromagnetic materials is not obtained in the HAM, W_c is not analytically differentiable to the rotation angle. As a result, the derivative of W_c has to be obtained by two field calculations at two different rotation angles. Therefore, this method is not recommended for the torque calculation in the HAM.

On the contrary, using the Maxwell stress tensor, $\mathbb{T}$, the electromagnetic torque can be calculated analytically at any arbitrary Δ_θ. For $\mathbb{T}$ given as,

$$\mathbb{T} = \begin{bmatrix} \frac{B_p^2 - B_q^2 - B_l^2}{2} & B_p B_q & B_p B_l \\ B_q B_p & \frac{-B_p^2 + B_q^2 - B_l^2}{2} & B_q B_l \\ B_l B_p & B_l B_q & \frac{-B_p^2 - B_q^2 + B_l^2}{2} \end{bmatrix}, \tag{3.16}$$

the force between two objects is calculated as,

$$\vec{F} = \frac{1}{\mu} \oint\limits_{S} \mathbb{T} \cdot d\vec{S}, \tag{3.17}$$

where the surface S should encompass the object for which the force is calculated. In rotating electrical machines, the surface S in equation (3.17) can be positioned

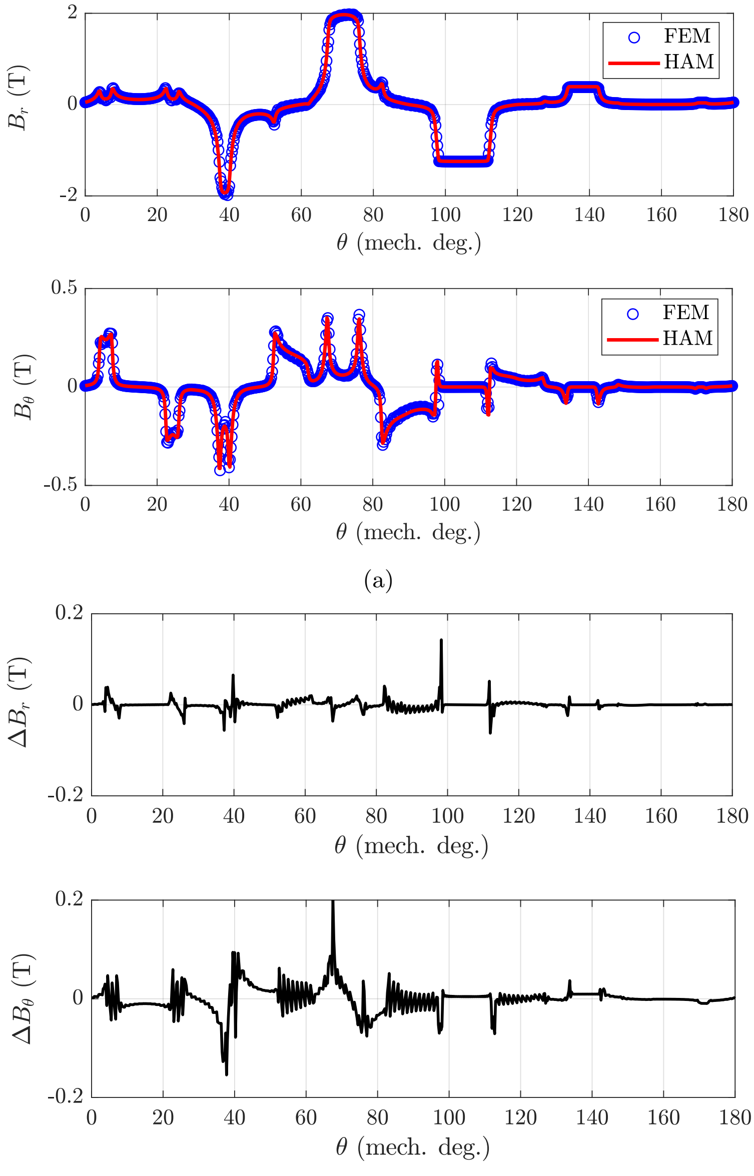

(a)

(b)

Figure 3.7: Magnetic flux density in the center of the airgap: (a) radial and circumferential components, B_r and B_θ, calculated by HAM and FEM, and (b) differences between B_r and B_θ obtained by HAM and FEM.

in the center of the airgap, and the electromagnetic torque is,

$$T_{em} = \frac{1}{\mu_0} \oint_S r \times \mathbb{T} \cdot dS. \tag{3.18}$$

In a 2D geometry, the torque is expressed as,

$$T_{em} = \frac{1}{\mu_0} \oint_S r B_r B_\theta \cdot dS = \frac{1}{\mu_0} \int_0^{2\pi} r B_r B_\theta d\left(L_{sk} r \theta\right) = \frac{L_{sk} r^2}{\mu_0} \int_0^{2\pi} B_r B_\theta d\theta. \tag{3.19}$$

In equation (3.19), the torque calculated by Maxwell stress tensor is written in the integral form, and hence, is sensitive to the spatial discretization of θ. However, since the airgap is modeled as a Fourier region in the HAM, the magnetic field has analytical expressions. Substituting B_r and B_θ by the Fourier series expressed in equations (A.22)-(A.25) in Appendix A, the torque is derived as,

$$T_{em} = \frac{2\pi L_{sk}}{\mu_0} \sum_{n=1}^{N_h} (b_n c_n - a_n d_n). \tag{3.20}$$

As such, a continuous analytical expression based on the Fourier coefficients is obtained, and the influence of the spatial discretization is not a concern.

To verify the torque obtained by the HAM, the torque profile for one electric revolution is first calculated for J_{dc} and $J_{ac,rms}$ both at 10 A/mm^2, as shown in Fig. 3.8 together with the FEM results. Both the curve shape and the magnitude match well, a clear 6^{th} harmonic is observed in both torque waveforms, and the maximum discrepancy along the two curves is less than 3%. To verify the torque for different current densities, the mean torque is shown in Fig. 3.9(a) from 2 A/mm^2 to 18 A/mm^2. As can be seen, the quadratic relation at low current levels ($\leq$ 6 A/mm^2) becomes more linear with the rise of the current densities, due to the saturation of the magnetic materials. The difference of the mean torque obtained by HAM and FEM is depicted in Fig. 3.9(b), that shows a maximum discrepancy less than 1.5 %. The torque ripple, T_{rip}, is shown in Fig. 3.9(c), and the difference compared to FEM results is presented in Fig. 3.9(d). The mismatch of the torque ripple is less than 6% for various current densities, indicating a good agreement between the HAM and FEM. Based on the above results, the HAM is a suitable tool for predicting the torque profile, mean torque and torque ripple.

3.6 Flux linkage, back-emf and phase voltage

For a coil with negligible slot leakage, the calculation of the flux can be obtained by integrating the normal (radial) component of the flux density at the inner radius of the tooth. However, this approach cannot be directly applied to machines if the slot leakage is significant. To calculate the flux linkage correctly, both the normal

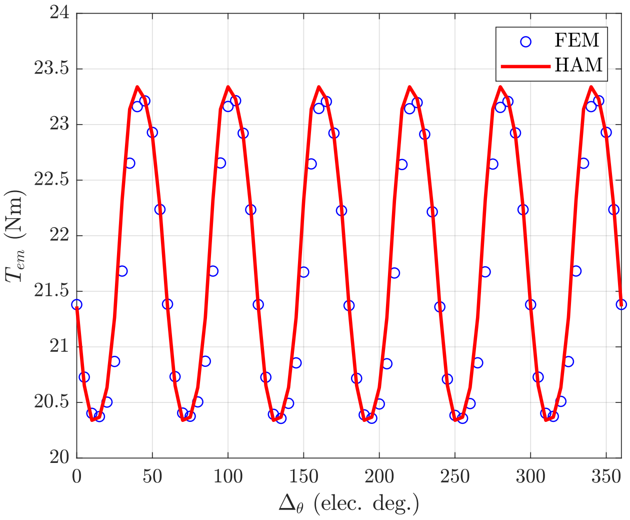

Figure 3.8: Electromagnetic torque, T_{em}, at different rotation angles, Δ_θ, when the current density is 10 A/mm^2 for both field winding and armature windings.

and tangential components of the flux density has to be considered on the four edges of a coil bundle. The difficulty comes when judging if the flux is inward or outward at each of the edge.

Herewith, a generalized method from another perspective is introduced, which calculates the flux linkage by means of discretization of coils and integration of flux from each segment. Assume a coil is filled by wires with in total N_t turns, as shown in Fig. 3.10. For ease of explanation, the wires are numbered, first in the ascending tangential direction, and then in the ascending normal direction. Due to the 2D geometry, each turn is divided into two wires. To differentiate them in the figure, the numbering is labeled with single or double primes that indicates the positive or negative orientations (wound in the positive or negative axial directions), respectively. Besides, the two halves of each turn are set to be symmetric from the centerline of the slot as can be seen in the figure, that the wire numbering ascends in opposite directions for the left and right coil bundles.

Note that the meshing in the MEC region inherently provides a network of discretizing the coil into small segments. By this, the values of wire size are predefined by the MEC elements.

For a random wire turn n_t, it forms an area with the wire height, h_{n_t}, and the distance between the corresponding two halves, w_{n_t}, as shown in Fig. 3.10. If the cross section of the wire itself is small enough, h_{n_t} is negligible compared to w_{n_t} and the flux passing through the two side edges can be ignored. It means the flux of such a turn can be calculated by integrating the normal flux density along the

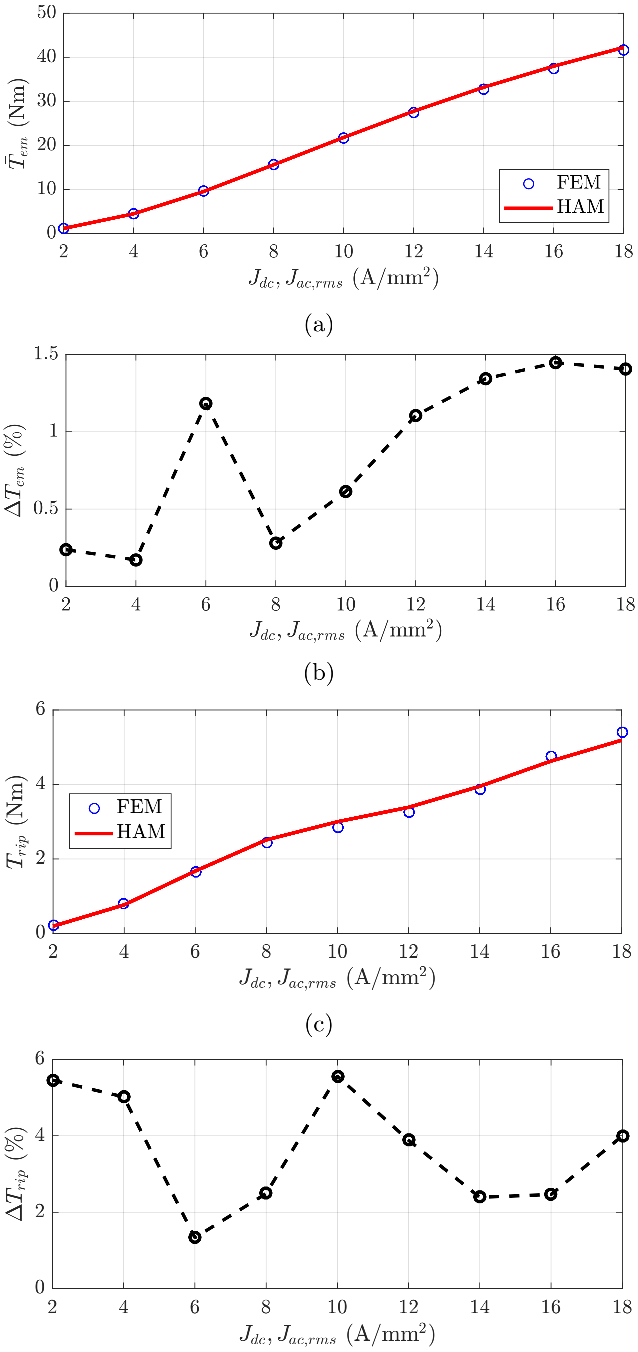

(a)

(b)

(c)

(d)

Figure 3.9: Comparison of the electromagnetic torque at different dc and ac current densities (J_{dc} and $J_{ac,rms}$): (a) the mean torque ($\bar{T}_{em}$), (b) the difference between the mean torque obtained by HAM and FEM (ΔT_{em}), (c) the torque ripple (T_{rip}), and (d) the difference between the torque ripple obtained by HAM and FEM (ΔT_{rip}).

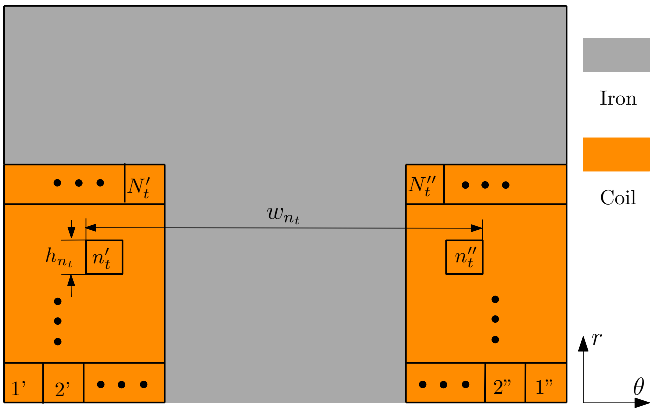

Figure 3.10: Discretization of a coil, assuming it is filled with wires (N_t is the number of turns, h_{n_t} represents the height of the turn numbered with n_t, and w_{n_t} represents the distance between the left and right halves of the turn.

bottom edge, giving the equation,

$$\phi_{n_t} = \int\limits_{0}^{w_{nt}} B_r L_{sk} d(r\theta). \tag{3.21}$$

The flux linkage linked by all the wires are therefore given as,

$$\Lambda = \sum_{n_t=1}^{N_t} \int\limits_{0}^{w_{nt}} B_r L_{sk} d(r\theta). \tag{3.22}$$

This result is derived under the assumption that the coil is filled with in total N_t turns, hence, the correct flux linkage has to be multiplied by the ratio of actual number of turns to N_t.

Using this method, the flux linkage is estimated in one electric revolution for phase A winding and field winding, respectively. In Fig. 3.11, the obtained results are presented. As can be seen, the waveforms obtained from HAM and FEM match very well with each other, that have the average discrepancies of 1.1% and 2.0% for Λ_A and Λ_f, respectively.

The phase voltage is obtained by summing the derivative of the flux linkage and the resistive voltage. In Fig. 3.12(a), it presents the voltage of phase A at the speed of 100 rpm. The induced back electromotive force (back-emf) is calculated by taking the derivative of the flux linkage when the armature reaction is not considered. The back-emf of phase A, e_A, is calculated for J_{dc} at 10 A/mm^2, and the result is shown in Fig. 3.12(b). Compared to the FEM results, a good match of both the waveforms and amplitudes are obtained by the HAM. The maximum discrepancy between the HAM and FEM results is 0.7 V for v_A and 0.6 V for e_A, respectively, which are both around 2%.

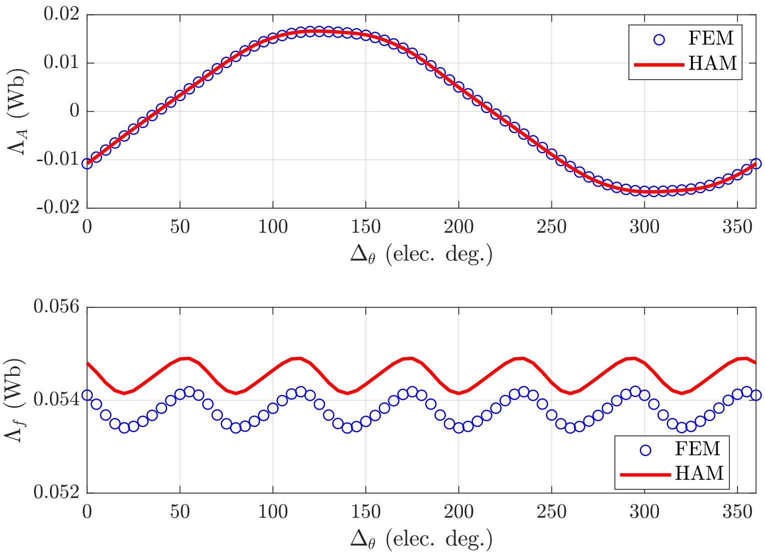

Figure 3.11: Variation of the flux linkages of phase A winding (Λ_A) and field winding (Λ_f) versus the rotation angle (Δ_θ).

3.7 Inductance

The inductances are important machine parameters, and it is necessary to predict the inductances accurately for the control system design by taking the nonlinear magnetic behavior into account [56]. In this section, the derivation of incremental (dynamic) inductances is explained. Generally, in VFRMs, there are respectively self inductances of field winding and armature windings, as well as the mutual inductances among them. The detailed definitions are explained in section 4.2. The derivation of the mutual inductance between the field winding and armature windings, M_{fph}, is introduced as an example. This method is applicable to obtain other inductance values.

For the incremental inductance at a certain current level i, the difference of the flux linkage is divided by the difference of the corresponding current [58], giving the equation,

$$M_{fph}(i) = \frac{d\Lambda}{di} = \left.\frac{\Lambda(i+\Delta i) - \Lambda(i-\Delta i)}{2\Delta i}\right|_{\Delta i \to 0}. \tag{3.23}$$

The value of M_{fph} depends on the field current and armature current simultaneously, herewith the value depending on the field current is derived, while the calculation of M_{fph} depending on the armature current is similar. The magnitude of Δi has to be small enough to obtain accurate results and is set to be 0.2% of the i value in the calculation. Assume a current density of 10 A/mm^2 for both $J_{ac,rms}$ and J_{dc}, the incremental M_{fph} is obtained by the HAM and FEM, respectively.

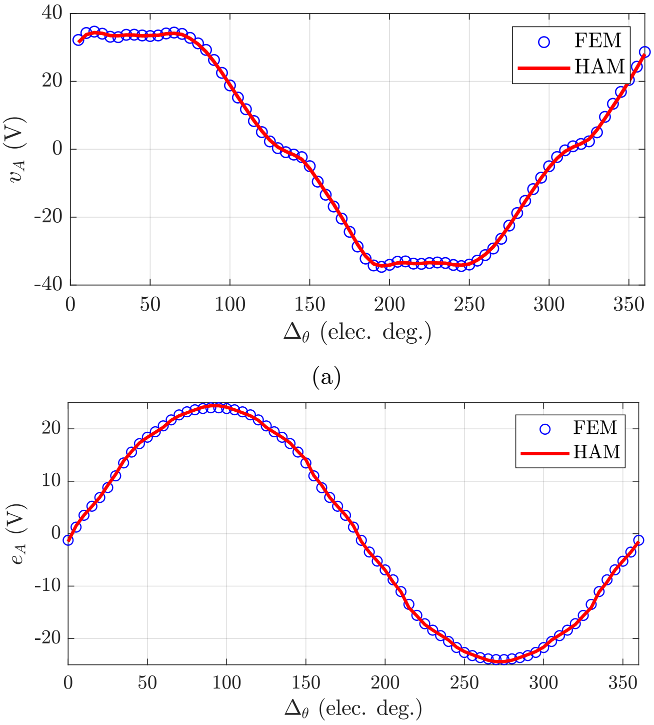

(a)

(b)

Figure 3.12: The obtained results using HAM and FEM for the speed of 100 rpm: (a) the voltage of phase A (v_A) versus the rotation angle (Δ_θ) when the current densities of the field winding and armature windings are both 10 A/mm^2, and (b) the back-emf of phase A (e_A) versus Δ_θ when the current density of the field winding is 10 A/mm^2.

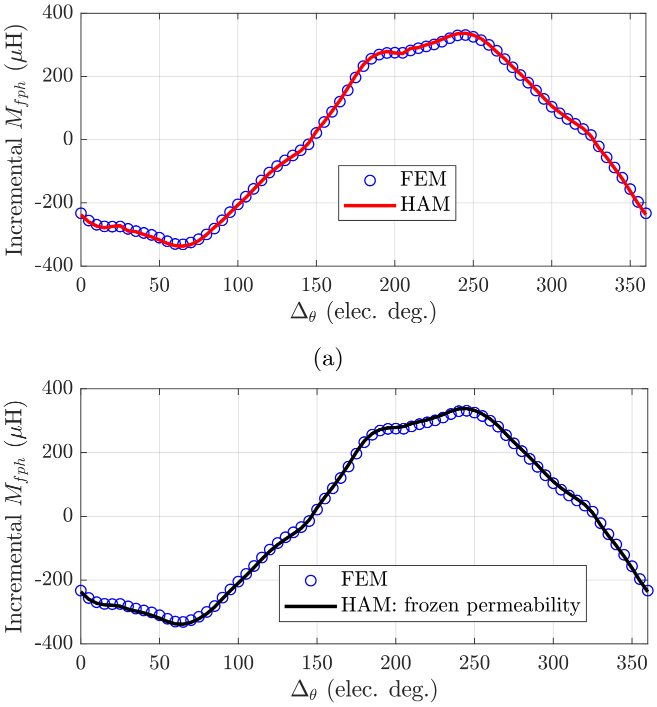

(a)

(b)

Figure 3.13: Incremental inductance (M_{fph}) versus rotation angle (Δ_θ) assuming the current density of both field winding and armature windings ($J_{ac,rms}$ and J_{dc}) is 10 A/mm^2: (a) obtained by the conventional method in HAM and FEM, (b) obtained by using the frozen permeability in HAM and the conventional method in FEM.

The results are compared in Fig. 3.13(a) for one electric revolution, where a good agreement between the two curves is obtained.

In addition to the aforementioned method by using equation (3.23), frozen permeability [49, 57] can be used to obtain the incremental inductance in the HAM. The principle is based on the assumption that the permeability does not change when Δi approaches zero. The procedure is described as follows:

- Step 1: Calculation is carried out for a given current i to obtain the flux linkage $\Lambda(i)$.
- Step 2: The relative permeability in all MEC elements in Step 1 is saved. This ensures that the magnetic saturation level remains the same.
- Step 3: Apply the previously saved permeability and 'freeze' the values, run the HAM by resetting the current at $(i + \Delta i)$ to obtain the flux linkage $\Lambda(i + \Delta i)$.
- Step 4: Calculate the incremental inductance by $M_{f,ph}(i) = \frac{\Lambda(i+\Delta i)-\Lambda(i)}{\Delta i}$.

Since the permeability is frozen, Step 3 is a linear calculation and no iteration is required to update the permeability. This can reduce the computation effort compared to the conventional method that has to iterate for both current levels at $(i - \Delta i)$ and $(i + \Delta i)$. Additionally, such linearity allows a random selection of Δi in Step 3, that does not influence the inductance value obtained in Step 4.

To verify the concept, incremental M_{fph} is obtained by using the above procedures and is compared with the FEM results using the conventional method, as shown in Fig. 3.13(b). A very good match between FEM and HAM is observed. Furthermore, the incremental M_{fph} is obtained at different field current levels as shown in Fig. 3.14, and a good agreement between the two curves is again presented, where the discrepancy is within 2.2%.

3.8 Losses

To use the modeling technique for machine design and performance prediction, the machine losses have to be estimated. Both the methods for evaluating iron losses and copper losses are introduced in this section.

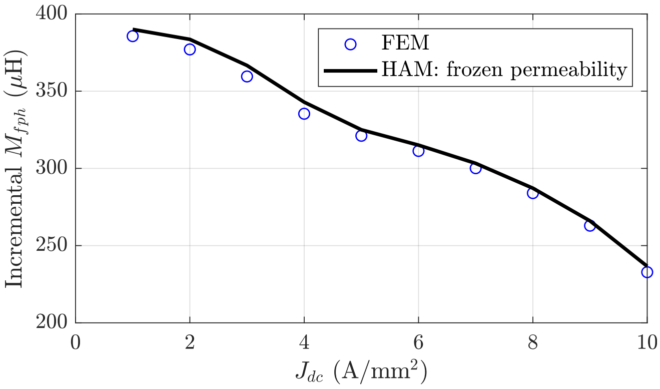

Figure 3.14: Comparison of the incremental inductance (M_{fph}) at various field current levels (J_{dc}), obtained by HAM using the frozen permeability and FEM using the conventional method (rotation angle Δ_θ is set at 180 elec. deg., and armature current density $J_{ac,rms}$ is fixed at 10 A/mm^2).

3.8.1 Iron losses

The iron loss is separated by three contributions: the static hysteresis loss, the classical eddy-current loss and excess loss [18, 42]. The iron loss density, p_{Fe}, is described by,

$$p_{Fe} = p_{hys} + p_{eddy} + p_{ex}, \tag{3.24}$$

where p_{hys}, p_{eddy} and p_{ex} is the hysteresis loss density, eddy current loss density and excess loss density, respectively. For sinusoidal flux density waveforms, the calculation of these three types of losses are given as,

$$p_{hys} = K_{hys}\hat{B}^{\alpha_h} f, \tag{3.25}$$

$$p_{eddy} = \frac{\pi^2 \sigma_{Fe} d_{lam}^2}{6}\left(\hat{B} f\right)^2, \tag{3.26}$$

$$p_{ex} = K_{ex}\left(\hat{B} f\right)^{1.5}, \tag{3.27}$$

where K_{hys} and K_{ex} are the hysteresis-loss and excess-loss coefficients, respectively, α_h is the exponent for hysteresis loss term, σ_{Fe} and d_{lam} are the conductivity and thickness of the lamination, respectively, $\hat{B}$ is the peak flux density and f is the excitation frequency.

Frequency domain equations, (3.25)-(3.27), are particularly useful when the data are presented in frequency terms. However, this is often not the case when time-stepped FE analysis is undertaken. Instead, the above equations are converted to

Table 3.2: Material-dependent constants for iron loss calculation.

Parameter	Description	value	unit
K_{hys}	Hysteresis-loss coefficient	158.62	-
K_{ex}	Excess-loss coefficient	2.17	-
α_h	Exponent for hysteresis loss term	1.8	
σ_{Fe}	Conductivity of lamination	1.69	$\times 10^6$ S/m
d_{lam}	Lamination thickness	0.27	mm

a time domain using instantaneous flux density,

$$P_{hys} = K_{hys}\frac{1}{T}\hat{B}^{\alpha_h}, \tag{3.28}$$

$$p_{eddy} = \sigma_{Fe}\frac{d_{lam}^2}{12}\left(\frac{dB}{dt}\right)^2, \tag{3.29}$$

$$p_{ex} = \frac{K_{ex}}{8.67}\left(\frac{dB}{dt}\right)^{1.5}. \tag{3.30}$$

In this thesis, the material-dependent iron loss constants are provided in Table 3.2. The values are obtained by curve fitting of the measurement data that are tested with sinusoidal excitations at various frequencies.

In the hybrid analytical modeling, the magnetostatic flux density is described in r and θ coordinates, hence, B_r and B_θ are used in equations (3.29)-(3.30) separately to obtain decomposed values of eddy current loss density and excess loss density, and the final loss densities are derived by summing up the components in the two axes [19, 39, 55, 82].

For each MEC element that representing ferromagnetic material, the loss density is estimated. The element iron loss is calculated by multiplying the loss density with element volume. The total iron loss is derived by summing up the loss for every element. The obtained values are listed in Table 3.3. As compared, the results from the HAM and FEM match well with each other, that the difference of the total iron loss is around 1%.

3.8.2 Copper losses

The copper losses of the machine includes losses from the field winding and armature windings. Ignoring the contribution of eddy currents, the loss in each of the winding is estimated using the equation,

$$P_{cu,d} = \frac{J_x^2 V_x \rho}{k_f}, \tag{3.31}$$

where x represents field winding and phase A, B, C windings, respectively, J_x represents the RMS phase current density or mean value of the field current

Table 3.3: The predicted iron losses of the VFRM.

		HAM (W)	FEM (W)	Difference (%)
Rotor	Hysteresis loss	12.45	12.49	0.3
	Eddy current loss	1.39	1.36	2.2
	Excess loss	1.24	1.15	7.8
	Total	15.08	15.00	0.5
Stator	Hysteresis loss	25.70	25.40	1.2
	Eddy current loss	2.13	2.14	0.5
	Excess loss	1.89	1.80	5.0
	Total	29.72	29.34	1.3
Machine	Total	44.80	44.34	1.0

density, k_f is the filling factor, V_x is the coil volume and ρ is the copper resistivity.

However, the copper loss in reality is more than the above. The occurrence of teeth alignment and un-alignment in VFRMs leads to a fast change of magnetic field in the slot, especially in the stator slot openings. The wires at these locations experience a rapid variation of flux density, hence, have high level of induced eddy currents, which can generate extra ac copper losses [98]. For high-speed machine or machine where efficiency is important, it is essential to have an estimation of the magnitude of such ac loss, to achieve a proper winding layout that prevents machine failure due to localized heating or to obtain accurate efficiency.

The eddy current and ac copper losses are difficult to calculate since they are related to a lot of factors, such as, machine geometry, winding layout, rotation speed, etc. It is possible to use transient time-stepped FEM that draw individual geometries for wires and simulates the losses for each conductor [66, 99]. This computation is very time consuming if the ac copper losses at various speeds are desired, since a transient simulation at each rotational speed has to be performed. Moreover, for each speed, the eddy currents have to be calculated until convergence at each time step. [52] Hence, to reduce the computational effort, a simplified calculation is done in the HAM under some certain assumptions.

Assumptions

The dynamic solution of the magnetic vector potential is governed by [61],

$$\nabla^2\vec{A} - \mu\sigma\frac{\partial\vec{A}}{\partial t} = -\mu\vec{J} - \mu\left(\nabla\times\vec{M}\right). \tag{3.32}$$

However, if the speed is relatively low, the influence of eddy currents on the solution of magnetic vector potential is relatively small, consequently, the field distribution is close to the situation when eddy currents are not considered. Therefore, it is possible to use the field solution obtained from quasi-static Maxwell equations combined with the data post-processing to estimate the ac copper losses [15].

Calculation method in the HAM

In each coil conductor, the change of magnetic field induces an electrical field based on Faraday's law,

$$\nabla \times \vec{E}_{eddy} = -\frac{\partial \vec{B}}{\partial t}. \tag{3.33}$$

Substituting the flux density by the expression of magnetic vector potential written in equation (2.3), this gives,

$$\vec{E}_{eddy} = -\frac{\partial \vec{A}}{\partial t} - \nabla\varphi, \tag{3.34}$$

where φ represents a scalar potential which describes the conservative electric field.

Assume the function of the scalar potential φ is $\varphi = \varphi(r, \theta, z)$, the gradient of φ is accordingly given by,

$$\nabla\varphi(r,\theta,z) = \frac{\partial\varphi}{\partial r}\mathbf{i} + \frac{\partial\varphi}{\partial\theta}\mathbf{j} + \frac{\partial\varphi}{\partial z}\mathbf{k}, \tag{3.35}$$

where $\mathbf{i}$, $\mathbf{j}$ and $\mathbf{k}$ are the standard unit vectors in the directions of the r-, θ- and z-coordinates. In case of 2D magnetostatic modeling, the electric field only has a z-component. It means $\nabla\varphi$ only contains a vector in the z-direction, hence, both terms $\frac{\partial\varphi}{\partial r}$ and $\frac{\partial\varphi}{\partial\theta}$ must be zero. Consequently, the expression of φ is not dependent to r- and θ-coordinates. Equation (3.35) reduces to,

$$\nabla\varphi(z) = \frac{\partial\varphi}{\partial z}\mathbf{k}. \tag{3.36}$$

This expression shows the position independence in the $r\theta$-plane, hence, $\nabla\varphi$ remains constant within the cross section of a wire conductor.

The electric field in equation (3.34) excites an eddy current, expressed by,

$$\vec{J}_{eddy} = \sigma\vec{E}_{eddy}, \tag{3.37}$$

where σ is the conductivity of copper. Assume a current source is used to impose the current in the conductor, the total current density, J_{tot}, is decomposed by the induced eddy current density (J_{eddy}) and the initial current density supplied by the current source (J_s), expressed as,

$$\vec{J}_{tot} = \vec{J}_{eddy} + \vec{J}_s. \tag{3.38}$$

As the current is imposed, the total current in the conductor should always be equal to the current supplied by the current source [2], which means

$$\int\limits_{S_{cond}} J_{tot}S_{cond} = \int\limits_{S_{cond}} J_s S_{cond}, \tag{3.39}$$

where S_{cond} is the cross section of the conductor. This gives the fact that the net eddy current is zero,

$$\int\limits_{S_{cond}} J_{eddy} dS_{cond} = \sigma \int\limits_{S_{cond}} E_{eddy} dS_{cond} = 0. \tag{3.40}$$

Substituting E_{eddy} by the expression in equation (3.34), this gives,

$$\sigma \int\limits_{S_{cond}} \left(-\frac{\partial \vec{A}_z}{\partial t} - \nabla \varphi \right) dS_{cond} = 0. \tag{3.41}$$

As explained above, the value of $\nabla \varphi$ is a constant within the cross section, hence, the value is calculated as,

$$\nabla \varphi = \frac{\int\limits_{S_{cond}} \left(-\frac{\partial \vec{A}_z}{\partial t} \right) dS_{cond}}{S_{cond}}. \tag{3.42}$$

After obtaining the eddy current density, the ac copper loss is calculated by,

$$P_{cu,a} = \rho \int\limits_{V} J_{tot}^2 dV, \tag{3.43}$$

where V is the conductor volume.

The above procedures for calculating the ac copper loss in HAM are summarized as follows:

1. Obtain the flux density distribution at different rotation angle Δ_θ;
2. Calculate the magnetic vector potential distribution A_z in the stator at each Δ_θ by post processing;
3. Calculate $\frac{dA_z}{dt}$ over the conductors;
4. Derive time instant $\nabla \varphi$ by equation (3.42);
5. Derive the induced electric field by equation (3.34);
6. Derive the induced eddy current by equation (3.37);
7. Calculate the total current density by equation (3.38);
8. Calculate the ac copper loss by equation (3.43).

To verify this method, an example is first given assuming a single conductor within the coil. The calculation results of the magnetic vector potential, eddy current and ac copper loss are given in the following.

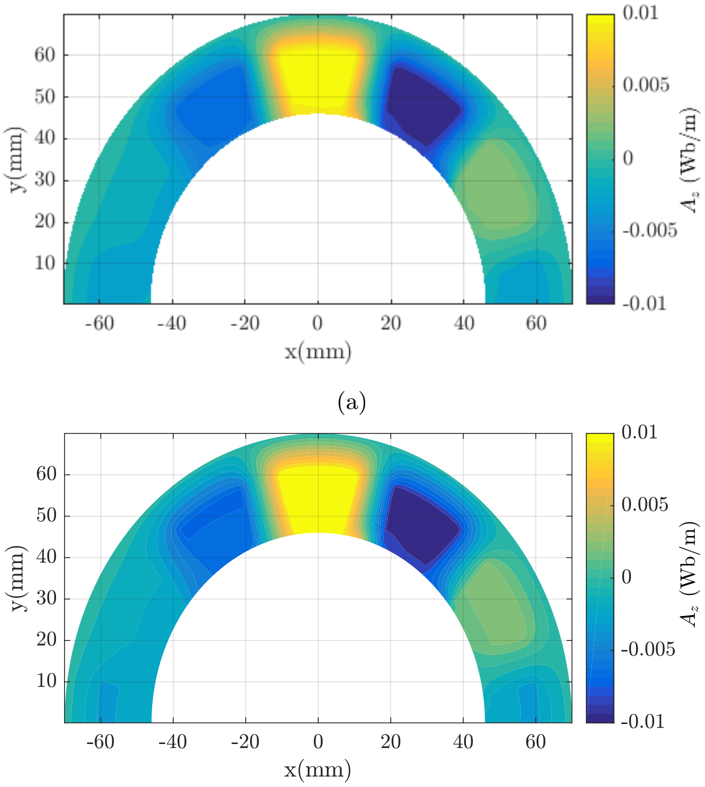

(a)

(b)

Figure 3.15: Magnetic vector potential distribution at rotation angle Δ_θ=0 deg. obtained by using (a) HAM, and (b) FEM.

Magnetic vector potential

To calculate the magnetic vector potential in the aforementioned Step 2, it is assumed that A_z is zero at the geometric infinity. With the obtained flux density distribution in the HAM, the vector potential is calculated as,

$$A_z = \int_{\infty}^{r} B_\theta dr. \tag{3.44}$$

To verify this, the result of HAM is shown in Fig. 3.15(a) for the stator, which matches with the solution from FEM that is shown in Fig. 3.15(b).

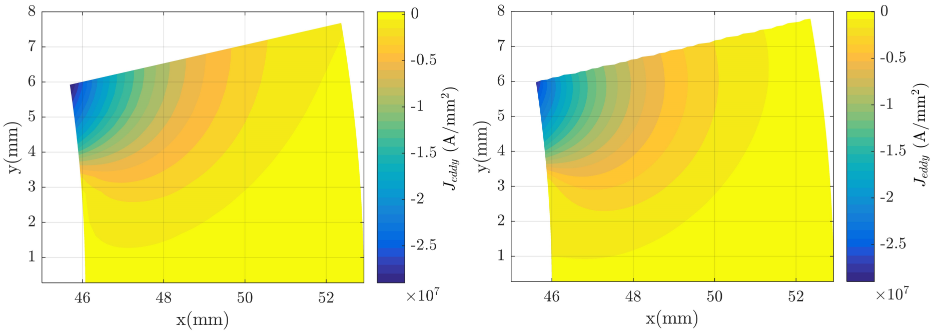

(a) (b)

Figure 3.16: Eddy current distribution of the coil bundle obtained by using (a) HAM, and (b) FEM.

Eddy current

The eddy current in the HAM is calculated by the aforementioned procedures, and the result for one coil bundle is shown in Fig. 3.16(a) at the speed of 50 rad/s. In FEM, it is possible to extract the total current density of a coil directly, and based on equation (3.38), the eddy current density is obtained by subtracting the current density caused by the current source. The result of FEM is shown in Fig. 3.16(b). As can be seen, both the pattern and magnitude of the distribution are similar in the two figures.

Ac copper loss

Using the obtained eddy current, the ac copper loss is calculated, and curves of the losses versus the rotation angle is presented in Fig. 3.17(a). The according copper loss without considering the ac effect is presented as a reference. The ac copper loss does not reduce to zero when the source current is zero due to the presence of eddy currents.

Furthermore, the relationship between ac copper loss and rotational speed is presented in Fig. 3.17(b), and the difference between the HAM and FEM results is shown in Fig. 3.17(c). As can be seen, the difference increases as the speed increases, that is the consequence when the field produced by the eddy currents becomes more dominant and the actual dynamic solution of the magnetic vector potential deviates more and more from the quasi-static problems. Additionally, the conductor has a large cross section, hence, the deviation starts to be significant at a relatively low speed.

For further illustration, the ac coil area is divided into two parts, which respectively represents a turn of conductor, as shown in Fig. 3.18(a). The obtained ac copper losses for the two conductors are presented in Fig. 3.18(b) and (c), respec-

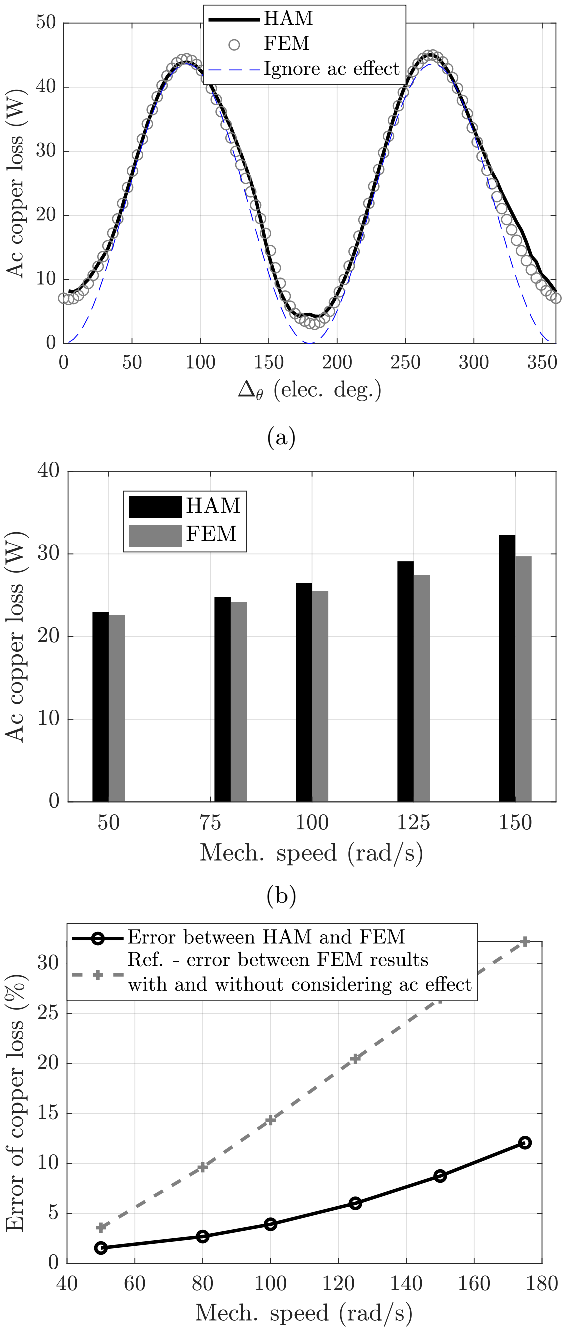

(a)

(b)

(c)

Figure 3.17: Ac copper losses calculated by HAM and FEM for the coil with a single conductor: (a) the ac copper losses versus the rotation angle (Δ_θ) at the speed of 80 rad/s, (b) the ac copper losses at various speeds, and (c) the difference of the ac copper losses at various speeds.

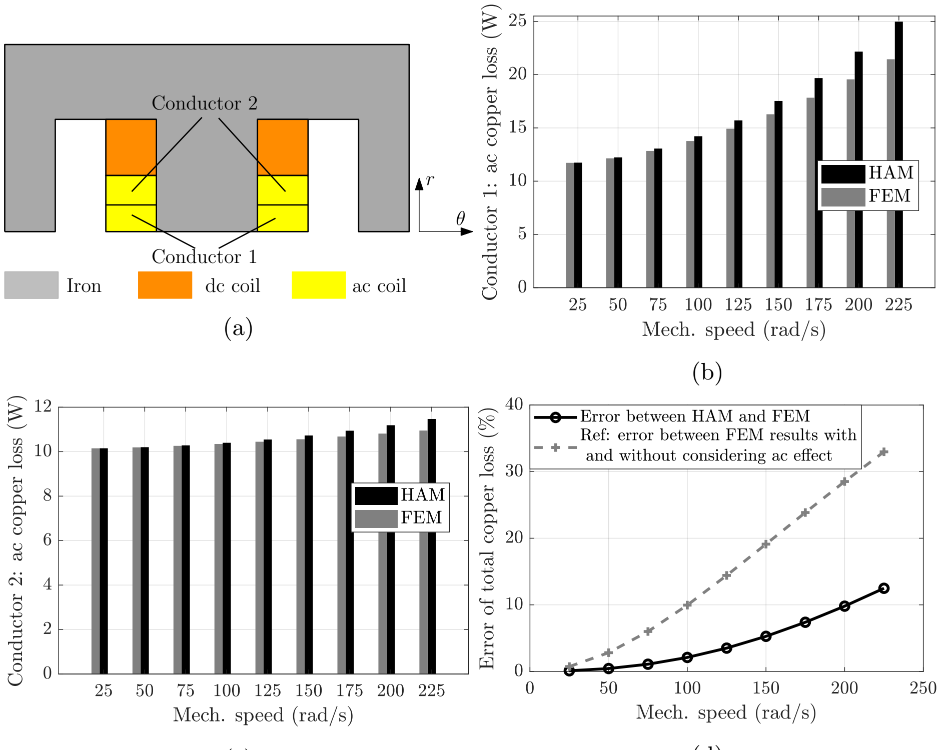

(a)

(b)

(c)

(d)

Figure 3.18: Two conductors in the ac coil: (a) the schematic graph, (b) the ac copper losses of conductor 1 at various speeds calculated by HAM and FEM, (c) the ac copper losses of conductor 2 at various speeds calculated by HAM and FEM, and (d) the difference of the total ac copper losses for the ac coil at various speeds obtained by HAM and FEM.

tively. The ac copper loss of conductor 1 is significantly higher than conductor 2, since it is positioned near the slot opening, hence, is much more influenced by the proximity effect. The differences of the ac copper losses obtained from HAM and FEM is 16.4% and 4.7%, respectively, at the speed of 225 rad/s for the two conductors. The total difference of the ac copper losses for the ac coil is shown in Fig. 3.18(d), which shows a discrepancy of 12.5% at 225 rad/s between the HAM and FEM results.

Such analysis in the HAM is useful as a fast assistance for winding design that can help with the determination of the initial wire size and configurations. Although there is difference between the HAM and FEM results, it is still much more accurate compared to directly using the copper loss without considering any ac effect, as can be seen in the reference curves shown in Fig. 3.17(c) and Fig. 3.18(d). Hence, the analysis is able to provide suggestive indications.

3.9 Efficiency and power factor

Using the machine quantities obtained in the previous sections, the efficiency and power factor can be estimated. The efficiency is calculated by,

$$\eta = \frac{T_{em}\omega_m}{P_{in}} = \frac{T_{em}\omega_m}{T_{em}\omega_m + P_{ml} + P_{cu,a} + P_{Fe}}, \tag{3.45}$$

where ω_m is the mechanical rotational speed in rad/s and P_{ml} is the mechanical loss.

The power factor is calculated by,

$$PF = \frac{P_{in}}{\sqrt{P_{in}^2 + Q^2}}, \tag{3.46}$$

where Q is the reactive power and is estimated as,

$$Q = \sqrt{m(V_{rms,ac} I_{rms,ac})^2 - P_{in}^2}, \tag{3.47}$$

where $V_{rms,ac}$ and $I_{rms,ac}$ are the RMS values of the phase voltage and current, respectively.

3.10 Summary and conclusions

The hybrid analytical modeling that incorporates saturation is applied to a benchmark 12/10 variable flux reluctance machine, which has both field and armature windings in the stator. The modeling allows geometric details, e.g., different tooth arcs in the slot opening and slot bottom. Meanwhile, the geometry of four coil bundles in a slot is successfully implemented.

On the basis of analytical expression of the magnetic field in the airgap, the torque is calculated using Maxwell stress tensor. The torque waveform, mean torque and torque ripple are estimated accurately. On the other hand, using the obtained magnetic field distribution in the stator, the flux linkage is derived considering the slot leakage. The phase voltage and back-emf are calculated by taking the derivative of the flux linkage. The incremental inductance is obtained by calculating the change of flux linkage over a small variation of current and by using the concept of frozen permeability, as a result, the dependence of inductance over rotor position/current level is estimated accurately.

The methods for loss prediction including the iron loss and copper loss are provided. The iron loss is derived based on the Bertotti equation, and each of the loss component, i.e., the hysteresis loss, classical eddy current loss and excess loss are estimated. The ac copper loss is derived by post-processing the magnetic field output from the HAM, and sequentially through the estimation of magnetic vector potential, electric field and eddy current. The result has a good agreement with FEM at relatively low speed, when the influence of the magnetic field caused by the eddy currents is not significant compared to the original field caused by the current source.

The content in this section extends the application of the hybrid analytical modeling to intensive analysis of the VFRM, and the above methods are valid for analyzing other types of machines.

Part II

Variable flux reluctance machines

Chapter 4

Topologies and configurations

4.1 Introduction

The design of VFRMs starts from the selection of machine topology. The stator/rotor pole combination, and its influence on the winding configuration and machine performances, is investigated in this chapter. This requires an extensive understanding of the working principle as is discussed first. Afterwards, the winding configurations and the winding factors of fundamental and harmonics are summarized for different topologies. The influence of the number of rotor poles on the unbalanced magnetic pull, flux linkage and electromagnetic torque is investigated, which provides arguments for the selection of pole numbers.

4.2 Operating principles

As explained in section 3.2, the VFRM consists of a concentrated field winding and armature windings together with a salient rotor. The field current creates a P_s-pole mmf and is modulated by the P_r-pole rotor. Simultaneously, it couples with the rotating field generated by the ac armature mmf and produces electromagnetic torque.

To understand the machine operating principle, the instantaneous torque is derived using the virtual work method [37, 85, 125],

$$T_{em} = \frac{dW_{ele}}{d\theta} - \frac{dW_{mag}}{d\theta}, \tag{4.1}$$

where θ is the virtual displacement in mechanical degree, W_{ele} is the electric energy and W_{mag} is the magnetic energy. The derivation of the electric energy, magnetic energy and electromagnetic torque is explained in the following subsections.

4.2.1 Electric energy

In a non-saturated VFRM, the flux linkage of each phase can be separated as,

$$\Lambda_a = \Lambda_{fa} + \Lambda_{aa} + \Lambda_{ba} + \Lambda_{ca}, \tag{4.2}$$

$$\Lambda_b = \Lambda_{fb} + \Lambda_{bb} + \Lambda_{ab} + \Lambda_{cb}, \tag{4.3}$$

$$\Lambda_c = \Lambda_{fc} + \Lambda_{cc} + \Lambda_{ac} + \Lambda_{bc}, \tag{4.4}$$

$$\Lambda_f = \Lambda_{ff} + \Lambda_{af} + \Lambda_{bf} + \Lambda_{cf}, \tag{4.5}$$

where the subscripts a, b, c and f represent phase A, B, C and field winding, respectively, and the notation Λ_{ij} represents the flux linkage in winding j caused

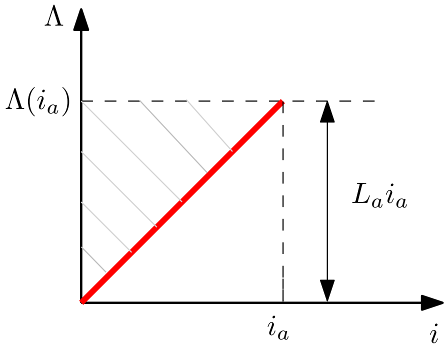

Figure 4.1: The Λ-i diagram of a system with a single winding that is excited to a current level of i_a (L_a is the self inductance of this single winding).

by the excitation of winding i. The expression of these flux linkages are given as,

$$\begin{bmatrix} \Lambda_{fa} \\ \Lambda_{fb} \\ \Lambda_{fc} \\ \Lambda_{af} \\ \Lambda_{bf} \\ \Lambda_{cf} \end{bmatrix} = \begin{bmatrix} M_{fa}i_f \\ M_{fb}i_f \\ M_{fc}i_f \\ M_{fa}i_a \\ M_{fb}i_b \\ M_{fc}i_c \end{bmatrix}, \begin{bmatrix} \Lambda_{ba} \\ \Lambda_{ca} \\ \Lambda_{ab} \\ \Lambda_{cb} \\ \Lambda_{ac} \\ \Lambda_{bc} \end{bmatrix} = \begin{bmatrix} M_{ab}i_b \\ M_{ca}i_c \\ M_{ab}i_a \\ M_{bc}i_c \\ M_{ca}i_a \\ M_{bc}i_b \end{bmatrix}, \begin{bmatrix} \Lambda_{aa} \\ \Lambda_{bb} \\ \Lambda_{cc} \\ \Lambda_{ff} \end{bmatrix} = \begin{bmatrix} L_{aa}i_a \\ L_{bb}i_b \\ L_{cc}i_c \\ L_{ff}i_f \end{bmatrix}, \tag{4.6}$$

where M_{fa}, M_{fb} and M_{fc} are the mutual inductances between the field winding and armature windings, M_{ab}, M_{bc} and M_{ca} are the mutual inductances between the armature windings, L_{ff}, L_{aa}, L_{bb} and L_{cc} are the self inductances of the field winding and armature windings, respectively, and i_a, i_b, i_c and i_f are the instantaneous currents of phase A, B, C and field winding, respectively.

During rotation, the electric energy provided to the machine is calculate as [118],

$$W_{ele} = \int i_a d\Lambda_a + \int i_b d\Lambda_b + \int i_c d\Lambda_c + \int i_f d\Lambda_f. \tag{4.7}$$

4.2.2 Magnetic energy

The magnetic energy is calculated using the definition: the energy stored in a magnetic field can be calculated as the energy required to establish this field [16]. If no mechanical energy and losses are taken into account, the required energy to establish the magnetic field in a system is the electric energy that provided to the windings to increase the currents from 0 to a certain level.

This concept is first applied to a simple system that has a single winding with a current level at i_a. The stored magnetic energy is the electric energy provided to

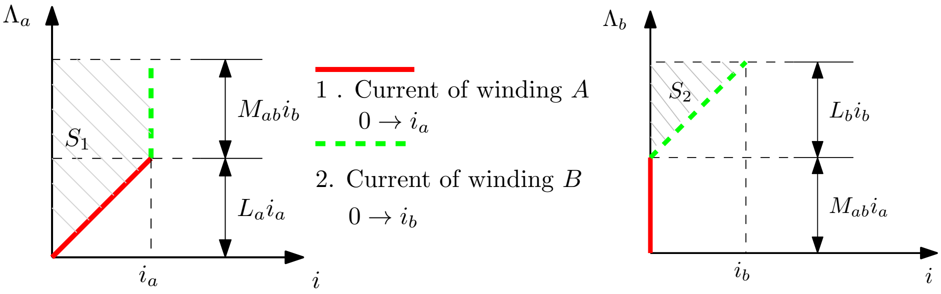

(a) Winding A.

(b) Winding B.

Figure 4.2: The Λ-i diagrams of a system with two windings that are excited with the given current profile: (a) the Λ-i diagram of winding A, and (b) the Λ-i diagram of winding B (L_a and L_b is the self inductance of winding A and B, respectively, and M_{ab} is the mutual inductance between the two windings).

this winding to increase its current from 0 to i_a, that is described as,

$$W_{mag} = \int e i dt = \int \frac{d\Lambda}{dt} i dt = \int_0^{\Lambda(i_a)} i d\Lambda, \tag{4.8}$$

where $\Lambda(i_a)$ is the flux linkage with current i_a. Assuming a linear magnetic material, equation (4.8) is represented by the dashed area shown in Fig. 4.1.

The concept is extended to a system that has two windings with the current levels of i_a and i_b, respectively. The stored magnetic energy in the system equals to the total electric energy that increases the two currents from 0 to i_a and i_b. It is worth mentioning that the calculation of such consumed energy is independent of the current profiles. As an example, a simple current profile is defined to calculate the stored magnetic energy: the current in winding A first increases from 0 to i_a, afterwards, the current in winding B increases from 0 to i_b.

The Λ-i diagrams of the system considering this current profile are shown in Fig. 4.2. The current in winding A is first excited, hence, the flux linkage of winding A is increased, shown as the solid line in Fig. 4.2(a). Although at this moment, the current of winding B remains at 0, however, due to the mutual inductance between the two windings, the flux linkage in winding B still changes, shown as the solid line in Fig. 4.2(b). Afterwards, the current in winding B is increased from 0 to i_b, hence, the flux linkage continues to change, shown as the dashed line in Fig. 4.2(b). Meanwhile, due to the mutual inductance, the flux linkage of winding A changes although its current remains at i_a, shown as the dashed line in Fig. 4.2(a). The stored magnetic energy in the system is the sum of the two identified areas in Fig. 4.2, expressed as,

$$W_{mag} = S_1 + S_2 = \frac{1}{2} L_a i_a^2 + M_{ab} i_a i_b + \frac{1}{2} L_b i_b^2. \tag{4.9}$$

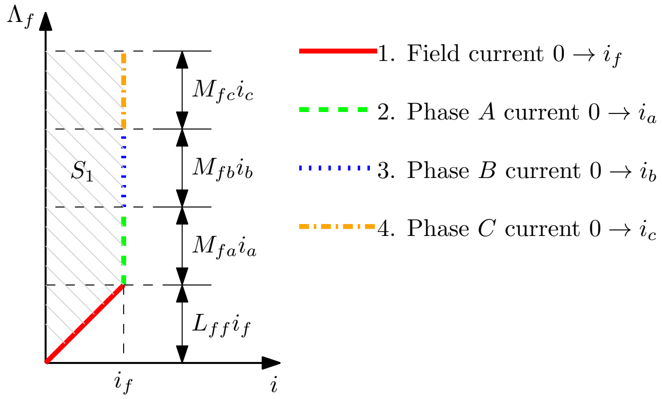
Λ_f
$M_{fc}i_c$
S_1
$M_{fb}i_b$
$M_{fa}i_a$
$L_{ff}i_f$
i_f
i
1. Field current $0 \rightarrow i_f$
2. Phase A current $0 \rightarrow i_a$
3. Phase B current $0 \rightarrow i_b$
4. Phase C current $0 \rightarrow i_c$

(a) Field winding.

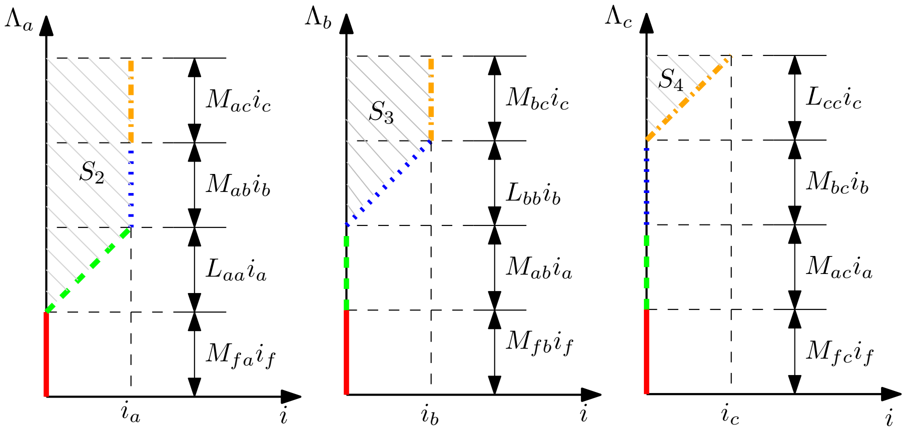
Λ_a
$M_{ac}i_c$
S_2
$M_{ab}i_b$
$L_{aa}i_a$
$M_{fa}i_f$
i_a
i
Λ_b
S_3
$M_{bc}i_c$
$L_{bb}i_b$
$M_{ab}i_a$
$M_{fb}i_f$
i_b
i
Λ_c
S_4
$L_{cc}i_c$
$M_{bc}i_b$
$M_{ac}i_a$
$M_{fc}i_f$
i_c
i

(b) Phase A winding. (c) Phase B winding. (d) Phase C winding.

Figure 4.3: The Λ-i diagrams of the VFRM when the field current, phase A current, phase B current and phase C current are excited subsequently: (a) the Λ-i diagram of the field winding, (b) the Λ-i diagram of phase A winding, (c) the Λ-i diagram of phase B winding, and (d) the Λ-i diagram of phase C winding.

The same concept is used to derive the stored magnetic energy in the VFRM. A current profile is defined as: the field current is first increased from 0 to i_f, and afterwards the phase currents A, B and C are increased from 0 to i_a, i_b and i_c subsequently. The Λ-i diagrams for this process are sketched in Fig. 4.3.

As the field current is first excited, the flux linkage of itself, Λ_f, is increased, shown as the solid line in Fig. 4.3(a). Due to the mutual inductances between the field winding and the armature windings, the flux linkages in phase A, B and C are changed, shown as the solid lines in Fig. 4.3(b), (c) and (d). Similar phenomena occur when the armature currents are excited. In the end, the stored magnetic energy in the VFRM is calculated as the sum of the dashed areas in Fig. 4.3, and the expression is,

$$\begin{aligned} W_{mag} =& S_1 + S_2 + S_3 + S_4 \\ =& \frac{1}{2} i_f \left(L_{ff} i_f\right) + i_f \left(M_{fa} i_a + M_{fb} i_b + M_{fc} i_c\right) + \frac{1}{2} i_a \left(L_{aa} i_a\right) \\ &+ \frac{1}{2} i_b \left(L_{bb} i_b\right) + \frac{1}{2} i_c \left(L_{cc} i_c\right) + i_a i_b M_{ab} + i_a i_c M_{ca} + i_b i_c M_{bc}. \end{aligned} \tag{4.10}$$

Notice that such analysis provides the calculation method for the total magnetic energy stored in a system, rather than the energy of an individual winding since the Λ-i diagram of each winding varies with the current profiles.

4.2.3 Electromagnetic torque

The terms of $\frac{dW_{ele}}{d\theta}$ and $\frac{dW_{mag}}{d\theta}$ in equation (4.1) are derived as,

$$\begin{aligned} \frac{dW_{ele}}{d\theta} =& \frac{d\left(\int i_a \frac{d\Lambda_a}{d\theta} d\theta + \int i_b \frac{d\Lambda_b}{d\theta} d\theta + \int i_c \frac{d\Lambda_c}{d\theta} d\theta + \int i_f \frac{d\Lambda_f}{d\theta} d\theta\right)}{d\theta} \\ =& i_a \frac{d\Lambda_a}{d\theta} + i_b \frac{d\Lambda_b}{d\theta} + i_c \frac{d\Lambda_c}{d\theta} + i_f \frac{d\Lambda_f}{d\theta} \\ =& i_a^2 \frac{dL_{aa}}{d\theta} + i_b^2 \frac{dL_{bb}}{d\theta} + i_c^2 \frac{dL_{cc}}{d\theta} + i_f^2 \frac{dL_{ff}}{d\theta} \\ &+ 2 i_f i_a \frac{dM_{fa}}{d\theta} + 2 i_f i_b \frac{dM_{fb}}{d\theta} + 2 i_f i_c \frac{dM_{fc}}{d\theta} \\ &+ 2 i_a i_b \frac{dM_{ab}}{d\theta} + 2 i_b i_c \frac{dM_{bc}}{d\theta} + 2 i_a i_c \frac{dM_{ca}}{d\theta}, \end{aligned} \tag{4.11}$$

and

$$\begin{aligned} \frac{dW_{mag}}{d\theta} =& \frac{1}{2} i_f^2 \frac{dL_{ff}}{d\theta} + i_f i_a \frac{dM_{fa}}{d\theta} + i_f i_b \frac{dM_{fb}}{d\theta} + i_f i_c \frac{dM_{fc}}{d\theta} \\ &+ \frac{1}{2} i_a^2 \frac{dL_{aa}}{d\theta} + \frac{1}{2} i_b^2 \frac{dL_{bb}}{d\theta} + \frac{1}{2} i_c^2 \frac{dL_{cc}}{d\theta} + i_a i_b \frac{dM_{ab}}{d\theta} + i_a i_c \frac{dM_{ca}}{d\theta} + i_b i_c \frac{dM_{bc}}{d\theta}. \end{aligned} \tag{4.12}$$

Consequently the torque is derived as,

$$\begin{aligned}
T_{em} =& \left(\frac{1}{2}i_f^2\frac{dL_{ff}}{d\theta}\right) + \left(i_f i_a\frac{dM_{fa}}{d\theta} + i_f i_b\frac{dM_{fb}}{d\theta} + i_f i_c\frac{dM_{fc}}{d\theta}\right) \\
&+ \left(\frac{1}{2}i_a^2\frac{dL_{aa}}{d\theta} + \frac{1}{2}i_b^2\frac{dL_{bb}}{d\theta} + \frac{1}{2}i_c^2\frac{dL_{cc}}{d\theta}\right) \\
&+ \left(i_a i_b\frac{dM_{ab}}{d\theta} + i_a i_c\frac{dM_{ca}}{d\theta} + i_b i_c\frac{dM_{bc}}{d\theta}\right) \\
=& T_{ff} + T_{f,ph} + T_{l,ph} + T_{m,ph}.
\end{aligned} \tag{4.13}$$

As such, the instantaneous electromagnetic torque, T_{em}, is separated into four torque components, T_{ff}, $T_{f,ph}$, $T_{l,ph}$ and $T_{m,ph}$, that respectively represent:

- T_{ff} - torque induced by the self inductance of the field winding;
- $T_{f,ph}$ - torque induced by the mutual inductances between the field winding and armature windings;
- $T_{l.ph}$ - torque induced by the self inductances of the armature windings;
- $T_{m,ph}$ - torque induced by the mutual inductances of the armature windings.

In the following content, the contribution of each torque component to the mean torque and torque ripple is identified.

Torque induced by the self inductance of the field winding

The self inductance of the field winding is first analyzed. The flux of a dc coil reaches the maximum when the rotor tooth aligns with the stator tooth, and reaches minimum when at the unaligned position. Hence, a varying flux linkage of a dc coil is obtained, as shown in Fig 4.4(a). The single dc coil contains a fundamental flux linkage, however, the superposition of all the dc coils eliminates the fundamental component as shown in Fig. 4.4(b). The explanation is given by the concept of distribution factor, calculated with the equation,

$$k_d = \frac{\sin\left(\frac{Q\alpha}{2}\right)}{Q\sin\left(\frac{\alpha}{2}\right)}, \tag{4.14}$$

where Q is the number of different phasors of coil flux and α is the electrical angle between two adjacent phasors. For a P_s-stator-pole/P_r-rotor-pole VFRM, define the greatest common divisor between P_s and P_r as g_{cd}. The according two co-prime numbers are defined by,

$$p_s = \frac{P_s}{g_{cd}}, \tag{4.15}$$

$$p_r = \frac{P_r}{g_{cd}}. \tag{4.16}$$

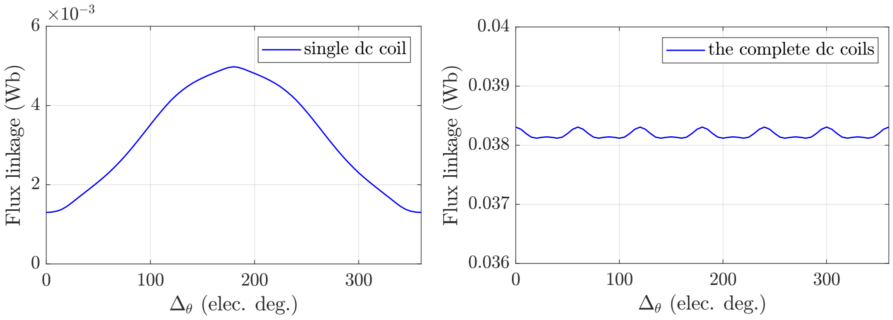

(a) (b)

Figure 4.4: (a) The open-circuit flux linkage of a single dc coil versus the rotation angle, and (b) the open-circuit flux linkage of the field winding versus the rotation angle.

The value of Q in equation (4.14) for dc coil flux is p_s in this case. The electric angle between two adjacent dc coil flux phasors is described as,

$$\alpha = \frac{2\pi}{p_s}. \tag{4.17}$$

The distribution factor for the fundamental dc coil phasors is calculated as,

$$k_{d,1} = \frac{\sin\left(p_s \frac{\alpha}{2}\right)}{p_s \sin\left(\frac{\alpha}{2}\right)} = \frac{\sin\left(p_s \cdot \frac{\pi}{p_s}\right)}{p_s \sin\left(\frac{\alpha}{2}\right)} = \frac{\sin(\pi)}{p_s \sin\left(\frac{\alpha}{2}\right)} = 0. \tag{4.18}$$

This means the fundamental is canceled out, leading to a nearly constant flux linkage of the field winding. As such, the self inductance of the field winding is described as

$$L_{ff} = L_{ff,0} + \sum_{n=2}^{\infty} L_{ff,n} \cos(n\Delta_\theta + \theta_{ff,n}), \tag{4.19}$$

where $L_{ff,0}$ is the dc component, $L_{ff,n}$ is the amplitude of the n^{th} harmonic, and $\theta_{ff,n}$ is the initial angle for the n^{th} harmonic. The torque created by this inductance is,

$$T_{ff} = \frac{1}{2} i_f^2 \frac{dL_{ff}}{d\theta} = \frac{1}{2} P_r i_f^2 \frac{dL_{ff}}{d\Delta_\theta} = \sum_{n=2}^{\infty} -\frac{1}{2} P_r n L_{ff,n} \sin\left(n\Delta_\theta + \theta_{ff,n}\right) i_f^2. \tag{4.20}$$

This torque component does not contribute to the mean torque, but only the torque ripple.

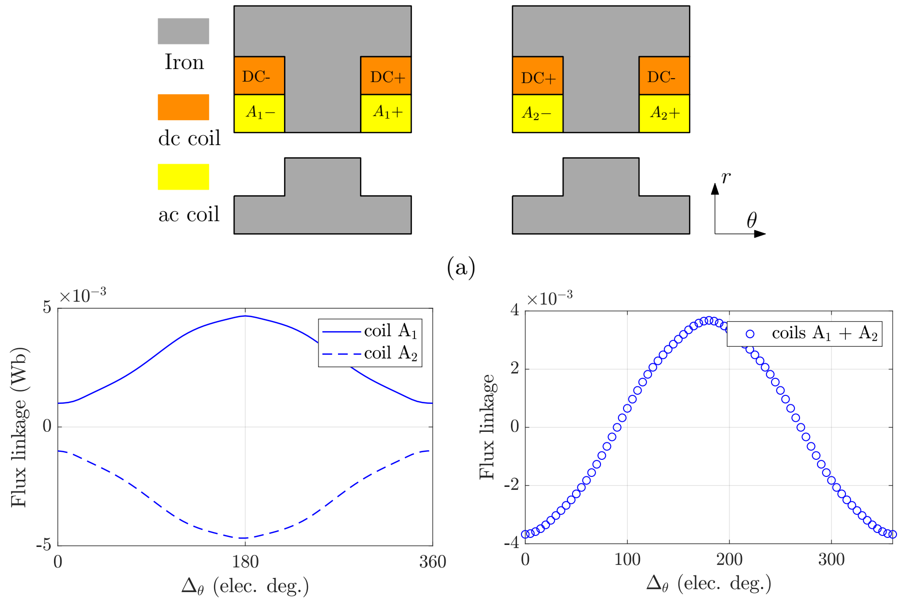

(a)

(b)

(c)

Figure 4.5: (a) The ac coils wound on the teeth with opposite dc coil orientations, (b) the individual flux linkage of the ac coils versus the rotation angle, and (c) the phase flux linkage versus the rotation angle.

Torque induced by the mutual inductances between the field and armature windings

The mutual inductances between the field winding and armature windings are first analyzed in this subsection. Notice that for ac coils wound on teeth with opposite dc coil orientations as shown in Fig. 4.5(a), the open-circuit flux linkages have opposite values as presented in Fig. 4.5(b), and the values are either always positive or negative. Although the waveform of a single coil shows a unipolar characteristic, a bi-polar phase flux linkage has to be ensured by the winding configuration, as shown in Fig. 4.5(c). This means that there is no dc component in the mutual inductances between the field winding and armature windings, and the expressions are given as,

$$M_{fa} = \sum_{n=1}^{\infty} \hat{M}_{fph,n} \cos\left(n\Delta_\theta + \theta_{fa,n}\right), \tag{4.21}$$

$$M_{fb} = \sum_{n=1}^{\infty} \hat{M}_{fph,n} \cos\left(n\Delta_\theta + \theta_{fa,n} - \frac{2n\pi}{3}\right), \tag{4.22}$$

$$M_{fc} = \sum_{n=1}^{\infty} \hat{M}_{fph,n} \cos\left(n\Delta_\theta + \theta_{fa,n} + \frac{2n\pi}{3}\right), \tag{4.23}$$

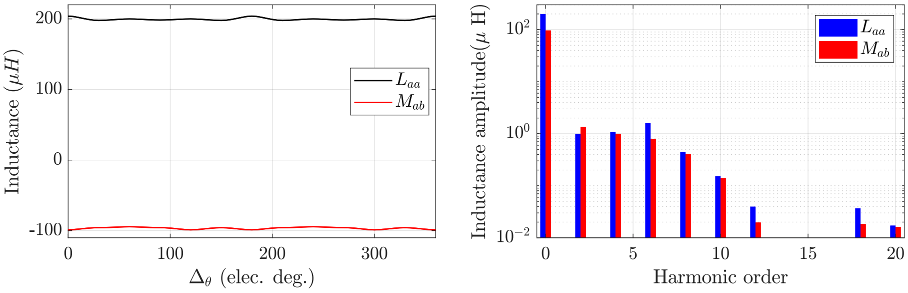

(a) (b)

Figure 4.6: The self inductance of the phase A winding (L_{aa}) and the mutual inductance between the phase A winding and phase B winding (M_{ab}): (a) variation of the inductances over the rotation angle, and (b) the amplitude spectrum of the inductances.

where $\hat{M}_{fph,n}$ is the amplitude of the n^{th} harmonic, and $\theta_{fa,n}$ is the initial angle for the n^{th} harmonic in phase A winding. Assuming the armature currents are sinusoidally commutated and are described as,

$$i_a = \hat{I}_{ac} \cos\left(\Delta_\theta + \gamma\right), \tag{4.24}$$

$$i_b = \hat{I}_{ac} \cos\left(\Delta_\theta - \frac{2\pi}{3} + \gamma\right), \tag{4.25}$$

$$i_c = \hat{I}_{ac} \cos\left(\Delta_\theta + \frac{2\pi}{3} + \gamma\right), \tag{4.26}$$

the torque induced by M_{fa}, M_{fb} and M_{fc} is derived as,

$$\begin{aligned} T_{f,ph} = & \sum_{n=3k-2}^{\infty} -\frac{3nP_r\hat{M}_{fph,n}i_f\hat{I}_{ac}}{2} \sin\left[(n-1)\Delta_\theta + \theta_{fa,n} - \gamma\right] \\ & + \sum_{n=3k-1}^{\infty} -\frac{3nP_r\hat{M}_{fph,n}i_f\hat{I}_{ac}}{2} \sin\left[(n+1)\Delta_\theta + \theta_{fa,n} + \gamma\right], \ (k \in \mathbb{Z}^+). \end{aligned} \tag{4.27}$$

where γ is the commutation angle and $\hat{I}_{ac}$ is the peak value of the armature current. In equation (4.27), the first term with $n = 1$ leads to a constant value, it means the fundamental of M_{fa}, M_{fb} and M_{fa} contributes to the mean torque.

Torque induced by the self inductances of the armature windings

There are dc component and even harmonics in the self inductances of the armature windings as shown in Fig. 4.6, hence, the self inductances are described as,

$$
\begin{aligned}
L_{aa} &= L_{ph,0} + \sum_{n=2k}^{\infty} \hat{L}_{ph,n} \cos\left(n\Delta_\theta + \theta_{aa,n}\right), && (4.28)\\
L_{bb} &= L_{ph,0} + \sum_{n=2k}^{\infty} \hat{L}_{ph,n} \cos\left(n\Delta_\theta + \theta_{aa,n} - \frac{2n\pi}{3}\right), && (4.29)\\
L_{cc} &= L_{ph,0} + \sum_{n=2k}^{\infty} \hat{L}_{ph,n} \cos\left(n\Delta_\theta + \theta_{aa,n} + \frac{2n\pi}{3}\right), && (4.30)
\end{aligned}
$$

where $L_{ph,0}$, $\hat{L}_{ph,n}$ and $\theta_{aa,n}$ are respectively the dc component, amplitude of the n^{th} harmonic, and initial phase of the n^{th} harmonic in L_{aa}. Consequently, the torque is described as,

$$
\begin{aligned}
T_{l,ph} = &-\frac{3}{8}P_r\hat{I}_{ac}^2 \sum_{n=6k-2}^{\infty} n\hat{L}_{ph,n} \sin\left[(n+2)\Delta_\theta + 2\gamma + \theta_{aa,n}\right]\\
&-\frac{3}{8}P_r\hat{I}_{ac}^2 \sum_{n=6k-4}^{\infty} n\hat{L}_{ph,n} \sin\left[(n-2)\Delta_\theta - 2\gamma + \theta_{aa,n}\right] \qquad (4.31)\\
&-\frac{3}{4}P_r\hat{I}_{ac}^2 \sum_{n=6k}^{\infty} n\hat{L}_{ph,n} \sin\left(n\Delta_\theta + \theta_{aa,n}\right), \ (k \in \mathbb{Z}^+).
\end{aligned}
$$

In this torque component, the second harmonic in L_{aa}, L_{bb} and L_{cc} contributes to the mean torque.

Torque induced by the mutual inductances of the armature windings

There are even harmonics in the mutual inductances of armature windings as shown in the spectrum in Fig. 4.6, hence, the inductances are described as

$$
\begin{aligned}
M_{ab} &= M_{ph,0} + \sum_{n=2k}^{\infty} \hat{M}_{ph,n} \cos\left(n\Delta_\theta + \theta_{ab,n}\right), && (4.32)\\
M_{bc} &= M_{ph,0} + \sum_{n=2k}^{\infty} \hat{M}_{ph,n} \cos\left(n\Delta_\theta + \theta_{ab,n} - \frac{2n\pi}{3}\right), && (4.33)\\
M_{ca} &= M_{ph,0} + \sum_{n=2k}^{\infty} \hat{M}_{ph,n} \cos\left(n\Delta_\theta + \theta_{ab,n} + \frac{2n\pi}{3}\right), && (4.34)
\end{aligned}
$$

where $M_{ph,0}$, $\hat{M}_{ph,n}$ and $\theta_{ab,n}$ are respectively the dc component, amplitude of the n^{th} harmonic and initial angle of the n^{th} harmonic in M_{ab}. The torque induced by these three inductances is described as,

$$\begin{aligned} T_{m,ph} = &-\frac{3}{4}P_r\hat{I}_{ac}^2\sum_{n=6k-4}^{\infty}n\hat{M}_{ph,n}\sin\left[(n-2)\,\Delta_\theta-2\gamma+\frac{2\pi}{3}+\theta_{ab,n}\right] \\ &-\frac{3}{4}P_r\hat{I}_{ac}^2\sum_{n=6k-2}^{\infty}n\hat{M}_{ph,n}\sin\left[(n+2)\,\Delta_\theta+2\gamma-\frac{2\pi}{3}+\theta_{ab,n}\right] \\ &+\frac{3}{4}P_r\hat{I}_{ac}^2\sum_{n=6k}^{\infty}n\hat{M}_{ph,n}\sin\left(n\Delta_\theta+\theta_{ab,n}\right),\ \ (k\in\mathbb{Z}^+). \end{aligned} \tag{4.35}$$

In this torque component, the second harmonic in M_{ab}, M_{bc} and M_{ca} contributes to the mean torque.

To verify the above equations, the torque components of a 12/10 VFRM are calculated by equations (4.20), (4.27), (4.31) and (4.35) using the inductances obtained from 2D FEM. Meanwhile, torque components T_{ff}, $(T_{l,ph}+T_{m,ph})$, T_{em} and $T_{f,ph}$ are calculated in the FEM by exciting merely field current, armature current and both of them with the following steps:

1. T_{ff} is calculated by merely applying the field current;
2. $T_{l,ph}$ is the summation of torques obtained by exciting phase A, B, and C individually;
3. The value of $(T_{l,ph}+T_{m,ph})$ is calculated by exciting the three-phase armature currents simultaneously;
4. T_{em} is simulated by exciting both the field and armature currents simultaneously;
5. $T_{f,ph}$ is derived by subtracting $(T_{ff}+T_{l,ph}+T_{m,ph})$ from T_{em}.

The results obtained by the equations and FEM are compared in Fig. 4.7. As it can be seen, the results show good agreement - the difference between the values obtained by the two methods is less than 0.6%.

As explained, the fundamental of the mutual inductances between field and armature windings, and the second harmonic in the self and mutual inductances of the armature windings, both contribute to the mean torque. However, since the amplitude of the second harmonic is relatively low, the contribution is modest. When the commutation angle γ is 90°, the expression of the mean torque is summarized as,

$$\bar{T}_{em}=\frac{3}{2}P_r\hat{M}_{fph,1}i_f\hat{I}_{ac}=\frac{3}{2}P_r\hat{\Lambda}_{fph,1}\hat{I}_{ac}, \tag{4.36}$$

where $\hat{\Lambda}_{fph,1}$ is the fundamental flux linkage. This expression is analogous to PMSMs. For saturated VFRMs, the value of $\hat{\Lambda}_{fph,1}$ can be calculated by integrating the incremental mutual inductance over current.

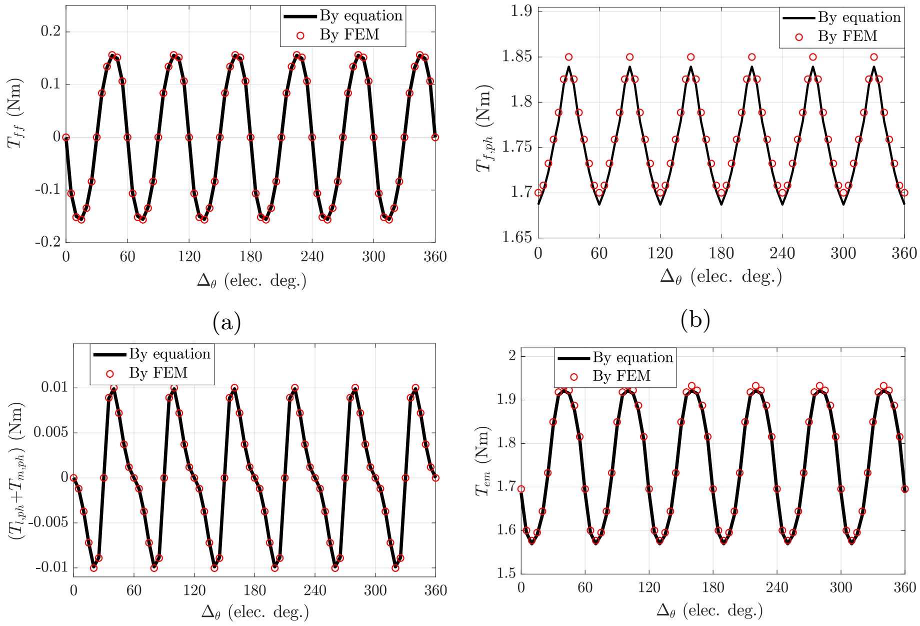

(a) (b) (c) (d)

Figure 4.7: The waveforms of torque components calculated by equations and FEM for: (a) T_{ff} - the torque induced by the self inductance of the field winding, (b) $T_{f,ph}$ - the torque induced by the mutual inductances between the field winding and armature windings, (c) $(T_{l,ph}+T_{m,ph})$ - the sum of the torque induced by the self inductances of the armature windings and the torque induced by the mutual inductances of the armature windings, and (d) T_{em} - the instantaneous total electromagnetic torque.

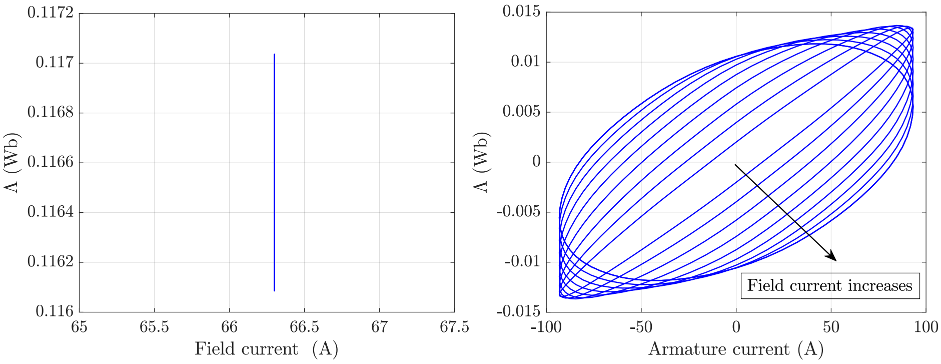

(a) (b)

Figure 4.8: The Λ-i diagrams of (a) the field winding, and (b) the armature windings with sinusoidal currents.

The torque production mechanism can also be explained by the energy conversion loops. The bi-polar phase flux linkage distinguishes VFRMs from other uni-polar reluctance machines, e.g., SRM, variable reluctance machine (SRM with an auxiliary dc winding) [8], etc. On one hand, the flux linkage of the field winding ideally moves along the line that is perpendicular to the i-axis, and does not form any loop for an electric period, as presented in Fig. 4.8(a). On the other hand, the Λ-i diagram of the armature windings is similar to PMSMs which forms enlosed ellipse areas as presented in Fig. 4.8(b). From the energy conversion theory, only the ellipse areas in Fig. 4.8(b) represent the mechanical work done by the electromagnetic torque in an electric period, while the line in Fig. 4.8(a) does not. Moreover, the shape of the ellipse varies by the ratio of the field current to armature current, resulting in different values of the mean torque. The influence of the current arrangement on the electromagnetic torque is further discussed in Chapter 5.

4.3 Winding factor

As derived in equation (4.36), the torque is strongly linked to the value of $\hat{\Lambda}_{fph,1}$, which can be expressed by,

$$\hat{\Lambda}_{fph,1} = k_w \frac{P_s}{m} \hat{\Lambda}_{fcoil,1}, \tag{4.37}$$

where k_w is the winding factor, m is the number of phases, and $\hat{\Lambda}_{fcoil,1}$ is the fundamental flux linkage of a single phase coil. Hence, the winding factor is an important factor that determines the torque production. In this section, the dependency of the number of poles on the winding factors is introduced. The result is used as one of the bases for the selection of the number of poles in section 4.6.

Table 4.1: Feasible stator-rotor pole combinations for three-phase VFRMs (m=3).

P_s	P_r
6	2, 4, 5, 7, 8, ...
12	2, 4, 5, 7, 8, 10, 11, 13, 14, 16, ...
18	2, 4, 5, 6, 7, 8, 10, 11, 12, 13, 14, 15, 16, 17, 19, 20, ...
...	

4.3.1 Pole combinations

There are a lot of stator and rotor pole combinations for VFRMs. In [76], the basic rule is given for feasible rotor pole numbers for a 6-stator-pole topology, described as,

$$P_r \neq km, \quad (k \in \mathbb{Z}^+), \tag{4.38}$$

where m is the number of phases. The value of P_r is possible to be odd or even number, leading to stator pole/rotor pole topologies of 6/4, 6/5, 6/7 and 6/8, etc.

This rule is extended to VFRMs with more stator poles. Since the field winding in the stator generates the field, the number of stator poles, P_s, must be an even number to build equal 'north' and 'south' poles. In addition, P_s also equals to the number of ac coils, hence, should be the multiple of number of phases, m. This gives the condition of,

$$P_s = 2n_1m, \quad (n_1 \in \mathbb{Z}^+). \tag{4.39}$$

Additionally, the m phases are balanced, hence, the selection of rotor pole should satisfy the following equation [77],

$$\frac{p_s}{m} = n_2, \quad (n_2 \in \mathbb{Z}^+), \tag{4.40}$$

where p_s is the parameter derived by equation (4.15). The possible pole combinations for three-phase VFRMs are listed in Table 4.1.

4.3.2 Winding configurations

To calculate the winding factor, the winding configuration is first investigated. As shown in Fig. 4.9 that illustrates 6, 12, and 18-stator-pole VFRMs, the adjacent ac coils are always wound on the teeth where dc coils have different orientations. In section 4.2 Fig. 4.5, it shows that such an arrangement leads to opposite flux polarities. Therefore, the electric angle between coil i and coil 1 is given as,

$$\alpha_{c,i} = 2\pi \frac{P_r i}{P_s} - \pi \quad (i \text{ is an even number}), \tag{4.41}$$

$$\alpha_{c,i} = 2\pi \frac{P_r i}{P_s} \quad (i \text{ is an odd number}), \tag{4.42}$$

where the second term on the right side of equation (4.41) describes the reverse of flux polarity. Therefore, the electric angle between two adjacent coils is,

$$\alpha_c = \frac{2\pi P_r}{P_s} - \pi. \tag{4.43}$$

For example, for a 6/4 VFRM, disregarding the reversed flux polarity caused by the dc coils, the electric angle between coils 1 and 2 in Fig. 4.9(a) is $2\pi \cdot \frac{4}{6} = 240°$. However, when considering the reversed flux polarity, the electric angle is actually 240°-180° = 60°. As such, the original phasor diagram of a 6/4 VFRM is shown in Fig. 4.10(a), which assumes the ac coils are connected in the same orientation. To determine groups of phase vectors, the angular displacement should be minimized, hence, coils 2, 4 and 6 should be backward-connected, as shown in Fig. 4.10(b). For ease of distinction, the coils with the same orientation as coil 1 are indicated as forward-connected coils, while the coils with a different orientation as coil 1 are indicated as backward-connected coils and are shown with a prime in the numbering.

4.3.3 Distribution factor

The distribution factor of the fundamental component is able to be calculated using equation (4.14). The derivation of Q and α in the equation is divided into three situations based on the value of p_s.

Values of p_s for three-phase VFRMs

For stator-rotor pole combinations listed in Table 4.1, the values of p_s are listed in Table 4.2. As explained in section 4.3.1, the values of p_s must be multiples of the number of phases m, hence, p_s is distinguished by its ratio to m, and are divided into three categories:

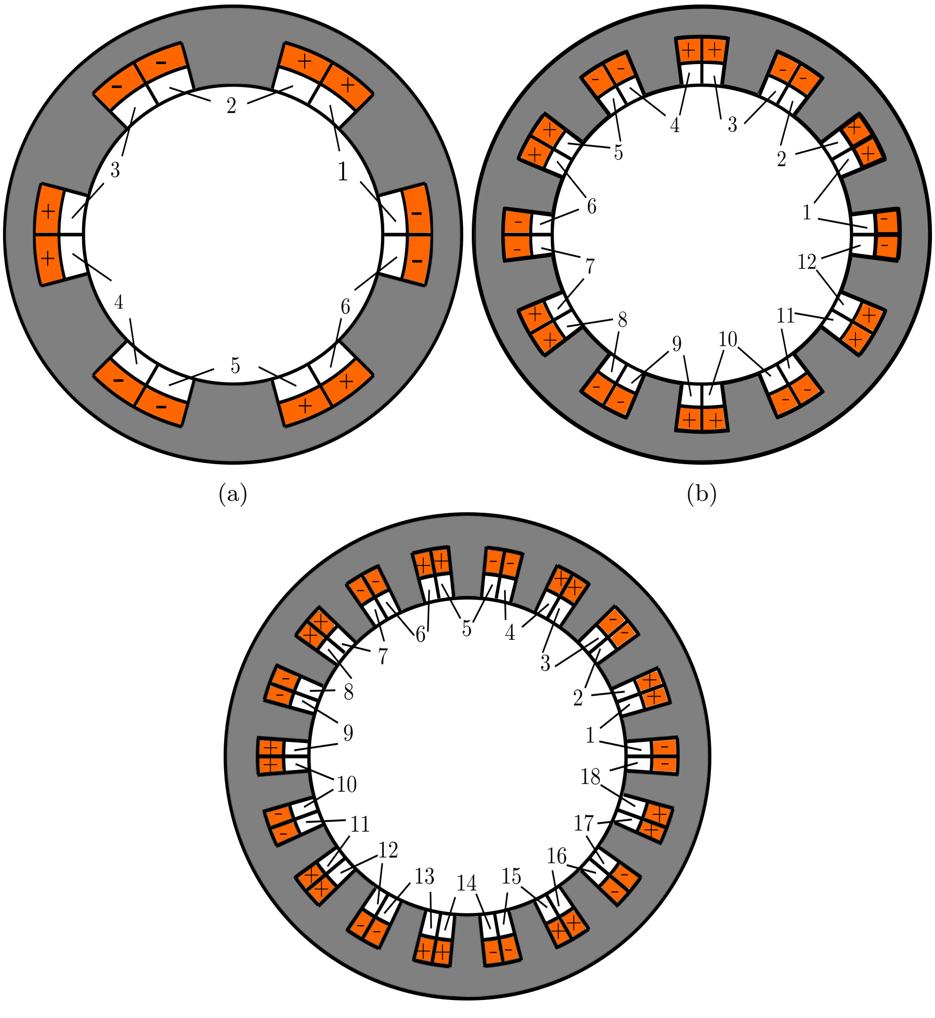
1
2
3
4
5
6
7
8
9
10
11
12
13
14
15
16
17
18
+
-

(a) (b)

(c)

Figure 4.9: Various VFRM stators with (a) 6 poles, (b) 12 poles, and (c) 18 poles.

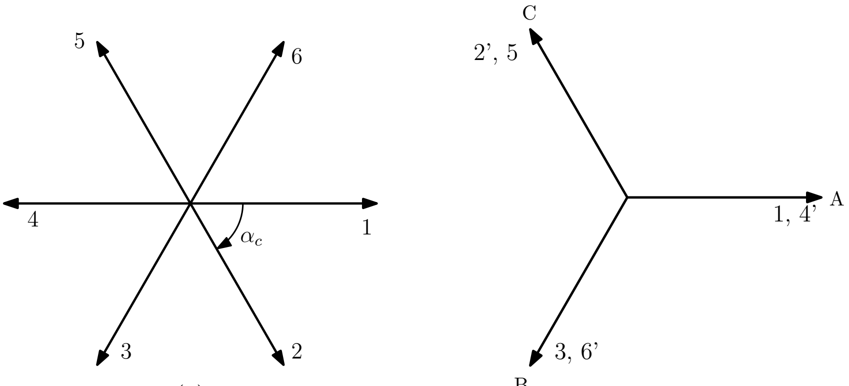

(a)

(b)

Figure 4.10: The 6/4 VFRM: (a) the original phasor diagram of the flux linkage assuming all the coils are in the same orientation, and (b) the winding configurations.

Table 4.2: Values of p_s (defined in equation (4.15)) for various three-phase VFRMs.

P_r	2	4	5	7	8
p_s	3	3	6	6	3

(a) The number of stator poles, P_s, is 6.

P_r	2	4	5	7	8	10	11	13	14	16
p_s	6	3	12	12	3	6	12	12	6	3

(b) The number of stator poles, P_s, is 12.

P_r	2	4	5	6	7	8	10	11	12	13	14	15	16	19	20
p_s	9	9	18	3	18	9	9	18	3	18	9	6	9	18	9

(c) The number of stator poles, P_s, is 18.

- $p_s/2m$ is an odd number, e.g., $p_s = 6, 18$;
- $p_s/2m$ is an even number, e.g., $p_s = 12$;
- p_s/m is an odd number, e.g., $p_s = 3, 9$.

Each of these three situations is discussed individually.

$p_s/2m$ is an odd number

For an arbitrary coil i and an according coil numbered as $(i + p_s/2)$, the original phase angle between them is,

$$\begin{aligned}\alpha_{c,i+p_s/2} - \alpha_{c,i} =& \alpha_c \cdot \frac{p_s}{2} = \left(2\pi \frac{P_r}{P_s} - \pi\right) \frac{p_s}{2} = 2\pi \frac{P_r}{P_s} \frac{p_s}{2} - \frac{p_s}{2}\pi \\ =& \pi p_r - \frac{p_s}{2}\pi = \left(p_r - \frac{p_s}{2}\right)\pi,\end{aligned} \tag{4.44}$$

where p_r is defined in equation (4.16). For $m = 3$, if $p_s/2m$ is an odd number, it means p_s is an even number and $p_s/2$ is an odd number. Since p_r and p_s are co-prime numbers, p_r must be an odd number. Hence, $(p_r - p_s/2)$ must be an even number and the result of equation (4.44) is equivalent to,

$$\alpha_{c,i+p_s/2} - \alpha_{c,i} = 0. \tag{4.45}$$

This indicates that these two coil phasors are in phase with each other.

Two examples, 12/10 VFRM ($p_s/2m = 1$) and 18/11 VFRM ($p_s/2m = 3$), are provided. For the 12/10 VFRM, coil i and the according coil $(i + 3)$ are in phase as indicated in Fig. 4.11(a), that coils 1 and 4, 2 and 5, 3 and 6 align with each other. For the 18/11 VFRM, coil i and the according coil $(i + 9)$ are in phase as indicated in Fig. 4.11(b), that the phasors of coils 1 and 10, 2 and 11, ..., are aligned. It gives the fact that coil i and coil $(i + p_s/2)$ must be connected in the same orientation.

In total $p_s/2$ phasors are evenly distributed in one revolution, hence, the original phase angle between two adjacent phasors is,

$$\alpha_{ph} = \frac{2\pi}{\frac{p_s}{2}} = \frac{4\pi}{p_s}. \tag{4.46}$$

On the other hand, $p_s/2$ phasors are divided by m phases, hence, the value of Q is,

$$Q = \frac{p_s}{2m}. \tag{4.47}$$

If $p_s/2m = 1$, e.g., in 12/10 VFRM, all the coils are forward-connected, $Q = 1$ and the distribution factor is 1. If $p_s/2m > 1$, e.g., in 18/11 VFRM, there

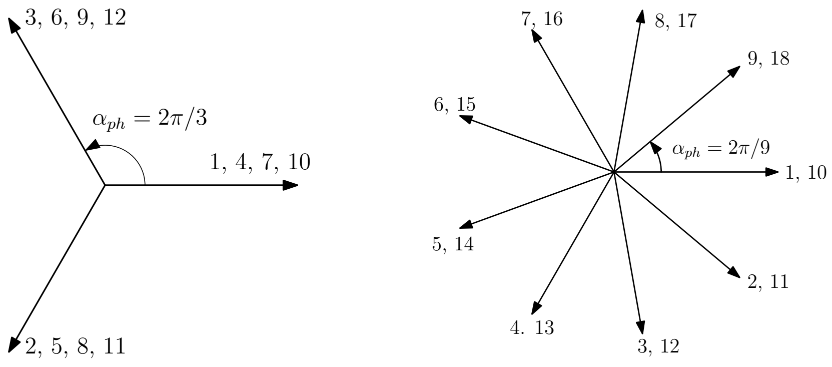
3, 6, 9, 12
$\alpha_{ph} = 2\pi/3$
1, 4, 7, 10
2, 5, 8, 11
7, 16
8, 17
9, 18
6, 15
$\alpha_{ph} = 2\pi/9$
1, 10
5, 14
2, 11
4. 13
3, 12

(a) (b)

Figure 4.11: The original phasor diagrams of the flux linkage assuming all the coils are in the same orientation for: (a) the 12/10 VFRM ($p_s/2m = 1$), and (b) the 18/11 VFRM ($p_s/2m = 3$).

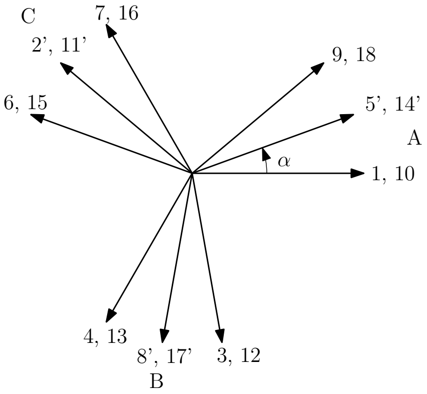
C
7, 16
2', 11'
9, 18
6, 15
5', 14'
A
α
1, 10
4, 13
8', 17'
3, 12
B

Figure 4.12: The winding configurations of the 18/11 VFRM.

is a backward-connected coil between two forward-connected coils as shown in Fig. 4.12, hence, the value of α for equation (4.14) is given by,

$$\alpha = \frac{\alpha_{ph}}{2} = \frac{2\pi}{p_s}. \tag{4.48}$$

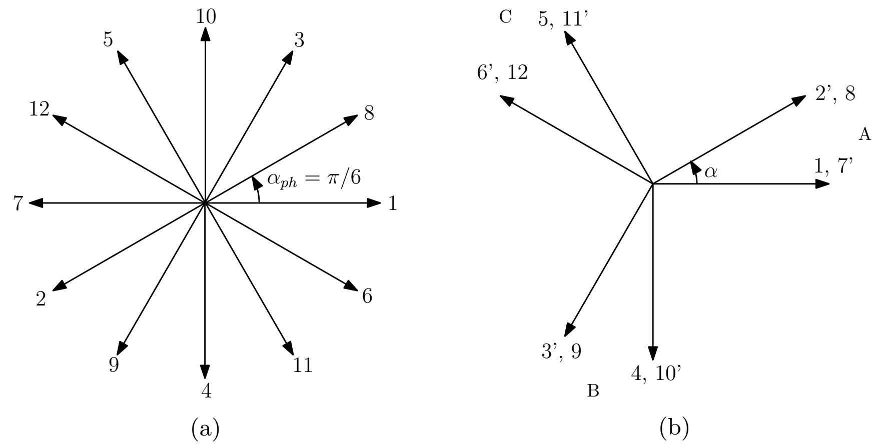

(a) (b)

Figure 4.13: The 12/11 VFRM ($p_s/2m = 2$): (a) the original phasor diagram of the flux linkage assuming all the coils are in the same orientation, and (b) the winding configurations.

$p_s/2m$ is an even number

The original phase angle between coil i and coil $(i + p_s/2)$ is again described by equation (4.44). If $p_s/2m$ is an even number, p_s and $p_s/2$ are both even numbers. Since p_s and p_r are co-prime numbers, p_r must be an odd number. Consequently, $(p_r - p_s/2)$ is an odd number, and the result of equation (4.44) is equivalent to,

$$\alpha_{c,i+p_s/2} - \alpha_{c,i} = \pi. \tag{4.49}$$

This indicates that these two coil phasors are out of phase. An example is given for the 12/11 VFRM in Fig. 4.13(a), as can be seen, since $p_s/2 = 6$, coils 1 and 7, 2 and 8,..., are out of phase.

In total p_s phasors are evenly distribued in one revolution, hence, the phase angle between two adjacent phasors is,

$$\alpha_{ph} = \frac{2\pi}{p_s}. \tag{4.50}$$

The winding configuration should ensure that any arbitrary coil i and coil $(i + p_s/2)$ are with different orientations, as shown in Fig. 4.13(b). As the phasors of the backward-connected coils are in phase with the forward-connected coils, the total number of different phasors is $p_s/2$. These $p_s/2$ phasors are divided by m phases, giving the value of Q as,

$$Q = \frac{p_s}{2m}. \tag{4.51}$$

In addition, the value of α for equation (4.14) is,

$$\alpha = \alpha_{ph} = \frac{2\pi}{p_s}, \tag{4.52}$$

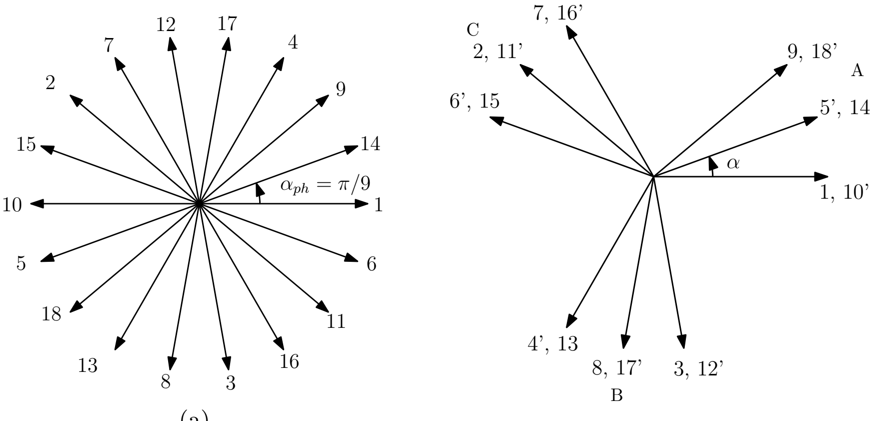

(a) (b)

Figure 4.14: The 18/20 VFRM: (a) the original phasor diagram of the flux linkage assuming all the coils are in the same orientation, and (b) the winding configurations ($p_s/m = 3$).

as can been in Fig. 4.13. The expressions of Q and α in equations (4.51) and (4.52) are the same as (4.47) and (4.48) that are derived when $p_s/2m$ is an odd number. Hence, these two situations can be combined under the condition that p_s/m is an even number.

p_s/m is an odd number

If p_s/m is an odd number, the original phase angle between coil i and coil $(i+p_s)$ is calculated as,

$$\begin{aligned}\alpha_{c,i+p_s} - \alpha_{c,i} =& \alpha_c p_s = \left(2\pi\frac{P_r}{P_s} - \pi\right) p_s = 2\pi\frac{P_r}{P_s} p_s - p_s\pi \\ =& 2\pi p_r - p_s\pi = (2p_r - p_s)\,\pi\end{aligned} \tag{4.53}$$

Since p_s is an odd number, the value of $(2p_r - p_s)$ must be an odd number and equation (4.53) is equivalent to,

$$\alpha_{c,i+p_s} - \alpha_{c,i} = \pi. \tag{4.54}$$

Hence, the original phasors of coil i and coil $(i + p_s)$ are out of phase. Two examples are given in Fig. 4.10(a) and Fig. 4.14(a) that shows the original phasor diagrams of 6/4 and 18/20 VFRMs, respectively. For the 6/4 VFRM, $p_s = 3$, hence, coils 1 and 4, 2 and 5, 3 and 6 are out of phase. Similar as in the 18/20 VFRM, $p_s = 9$, hence, coils 1 and 10, 2 and 11, 3 and 12... are out of phase.

In total $2p_s$ phasors are evenly distributed in one revolution, hence, the phase angle between two adjacent phasors is,

$$\alpha_{ph} = \frac{\pi}{p_s}. \tag{4.55}$$

Table 4.3: Values of Q and α for equation (4.14).

p_s/m	Q	α
1 or 2	1	-
odd number > 1	p_s/m	π/p_s
even number > 2	$p_s/2m$	$2\pi/p_s$

Table 4.4: The distribution factor of fundamental flux linkage/back-emf for various VFRMs.

	P_r								
P_s	2	4	5	7	8	10	11	13	14
6	1	1	1	1	1	1	1	1	1
12	1	1	0.966	0.966	1	1	0.966	0.966	1
18	0.960	0.960	0.960	0.960	0.96	0.96	0.960	0.960	0.960

The winding configuration should ensure that any arbitrary coil i and coil $(i+p_s)$ are with different orientations, as shown in Fig. 4.10(b) and Fig. 4.14(b). Since the phasors of the backward-connected coils are in phase with the forward-connected coils, the total number of different phasors is p_s. These p_s phasors are divided by m phases, giving the value of Q as,

$$Q = \frac{p_s}{m}. \tag{4.56}$$

If $p_s/m = 1$, e.g., in 6/4 VFRM, $Q = 1$ and the distribution factor is 1. If $p_s/m > 1$, e.g., in 18/20 VFRM, the value of α is,

$$\alpha = \alpha_{ph} = \frac{\pi}{p_s}, \tag{4.57}$$

as can be seen in Fig. 4.14.

The values of Q and α are summarized in Table 4.3, and the distribution factor of fundamental is given in Table 4.4.

4.3.4 Harmonic cancellation of distribution factor

For a harmonic order n, the distribution factor is calculated as [30, 68],

$$k_{dn} = \frac{\sin\left(n\frac{Q\alpha}{2}\right)}{Q\sin\left(n\frac{\alpha}{2}\right)}. \tag{4.58}$$

However, this equation cannot be directly applied to VFRMs, since the phase angle may flip for higher harmonics, and consequently, the electric angle between two adjacent phasors are not directly given by $n\alpha$. To perform a thorough analysis, the higher harmonics are analyzed for three types of stator pole/rotor pole combinations, similar to subsection 4.3.3.

Based on equations (4.41)-(4.42) that give the phase angle for the fundamental component, the original phase angle between coil i and coil 1 for the n^{th} harmonic is expressed as,

$$\alpha_{cn,i} = 2\pi \frac{P_r i}{P_s} n - \pi \quad (i \text{ is an even number}), \tag{4.59}$$

$$\alpha_{cn,i} = 2\pi \frac{P_r i}{P_s} n \quad (i \text{ is an odd number}). \tag{4.60}$$

The original phase angle between two adjacent coils is therefore calculated as,

$$\alpha_{cn} = \frac{2\pi P_r}{P_s} n - \pi, \tag{4.61}$$

where the term π represents the reversed flux polarity caused by the dc coil orientation.

$p_s/2m$ is an odd number

For the situation $p_s/2m$ is an odd number, coil i and coil $(i+p_s/2)$ are connected in the same orientation as discussed in section 4.3.3. For the n^{th} harmonic, the phase angle between coil i and coil $(i+p_s/2)$ is calculated as,

$$\begin{aligned}\alpha_{cn,i+p_s/2} - \alpha_{cn,i} =& \alpha_{cn} \cdot \frac{p_s}{2} = \left(2\pi \frac{P_r}{P_s} n - \pi\right) \frac{p_s}{2} = 2\pi \frac{P_r}{P_s} \frac{p_s}{2} n - \frac{p_s}{2}\pi \\ =& \pi n p_r - \frac{p_s}{2}\pi = \left(n p_r - \frac{p_s}{2}\right)\pi.\end{aligned} \tag{4.62}$$

Since p_r and $p_s/2$ are both odd numbers if $p_s/2m$ is an odd number as explained in section 4.3.3, the following relationship is deduced,

$$\alpha_{cn,i+p_s/2} - \alpha_{cn,i} = \begin{cases} 0 \ (n \text{ is an odd number}) \\ \pi \ (n \text{ is an even number}) \end{cases}. \tag{4.63}$$

Equation (4.63) indicates that for even harmonics, the two phasors of coil i and coil $(i+p_s/2)$ are out of phase, hence the even harmonics are canceled out, and the distribution factor is 0. On the contrary, the odd harmonics of these two phasors are in phase with each other. If $p_s/2m = 1$, as $Q = 1$, the distribution factor is 1 for all odd harmonics. If $p_s/2m > 1$, the phase angle between two adjacent phasors is $n\alpha$ and the distribution factor can be calculated using equation (4.58).

$p_s/2m$ is an even number

If $p_s/2m$ is an even number, coil i and coil $(i + p_s/2)$ are connected in different orientations as explained in section 4.3.3. For the n^{th} harmonic, the phase angle between coil i and coil $(i + p_s/2)$ is calculated as,

$$\alpha_{cn,i+p_s/2} - \alpha_{cn,i} = \alpha_{cn} \cdot \frac{p_s}{2} + \pi = \left(np_r - \frac{p_s}{2}\right)\pi + \pi, \tag{4.64}$$

where the term $+\pi$ indicates the different orientations. Since p_r is an odd number and $p_s/2$ is an even number if $p_s/2m$ is an even number, the same expression as equation (4.63) is deduced. This means the even harmonics are canceled out such that the distribution factor is 0; while for the odd harmonics, equation (4.58) can be used. As such, the condition, $p_s/2m$ is an even number, can be combined with the previous condition, $p_s/2m$ is an odd number, to the condition that p_s/m is an even number.

p_s/m is an odd number

If p_s/m is an odd number, coil i and coil $(i + p_s)$ are connected in different orientations as explained in section 4.3.3. For the n^{th} harmonic, the phase angle between coil i and coil $(i + p_s)$ is calculated as,

$$\begin{aligned}\alpha_{cn,i+p_s} - \alpha_{cn,i} =& \alpha_{cn} \cdot p_s + \pi = \left(2\pi \frac{P_r}{P_s} n - \pi\right) p_s + \pi \\ &= (2np_r - p_s + 1)\,\pi.\end{aligned} \tag{4.65}$$

Since p_s is an odd number, equation (4.65) leads to,

$$\alpha_{cn,i+p_s/2} - \alpha_{cn,i} = 0. \tag{4.66}$$

For all the harmonics, the phasors of coil i and coil $(i+p_s)$ are in phase with each other. For $p_s/m = 1$, as $Q = 1$, the distribution is 1 for all the harmonics. If $p_s/m > 1$, the adjacent phase angle is $n\alpha$ for the odd harmonics.

However, for even harmonics, the situation is more complicated since the phase angle is flipped for every other phasors as explained in [117]. An example is shown in Fig. 4.15 for the second and third harmonics in the 18/20 VFRM, where the second harmonic of the phasors of coil 5 and coil 14 are flipped. To show it more clearly, the phasor diagrams of even harmonics is summarized in Fig. 4.16. The phasors are divided into two groups, the phase angle between adjacent phasors is $2n\alpha$, while the number of phasors in the two groups are $(Q+1)/2$ and $(Q-1)/2$, respectively. Since the centerline of these two groups are out of phase, the magnitude of the resultant phasor is calculated by [117],

$$\left|\vec{\Lambda}_{res}\right| = \left(\frac{Q+1}{2} k_{dn,group1} - \frac{Q-1}{2} k_{dn,group2}\right)\left|\vec{\Lambda}\right|, \tag{4.67}$$

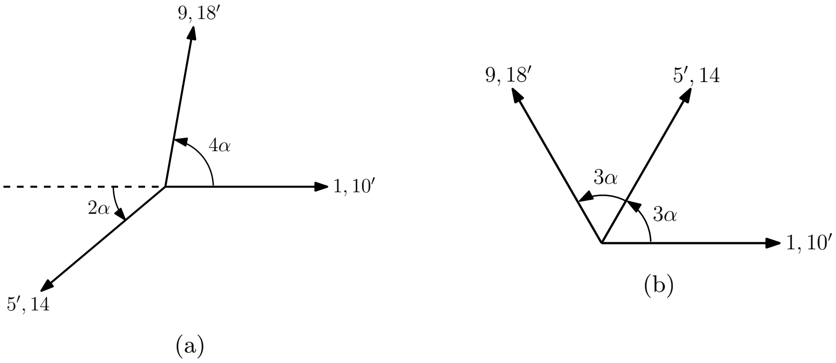

Figure 4.15: The phasor diagrams of the flux linkage for the 18/20 VFRM: (a) the second harmonic, and (b) the third harmonic.

Table 4.5: Expressions for calculating distribution factors of harmonics.

p_s/m	Odd harmonics	Even harmonics	Topology examples
1	1	1	6/2, 6/4, 12/8
2	1	0	6/5, 12/2, 12/10
Odd number > 1	equation (4.58)	equation (4.70)	18/8, 18/14, 18/20
Even number > 2	equation (4.58)	0	12/5, 12/7, 18/11

where $\left|\vec{\Lambda}\right|$ is the magnitude of a single phasor. Using equation (4.58) to calculate $k_{dn,group1}$ and $k_{dn,group2}$, it gives,

$$k_{dn,group1} = \frac{\sin\left(n\frac{Q+1}{2}\alpha\right)}{\frac{Q+1}{2}\sin\left(n\alpha\right)}, \tag{4.68}$$

$$k_{dn,group2} = \frac{\sin\left(n\frac{Q-1}{2}\alpha\right)}{\frac{Q-1}{2}\sin\left(n\alpha\right)}. \tag{4.69}$$

The distribution factor is therefore deduced as,

$$k_{dn} = \frac{\left|\vec{\Lambda}_{res}\right|}{Q\left|\vec{\Lambda}\right|} = \frac{\sin\left(n\frac{Q+1}{2}\alpha\right)}{Q\sin\left(n\alpha\right)} - \frac{\sin\left(n\frac{Q-1}{2}\alpha\right)}{Q\sin\left(n\alpha\right)}. \tag{4.70}$$

The equations for calculating distribution factors for different harmonics are summarized in Table 4.5, together with some topology examples for each situation.

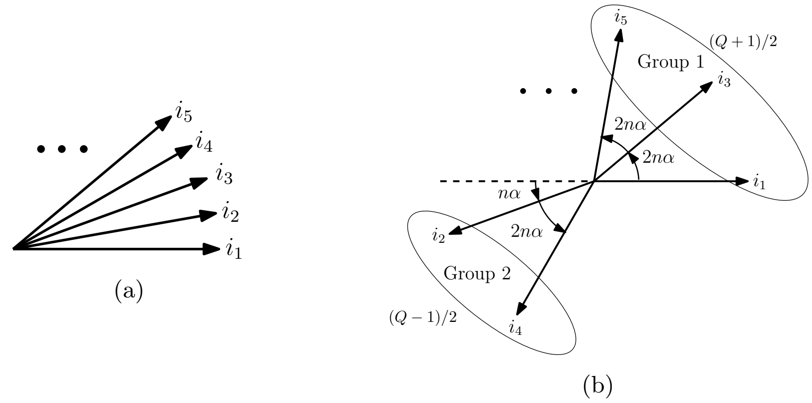

Figure 4.16: The phasor diagrams of the VFRMs with p_s/m as an odd number higher than one: (a) fundamental component, and (b) even harmonics. [117]

4.3.5 Pitch factor

The pitch factor is defined as: the ratio of resultant flux linkage/back-emf of the two coil bundles to twice the flux linkage/back-emf of one coil bundle. For concentrated windings, the electric angle between the two coil bundles is,

$$\beta = \frac{2\pi P_r}{P_s}. \tag{4.71}$$

The pitch factor is calculated as,

$$k_p = \cos\left(\frac{\beta}{2}\right). \tag{4.72}$$

For higher harmonic order n, the pitch factor is calculated by [117],

$$k_{pn} = \cos\left(n\frac{\beta}{2}\right). \tag{4.73}$$

Disregarding the skew factor, the winding factor is calculated by,

$$k_{wn} = k_{dn}k_{pn}. \tag{4.74}$$

As a summary, the distribution factor and pitch factor are listed in Appendix C for various VFRMs.

4.4 Influence of the number of rotor poles

In the previous section, the winding factor is calculated. However, based on equation (4.37), to predict the flux linkage $\hat{\Lambda}_{fph,1}$, not only the winding factor has to be derived, but also the flux linkage of the coil itself, $\hat{\Lambda}_{fcoil,1}$, has to be considered. Assuming the harmonics are ignored, the flux linkage of a single coil is represented as,

$$\Lambda_{fcoil,1} = \frac{(\Lambda_{fcoil,\max} - \Lambda_{fcoil,\min})}{2} \cos(\Delta_\theta) + \frac{\Lambda_{fcoil,\max} + \Lambda_{fcoil,\min}}{2}, \quad (4.75)$$

where $\Lambda_{fcoil,\max}$ and $\Lambda_{fcoil,\min}$ are the maximum and minimum values, respectively. The magnitude of fundamental is therefore,

$$\hat{\Lambda}_{fcoil,1} = \frac{\Lambda_{fcoil,\max} - \Lambda_{fcoil,\min}}{2}. \quad (4.76)$$

For VFRMs with the same number of stator poles (P_s) and the same winding factor, the number of rotor poles (P_r) is divided into three situations, i.e., $P_s \approx P_r$ (e.g., 12/10 topology), $P_s \ll P_r$ (e.g., 12/22 topology), and $P_s \gg P_r$ (e.g., 12/2 topology). In the following content, the term $(\Lambda_{fcoil,\max} - \Lambda_{fcoil,\min})$ is analyzed for these three situations.

Flux linkage in VFRMs with $P_r \approx P_s$

The flux linkage is strongly influenced by the teeth widths. If the teeth widths are too large, it leads to the relationship of,

$$w_{ts} > (\tau_r - w_{tr}), \quad (4.77)$$

where w_{ts}, w_{tr} and τ_r represents respectively the stator tooth width, rotor tooth width and rotor pole pitch. There is continuously overlapping area between the stator tooth and rotor tooth as shown in Fig. 4.17, and consequently, the flux variation between the aligned and unaligned positions is small. On the other hand, if the teeth widths are too small, the alignment area is small as shown in Fig. 4.18(a) and Fig. 4.18(b), which leads to a small $(\Lambda_{fcoil,\max} - \Lambda_{fcoil,\min})$ as well.

The relationship among $(\Lambda_{fcoil,\max} - \Lambda_{fcoil,\min})$ and teeth widths is shown in Fig. 4.19(a) for a 12/10 VFRM. The teeth width in the figure is described using the terms k_{ts} and k_{tr} that represent the ratios of stator/rotor tooth width to stator/rotor slot pitch, respectively. The dashed lines indicate the situations of $w_{ts} = \tau_r - w_{tr}$, small w_{tr} and small w_{ts}, respectively. The value of $(\Lambda_{fcoil,\max} - \Lambda_{fcoil,\min})$ is maximized when k_{tr} is around 0.45 and k_{ts} is 0.5. At this moment, w_{tr} is approximate to w_{ts} and is close to half of the stator slot pitch.

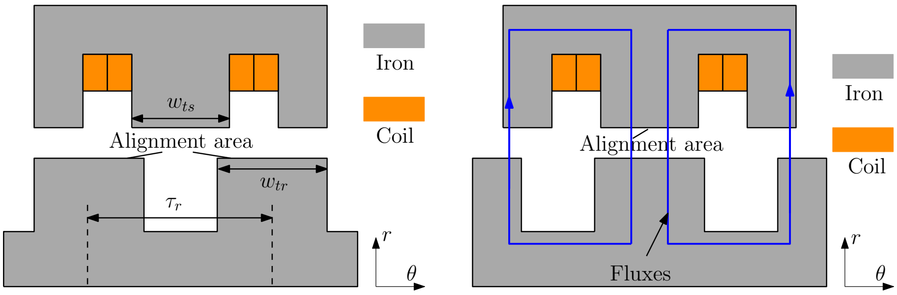
w_{ts}
Alignment area
w_{tr}
τ_r
Iron
Coil
r
θ
Alignment area
Fluxes
Iron
Coil
r
θ

(a) (b)

Figure 4.17: The fraction of a 12/10 VFRM with the relationship of $w_{ts} > (\tau_r - w_{tr})$ (a) at the unaligned position, and (b) at the aligned position.

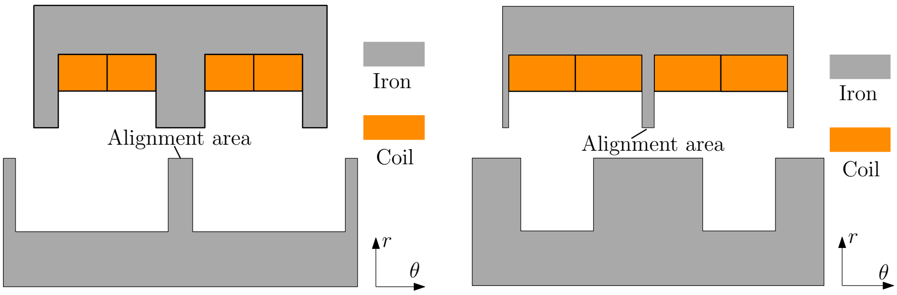
Alignment area
Iron
Coil
r
θ
Alignment area
Iron
Coil
r
θ

(a) (b)

Figure 4.18: The fraction of a 12/10 VFRM at the aligned position: (a) with a small rotor tooth width, and (b) with a small stator tooth width.

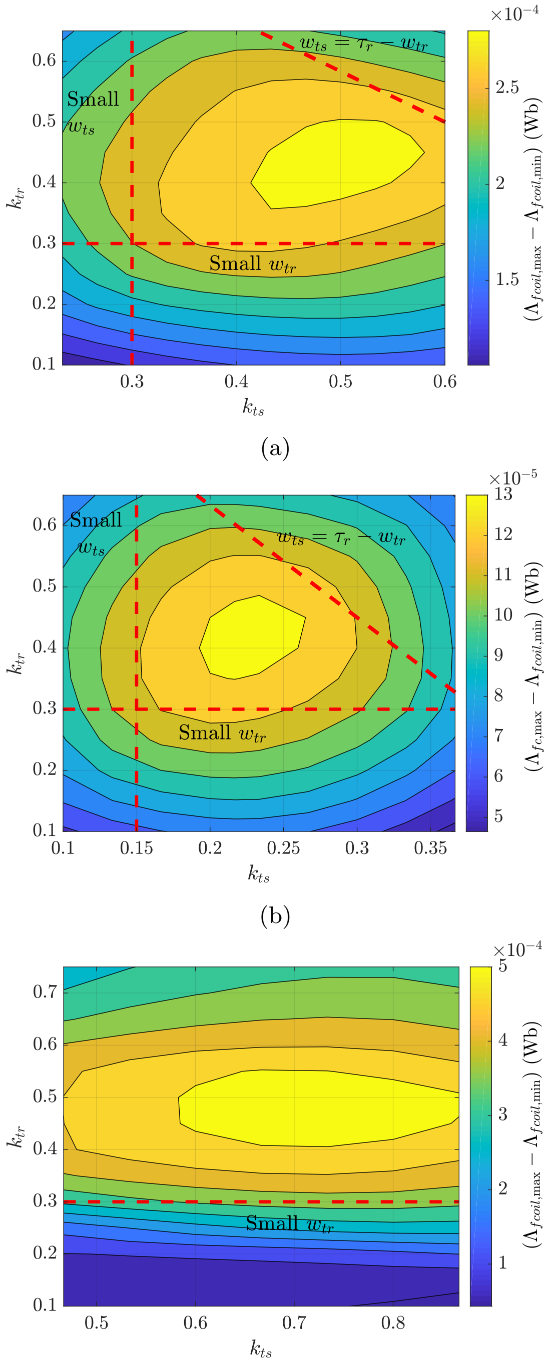

(a)

(b)

(c)

Figure 4.19: The values of coil flux linkage $(\Lambda_{fcoil,\max} - \Lambda_{fcoil,\min})$ by varying stator and rotor teeth widths in (a) 12/10 VFRM, (b) 12/22 VFRM, and (c) 12/2 VFRM (k_{ts} and k_{tr} are the ratios of the stator/rotor tooth width to stator/rotor slot pitch.

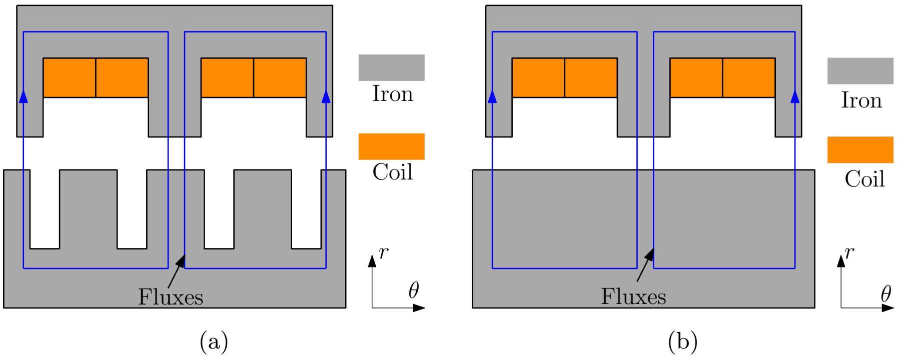

(a) (b)

Figure 4.20: The flux paths at the aligned position for the fraction of (a) a 12/22 VFRM, and (b) a 12/2 VFRM.

Flux linkage in VFRMs with $P_s \ll P_r$

The analysis for this situation is similar to $P_r \approx P_s$. The relationship among $(\Lambda_{fcoil,\max} - \Lambda_{fcoil,\min})$ and teeth widths is calculated for a 12/22 VFRM, in which the dimensions are the same as the previous 12/10 VFRM except the teeth widths. The result is shown in Fig. 4.19(b). The value of $(\Lambda_{fcoil,\max} - \Lambda_{fcoil,\min})$ is maximized when k_{tr} is around 0.45 and k_{ts} is 0.23. Since $P_s \ll P_r$, for relatively small k_{ts}, the stator tooth width is already comparable to rotor tooth width.

Additionally, the flux path at the aligned position for the topology of $P_s \ll P_r$ is different from the topology of $P_r \approx P_s$. For a 12/10 VFRM, the flux passes through adjacent rotor teeth as shown in Fig. 4.17(b), while for a 12/22 VFRM, it passes through every other rotor tooth as shown in Fig. 4.20(a), which means the middle tooth is ‘obsolete’ at the aligned position.

Flux linkage in VFRMs with $P_s \gg P_r$

The relationship among $(\Lambda_{fcoil,\max} - \Lambda_{fcoil,\min})$ and teeth widths is shown in Fig. 4.19(c) for a 12/2 VFRM. Due to the lack of rotor teeth, there is intrinsically no alignment area at the unaligned position for almost all combinations of teeth widths. The condition of $w_{ts} < \tau_r - w_{rt}$ is satisfied for almost all values of w_{ts}. Therefore, this condition is not indicated in the figure.

Additionally, the flux path at the aligned position for the topology of $P_s \gg P_r$ is different from the previous situations. There is no other rotor tooth that the flux can go through, it has to enter and leave the same rotor tooth surface as shown in Fig. 4.20(b). Hence, the rotor tooth width is preferred to be much larger than the stator tooth width. However, such a large rotor tooth width maintains a continuous overlapping area for a wide range of rotation angle, that leads to abundance of harmonics as can be seen in Fig. 4.21(a).

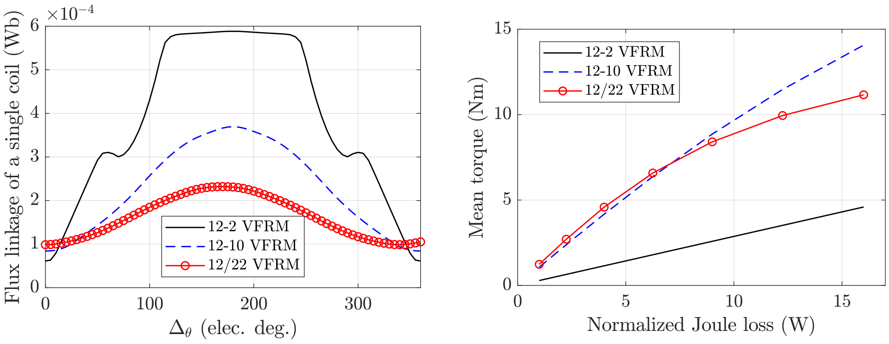

(a) (b)

Figure 4.21: Comparison of 12/2, 12/10 and 12/22 VFRMs: (a) the flux linkage of a single coil versus the rotation angle (Δ_θ), and (b) the mean electromagnetic torque.

Influence of the number of rotor poles on the mean torque

In addition to the influence on the coil flux linkage, the number of rotor poles, P_r, has a direct effect on the torque based on equation (4.36). The mean torque is estimated with the teeth widths that provide the maximum ($\Lambda_{fcoil,\max} - \Lambda_{fcoil,\min}$) for the three VFRMs, and the result is shown in Fig. 4.21(b). The torque in the 12/2 VFRM is much lower than the other two, therefore, the topology with $P_s \gg P_r$ is not preferred. The torque of a 12/22 VFRM may be slightly higher than the 12/10 VFRM at a relatively low current density, however, the machine soon starts to saturate and the torque becomes much lower than 12/10 VFRM for a higher current density. This is due to small teeth widths in the 12/22 VFRM that lead to a relatively high flux density. Moreover, having more rotor poles means higher electric frequency that requires a higher switching frequency of the power electronic circuit. Therefore, the topology of $P_r \approx P_s$ is preferred.

4.5 Unbalanced magnetic pull

There is unbalanced magnetic pull for topologies with an odd number of rotor poles [75]. Force is derived in x- and y-directions by FEM for the 6/5 VFRM, and the results are shown in Fig. 4.22. As can be seen, the unbalanced magnetic pull (UMP) is over 2×10^3 N with a current density of 5 A/mm^2 for both the field current and armature current, and this value rises with an increasing current density. Such a high UMP leads to an additional bearing wear and may generate loud acoustic noise. Therefore, the odd number of rotor poles is not recommended.

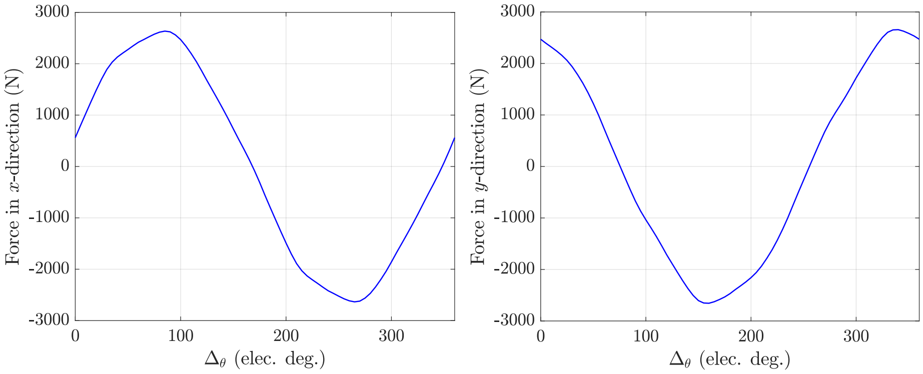

(a) (b)

Figure 4.22: Unbalanced magnetic pull of a 6/5 VFRM: (a) the force in the x-direction versus the rotation angle, and (b) the force in the y-direction versus the rotation angle.

4.6 Selection of stator and rotor poles

The previous sections provide the arguments in the aspects of fundamental winding factors, harmonic cancellation, torque comparison, etc. Taking the unbalanced magnetic pull into account, the odd number of rotor poles is not desired. Hence, topologies such as 6/5, 6/7,... are out of consideration. According to section 4.4, it is beneficial for the torque production to select topologies with similar values of P_s and P_r. Therefore, topologies such as 6/4, 12/8, 12/10, 24/20... are preferred.

On the other hand, based on section 4.3, for VFRMs with p_s/m equals to an even number, e.g., 12/10, 24/20 topologies, the even harmonics are canceled out in the back-emf. This is beneficial for torque ripple reduction, hence, is more suitable for applications that requires minimization of torque ripple and acoustics.

For the application of 48 V mild hybrid traction, the rotational speed is extended to around 18 krpm as introduced in Chapter 6. This is a relatively high speed, and a smaller number of rotor poles is more preferable. At 18 krpm, the electric frequency of a 12/10 VFRM is 3000 Hz, and this is doubled for a 24/20 topology. For the same hardware of power electronics, suppose the machine drives operate at the same switching frequency, the total harmonic distortion (THD) in the current of the 24/20 VFRM is higher than the 12/10 VFRM. To reduce the THD, the switching frequency of the 24/20 VFRM has to be increased, consequently, the switching loss rises. As such, the 12/10 VFRM is selected for further research.

4.7 Summary and conclusions

The research in this chapter aims for the topology selection, which requires an extensive understanding of the machine operating principle. The electromagnetic torque production mechanism is introduced based on the analysis of four kinds of inductances: the self inductance of the field winding, the mutual inductances between field winding and armature windings, the self inductances of the armature windings and the mutual inductances of the armature windings. Each type of the inductance induces a torque component, and the contributions to the mean torque and torque ripples are analyzed individually. It is found that the fundamental of the mutual inductances between the field winding and the armature windings, mainly contributes to the mean torque.

The winding factors for different numbers of stator and rotor poles are mathematically analyzed, and provide the fact that with a proper selection of pole numbers, the even harmonics in the back-emf/flux linkage can be canceled out. Additionally, the dependence of flux path, flux linkage and torque on the number of rotor poles is analyzed. The result suggests a maximized torque for the situation when the number of rotor poles is close to the number of stator poles. Moreover, the magnetic pull is analyzed for an odd number of rotor poles, which shows a large magnitude. The selection rule of the VFRM topology is given based on the aforementioned aspects, and the 12/10 VFRM is the final choice.

Chapter 5

Design considerations

Part of the content in this chapter is published in:

J. Bao, B. L. J. Gysen, K. Boynov, J. J. H. Paulides and E. A. Lomonova, ‘Torque ripple reduction for 12-stator/10-rotor-pole variable flux reluctance machines by rotor skewing or rotor teeth non-uniformity’, in IEEE Transactions on Magnetics, vol. 53, no. 11, pp. 1-5, 2017.

J. Bao, B. L. J. Gysen, K. Boynov, J. J. H. Paulides, K. Bastiaens and E. A. Lomonova, ‘Analysis and minimization of torque ripple for variable flux reluctance machines’, IEEE International Electric Machines and Drives Conference (IEMDC), pp. 1-7, 2017.

J. Bao, B. L. J. Gysen, K. Boynov, S. Alexandrov and E. A. Lomonova, ‘Field weakening capability of 12-stator/10-rotor-pole variable flux reluctance machines’, Twelfth International Conference on Ecological Vehicles and Renewable Energies (EVER), pp. 1-5, 2017.

5.1 Introduction

In this chapter, the analysis towards minimizing the torque ripples, widening the speed range and deriving the scaling laws is presented for the 12/10 VFRM, which gives more insight into the relationship of machine geometry and performance. The torque ripples are analyzed based on the inductances and torque equations derived in Chapter 4, and are minimized by machine geometry adjustment and harmonic injection. In addition, the *dq*-reference frame of VFRMs is introduced. The influence of dc and ac currents on the torque-speed characteristic is given, and the enhancement of speed extension capability is achieved by proper current arrangement. Additionally, the scaling laws are summarized for torque production in both non-saturated and saturated VFRMs.

5.2 Torque ripple minimization

A drawback of VFRMs is the presence of a relatively high torque ripple due to its doubly salient structure [10, 11]. To reduce the torque ripples, the sources of the torque ripples are first analyzed. The dominant harmonics are analyzed for each of the four torque components obtained in section 4.2.3, i.e., T_{ff}, $T_{f,ph}$, $T_{l,ph}$ and $T_{m,ph}$. The normalized amplitude spectrum of the torque components is presented for a 12/10 VFRM, as shown in Fig. 5.1.

For the field winding, the winding factor is zero except for the harmonics with the integer multiple of 6. Consequently, T_{ff} contains a large torque ripple at these harmonic orders based on equation (4.20), and this can be seen in Fig. 5.1.

For the mutual inductances between the field winding and armature windings, the distribution factors of the even harmonics are all zero as explained in section 4.3.4, hence, the torque ripple contains only even harmonics according to equation (4.27). Moreover, among the odd harmonics of the mutual inductance, the 5^{th} harmonic dominates, hence, a relatively large 6^{th} harmonic is induced in $T_{f,ph}$, as presented in Fig. 5.1.

For the other two torque components that are respectively induced by the self and mutual inductances of the armature windings, $T_{l,ph}$ and $T_{m,ph}$, the 6^{th} harmonic also dominates. However, the contributions are modest compared to T_{ff} and $T_{f,ph}$ as can be seen in Fig. 5.1, where the magnitudes of the 6^{th} harmonic are significantly smaller. One of the reasons is that the 6^{th} harmonic in $T_{l,ph}$ or $T_{m,ph}$ is contributed by the 4^{th}, 6^{th} and 8^{th} harmonics of the inductances, however, the contributions from these three harmonics counteract with each other to some extent.

As a summary, the 6^{th} harmonic dominates in the torque ripple of a 12/10 VFRM, and is mainly contributed by T_{ff} and $T_{f,ph}$. In the following content, three torque

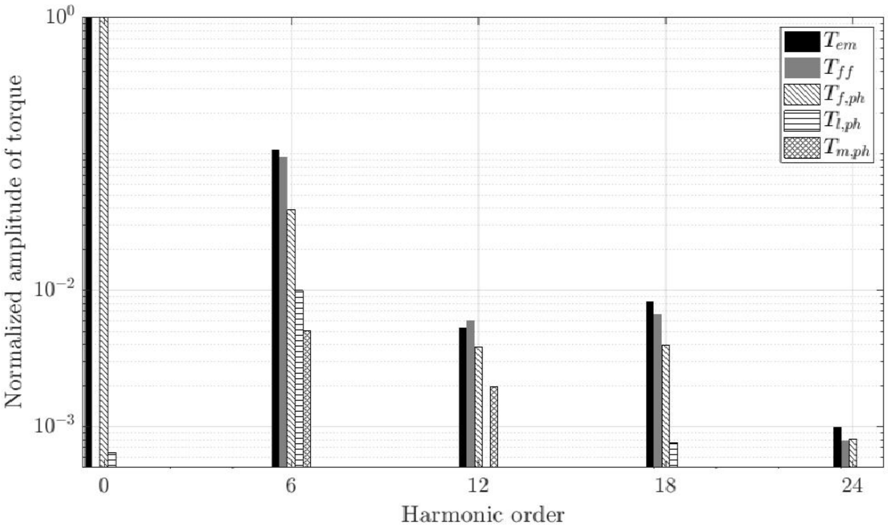

Figure 5.1: Normalized amplitude spectrum of the torque components for a non-saturated 12/10 VFRM.

ripple reduction approaches, i.e., rotor skewing, rotor teeth non-uniformity and harmonic injection, are investigated to eliminate T_{ff} and $T_{f,ph}$ for both non-saturated and saturated VFRMs.

5.2.1 Rotor skewing

Skewing is one of the most effective solutions that is widely used in other types of machines [103]. Compared with continuous skewing, stepped rotor skewing is often applied as a more practical alternative that simplifies the manufacturing process and reduces cost [29, 46]. The analysis in this subsection merely focuses on the geometry with two modules, since the working principle is the same for more modules.

The geometry of a step-skewed rotor with two modules is shown in Fig. 5.2(a). The individual laminations of the front and rear modules are aligned, however, between the two modules, there is a skewing angle, θ_{sk}. Assume the front half of the machine generates a back-emf of

$$E_{front} = \hat{E}\sin(P_r\omega_m t), \tag{5.1}$$

where ω_m is the mechanical rotational speed. The back-emf of the rear half of the machine is accordingly

$$E_{rear} = \hat{E}\sin(P_r\omega_m t + P_r\theta_{sk}). \tag{5.2}$$

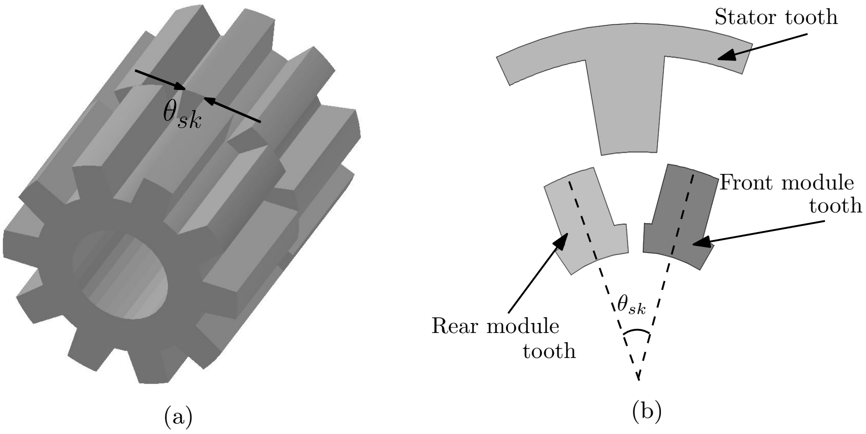

(a) (b)

Figure 5.2: (a) The 3D geometry of a step-skewed rotor with two modules for the 12/10 VFRM, and (b) the rotor position when the armature current is zero to maximize the mean torque.

The resultant back-emf is therefore

$$E_{tot} = 2\hat{E}\sin\left(P_r\omega_m t + \frac{P_r\theta_{sk}}{2}\right)\cos\left(\frac{P_r\theta_{sk}}{2}\right). \tag{5.3}$$

The armature current should be in phase with the back-emf in equation (5.3) to reach the maximum mean torque. It means the sinusoidal current reaches zero when the centerline of the two modules aligns with the stator tooth, as shown in Fig. 5.2(b). As such, the ratio of the mean torque in a skewed machine to the mean torque in an un-skewed machine is

$$\frac{\bar{T}'_{em}}{\bar{T}_{em}} = \cos\left(\frac{P_r\theta_{sk}}{2}\right). \tag{5.4}$$

Effect of the method for non-saturated machines

First the influence of skewing is analyzed in a non-saturated machine. To simplify the simulation, the two modules are represented by two 2D un-skewed machines whose rotors are relatively displaced by θ_{sk}, [24]. The 3D effect, i.e., the axial interaction between adjacent step-skewed rotor modules [70], is not considered.

As explained above, the 6^{th} harmonic dominates in both T_{ff} and $T_{f,ph}$. In an un-skewed machine, they are described as,

$$T_{ff,6} = -3\hat{L}_{ff,6}P_r i_f^2\sin(6\Delta_\theta + \theta_{ff,6}), \tag{5.5}$$

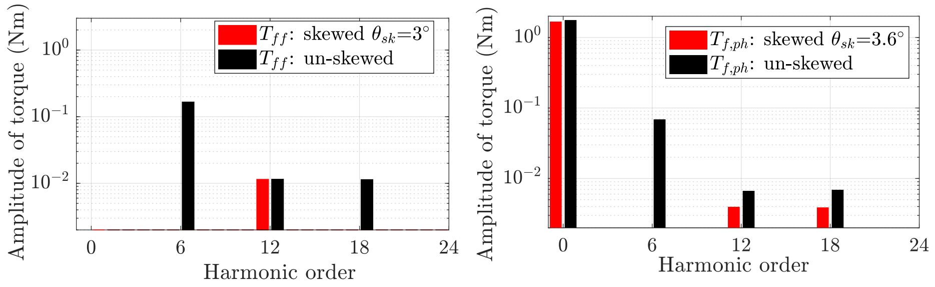

(a) (b)

Figure 5.3: (a) Spectrum of T_{ff} when $\theta_{sk} = 3°$ and (b) spectrum of $T_{f,ph}$ when $\theta_{sk} = 3.6°$.

$$\begin{aligned} T_{f,ph,6} =& -\frac{15}{2}P_r\hat{M}_{fph,5}i_f\hat{I}_{ac}\cos\left(6\Delta_\theta + \theta_{fa,5}\right) \\ &+\frac{21}{2}P_r\hat{M}_{fph,7}i_f\hat{I}_{ac}\cos\left(6\Delta_\theta + \theta_{fa,7}\right) \\ &\approx -\frac{15}{2}P_r\hat{M}_{fph,5}i_f\hat{I}_{ac}\cos\left(6\Delta_\theta + \theta_{fa,5}\right), \end{aligned} \tag{5.6}$$

based on equations (4.20) and (4.27) assuming $\gamma = 90°$. Since the magnitude of $\hat{M}_{fph,7}$ is significantly smaller than $\hat{M}_{fph,5}$, the influence of $\hat{M}_{fph,7}$ is ignored in equation (5.6).

In a skewed machine, equations (5.5) and (5.6) become,

$$\begin{aligned} T'_{ff,6} =& -\frac{3}{2}\hat{L}_{ff,6}P_r i_f^2\left[\sin\left(6\Delta_\theta + \theta_{ff,6} - 3P_r\theta_{sk}\right)\right. \\ &\left.+\sin\left(6\Delta_\theta + \theta_{ff,6} + 3P_r\theta_{sk}\right)\right], \end{aligned} \tag{5.7}$$

$$\begin{aligned} T'_{f,ph,6} \approx& -\frac{15P_r\hat{M}_{fph,5}i_f\hat{I}_{ac}}{4}\left[\cos\left(6\Delta_\theta + \theta_{fph,5} - 2.5P_r\theta_{sk}\right)\right. \\ &\left.+\cos\left(6\Delta_\theta + \theta_{fph,5} + 2.5P_r\theta_{sk}\right)\right]. \end{aligned} \tag{5.8}$$

According to equations (5.7) and (5.8), $T_{ff,6}$ and $T_{f,ph,6}$ can be canceled out when $\theta_{sk} = 3°$ and 3.6°, respectively. This is verified by the spectra presented in Fig. 5.3, which show the elimination of $T_{ff,6}$ and $T_{f,ph,6}$ with a properly selected θ_{sk}.

For VFRMs with different geometric dimensions or currents, the contributions of $T_{ff,6}$ and $T_{f,ph,6}$ vary, therefore, the optimum skewing angle is different. If $T_{ff,6}$ dominates in an un-skewed structure, it is preferred to make θ_{sk} close to 3°, such that $T_{ff,6}$ is eliminated. An example is given for the VFRM with the geometries and dimensions presented in Fig. 5.4 and Table 5.1. For the rotor tooth outer arc (α_{ro}) at 14.5°, the relationship between the torque ripple and skewing angle is shown in Fig. 5.5(a), where the optimum skewing angle is 3°. If α_{ro} is changed

Table 5.1: The dimensions of a 12/10 VFRM which is the benchmark example for analyzing torque ripple reduction and field weakening capability.

Symbol	Description	Value	Unit
R_{so}	Outer diameter	70	mm
L_{sk}	Stack length	87.5	mm
R_{ro}	Rotor outer diameter	42	mm
R_{sh}	Shaft diameter	17	mm
h_{sy}	Stator yoke height	7.5	mm
h_{ry}	Rotor yoke height	13	mm
α_{si}	Stator tooth inner arc	15	deg.
α_{so}	Stator tooth outer arc	15	deg.
α_{ro}^*	Rotor tooth outer arc	15	deg.
α_{ri}	Rotor tooth inner arc	21	deg.
N_{dc}	Number of turns per dc coil	40	-
N_{ac}^*	Number of turns per ac coil	10	-

Notes: α_{ro}^* is varied to 14.5°, 16° and 17° for rotor skewing in section 5.2.1 and rotor teeth non-uniformity in section 5.2.2. N_{ac}^* is set to be 6 in section 5.3 for analyzing field weakening.

to 16°, the contribution from $T_{f,ph,6}$ is comparable to $T_{ff,6}$. The relationship between the skewing angle and the torque ripple changes, as shown in Fig. 5.5(a). For α_{ro} at 17°, $T_{f,ph,6}$ becomes dominant, the optimum skewing angle moves closer to 3.6°. However, due to the existence of other remained small harmonic contents, e.g., $M_{fph,7}$, $L_{ff,12}$, etc., the optimum skewing angle deviates from 3.6°, as shown in Fig. 5.5(a) with the dotted line.

Additionally, the relationship between the mean torque and θ_{sk} is shown in Fig. 5.6(a). The analytical result by using equation (5.4) is in agreement with the FEM result.

Effect of the method for saturated machines

Saturation changes both the magnitudes and phases of inductances. Therefore, the relationship between the torque components may alter significantly between non-saturated and saturated machines. Accordingly, the relationship between the torque ripple and skewing angle changes. Such effect can be seen in the comparison in Fig. 5.5(a) and (b) for $\alpha_{ro} = 16°$. On the other hand, saturation almost does not change the relationship between the average torque and skewing angle, as can be seen in the comparison between Fig. 5.6(a) and (b). Above all, the method of stepped rotor skewing works effectively for torque ripple reduction in both non-saturated and saturated VFRMs. Moreover, if more modules are used, the torque ripple can be further reduced [73].

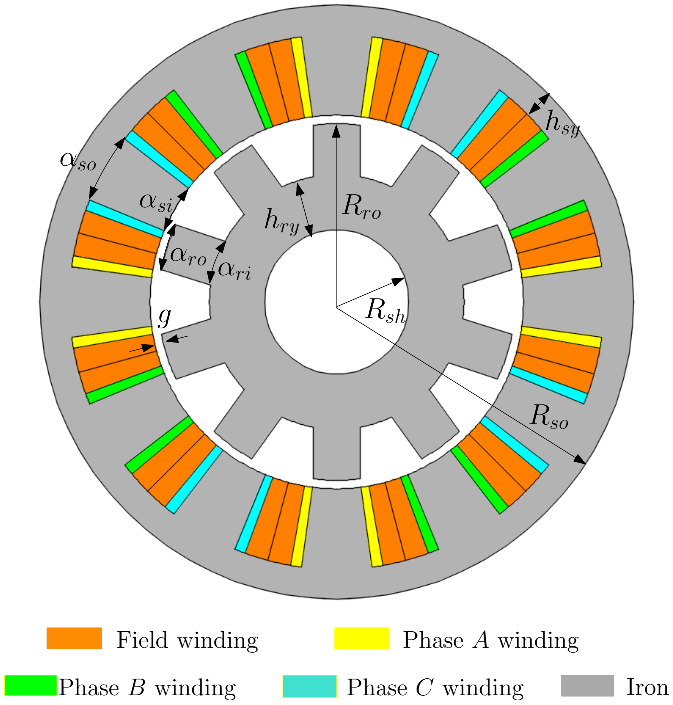
α_{so}
h_{sy}
α_{si}
h_{ry}
R_{ro}
α_{ro}
α_{ri}
g
R_{sh}
R_{so}
Field winding
Phase A winding
Phase B winding
Phase C winding
Iron

Figure 5.4: The geometry of a 12/10 VFRM which is the benchmark example for analyzing torque ripple reduction and field weakening capability.

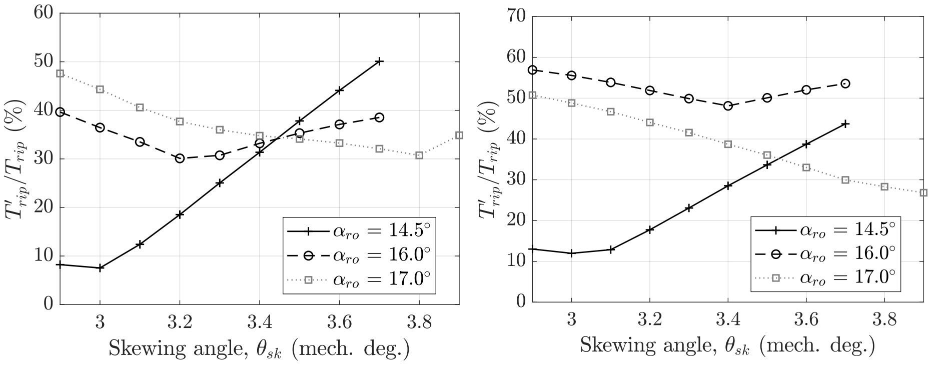

(a) (b)

Figure 5.5: Ratio of the torque ripples between a skewed machine (T'_{rip}) with rotor skewing and an un-skewed machine (T_{rip}) for different rotor tooth outer arcs (α_{ro}): (a) the machine is not saturated, and (b) the machine is saturated.

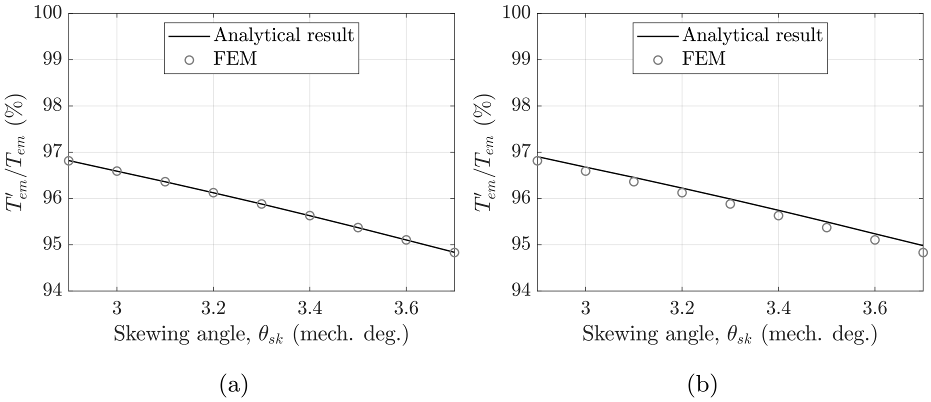

(a) (b)

Figure 5.6: Ratio of the mean torques between a skewed machine (T'_{em}) with rotor skewing and an un-skewed machine (T_{em}) for the rotor tooth outer arc at 16°: (a) the machine is not saturated, and (b) the machine is saturated.

5.2.2 Rotor teeth non-uniformity

The working principle of rotor skewing is to generate opposing torque ripple in different modules, therefore to reduce the resultant torque ripple. In this subsection, a method with a different working principle is analyzed. The geometry is shown in Fig. 5.7, where every other rotor tooth is skewed and the skewing angle remains the same along the stack length [24].

The flux of one coil still reaches maximum when a rotor tooth aligns with the corresponding stator tooth, and reaches minimum when they un-align. With a skewing angle of θ_{sk2}, the flux of two coils is shown in Fig. 5.7(b). As can be seen, the fundamental frequency of the flux of a single coil is half of the electric frequency. However, the sum of the two has the same period as an un-skewed structure. By properly tuning θ_{sk2}, the harmonics in the resultant flux are attenuated.

Effect of the method for non-saturated machines

Similar to the analysis in section 5.2.1, this method is analyzed for different values of rotor tooth outer arc as well. The selection of θ_{sk2} should consider the relationship between torque components. Based on 2D FEM, the influence of θ_{sk2} on $\hat{L}_{ff,6}$ and $\hat{M}_{fph,5}$ is given in Fig. 5.8, where $\hat{L}_{ff,6}$ and $\hat{M}_{fph,5}$ are minimized with $\theta_{sk2} = 2.9°$ and $\theta_{sk2} = 3.6°$, respectively. As a result, for dominant $T_{ff,6}$, the optimum skewing angle is close to $\theta_{sk2} = 2.9°$, as shown for $\alpha_{ro} = 14.5°$ in Fig. 5.9(a). For $\alpha_{ro} = 16°$ when $T_{ff,6}$ is comparable to $T_{f,ph,6}$, the optimum value of θ_{sk2} moves to 3.1°. For $\alpha_{ro} = 17°$, the relationship between the torque ripple and skewing angle changes, as $T_{f,ph,6}$ is much more dominant than $T_{ff,6}$. Due to

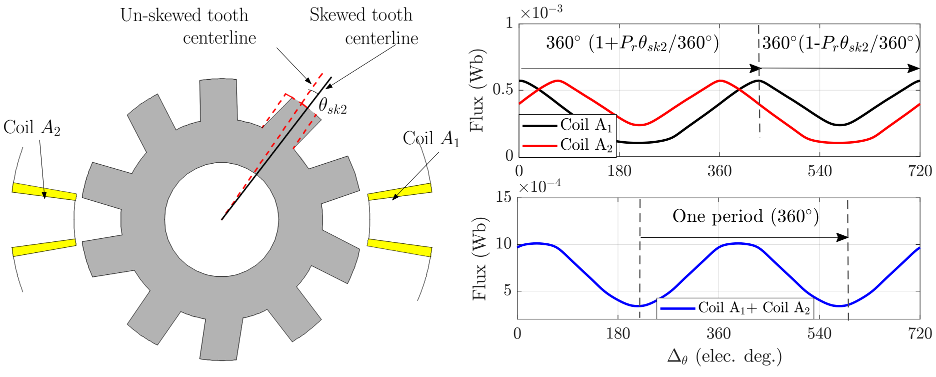
Un-skewed tooth centerline
Skewed tooth centerline
θ_{sk2}
Coil A_2
Coil A_1
$\times 10^{-3}$
360° (1+$P_r\theta_{sk2}$/360°)
360°(1-$P_r\theta_{sk2}$/360°)
Flux (Wb)
1
0.5
0
Coil A$_1$
Coil A$_2$
0
180
360
540
720
$\times 10^{-4}$
15
10
5
One period (360°)
Coil A$_1$+ Coil A$_2$
Flux (Wb)
0
180
360
540
720
Δ_θ (elec. deg.)

(a) (b)

Figure 5.7: (a) The geometry of a rotor with non-uniformly distributed teeth, and (b) flux waveforms of coil A$_1$ and A$_2$ and the resultant flux of the two coils.

the contribution from other small harmonic contents, the optimum skewing angle is 3.8°, although the inductance $\hat{M}_{fph,5}$ is eliminated at 3.6°. Additionally, the ratio of the mean torque in a skewed machine to the mean torque in an un-skewed machine is shown in Fig. 5.10(a).

Effect of the method for saturated machines

If the machine is saturated, the influence of θ_{sk2} on the torque ripples and the mean torque is shown in Figs. 5.9(b) and 5.10(b), respectively. As a result, the torque ripples are affected significantly by saturation while the mean torque is not.

Above all, the selection of the skewing angle is of crucial importance for torque ripple reduction. The effect of the rotor skewing and rotor teeth non-uniformity is similar in both non-saturated and saturated machines. The torque ripple is reduced at least 50% for different situations with a mean torque reduction no more than 5%. The final selection of the skewing angle should consider the torque ripples at different torque levels as well as the influence on the mean torque.

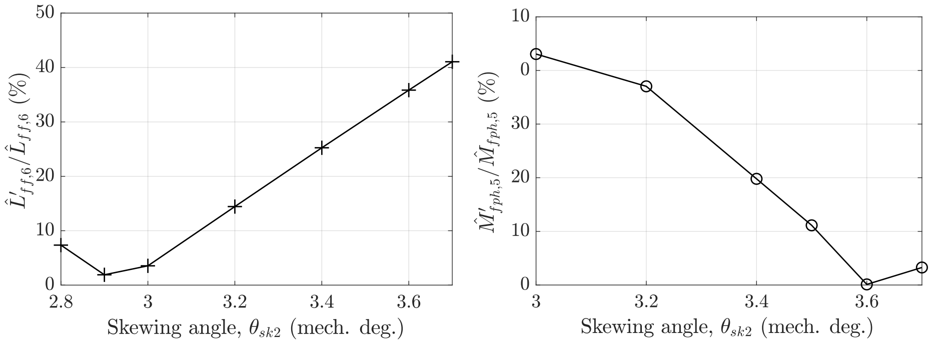

(a) (b)

Figure 5.8: Ratio of the inductances between a skewed machine with rotor teeth non-uniformity and an un-skewed machine: (a) the amplitude of the 6^{th} harmonic in the self inductance of the field winding ($\hat{L}_{ff,6}$), and (b) the amplitude of the 5^{th} harmonic in the mutual inductance between the field winding and armature windings ($\hat{M}_{fph,5}$).

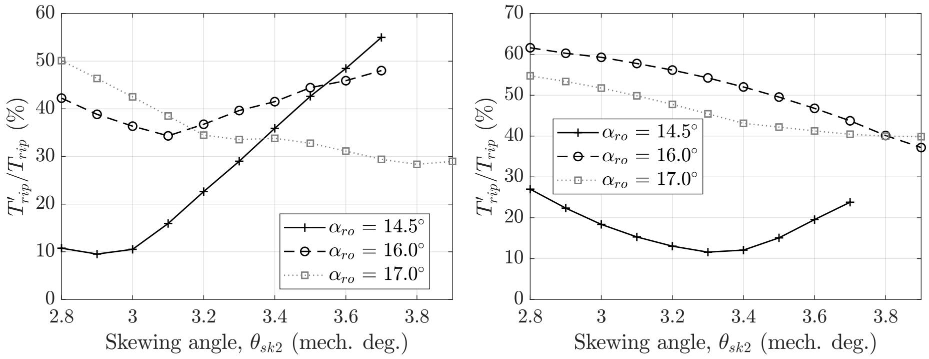

(a) (b)

Figure 5.9: Ratio of the torque ripples between a skewed machine (T'_{rip}) with rotor teeth non-uniformity and an un-skewed machine (T_{rip}) for different rotor tooth outer arcs (α_{ro}): (a) the machine is not saturated, and (b) the machine is saturated.

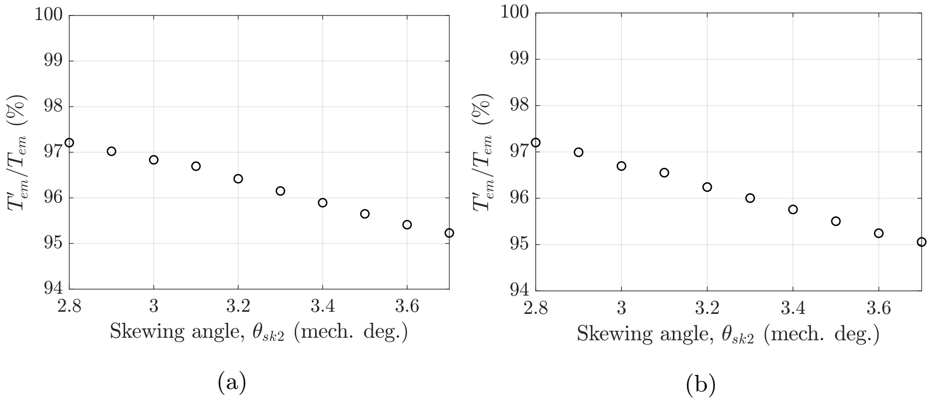

(a) (b)

Figure 5.10: Ratio of the mean torques between a skewed machine (T'_{em}) with rotor teeth non-uniformity and an un-skewed machine (T_{em}) for rotor tooth outer arc (α_{ro}) at 16°: (a) the machine is not saturated, and (b) the machine is saturated.

5.2.3 Harmonic current injection

In this subsection, the method of harmonic injection is discussed for torque ripple reduction. The method is categorized in armature current injection and field current injection for both non-saturated and saturated machines. Results are compared in the aspects of torque ripple and mean torque for these two injection approaches.

Armature current harmonic injection for non-saturated VFRMs

Harmonic injection into armature current is first analyzed for the situation of a non-saturated machine. As aforementioned, $\hat{M}_{fph,5}$ dominates, hence, the previous torque expression of $T_{f,ph}$ in equation (4.13), is simplified to,

$$\begin{aligned} T_{f,ph} \approx & - P_r i_f i_a \hat{M}_{fph,1} \sin\left(\Delta_\theta + \theta_{fa,1}\right) - 5P_r i_f i_a \hat{M}_{fph,5} \sin\left(5\Delta_\theta + \theta_{fa,5}\right) \\ & - P_r i_f i_b \hat{M}_{fph,1} \sin\left(\Delta_\theta + \theta_{fa,1} - \frac{2\pi}{3}\right) \\ & - 5P_r i_f i_b \hat{M}_{fph,5} \sin\left(5\Delta_\theta + \theta_{fa,5} + \frac{2\pi}{3}\right) \\ & - P_r i_f i_c \hat{M}_{fph,1} \sin\left(\Delta_\theta + \theta_{fa,1} + \frac{2\pi}{3}\right) \\ & - 5P_r i_f i_c \hat{M}_{fph,5} \sin\left(5\Delta_\theta + \theta_{fa,5} - \frac{2\pi}{3}\right). \end{aligned} \tag{5.9}$$

Suppose a 5^{th} harmonic is injected into the armature currents that is written as,

$$i_a = \hat{I}_{ac} \cos\left(\Delta_\theta + \gamma\right) + \hat{I}_{ac,5} \cos\left(5\Delta_\theta + \gamma_5\right), \tag{5.10}$$

$$i_b = \hat{I}_{ac} \cos\left(\Delta_\theta - \frac{2}{3}\pi + \gamma\right) + \hat{I}_{ac,5} \cos\left(5\Delta_\theta + \gamma_5 - 5 \times \frac{2\pi}{3}\right), \tag{5.11}$$

$$i_c = \hat{I}_{ac} \cos\left(\Delta_\theta + \frac{2}{3}\pi + \gamma\right) + \hat{I}_{ac,5} \cos\left(5\Delta_\theta + \gamma_5 + 5 \times \frac{2\pi}{3}\right), \tag{5.12}$$

where $\hat{I}_{ac,5}$ and γ_5 are the amplitude and phase angle of the 5^{th} harmonic of the armature currents, respectively. The difference of $T_{f,ph}$ with and without the harmonic injection is derived as,

$$\begin{aligned}\Delta T_{f,ph} \approx & -\frac{3P_r i_f \hat{M}_{fph,1} \hat{I}_{ac,5}}{2} \sin\left(6\Delta_\theta + \theta_{fa,1} + \gamma_5\right) \\ & + \frac{15P_r i_f \hat{M}_{fph,5} \hat{I}_{ac,5}}{2} \sin\left(\gamma_5 - \theta_{fa,5}\right).\end{aligned} \tag{5.13}$$

The first and second terms in equation (5.13) represent the torque ripple and mean torque induced by the armature current harmonic injection, respectively.

To eliminate the 6^{th} harmonic in the torque ripple, the torque ripple caused by the injected harmonic current should counteract the original torque ripple, hence, the following condition should be satisfied,

$$-\frac{3}{2} P_r \hat{M}_{fph,1} i_f \hat{I}_{ac,5} \sin\left(6\Delta_\theta + \gamma_5 + \theta_{fa,1}\right) + T_{ff,6} + T_{f,ph,6} = 0. \tag{5.14}$$

Note that the influence of harmonic injection on $T_{l,ph}$ or $T_{m,ph}$ is not considered, since these two torque components are significantly smaller as previously explained.

The benchmark example given in Table 5.1 is used to verify the analysis. Using equation (5.14), it is calculated that the amplitude and phase angle of the injected harmonic current should be around 1.5 A and 20° respectively. On the other hand, the FEM result is presented in Fig. 5.11(a), which shows the dependence of the torque ripple on the values of $\hat{I}_{ac5}$ and γ_5. The torque ripple is mostly reduced by 87% at $\hat{I}_{ac5} = 1.5$ A (around 10% of $\hat{I}_{ac}$) and $\gamma_5 = 20°$ as expected.

Additionally, the mean torque almost does not change based on equation (5.13). Since the values of $\hat{I}_{ac,5}$ and $\hat{M}_{f,ph5}$ are much smaller than $\hat{I}_{ac}$ and $\hat{M}_{fph,1}$, the second term in equation (5.13) is significantly smaller than the original mean value of $T_{f,ph}$ given in equation (4.36). This is verified by the FEM result presented in Fig. 5.11(b), that the mean torque varies less than 0.3% with and without harmonic injection. Above all, the torque ripple is decreased by 87% using armature current harmonic injection while the mean torque is not reduced.

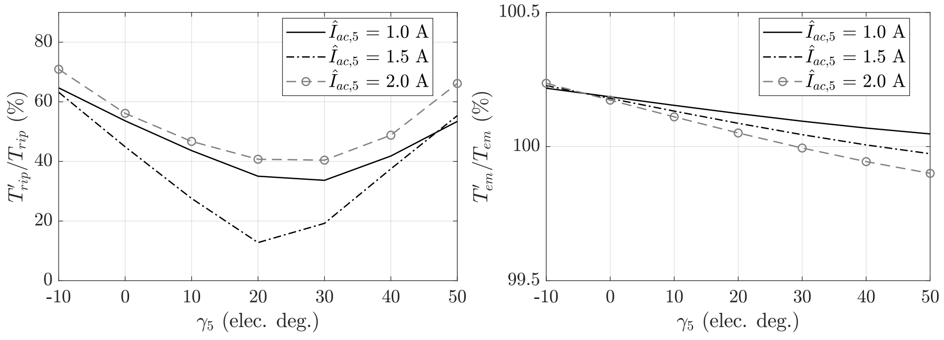

(a) (b)

Figure 5.11: The influences of the amplitude ($\hat{I}_{ac,5}$) and phase angle (γ_5) of the armature harmonic current on: (a) the ratio of the torque ripple with harmonic injection (T'_{rip}) to the torque ripple without harmonic injection (T_{rip}), and (b) the ratio of the mean torque with harmonic injection ($\bar{T}'_{em}$) to the mean torque without harmonic injection ($\bar{T}_{em}$).

Field current harmonic injection for non-saturated VFRMs

Injecting harmonics into the field current is investigated in this subsection. The current with the n^{th} harmonic is described as,

$$i_f = I_{f,0} + \hat{I}_{f,n}\cos\left(n\Delta_\theta + \gamma_n\right), \tag{5.15}$$

where $\hat{I}_{f,n}$ and γ_n are the amplitude and phase angle of the n^{th} harmonic of the field current, respectively. The differences of $T_{f,ph}$ and T_{ff} with and without harmonic injection are approximately,

$$\begin{aligned}
\Delta T_{f,ph} \approx & -\frac{3P_r\hat{I}_{f,n}\hat{I}_{ac}\hat{M}_{fph,1}}{4}\sin\left[n\Delta_\theta + \theta_{fa,1} + \gamma_n - \gamma\right] \\
& + \frac{3P_r\hat{I}_{f,n}\hat{I}_{ac}\hat{M}_{fph,1}}{4}\sin\left[n\Delta_\theta - \theta_{fa,1} + \gamma_n + \gamma\right] \\
& - \frac{15P_r\hat{I}_{f,n}\hat{I}_{ac}\hat{M}_{fph,5}}{4}\sin\left[\left(n+6\right)\Delta_\theta + \theta_{fa,5} + \gamma_n + \gamma\right] \\
& + \frac{15P_r\hat{I}_{f,n}\hat{I}_{ac}\hat{M}_{fph,5}}{4}\sin\left[\left(n-6\right)\Delta_\theta - \theta_{fa,5} + \gamma_n - \gamma\right],
\end{aligned} \tag{5.16}$$

$$\begin{aligned}\Delta T_{ff} \approx &-\frac{3}{2}P_r\hat{I}_{f,n}^2\hat{L}_{ff,6}\sin(6\Delta_\theta+\theta_{ff,n})\\&+\frac{3}{4}P_r\hat{I}_{f,n}^2\hat{L}_{ff,6}\sin\left[(2n-6)\,\Delta_\theta-\theta_{ff,n}+2\gamma_n\right]\\&-3P_rI_{f0}\hat{I}_{f,n}\hat{L}_{ff,6}\sin\left[(n+6)\,\Delta_\theta+\theta_{ff,n}+\gamma_n\right]\\&-\frac{3}{4}P_r\hat{I}_{f,n}^2\hat{L}_{ff,6}\sin\left[(2n+6)\,\Delta_\theta+\theta_{ff,n}+2\gamma_n\right]\\&+3P_rI_{f0}\hat{I}_{f,n}\hat{L}_{ff,6}\sin\left[(n-6)\,\Delta_\theta-\theta_{ff,n}+\gamma_n\right].\end{aligned}\tag{5.17}$$

To eliminate the 6^{th} torque ripple, a 6^{th} harmonic should be injected in the field current. In equation (5.16), the first and second terms represent the change in the 6^{th} harmonic of the torque ripple, the third term indicates the change in the 12^{th} harmonic of the torque ripple, and the fourth term gives the change in the mean torque; while in equation (5.17), the first and second terms represent the change in the 6^{th} harmonic of the torque ripple, the third and fourth terms indicate respectively the change in the 12^{th} and 18^{th} harmonics of the torque ripple, and the fifth term gives the change in the mean torque.

The change in the 6^{th} harmonic of the torque ripple should counteract the original ripples, giving the condition of,

$$\begin{aligned}&\frac{3P_r\hat{I}_{f,6}\hat{I}_{ac}\hat{M}_{fph,1}}{4}\cos\left[6\Delta_\theta+\theta_{fa,1}+\gamma_6\right]\\&+\frac{3P_r\hat{I}_{f,6}\hat{I}_{ac}\hat{M}_{fph,1}}{4}\cos\left[6\Delta_\theta-\theta_{fa,1}+\gamma_6\right]\\&+\frac{3}{4}P_r\hat{I}_{f,6}^2\hat{L}_{ff,6}\sin\left[6\Delta_\theta-\theta_{ff,6}+2\gamma_6\right]\\&-\frac{3}{2}P_r\hat{I}_{f,6}^2\hat{L}_{ff,6}\sin(6\Delta_\theta+\theta_{ff,6})+T_{f,ph,6}+T_{ff,6}=0,\end{aligned}\tag{5.18}$$

assuming $\gamma = 90°$. To investigate the effectiveness of the field harmonic injection, the same benchmark example listed in Table 5.1 is used. The torque ripple reduction with respect to the amplitude and phase angle of the field harmonic current is shown in Fig. 5.12(a). The torque ripple reaches its minimum with $\hat{I}_{f,6} = 1.1$ A and $\gamma_6 =$ -70°. This minimum value is slightly higher than the value using armature current harmonic injection. It is caused by the extra 12^{th} and 18^{th} harmonics of torque ripple expressed in equations (5.16) and (5.17). Such effect is presented in Fig. 5.13, where the 12^{th} and 18^{th} harmonics are compared for the two injection methods. On the other hand, the mean torque is reduced by 0.8% at the point of $\hat{I}_{f,6} = 1.1$ A and $\gamma_6 = -70°$, as can be seen in Fig. 5.12(b).

It is worth mentioning that a relatively large harmonic in the field current may require a high voltage for the field winding, which is expressed by,

$$\Delta u \approx 6L_{ff,0}\hat{I}_{f,6}\sin\left(6\Delta_\theta+\gamma_6\right)\omega_rP_r,\tag{5.19}$$

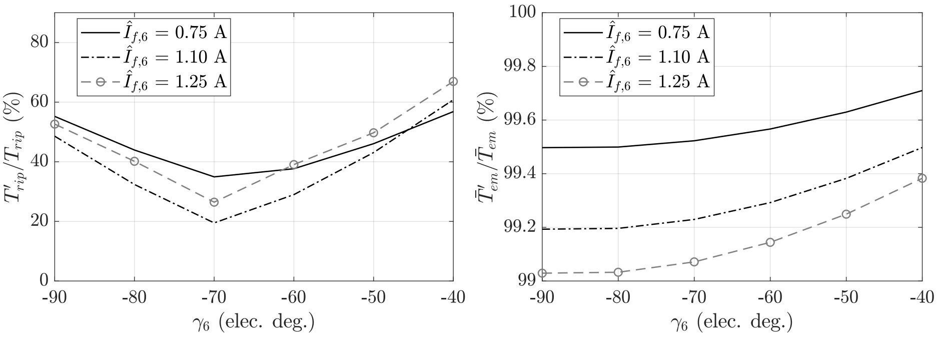

(a) (b)

Figure 5.12: The influences of the amplitude ($\hat{I}_{f,6}$) and phase angle (γ_6) of the field harmonic current on: (a) the ratio of the torque ripple (T'_{rip}) with harmonic injection to the torque ripple (T_{rip}) without harmonic injection, and (b) the ratio of the mean torque with harmonic injection ($\bar{T}'_{em}$) to the mean torque without harmonic injection ($\bar{T}_{em}$).

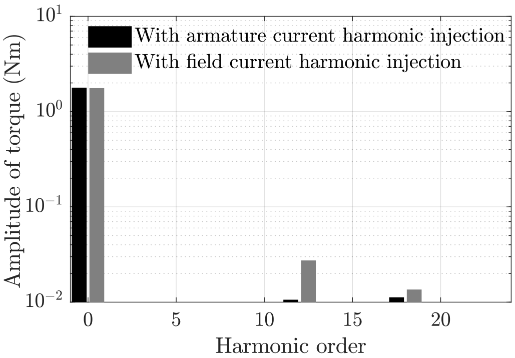

Figure 5.13: The comparison of the amplitude spectra of the torque for armature current harmonic injection and field current harmonic injection.

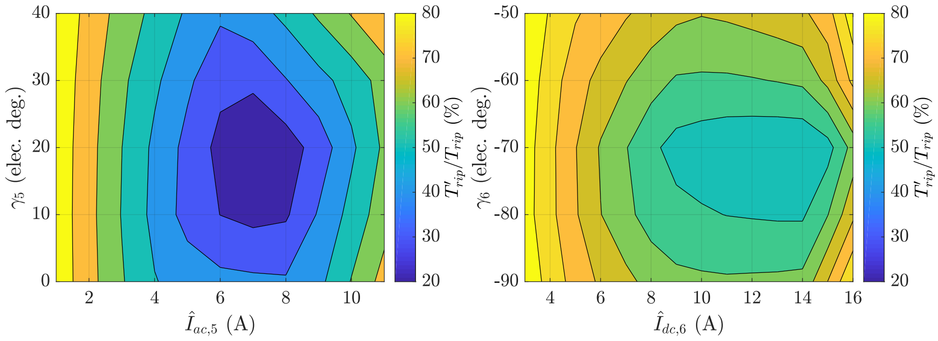

(a) (b)

Figure 5.14: The ratio of the torque ripple with harmonic injection (T'_{rip}) to the torque ripple without harmonic injection (T_{rip}) for different amplitudes ($\hat{I}_{ac,5}$, $\hat{I}_{f,6}$) and phase angles (γ_5, γ_6) of the harmonic currents: (a) by using armature current harmonic injection, and (b) by using field current harmonic injection.

where Δu represents the induced voltage by field current harmonic injection. Since the dc component of the inductance, $L_{ff,0}$, is relatively large, when $\hat{I}_{f,6}$ is 1.1 A, the amplitude of Δu reaches 170 V at 3000 rpm, hence, must be taken into account. For armature current harmonic injection, the increase of voltage is much more limited as the magnitude of $\hat{M}_{fph,n}$ is much smaller compared to $L_{ff,0}$.

Influence of saturation

The effectiveness of the aforementioned two injection methods is discussed in this subsection for a saturated machine. The torque ripple and mean torque are calculated. Parameters, i.e. amplitudes and phase angles of injected currents, are swept to seek the optimum values. The obtained results are presented in Figure 5.14 and Figure 5.15. As it can seen in Figure 5.14, armature current harmonic injection reduces the torque ripple up to 80%, while field current harmonic injection only reduces it up to 49% [71]. Meanwhile, at the point with minimum torque ripple, the mean torque is reduced by 0.2% and 2.8% respectively by using armature current injection and field current injection. In this sense, armature current harmonic injection has a better performance.

As a summary, the rotor skewing, rotor teeth non-uniformity and harmonic injection are effective for torque ripple reduction, and these methods are possible to be combined for even better results.

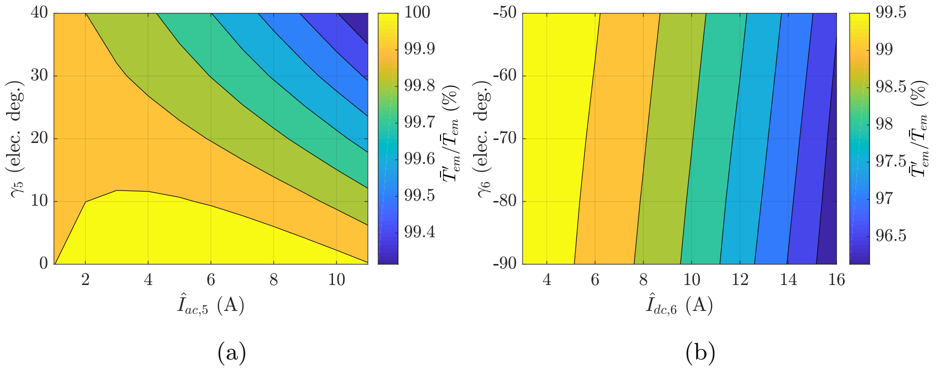

Figure 5.15: The ratio of the mean torque with harmonic injection (T'_{em}) to the mean torque without harmonic injection (T_{em}) for different amplitudes ($\hat{I}_{ac,5}$, $\hat{I}_{f,6}$) and phase angles (γ_5, γ_6) of the harmonic currents: (a) by using armature current harmonic injection, and (b) by using field current harmonic injection.

5.3 Field weakening capability

The arrangement of field current and armature current influences significantly the working envelope of a VFRM. The effect on the knee point in the torque-speed curve and the speed extension capability is discussed in this section.

5.3.1 *DQ*-reference frame

Generally, the *dq*-reference frame is desired in control to have the system variables as constants and to use standard PI regulators. The *dq* current errors are dc instead of sinusoidal ac signals, hence, the control bandwidth can be significantly lower. [68] In PMSMs, the *dq*-reference frame based on rotor frame is recommended in the dynamic modeling. The *d*-axis is defined as the centerline of the rotor magnetic poles, while the *q*-axis is defined half pole pitch shifted from the *d*-axis. The *d*-axis points to the peak airgap magnetic field created by the rotor while the *q*-axis always points to the zero field.

However, the characteristic of the airgap rotating magnetic field in VFRMs is different from PMSMs. In [127], the open-circuit airgap radial field harmonics and armature reaction airgap radial field harmonics are presented for a 12/10 flux switching machine. Similar calculation is performed for the 12/10 VFRM, and the predicted rotating field using FEM is presented in Figs. 5.16 and 5.17. Based on Fig. 5.16(b), different harmonics of the open-circuit airgap rotating field have different rotating speeds, e.g., the 6^{th} harmonic is a static field, the 4^{th} harmonic rotates with the electric frequency while the frequency of the 24^{th} harmonic is tripled. In addition, the armature reaction rotating field is synchronous to the

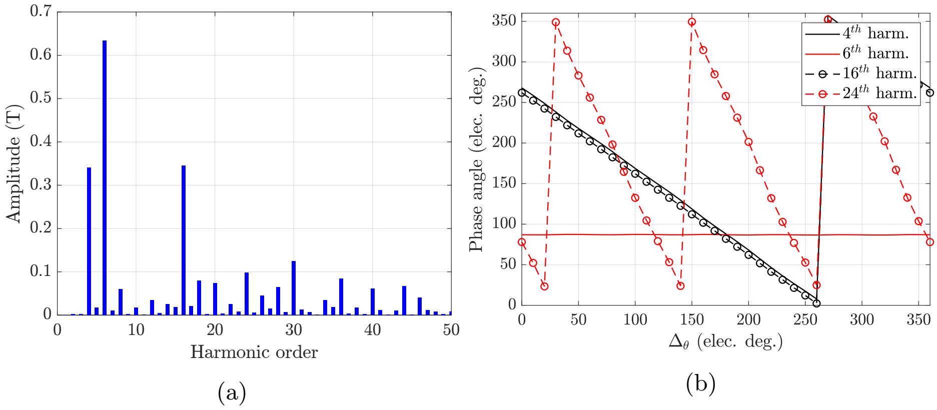

Figure 5.16: Harmonics of the open-circuit air-gap radial magnetic field: (a) the amplitude at rotation angle $\Delta_\theta = 0^\circ$, and (b) the relationship between the phase angles and Δ_θ of several harmonics.

open-circuit magnetic field as presented in Fig. 5.16(b) and Fig. 5.17(b). However, there is not a clear fundamental rotating magnetic field in the VFRM as can be seen in Figs. 5.16(a) and 5.17(a), where the harmonics with the order of 4, 6... dominate in the open-circuit or armature reaction airgap magnetic field. Hence, the definition of *dq*-axes for PMSMs can not be directly applied to VFRMs.

This thesis uses the concept explained in [117], which uses the open-circuit flux linkage waveform, to define *dq*-axes. The flux linkage of a phase reaches the peak values when the centerline of a stator tooth aligns with the centerline of a rotor tooth or between the centerlines of two adjacent rotor teeth. These two lines are defined as the positive and negative *d*-axes as indicated in Fig. 5.18. Accordingly, the *q*-axes are located in the middle between two adjacent *d*-axes.

The *dq*-axes inductance is calculated as,

$$\begin{aligned} L_d &= \frac{3}{2}L_{ph,0} + \frac{3}{2}\hat{L}_{ph,2}, \\ L_q &= \frac{3}{2}L_{ph,0} - \frac{3}{2}\hat{L}_{ph,2}, \end{aligned} \tag{5.20}$$

where $L_{ph,0}$ and $\hat{L}_{ph,2}$ is the dc component and amplitude of the 2^{nd} harmonic of the self inductance, respectively, as explained in section 4.2.3. As shown in Fig. 4.6, the magnitude of the 2^{nd} harmonic, $\hat{L}_{ph,2}$, is relatively small, around 0.9% of the dc component $L_{ph,0}$. Therefore, the saliency ratio of the VFRM is small. The expressions of voltage and torque in *dq*-axes are similar to PMSMs,

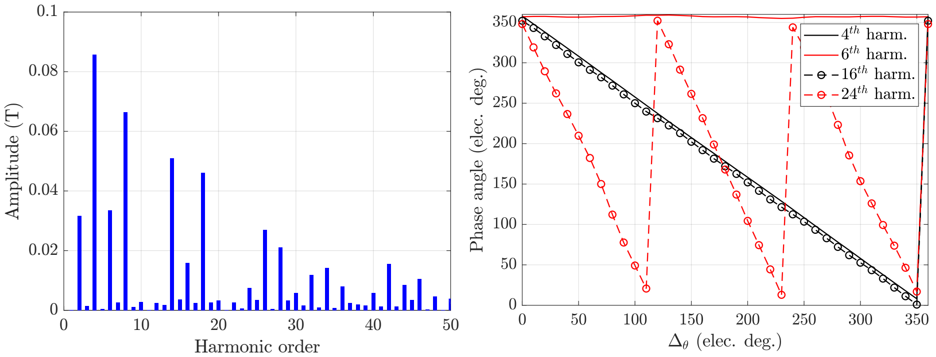

(a) (b)

Figure 5.17: Harmonics of the air-gap radial magnetic field generated by armature currents: (a) the amplitude at rotation angle $\Delta_\theta = 0°$, and (b) the relationship between the phase angles and Δ_θ of several harmonics.

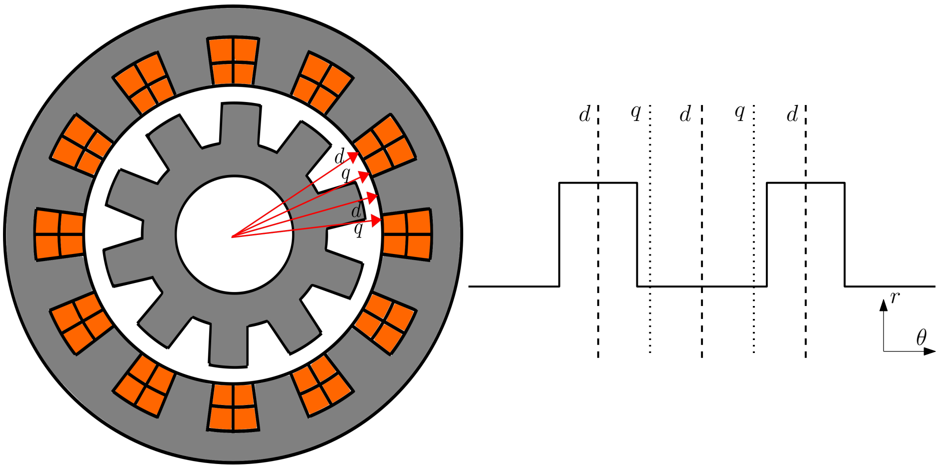

Figure 5.18: The dq-axes indicated for a 12/10 VFRM.

which are given as,

$$U_d = \omega_e L_q I_q, \tag{5.21}$$

$$U_q = \left(\hat{M}_{fph,1} i_f - L_d I_d\right) \omega_e, \tag{5.22}$$

$$\bar{T}_{em} = \frac{3}{2} P_r \left[\hat{M}_{fph,1} i_f I_q + (L_d - L_q) I_d I_q\right], \tag{5.23}$$

$$I_q = \hat{I}_{ac} \sin(\gamma), \tag{5.24}$$

$$I_d = \hat{I}_{ac} \cos(\gamma). \tag{5.25}$$

The voltage drop on the phase resistance is neglected in the equations. For the 48 V mild hybrid system explained in Chapter 6, the machine has to operate at a high speed with a relatively low source voltage, hence, the number of turns of the armature windings is small. This leads to a relatively small resistance value, as mentioned in section 7.4, and hence, the resistive voltage is low, and is ignored in the following analysis for speed extension capability.

5.3.2 Torque-speed characteristic

To reach a theoretical infinite speed, U_d/ω and U_q/ω should approach zero, this is satisfied when,

$$\frac{U_d}{\omega} \to 0 \Rightarrow I_q \to 0, \tag{5.26}$$

$$\frac{U_q}{\omega} \to 0 \Rightarrow \hat{M}_{f,ph1} i_f = L_d I_d. \tag{5.27}$$

This means,

$$\sin(\gamma) \to 0, \tag{5.28}$$

$$\hat{M}_{fph,turn} N_{ac} N_{dc} i_f = L_{d,turn} N_{ac}^2 I_d \approx L_{d,turn} N_{ac}^2 \hat{I}_{ac}, \tag{5.29}$$

where $\hat{M}_{fph,turn}$ and $L_{d,turn}$ are respectively the values of $\hat{M}_{fph,1}$ and L_d for a single turn, while N_{dc} and N_{ac} are respectively the number of turns for the field winding and armature windings. By rewriting equation (5.29), it is concluded that when,

$$\frac{\hat{\mathcal{F}}_{ac}}{\mathcal{F}_{dc}} = \frac{\hat{M}_{fph,turn}}{L_{d,turn}}, \tag{5.30}$$

the speed can approach infinity in theory, where $\hat{\mathcal{F}}_{ac}$ and $\mathcal{F}_{dc}$ are respectively the peak *mmf* of the armature current and *mmf* of the field current,

$$\hat{\mathcal{F}}_{ac} = N_{ac} \hat{I}_{ac}, \tag{5.31}$$

$$\mathcal{F}_{dc} = N_{dc} i_f. \tag{5.32}$$

Hence, the speed extension capability is strongly dependent on the current.

A factor, K_{fw}, is defined to describe such relationship [108],

$$K_{fw} = \frac{\hat{\mathcal{F}}_{ac}}{\mathcal{F}_{dc}} \frac{L_{d,turn}}{\hat{M}_{fph,turn}}. \tag{5.33}$$

Based on equation (5.30), if K_{fw} is unity, the field weakening capability is maximized. In PM machines, e.g., PM flux switching machines, the excitation field built by PMs can be significantly high while $L_{d,turn}$ is much more limited, the field weakening capability may be inferior since K_{fw} is much smaller than unity [56]. However, in VFRMs, the control freedom of both armature current and field current offers the freedom of tuning K_{fw}. In the following content, the influence of current on maximum continuous torque, base speed and field weakening capability is explained.

Maximum continuous torque

In the constant torque region of the working envelope, the relationship between the mean torque and mmf is derived by re-writing equation (5.23), which gives,

$$\begin{aligned} \bar{T}_{em} &= \frac{3}{2} P_r \hat{M}_{fph,1} i_f \hat{I}_{ac} = \frac{3}{2} P_r \left(\hat{M}_{fph,turn} N_{dc} N_{ac} \right) i_f \hat{I}_{ac} \\ &= \frac{3}{2} P_r \hat{M}_{fph,turn} \mathcal{F}_{dc} \hat{\mathcal{F}}_{ac}. \end{aligned} \tag{5.34}$$

To ensure equal thermal loading in all the windings, the maximum continuous RMS current densities, $J_{\max}$, are considered to be equal for the field and armature windings. As such, the values of $\hat{\mathcal{F}}_{ac}$ and $\mathcal{F}_{dc}$ are varied by assigning different slot areas for field and armature windings. Equation (5.34) is converted to,

$$\begin{aligned} \bar{T}_{em} &= \frac{3\sqrt{2}}{2} P_r \hat{M}_{fph,turn} J_{\max}^2 S_{dc} S_{ac} \\ &= \frac{3\sqrt{2}}{2} P_r \hat{M}_{fph,turn} J_{\max}^2 S_{dc} \left(\frac{S_{slot}}{2} - S_{dc} \right), \end{aligned} \tag{5.35}$$

where S_{dc}, S_{ac} and S_{slot} represent the areas of the dc coil bundle, ac coil bundle and a single slot, respectively. The maximum value of equation (5.35) is reached when $S_{dc} = S_{ac} = S_{slot}/4$, or in other words, $\hat{\mathcal{F}}_{ac} = \sqrt{2}\mathcal{F}_{dc}$. Such relationship is verified by the curve shown in Fig. 5.19(a).

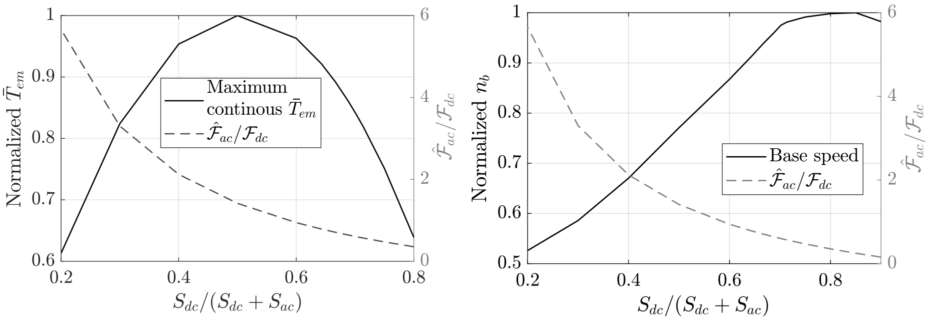

(a) (b)

Figure 5.19: (a) Dependence of the maximum continuous torque ($\bar{T}_{em}$) on the ratio between the mmfs of armature and field windings ($\hat{\mathcal{F}}_{ac}/\mathcal{F}_{dc}$), and (b) dependence of the base speed (n_b) on $\hat{\mathcal{F}}_{ac}/\mathcal{F}_{dc}$, ($S_{dc}$ and S_{ac} in the x-label are slot areas assigned for dc and ac coil bundles, respectively).

Base speed for continuous operation

The expression of the base speed in rpm is,

$$\begin{aligned} n_b =& \frac{U_s}{\sqrt{\left(\hat{M}_{fph,1} i_f\right)^2 + \left(L_q \hat{I}_{ac}\right)^2}} \frac{60}{2\pi P_r} \\ =& \frac{\frac{60 U_s}{2\pi P_r N_{ac} J_{\max} S_{slot}}}{\sqrt{\left(\hat{M}_{fph,turn} \frac{S_{dc}}{S_{slot}}\right)^2 + L_{q,turn}^2 \left(\frac{1}{2} - \frac{S_{dc}}{S_{slot}}\right)^2}}, \end{aligned} \tag{5.36}$$

where U_s is the dc source voltage level. The base speed reaches the maximum when the derivative of the denominator of equation (5.36) reaches zero, that is

$$\frac{S_{dc}}{S_{slot}} = \frac{L_{q,turn}^2}{2\hat{M}_{fph,turn}^2 + 2L_{q,turn}^2}. \tag{5.37}$$

Such relationship is verified by the given VFRM in Table 5.1. Using equation (5.36), the maximum n_b is reached when $S_{dc} = 0.84(S_{dc} + S_{ac})$ or in other word ($\hat{\mathcal{F}}_{ac} = 0.27\mathcal{F}_{ac}$), and it matches the 2D FEM result shown in Fig. 5.19(b).

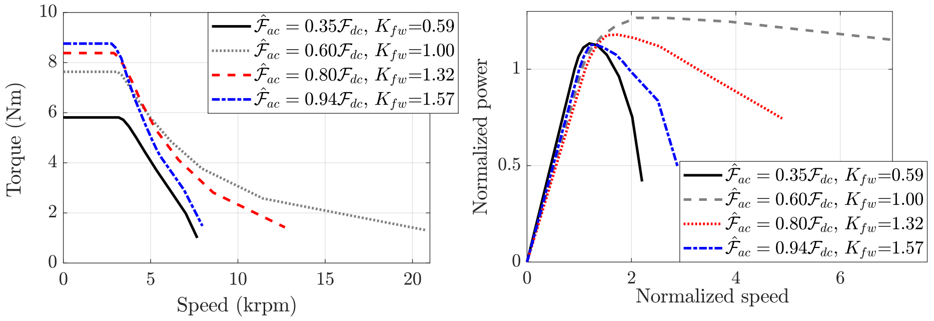

(a) (b)

Figure 5.20: (a) Dependence of the torque-speed curves on the mmfs of the field winding ($\mathcal{F}_{dc}$) and armature winding ($\hat{\mathcal{F}}_{ac}$), and (b) dependence of the normalized power-speed curves on $\mathcal{F}_{dc}$ and $\hat{\mathcal{F}}_{ac}$, (K_{fw} is the factor defined in equation (5.33)).

Torque-speed characteristics by varying commutation angle

The field weakening is realized by varying the commutation angle from 90° to 170° in this subsection, while the current densities of armature windings and field winding are fixed, i.e. at J_{max}. This means K_{fw} is kept fixed in the entire speed range. In Fig. 5.20, it shows the FEM results of torque-speed curves for different $\hat{\mathcal{F}}_{ac}/\mathcal{F}_{dc}$ and the corresponding normalized power-speed curves. The unit power value is specified as the multiple of the knee speed and knee torque for each situation, while the unit speed value is specified at the knee speed of the solid line in Fig. 5.20(a). As can be seen, for the situations when K_{fw} is far away from unity, the field weakening capability is very poor, e.g., when $K_{fw} = 0.59$, the power drops by 72% when the speed is less than twice extended. However, when K_{fw} is close to unity, the rotational speed is extended by at least 7 times with a power drop of 9%.

Expansion of torque-speed working envelope

In the above analysis, the factor K_{fw} is fixed for the entire speed range at the value of nominal working point. However, to meet the requirement of nominal torque or speed, the value of K_{fw} in a lot of circumstances is far from unity, e.g., the maximum continuous torque is reached when $\hat{\mathcal{F}}_{ac} = \sqrt{2}\mathcal{F}_{dc}$ such that $K_{fw} = 2.3$. Hence, merely varying commutation angle is not sufficient for speed extension.

In this case, the flexibility of controlling both armature current and field current in VFRMs provides the opportunity for adjusting K_{fw} such that the working envelope can be extended [9]. To show the effectiveness of tuning K_{fw} dynamically, two examples are given for $K_{fw} < 1$ and $K_{fw} > 1$ at the nominal working point. For better distinction in the following content, the value of K_{fw} at the nominal working point is denoted as $K_{fw,nom}$, while the adjusted K_{fw} is denoted as $K_{fw,adj}$.

For the situation that $K_{fw,nom}$ is smaller than unity, the field current should be reduced to tune K_{fw} in the speed extension region. An example is given for the situation of $\hat{\mathcal{F}}_{ac} = 0.35\mathcal{F}_{dc}$, $K_{fw,nom} = 0.59$. The current density of the field current is adjusted to be 0.59 times of the original value to make K_{fw} equal to unity. The torque-speed curves are presented in Fig. 5.21(a) for the current arrangements with $K_{fw,nom} = 0.59$ and adjusted $K_{fw,adj} = 1$ respectively. As it can be seen, the two curves intersect at a speed around 6 krpm.

To maximize the working envelope, for a speed smaller than 6 krpm, the currents are arranged to keep K_{fw} at $K_{fw,nom}$, while for a speed higher than 6 krpm, it is desired to tune K_{fw} to unity. The result for such current arrangement is shown in Fig. 5.21(e). Compared to the original normalized power shown as the solid line in Fig. 5.21(c), the power in Fig. 5.21(e) is significantly increased at high speed.

For the situation that $K_{fw,nom}$ is higher than unity, the armature current should be reduced to tune K_{fw}. As an example, the effect of tuning K_{fw} is analyzed for the situation of $\hat{\mathcal{F}}_{ac} = 0.94\mathcal{F}_{dc}$, $K_{fw,nom} = 1.57$. The torque-speed curves and normalized power-speed curves are presented in Figs. 5.21(b) and (d), respectively. The improved power-speed curve is shown in Figs. 5.21(f), where the working envelope is largely extended comparing to the original power-speed curve shown in Fig. 5.21(d).

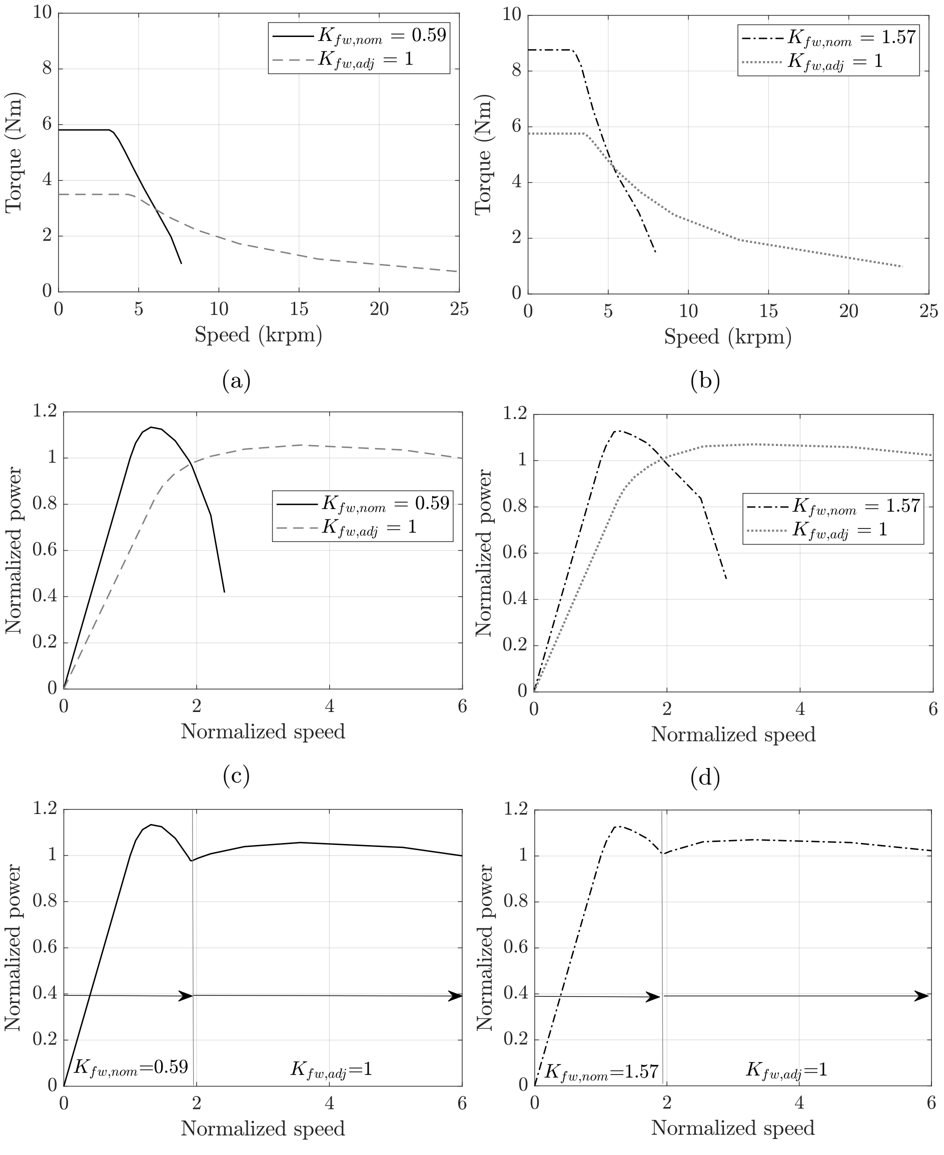

(a) (b)

(c) (d)

(e) (f)

Figure 5.21: (a) Torque-speed curves for $K_{fw,nom}$=0.59 and $K_{fw,adj}$=1, (b) torque-speed curves for $K_{fw,nom} = 1.57$ and $K_{fw,adj} = 1$, (c) normalized power-speed curves for $K_{fw,nom} = 0.59$ and $K_{fw,adj} = 1$, (d) normalized power-speed curves for $K_{fw,nom} = 0.59$ and $K_{fw,adj} = 1$, (e) normalized power-speed curve after improvement with $K_{fw,nom} = 0.59$, and (f) normalized power-speed curve after improvement with $K_{fw,nom} = 1.57$ ($K_{fw,nom}$ is the value of factor K_{fw} at the nominal working point, $K_{fw,adj}$ is the adjusted K_{fw} for speed extension).

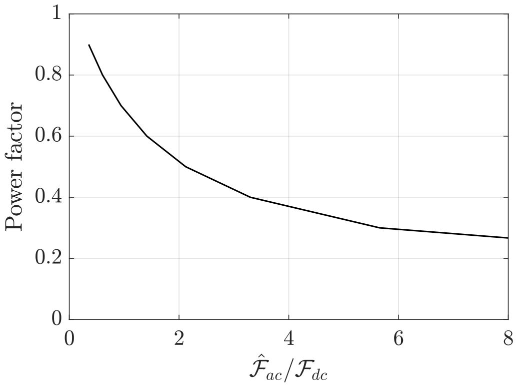

Figure 5.22: Dependence of the power factor on the ratio between the mmfs of armature and field windings ($\hat{\mathcal{F}}_{ac}/\mathcal{F}_{dc}$).

5.4 Power factor

The power factor (PF) of VFRMs is strongly influenced by the current arrangement. Based on equations (5.21)-(5.22), the power factor in the constant torque region is,

$$
\begin{aligned}
PF &= \frac{U_q}{\sqrt{U_q^2+U_d^2}} = \frac{\hat{M}_{fph,1} i_f \omega_e}{\omega_e \sqrt{\left(\hat{M}_{fph,1} i_f\right)^2 + \left(L_q I_q\right)^2}} \\
&= \frac{\hat{M}_{fph,turn} N_{dc} N_{ac} i_f}{\sqrt{\left(\hat{M}_{fph,turn} N_{dc} N_{ac} i_f\right)^2 + \left(L_{q,turn} N_{ac}^2 \hat{I}_{ac}\right)^2}} \\
&= \frac{\hat{M}_{fph,turn} N_{dc} i_f}{\sqrt{\left(\hat{M}_{fph,turn} N_{dc} i_f\right)^2 + \left(L_{q,turn} N_{ac} \hat{I}_{ac}\right)^2}} \\
&= \frac{\hat{M}_{fph,turn} \mathcal{F}_{dc}}{\sqrt{\left(\hat{M}_{fph,turn} \mathcal{F}_{dc}\right)^2 + \left(L_{q,turn} \widehat{\mathcal{F}}_{ac}\right)^2}} = \frac{\hat{M}_{fph,turn}}{\sqrt{\left(\hat{M}_{fph,turn}\right)^2 + \left(L_{q,turn} \frac{\widehat{\mathcal{F}}_{ac}}{\mathcal{F}_{dc}}\right)^2}}.
\end{aligned}
\tag{5.38}
$$

Hence, it is desired to have a smaller $\hat{\mathcal{F}}_{ac}/\mathcal{F}_{dc}$ to reach a higher power factor, and such relationship is shown in Fig. 5.22 for the VFRM with the dimensions listed in Table 5.1.

5.5 Scaling of outer dimensions

Giving the torque level of an existing design, the initial outer dimensions of a new design can be determined using a scaling law [112], which gives a rough prediction of torque with respect to the outer diameter and stack length. The result of the analysis in this section is used in Chapter 6 for initial sizing of a design.

The expression of the scaling law is written as,

$$\bar{T}_{em} \sim D_{so}^{n_1} L_{sk}^{n_2}, \tag{5.39}$$

where D_{so} is the stator outer diameter, n_1 and n_2 are the exponents of the outer diameter and stack length, respectively.

To derive the values of n_1 and n_2, the dimensions of the VFRM are radially scaled and axially scaled, respectively. Before starting the analysis, an assumption is made that the thermal condition keeps the same. Assuming the heat transfer mainly occurs on the outer surface area, the convective heat transfer is calculated as,

$$Q = h_c \pi D_{so} L_{sk} (T_{surf} - T_{amb}), \tag{5.40}$$

where h_c is the heat transfer coefficient, T_{surf} and T_{amb} are the machine surface temperature and coolant temperature, respectively. Using the expression in equation (3.31), the current density is derived as,

$$J = \sqrt{\frac{h_c \pi D_{so} L_{sk} (T_{surf} - T_{amb}) k_f}{V_{coil} \rho}}. \tag{5.41}$$

Assuming h_c, T_{surf}, T_{amb} and k_f are invariant, the relationship between the current density and the machine outer dimensions is written as,

$$J \sim \sqrt{\frac{D_{so} L_{sk}}{V_{coil}}}. \tag{5.42}$$

This gives the pre-condition for the following content. For ease of distinction, the parameters for the radial-scaled, axial-scaled and un-scaled VFRMs are written with the subscripts of r, a and u, respectively.

Radial scaling

The assumptions of radial scaling are:

- the rotor inner diameter, D_{ri}, stator inner and outer diameters, D_{si} and D_{so} are all scaled by a factor of $X_{sf,r}$;

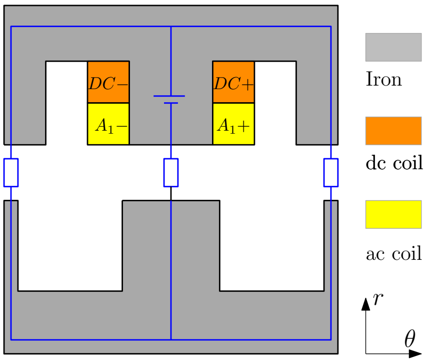

Figure 5.23: A simple MEC for part of the VFRM at the aligned position.

- the airgap length and tooth arcs remain fixed.

The coil volume under such conditions has the relationship of $V_{coil,r} = X_{sf,r}^2 V_{coil,u}$, hence, the current density is calculated as,

$$\frac{J_r}{J_u} = \sqrt{\frac{D_{so,r}}{D_{so,u}}} \cdot \sqrt{\frac{V_{coil,u}}{V_{coil,r}}} \cdot \sqrt{\frac{L_{sk,r}}{L_{sk,u}}} = \sqrt{X_{sf,r}} \cdot \sqrt{\frac{1}{X_{sf,r}^2}} \cdot 1 = \sqrt{\frac{1}{X_{sf,r}}}, \tag{5.43}$$

when the end windings are neglected.

For a non-saturated VFRM, based on equation (4.36), the torque is expressed as

$$\bar{T}_{em} = \frac{3}{2} P_r \hat{\Lambda}_{fph,1} \hat{I}_{ac} = \frac{3}{2} P_r \hat{\phi}_{fph,1} N_{ac} \hat{I}_{ac} = \frac{3}{2} P_r \hat{\phi}_{fph,1} \hat{J}_{ac} S_{ac}, \tag{5.44}$$

where S_{ac} is the area of the ac coil bundle. To investigate the relation of $\hat{\phi}_{f,ph1}$ with respect to outer dimensions, a simple MEC is drawn in Fig. 5.23 when the field winding is excited. The mmf of the dc coil in the figure is linear to the current density, J_{dc}, and the dc coil bundle area, S_{dc}. The permeances of the iron parts are neglected, and the permeance of the airgap is linear to the tooth arc length. Therefore, the flux has the following relation,

$$\hat{\phi}_{f,ph1} \text{ is proportional to } J_{dc} S_{dc} D_{si} \alpha_{si}, \tag{5.45}$$

where α_{si} is the angle of the stator tooth inner arc. With the definitions of radial scaling, the coil areas have the relation of,

$$\frac{S_{dc,r}}{S_{dc,u}} = X_{sf,r}^2. \tag{5.46}$$

Substituting equations (5.43) and (5.46) into equation (5.45) gives,

$$\frac{\hat{\phi}_{fph,1,r}}{\hat{\phi}_{fph,1,u}} = \frac{J_{dc,r}}{J_{dc,u}} \cdot \frac{S_{dc,r}}{S_{dc,u}} \cdot \frac{D_{si,r}}{D_{si,u}} = \sqrt{\frac{1}{X_{sf,r}}} \cdot X_{sf,r}^2 \cdot X_{sf,r} = X_{sf,r}^{2.5}. \tag{5.47}$$

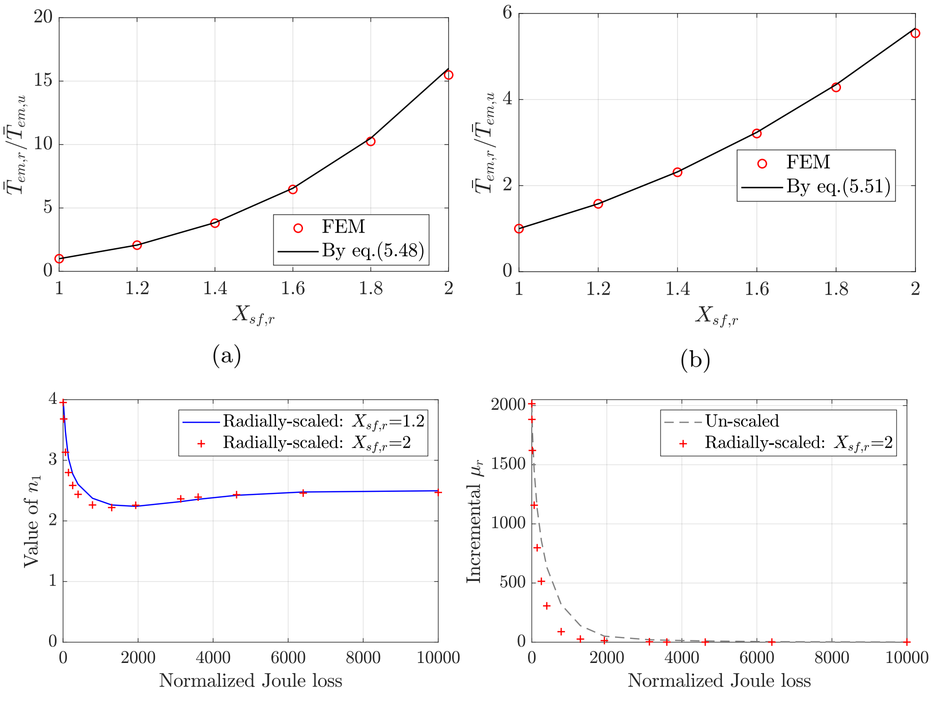

(a) (b)

(c) (d)

Figure 5.24: (a) The ratio of the mean torque with radial scaling ($\bar{T}_{em,r}$) to the mean torque without scaling ($T_{em,u}$) for a non-saturated VFRM ($X_{sf,r}$ is the radial scaling factor), (b) the ratio of $\bar{T}_{em,r}$ to $T_{em,u}$ for a saturated VFRM, (c) the variation of n_1 in equation (5.39) as the current density increases, and (d) the variation of incremental relative permeability in un-scaled and radially-scaled VFRMs.

Replacing $\hat{\phi}_{fph,1}$ in equation (5.44) with (5.47), it is deduced that,

$$\frac{\bar{T}_{em,r}}{\bar{T}_{em,u}} = \frac{\hat{\phi}_{f,ph1,r}}{\hat{\phi}_{f,ph1,u}} \cdot \frac{\hat{J}_{ac,r}}{\hat{J}_{ac,u}} \cdot \frac{S_{ac,r}}{S_{ac,u}} = X_{sf,r}^{2.5} \cdot \sqrt{\frac{1}{X_{sf,r}}} \cdot X_{sf,r}^{2} = X_{sf,r}^{4} \sim D_{so}^{4}, \quad (5.48)$$

suggesting that the torque production of the VFRM is proportional to D_{so}^4. This is verified by the curve shown in Fig. 5.24(a), which provides the relationship between torque and radial scaling factor. As can be seen, the result obtained by equation (5.48) matches with the FEM results.

In a saturated VFRM, the contribution of the iron permeance is not negligible and the MEC is much more complex than shown in Fig. 5.23, hence, the expression of $\hat{\phi}_{fph,1}$ is not derived by MEC. Assuming the relative permeability in the iron reaches unity and the flux density in the stator tooth reaches the saturation level, B_{sat}. The flux is expressed as,

$$\hat{\phi}_{fph,1} = \int_S BdS = B_{sat} D_{si} \cos\left(\frac{\alpha_{si}}{2}\right) L_{sk}. \tag{5.49}$$

Since D_{si} is linear to $X_{sf,r}$ and α_{si} remains constant, equation (5.49) leads to,

$$\hat{\phi}_{fph,1} \text{ is proportional to } X_{sf,r}. \tag{5.50}$$

Substituting equation (5.50) into (5.44) gives,

$$\frac{\bar{T}_{em,r}}{\bar{T}_{em,u}} = \frac{\hat{\phi}_{fph,1,r}}{\hat{\phi}_{fph,1,u}} \cdot \frac{\hat{J}_{ac,r}}{\hat{J}_{ac,u}} \cdot \frac{S_{ac,r}}{S_{ac,u}} = X_{sf,r} \cdot \sqrt{\frac{1}{X_{sf,r}}} \cdot X_{sf,r}^2 = X_{sf,r}^{2.5}, \tag{5.51}$$

meaning that the torque production is proportional to $D_{so}^{2.5}$. The curve of torque versus radial scaling factor shown in Fig. 5.24(b) verifies this relationship.

To further investigate the value of n_1 in addition to the above two situations, the current density is varied for VFRMs with two different radial scaling factors. The value of $\bar{T}_{em,r}/\bar{T}_{em,u}$ is calculated, and n_1 is derived as,

$$n_1 = \log_{X_{sf,r}} \left(\frac{\bar{T}_{em,r}}{\bar{T}_{em,u}}\right). \tag{5.52}$$

The variation of n_1 is drawn in Fig. 5.24(c). As presented, in both curves, n_1 starts from 4, gradually reduces due to the local saturation and finally reaches 2.5 when the incremental μ_r reaches unity in the flux path. It is worth mentioning that increasing the radius potentially increases the magnetic flux density in the VFRMs. Such phenomena is illustrated in Fig. 5.24(d), where the incremental relative permeability is compared for un-scaled and scaled VFRMs. As can be seen, the value of incremental μ_r becomes much smaller in a scaled-up VFRM at some certain range. This tends to decrease the value of $\bar{T}_{em,r}/\bar{T}_{em,u}$ and consequently, n_1 drops to a level less than 2.5 at this range.

Axial scaling

The definition of axial scaling is that the radial dimensions remain constant while the stack length is scaled by a factor of $X_{sf,a}$. Based on equation (5.42), the current density does not change, and the torque has the relation of,

$$\frac{\bar{T}_{em,r}}{\bar{T}_{em,u}} = X_{sf,a}. \tag{5.53}$$

This indicates that the torque is linear to the stack length.

For two VFRMs with the same volume but different outer diameters and stack lengths, the torque is compared as,

$$\begin{aligned}\frac{\bar{T}_{em2}}{\bar{T}_{em1}} &= \left(\frac{D_{so2}}{D_{so1}}\right)^{n_1}\left(\frac{L_{sk2}}{L_{sk1}}\right) = \left(\frac{D_{so2}}{D_{so1}}\right)^{n_1-2}\left(\frac{D_{so2}^2 L_{sk2}}{D_{so1}^2 L_{sk1}}\right)\\ &= \left(\frac{D_{so2}}{D_{so1}}\right)^{n_1-2}.\end{aligned} \tag{5.54}$$

According to Fig. 5.24(c), n_1 is larger than 2. Hence, $\bar{T}_{em2}/\bar{T}_{em1} > 1$ if $D_{so2} > D_{so1}$, and vice versa. It indicates that a wider VFRM is more preferred from the torque point of view. However, this conclusion does not take the influence of end windings into account.

5.6 Summary and conclusions

The high level of torque ripples is a disadvantage of VFRMs. In this chapter, three different reduction methods using rotor skewing, rotor teeth non-uniformity and harmonic injection in field or armature currents are analyzed individually. The effectiveness of these methods is verified in non-saturated and saturated machines. The analysis of torque ripple shows significant contributions from $T_{ff,6}$ and $T_{f,ph,6}$. For the methods of skewing and rotor teeth non-uniformity, the relationship between the torque ripple components strongly influences the selection of the skewing angle. In addition, saturation has a significant impact on the relationship between torque ripple reduction and skewing angle, while the average torque is almost not affected. Above all, the effectiveness of the rotor skewing with two rotor modules and the rotor teeth non-uniformity is similar, that the torque ripple is at least reduced by 50% with no more than 5% average torque reduction. Regarding armature current/field current harmonic injection, both of them are able to significantly reduce the torque ripple for a non-saturated machine, while for a saturated machine, the performance of field current harmonic injection is degraded. As such, harmonic injection into armature current is recommended, which is able to reduce 80% of the torque ripple in both non-saturated and saturated machines without reduction of the average torque.

The dependency of the torque-speed curves on the mangetomotive forces of dc current and ac current is analyzed. To maximize the constant power region, a unity K_{fw} is desired. For the situation with K_{fw} differs from unity, it is possible to adjust the field current or armature current to tune the value of K_{fw}. The effectiveness of such current adjustment is verified for two examples, and the result of 2D FEM shows that the speed is capable to be extended by 6 times the base speed in the constant power region. Furthermore, the dependency of the power factor on currents is also investigated. Generally, a lower ratio of ac current to dc current is beneficial for increasing the power factor.

The scaling laws including radial scaling and axial scaling are analyzed, which can give a prediction of torque with respect to the outer diameter and stack length. The result shows that the mean torque is more dependent on the diameter than the stack length for both non-saturated and saturated situations.

Chapter 6

Design for mild hybrid system

6.1 Introduction

The design and optimization of a 12/10 VFRM for 48 V mild hybrid system is elaborated in this chapter. Given the initial sizing, the optimization of the lamination geometry is performed using the coordinate descent method. The winding design is discussed explicitly considering the ac copper losses. Finally, the parameters of the prototype and the predicted performances are provided.

6.2 Machine requirements

The electric vehicles normally require a constant torque region at low speed for starting or climbing hill, and a constant power region for higher speed [62, 91, 92]. The torque-speed characteristic for the 48 V mild hybrid application is shown in Fig. 6.1. The continuous operating power is 5 kW with a maximum continuous torque of 16 Nm at 3000 rpm. The maximum speed should be extended to 18000 rpm. The transient overload peak torque and peak power is 45 Nm and 10 kW, and the duration time is 10 seconds. The power factor should be larger than 0.7 and the peak line current is limited to 500 A considering the drive constraints.

A compact design is required in automotive applications, the total dimension of the machine is considered to be within a length of 175 mm and a diameter of 165 mm. Subtracting the space occupied by the cooling jacket, housing, end windings, bearings, electronics, etc., the stack length is given for 87.5 mm and the outer diameter is 140 mm. The machine is assumed to work under water cooling with a coolant temperature of 65°C. The above design requirements are summarized in Table 6.1.

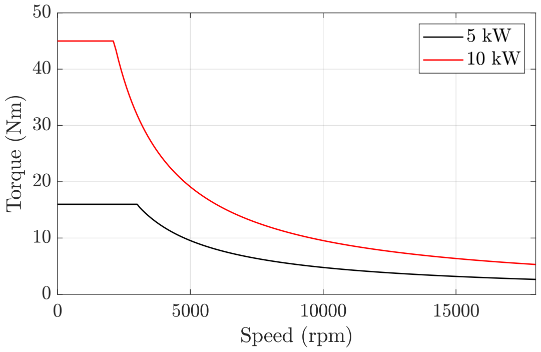

Figure 6.1: Torque-speed characteristic of the VFRM for automotive 48 V mild hybrid system.

Table 6.1: Machine requirements for automotive 48 V mild hybrid system.

Parameter	Description	value	Unit
P_{nom}	Continuous power	5	kW
P_{peak}	Peak power	10	kW
T_{nom}	Maximum continuous torque	16	Nm
T_{peak}	Peak torque	45	Nm
n_{nom}	Continuous speed at T_{nom} for 5 kW	3000	rpm
n_{max}	Maximum speed for 5 kW	18000	rpm
D_{so}	Stator outer diameter	140	mm
L_{sk}	Stack length	87.5	mm
T_{amb}	Coolant temperature	65	°C

6.3 Selection of the soft magnetic material

The selection of the soft magnetic material strongly influences the machine performance. The requirements of large peak torque and maximum speed as well as the desire of high efficiency require a lamination steel with a high saturation flux density and low iron losses. The characteristics of three electrical steel grades from Cogent, i.e., NO20, NO27 and NO30 [33], are shown in Fig. 6.2, respectively. These steels are designed to improve the performance of energy efficient applications by reducing iron losses to a minimum at high magnetization frequencies, which results in highly efficient solutions for applications such as high speed rotational motors and generators for hybrid and full electric vehicles [32]. The flux density provided by the datasheet is up to 1.8 T, where the relatively permeability is 20, 17 and 18 for the three steels, respectively. Electrical steel NO20 has higher μ_r in the *B*-*H* curve as shown in Fig. 6.2(a) and less iron loss density at higher frequency as shown in Fig. 6.2(c), however, due to its higher price, it is not considered for the design. Moreover, taking into account that NO27 has less iron loss density compared to NO30 as shown in Fig. 6.2(b) and Fig. 6.2(c), it is the final choice for the machine. The *B*-*H* curve of NO27 is extended until $\mu_r = 1$ by using the curve fitting tool in software Altair Flux2D, and the final *B*-*H* curve is shown in Fig. 6.2(d).

6.4 Initial sizing

6.4.1 Outer dimensions

In section 5.5, the scaling laws are given for the relation between the torque and stator outer dimensions. The equations are used to verify the feasibility of using a 12/10 VFRM to reach the peak torque requirement.

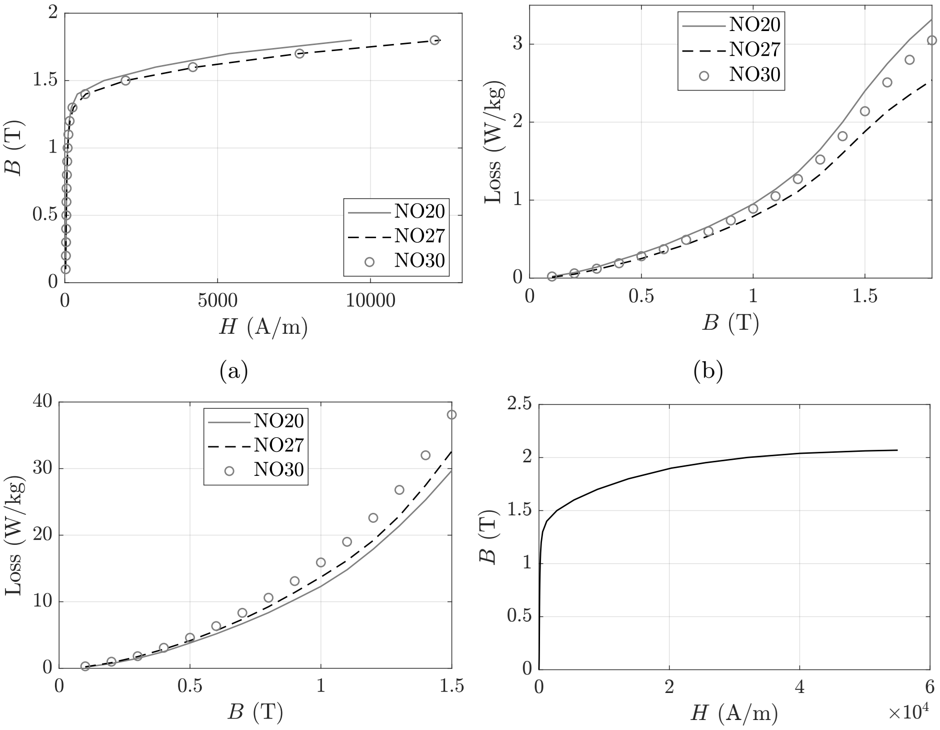

(a) (b)

(c) (d)

Figure 6.2: Comparison of Cogent electrical steel grades NO20, NO27 and NO30: (a) *B*-*H* curves in datasheet, (b) iron loss density at 50 Hz in datasheet, (c) iron loss density at 400 Hz in datasheet, and (d) extended *B*-*H* curve of NO27 up to $\mu_r = 1$.

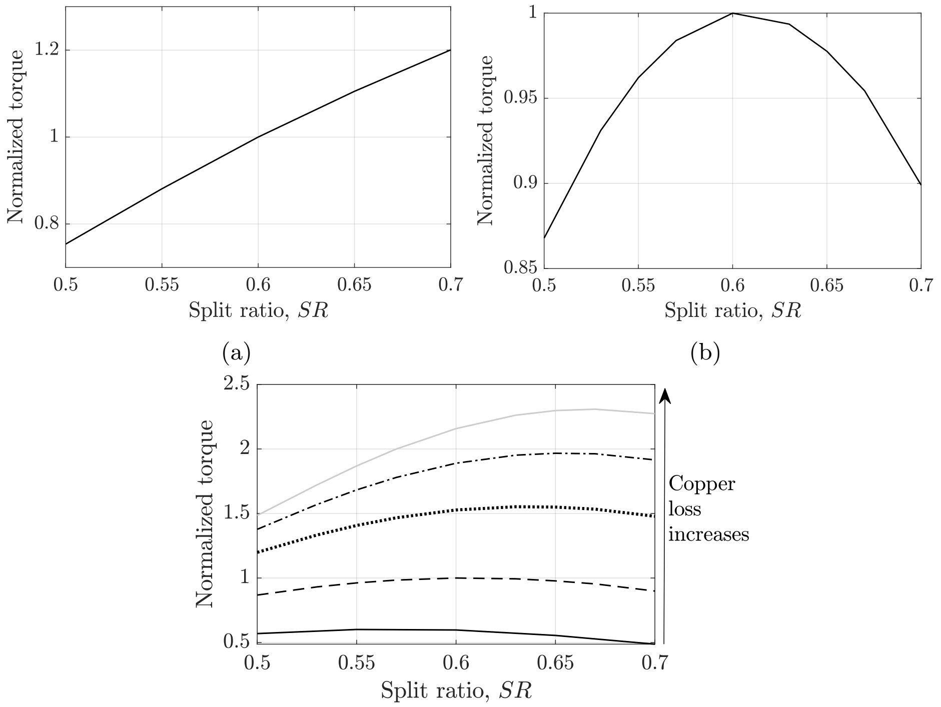

(a)

(b)

(c)

Figure 6.3: (a) The relationship between the mean torque and split ratio with the same mmf (normalized torque is defined at split ratio = 0.6), (b) the relationship between the torque and split ratio with the same copper loss, and (c) the relationship between the torque and split ratio as the copper loss increases.

It has been reported a 12/10 VFRM designed for EV traction applications in [78, 131]. The machine is able to reach a peak torque of 150 Nm with an outer diameter of 265 mm and a stack length of 50.8 mm. It means that for a VFRM with the outer dimensions listed in Table 6.1 (D_{so} = 140 mm and L_{sk} =87.5 mm), it can reach 52 Nm based on equations (5.51) and (5.53), which exceeds the limit of 45 Nm. Although the cooling capability and thermal condition are not provided in the literature, it still verifies the feasibility to some extent.

6.4.2 Split ratio

The analysis of split ratio (SR), which is defined as the ratio of rotor outer radius to stator outer radius, determines the initial rotor outer diameter, D_{ro}. A higher split ratio means a larger airgap area, hence, with the same mmf, the torque increases with the split ratio as can be seen in Fig. 6.3(a). On the other hand, the coil area varies as split ratio changes, and based on equation (5.42), the mmf

should be,

$$\mathcal{F} = JS_{coil} \sim \sqrt{\frac{D_{so}L_{sk}}{V_{coil}}} S_{coil} = \sqrt{D_{so}S_{coil}}, \tag{6.1}$$

to keep the same copper loss. Hence, if the split ratio increases, S_{coil} decreases, and mmf decreases accordingly.

The influence from both the airgap area and mmf leads to a relationship between the torque and split ratio shown in Fig. 6.3(b). With the increase of split ratio, the torque increases first since the airgap area plays a more important role, hereafter, the torque decreases since the influence of mmf becomes more dominant.

Additionally, saturation influences the relationship between torque and split ratio as well. As shown in Fig. 6.3(c), the optimum split ratio gradually increases as the saturation level increases. This is because a higher split ratio helps to decrease the flux density due to the smaller mmf and larger tooth width. Hence, for a high peak torque level, a relatively high split ratio is suggested for initial sizing. The split ratio taken in [78] is 0.68. Considering the fact that the reachable torque is 52 Nm by scaling this design, which is slightly higher than the required 45 Nm peak torque, the initial split ratio for the prototype design is set to be 0.65.

6.4.3 Stator and rotor tooth widths

The straight tooth shape is used for initial sizing, where the two side lines of the tooth are in parallel. As analyzed in section 4.4, when the rotor tooth outer arc, α_{ro}, and the stator tooth inner arc, α_{si}, are close to half of the slot pitch, the highest amplitude of coil flux linkage is reached. Simultaneously, based on equation (6.1), the stator tooth arc affects the slot area and furthermore the mmf. Considering these factors, the relationship between torque and tooth arcs is illustrated in Fig. 6.4. The maximum normalized torque is reached within the middle circle, hence, the initial size of the tooth arcs is selected within this region.

6.5 Optimization

6.5.1 Objective

The optimization goal is to maximize the efficiency at the maximum continuous torque, T_{nom}, with the speed of n_{nom} listed in Table 6.1. The efficiency, η_{nom}, is expressed as,

$$\eta_{nom} = \frac{T_{nom}\omega_{nom}}{T_{nom}\omega_{nom} + P_{cu} + P_{Fe}}, \tag{6.2}$$

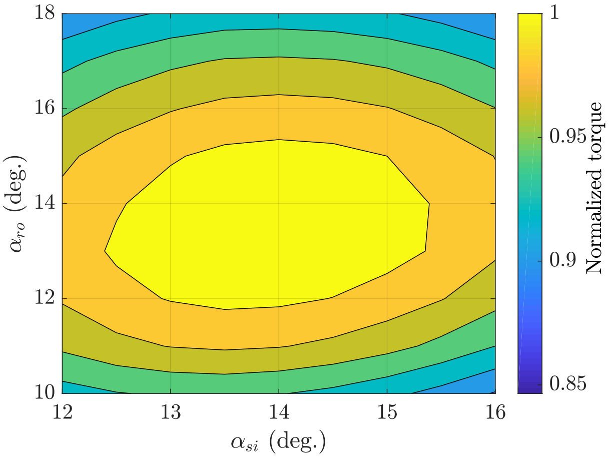

Figure 6.4: The relationship among the normalized mean torque ($\bar{T}_{em}$), stator tooth inner arc (α_{si}), and rotor tooth outer arc (α_{ro}).

where ω_{nom} is the speed in rad/s at n_{nom}, P_{cu} is the copper loss, P_{Fe} is the iron loss, and mechanical losses are not included.

6.5.2 Algorithm

For the optimization of lamination geometry, coordinate descent method is performed, which successively minimizes the objective along coordinate directions to find the minimum of a function. At each iteration, the algorithm determines a coordinate via minimizing the cost function, while other coordinates are fixed [126].

The cost function in this optimization is defined as maximizing the value of η_{nom}, or in other words, minimizing the losses, $(P_{cu} + P_{Fe})$. The coordinate vectors are the parameters involved in the optimization, i.e., split ratio (SR), ratio between the mmfs of armature and field windings ($\hat{\mathcal{F}}_{ac}/\mathcal{F}_{dc}$), stator yoke height ($h_{sy}$), rotor yoke height ($h_{ry}$), stator tooth inner arc (α_{si}), rotor tooth inner arc (α_{ri}) and rotor tooth outer arc (α_{ro}). The flowchart of the optimization procedure is shown in Fig. 6.5.

The sequence of the coordinate vectors is determined by a sensitivity analysis shown in Fig. 6.6, which presents the change of torque level versus dimensions. The analysis is performed with a constant copper loss. This is because the calculation shows that the copper loss is much more dominant than the iron loss at the maximum continuous torque, and if the influence of iron loss is disregarded, the torque calculation under a certain copper loss directly gives an indication on the efficiency based on equation (6.2).

As can be seen in Fig. 6.6, the torque is most sensitive to the split ratio, and is

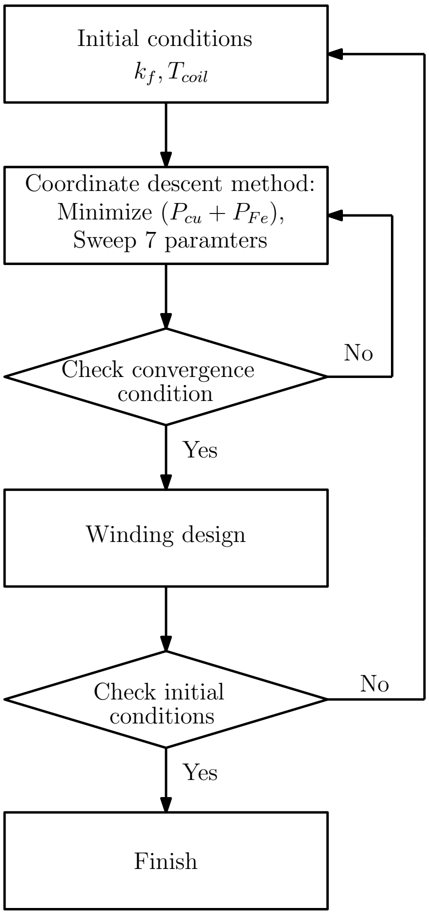
Initial conditions
k_f, T_{coil}
Coordinate descent method:
Minimize $(P_{cu} + P_{Fe})$,
Sweep 7 paramters
Check convergence condition
No
Yes
Winding design
Check initial conditions
No
Yes
Finish

Figure 6.5: Optimization flowchart.

more sensitive to $\hat{\mathcal{F}}_{ac}/\mathcal{F}_{dc}$, stator tooth inner arc, rotor tooth outer arc and stator yoke height than to the rotor tooth inner arc and rotor yoke height. The reason is that the rotor tooth inner arc and rotor yoke height only influence part of the flux tube, while other parameters directly affect the teeth alignment area, mmf sources or both of them. Consequently, the sequence of the coordinate vectors is chosen to start with the split ratio, followed by $\hat{\mathcal{F}}_{ac}/\mathcal{F}_{dc}$, α_{si}, α_{ro}, h_{sy}, and finally α_{ri} and h_{ry}. As such, the variable vector of the optimization problem is,

$$\mathbf{x} = [SR\ \hat{\mathcal{F}}_{ac}/\mathcal{F}_{dc}\ \alpha_{si}\ \alpha_{ro}\ h_{sy}\ \alpha_{ri}\ h_{ry}]. \tag{6.3}$$

The objective and constraints of the coordinate descent method is expressed as,

$$\begin{aligned}
&\min(P_{cu} + P_{Fe})\\
&\text{subject to}\\
&g_1(\mathbf{x}) = \bar{T}_{em} - T_{nom} = 0,\\
&g_2(\mathbf{x}) = T_{peak} - \bar{T}_{em,p} \leq 0,\\
&g_3(\mathbf{x}) = D_{so} - 70 = 0,\\
&g_4(\mathbf{x}) = L_{sk} - 87.5 = 0,\\
&g_5(\mathbf{x}) = SR \cdot D_{so} + g + h_{sy} - D_{so} < 0,\\
&g_6(\mathbf{x}) = D_{sh} + h_{ry} - SR \cdot D_{so} < 0,\\
&g_7(\mathbf{x}) = \alpha_{si} < 30^\circ,\\
&g_8(\mathbf{x}) = \alpha_{ro} < 36^\circ,\\
&g_9(\mathbf{x}) = \alpha_{ri} < 36^\circ,\\
&g_{10}(\mathbf{x}) = cos(\phi) - 0.7 \leq 0,\\
&g_{11}(\mathbf{x}) = V_{f,max} - 48 \leq 0,\\
&g_{12}(\mathbf{x}) = V_{ph,max} - 48 \leq 0,
\end{aligned} \tag{6.4}$$

where $\bar{T}_{em,p}$ is the achievable peak torque, D_{sh} is the shaft diameter provided by the manufacturer, $V_{ph,max}$ is the maximum phase voltage and $V_{f,max}$ is the maximum field winding voltage which should both not exceed the specified dc bus voltage.

After the coordinate descent method is performed for the seven parameters in the variable vector for one cycle, the cost function is reduced. However, since parameters interact with each other, this cycle has to be iterated until the convergence is obtained within a certain level, e.g., 0.2%.

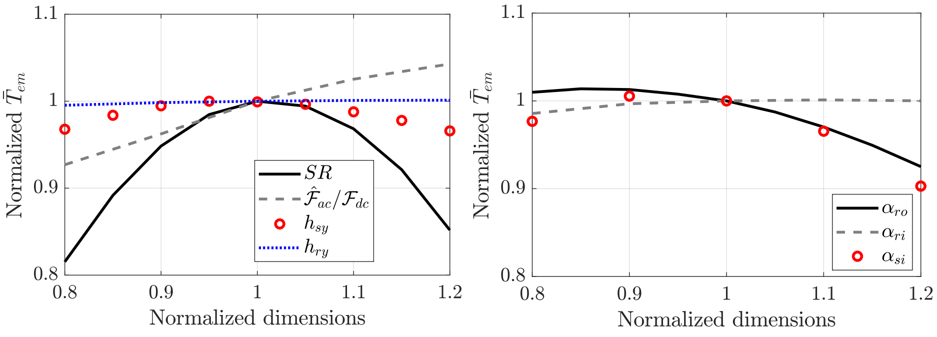

(a) (b)

Figure 6.6: Sensitivity analysis: relationship between the normalized torque ($\bar{T}_{em}$) and normalized dimensions for (a) split ratio (SR), ratio between the mmfs of armature and field windings ($\hat{\mathcal{F}}_{ac}/\mathcal{F}_{dc}$), stator yoke height ($h_{sy}$) and rotor yoke height (h_{ry}), and (b) rotor tooth outer arc (α_{ro}), rotor tooth inner arc (α_{ri}) and stator tooth inner arc (α_{si}).

6.5.3 Stator geometry adjustment

As the copper loss is significantly higher than the iron loss at the working point of 16 Nm 3000 rpm, the filling factor is crucial for the efficiency. Therefore, rectangular wires are recommended since normally a higher filling factor can be achieved compared to using round wires. The stator geometry, accordingly, is adjusted as shown in Fig. 6.7(a). Compared to the conventional geometry shown in Fig. 6.7(b), it is beneficial for improving the filling factor without torque reduction. To explain this, the torque comparison of these two stator geometries is presented in Fig. 6.8(a). As can be seen, the torque of the adjusted geometry is the same as the conventional geometry at $h_{sy} = 1.13h_{sy,c}$. At the moment, the slot areas of the two geometries are almost the same as shown in Fig. 6.8(b). However, for the adjusted stator that has a straight line instead of an arc in the conventional stator, the actual available space for the coil is larger. Moreover, it is beneficial for the heat conduction since the coil can be directly attached to the yoke without a gap in between.

6.5.4 3D effect

To obtain the copper losses, assumptions are required for the coil temperature and filling factor at the beginning of the algorithm, as indicated in the first step in Fig. 6.5. The initial assumption of filling factor is validated after the winding design is performed, and the coil temperature at the continuous working mode is validated by a 2D static thermal FEM.

The end-effect is estimated by an increase in the resistance/copper loss by the

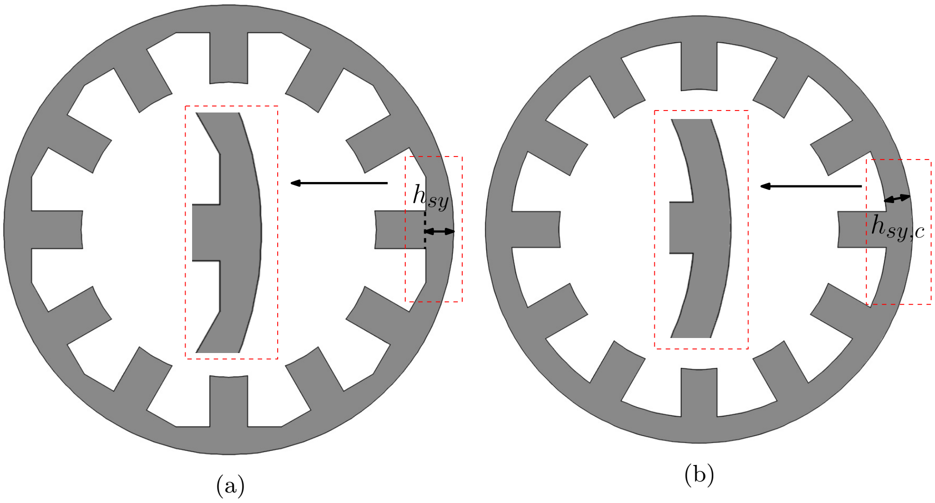

(a) (b)

Figure 6.7: The geometries of (a) the adjusted stator with a yoke height of h_{sy}, and (b) the conventional stator with a yoke height of $h_{sy,c}$.

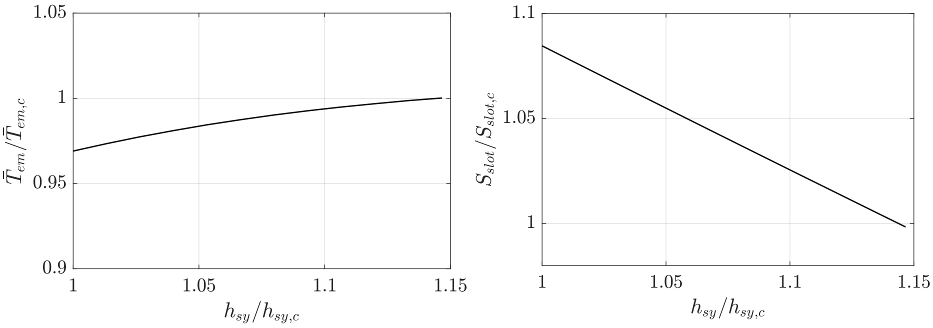

(a) (b)

Figure 6.8: Comparison of the adjusted stator geometry shown in Fig. 6.7(a) with the conventional stator geometry shown in Fig. 6.7(b): (a) the ratio of the mean torques between the adjusted stator ($\bar{T}_{em}$) and the conventional stator ($\bar{T}_{em,c}$), and (b) the ratio of the slot areas between the adjusted stator (S_{slot}) and the conventional stator ($S_{slot,c}$), (conventional stator yoke height $h_{sy,c} = 7.5$ mm, and $\bar{T}_{em,c} = 16$ Nm).

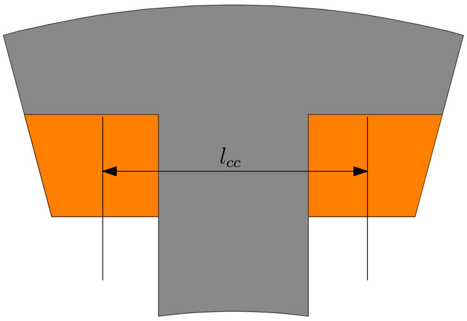

Figure 6.9: Illustration of l_{cc} in equation (6.5), the distance between the center of two coil bundles, for end winding calculation.

expression,

$$\frac{P_{cu,end}}{P_{cu,0}} = \frac{r_{end}}{r_0} = \frac{\pi l_{cc} + 2L_{sk} + l_z}{2L_{sk}}, \tag{6.5}$$

where $P_{cu,end}$, $P_{cu,0}$, r_{end} and r_0 are the copper losses and resistances with and without end-effect, respectively, l_{cc} is the distance between the center of two coil bundles as shown in Fig. 6.9, and l_z represents a small additional spacing in the axial direction.

On the other hand, considering the 3D effect ratio and stacking factor, the required peak torque in the optimization, T_{peak} in inequality constraint (6.4), is set to be 49 Nm, which is higher than the required 45 Nm. The 3D effect ratio is defined as the ratio of the torque obtained by 3D FEM to the torque obtained by 2D FEM, and is estimated to be 95% at the peak torque based on a comparison between 2D and 3D FEM results of the VFRM.

With the initial assumptions of $k_f = 0.6$ and $T_{coil} = 150°\text{C}$, the obtained dimensions after the optimization are listed in Table 6.2, together with the magnetomotive forces for respectively the maximum continuous torque and peak torque, which is a decisive factor for the winding design discussed in section 6.6.

Table 6.2: Machine dimensions and mmf after optimization.

Symbol	Description	Value	Unit
D_{so}	Outer diameter	140	mm
L_{sk}	Stack length	87.5	mm
SR	Rotor outer radius/stator inner radius	0.65	-
α_{si}	Stator tooth inner arc	15.5	deg.
α_{ro}	Rotor tooth outer arc	11.5	deg.
α_{ri}	Rotor tooth inner arc	27	deg.
h_{sy}	Stator yoke height	8.6	mm
h_{ry}	Rotor yoke height	20.5	mm
$\mathcal{F}_{dc,nom}$	mmf of dc coil at T_{nom}	598	A· turns
$\hat{\mathcal{F}}_{ac,nom}$	Peak mmf of ac coil at T_{nom}	507	A· turns
$\mathcal{F}_{dc,peak}$	mmf of dc coil at T_{peak}	1550	A· turns
$\hat{\mathcal{F}}_{ac,peak}$	Peak mmf of ac coil at T_{peak}	1426	A· turns

6.6 Winding design

The winding design aims for maximizing the filling factor, simplifying manufacturing and achieving low ac copper losses. In this section, the selection of number of turns, coil connection topology, winding method and wire dimensions are discussed.

6.6.1 Coil connections

The number of turns is related to the voltage per turn and coil connection topology. There are several ways to connect the ac coils, i.e., in series or in parallel, star-connected or delta-connected. Four connection topologies are shown in Fig. 6.10. Based on section 4.3, the even harmonics of coil A_1 and coil A_2 are out of phase in the 12/10 VFRM, such that these two coils should always be connected in series to obtain a more sinusoidal back-emf. The maximum voltage for the sum of coil A_1 and coil A_2 is 4.8 V/turn at the working point of 16 Nm 3000 rpm. With the limitation of bus voltage, the number of turns for each connection topology is calculated using,

$$N_{ac} = \left\lfloor \frac{48}{V_{ph,\max}} \right\rfloor, \quad \text{delta connection,} \tag{6.6}$$

$$N_{ac} = \left\lfloor \frac{48}{V_{ph,\max} \times \sqrt{3}} \right\rfloor, \quad \text{star connection,} \tag{6.7}$$

and the results are list in Table 6.3.

As the peak line current is constrained to 500 A, the allowed mmf per ac coil is limited, which is 1443 A·turns for topologies (a) and (b), and is only 1000 A·turns

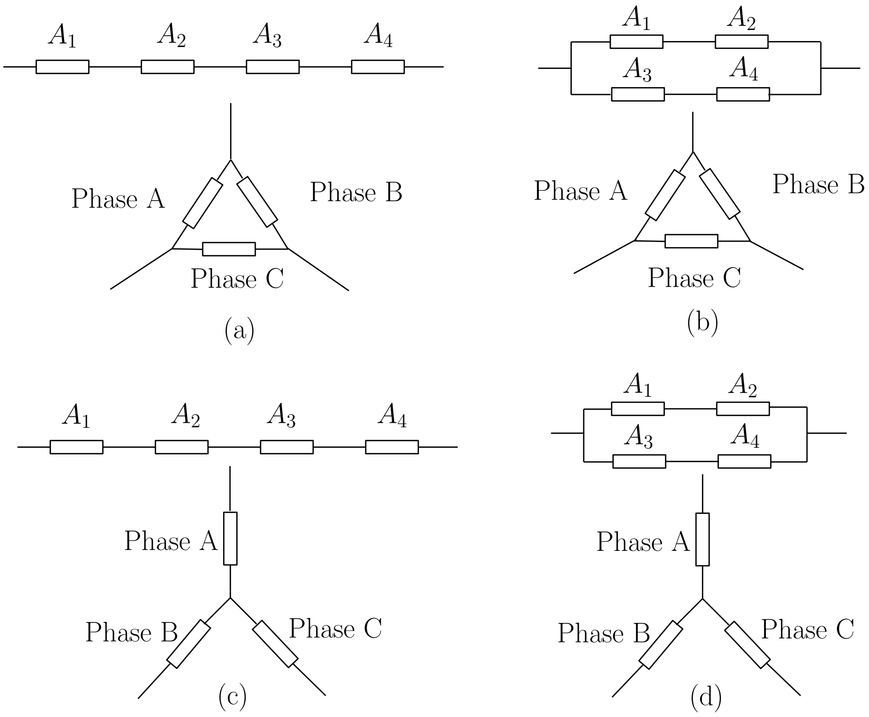

Figure 6.10: The connection topologies for ac coils: (a) delta connection with coils connected in series, (b) delta connection with coils connected in parallel, (c) star connection with coils connected in series, and (d) star connection with coils connected in parallel.

Table 6.3: Number of turns per phase coil.

Connection topology	Number of turns
(a) delta/in series	5
(b) delta/in parallel	10
(c) star/in series	2
(d) stat/in parallel	5

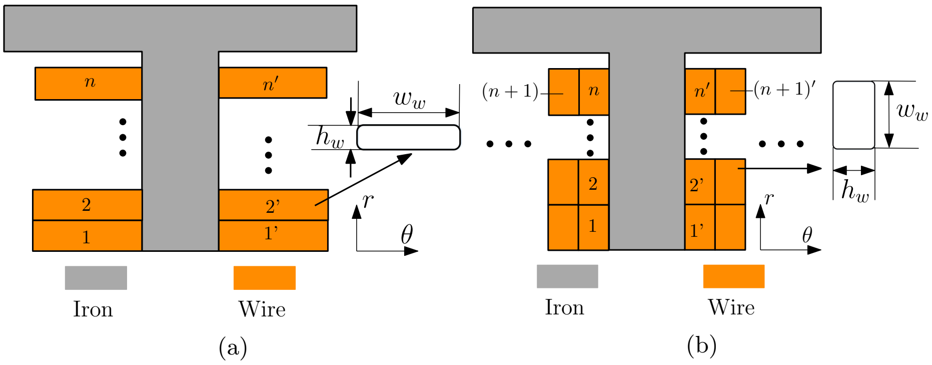

Figure 6.11: (a) Sketch of an edge-wound coil, and (b) sketch of a helical-wound coil (h_w and w_w are respectively the width and height of the wire).

and 1250 A·turns for topologies (c) and (d). As a consequence, the mmf of the latter two topologies is smaller than the value of $\hat{\mathcal{F}}_{ac,peak}$ listed in Table 6.2, hence, are not able to fulfill the peak torque requirement and are not selected.

Similarly, the limit of number of turns per dc coil is respectively 20 by connecting all dc coils in series and is 40 by paralleling two branches. The final number of turns are determined by the wire dimensions, the placement of conductors, etc., which will be explained in the next section.

6.6.2 Coil design

For simplicity of prototyping, same wire dimensions are used for the ac coils and dc coils. Two winding methods are considered, i.e., edge-wound coil and helical-wound coil, for which the sketches are shown in Fig. 6.11. The wires are wound neatly next to each other. For the edge-wound coil, the coil is wound on the edge, while the helical-wound coil is wound on the flat side which allows paralleling placement, e.g., in Fig. 6.11(b), the $(n+1)^{th}$ turn is wound continuously next to the n^{th} turn.

The choice of wire dimension, number of turns, filling factor and wiring layout are provided for the two methods, as shown in Table 6.4 and Fig. 6.12. The ac copper losses at 3000 rpm and 18000 rpm are calculated by 2D transient FEM.

In both winding methods, the ac coils are more affected by the ac effect compared to the dc coils as can be seen in Table 6.5, since they are located closer to the slot opening where the leakage flux varies more significantly. On the other hand, the helical-wound coil is less influenced by the proximity effect, and the induced eddy current is lower than the edge-wound coil. A comparison of the current density distribution between the two winding methods are presented in Fig. 6.13 for 3000 rpm and 18000 rpm, respectively, where the maximum current density in the helical-wound coil is lower at both speeds. Such effect can also be seen in

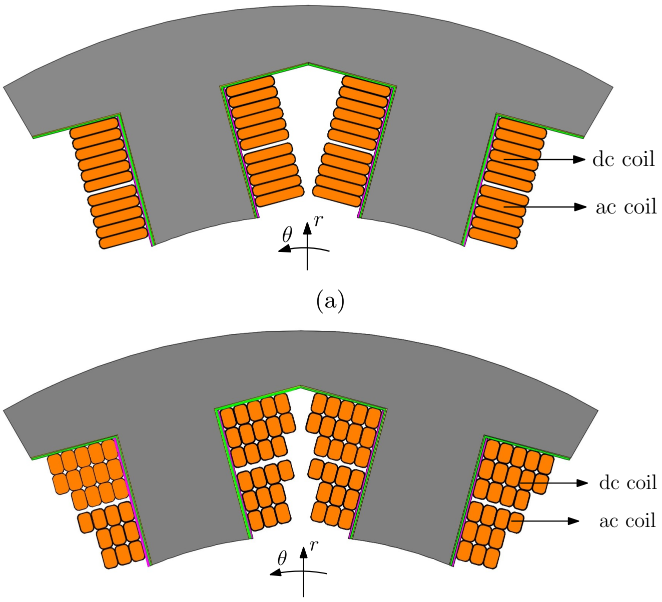

(a)

(b)

Figure 6.12: Schematic graph of (a) edge-wound coils with $N_{ac} = 5$ and $N_{dc} = 6$, and (b) helical-wound coils with $N_{ac} = 10$ and $N_{dc} = 14$ (N_{ac} and N_{dc} are the numbers of turns per ac and dc coils, respectively).

Table 6.4: Information of the edge-wound coil and helical-wound coil in the design.

	Description	Edge-wound	Helical-wound
N_{ac}	Number of turns per ac coil	5	10
N_{dc}	Number of turns per dc coil	6	14
h_w (mm)	Height of wire	1.25	1.5
w_w (mm)	Width of wire	5.6	2.24
$^*S_w$ (mm^2)	Cross section of wire	6.785	3.145
k_f	filling factor	0.57	0.58

Notes: * Nominal cross-section area listed in international standard CEI IEC 60317-0-2.

Table 6.5: The ratio of copper losses considering ac effect to the copper losses without considering ac effect.

		Nominal (W) 16 Nm @ 3 krpm	Max. speed (W) 2.7 Nm @ 18 krpm
Edge-wound	ac coil	109.8%	292.3%
	dc coil	100.2%	101.1%
Helical-wound	ac coil	104.9%	262.4%
	dc coil	100.1%	101.2%

Table 6.6: The ac copper loss of a single ac/dc coil by using different winding methods (T_{coil} = 150°C).

		Nominal (W) 16 Nm @ 3 krpm	Max. speed (W) 2.7 Nm @ 18 krpm
Edge-wound	ac coil	25.6 W	50.1 W
	dc coil	54.6 W	55.1 W
	total	80.2 W	105.2 W
Helical-wound	ac coil	26.4 W	48.5 W
	dc coil	50.4 W	51.0 W
	total	76.8 W	99.5 W

Table 6.5, where the helical-wound coils have lower ratios of copper losses between considering and not considering ac effect. Hence, the ac copper loss is lower in the helical-wound coil as listed in Table 6.6. As a result, the winding design shown in Fig. 6.12(b) that is with the helical-wound coil, is selected, and a filling factor of 0.58 is reached, which is close to the initial assumption (k_f=0.6) given for the lamination geometry optimization in section 6.5.

A static thermal analysis is performed in 2D FEM, assuming 0.2 mm slot liners, 0.1 mm glue (between slot liner and lamination), Grade 1 wire insulation, and epoxy filled in the slot, respectively with the thermal conductivity of 0.3 W/mK, 0.2 W/mK, 0.1 W/mK and 1 W/mK. The obtained ac copper losses are set to be evenly distributed in the wires. A convective heat transfer coefficient of 1000 W/Km^2 is set at the machine outer surface to account for the water cooling. The analysis shows that the maximum temperature of the dc coils and ac coils are 148°C and 151°C, respectively, with the losses estimated for the working point of 16 Nm 3000 rpm. This is within the temperature limit of F or H NEMA insulation class. Additionally, the transient thermal analysis shows a temperature rise from 65°C (coolant temperature) up to 141°C and 156°C for the dc and ac coils, respectively, after 10 seconds of operating at the peak torque.

With the above lamination geometry and winding design, the obtained efficiency is 83% at 16 Nm 3000 rpm. The efficiency map is presented in Fig. 6.14 assuming 150°C wire temperature, where the maximum efficiency of 90% is reached around 1 Nm 12000 rpm. The efficiency is relatively high at the low torque level and the field weakening region, since both the field current and armature current are

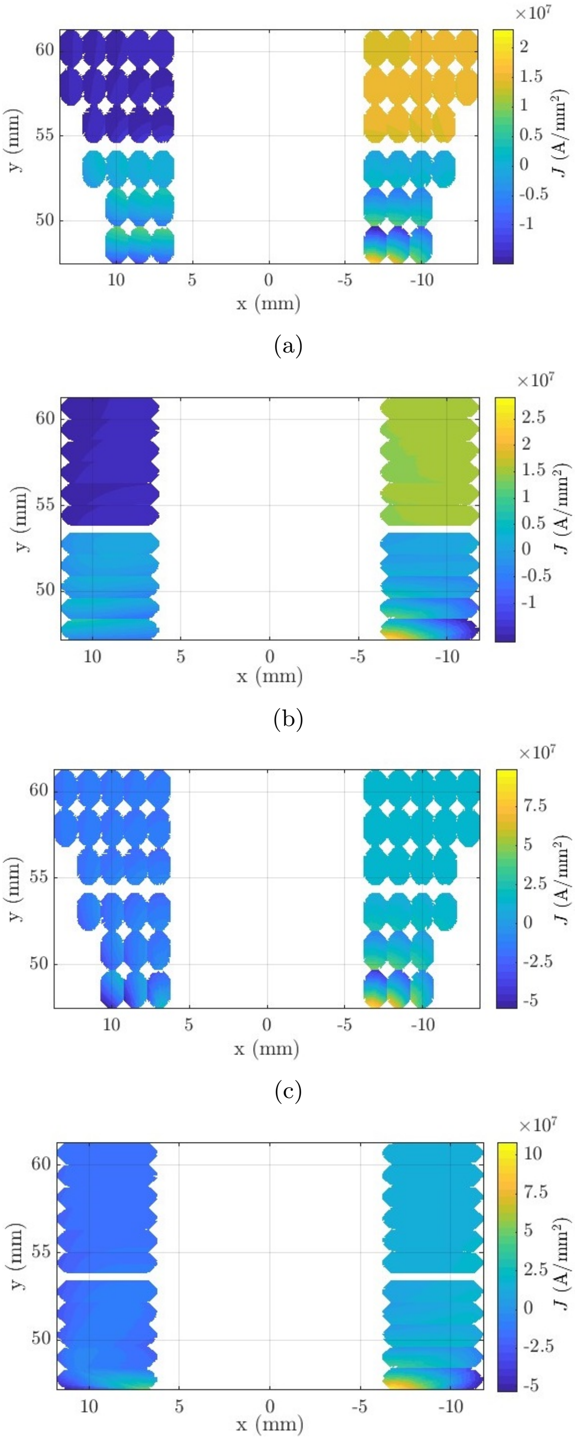

(a)

(b)

(c)

(d)

Figure 6.13: Current density distribution of (a) helical-wound coils at 3 krpm, (b) edge-wound coils at 3 krpm, (c) helical-wound coils at 18 krpm, and (d) edge-wound coils at 18 krpm.

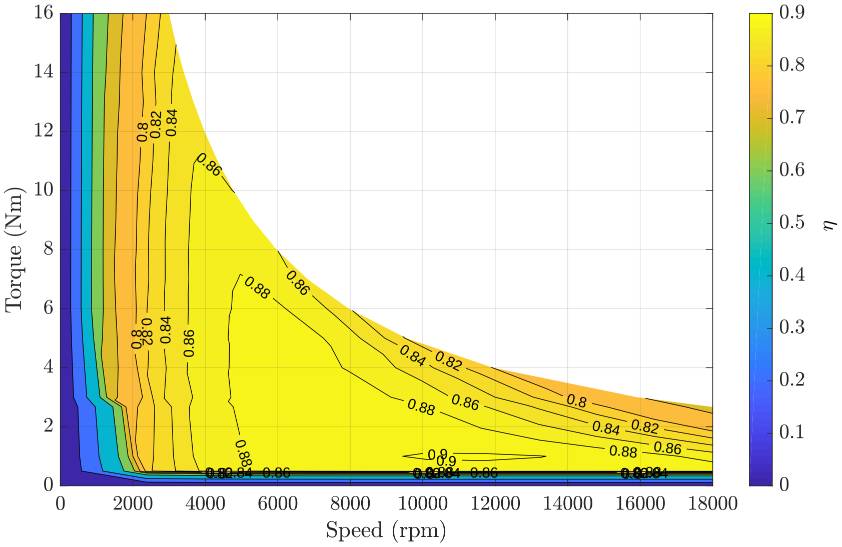

Figure 6.14: The efficiency map.

controllable. The efficiency drops at higher torque level, since the torque/current ratio decreases due to the saturation.

The mechanical losses are not included in the efficiency calculation as mentioned in section 6.5. To make a rough prediction, the windage loss is estimated using the empirical equation in [27], which is derived for an SRM that also has a salient rotor structure similar to the VFRM. With a rotor diameter of 75 mm and an airgap length of 0.3 mm, the windage loss is estimated to be around 20 W at 18000 rpm. Although the parameters and dimensions are not the same in the designed VFRM, it still gives an indication about the magnitude of the losses. However, due to the rotor saliency, the air flows inside the machine is complex, and detailed analysis is not discussed in this thesis.

6.6.3 Integrated-coil topology

The field winding and armature winding are separated in the previous geometries. In this subsection, the winding topology of integrated field and armature windings is introduced for copper loss reduction [132], in which the coil current is the superposition of the field current and armature current. If the mmf in the VFRM with the integrated-coil topology is assumed to be the same as with the separate-coil topology, the current density of a coil is defined as,

$$J_{int} = \pm\frac{2J_{dc}S_{dc}}{S_{slot}} + \frac{\hat{J}_{ac}\left(S_{slot}-2S_{dc}\right)}{S_{slot}}\sin\left(\omega_e t\right), \tag{6.8}$$

where S_{dc}, S_{ac} and S_{slot} are the areas of a dc coil bundle, an ac coil bundle and a single slot, respectively.

The copper loss of the separate-coil topology is given as,

$$\begin{aligned} P_{cu,sep} &= 24\frac{J_{dc}^2 S_{dc} L_{sk}}{k_f} + 24\frac{\frac{\hat{J}_{ac}^2}{2} S_{ac} L_{sk}}{k_f} \\ &= 24\frac{J_{dc}^2 S_{dc} L_{sk}}{k_f} + 6\frac{\hat{J}_{ac}^2 \left(S_{slot} - 2S_{dc}\right) L_{sk}}{k_f}, \end{aligned} \tag{6.9}$$

while for the integrated-coil topology, it is expressed as,

$$\begin{aligned} P_{cu,int} &= \frac{1}{2\pi}\int_0^{2\pi} 12\frac{J_{int}^2 S_{slot} L_{sk}}{k_f} d\left(\omega_e t\right) \\ &= \frac{6 S_{slot} L_{sk}}{\pi k_f}\int_0^{2\pi}\left[\pm\frac{2J_{dc}S_{dc}}{S_{slot}} + \frac{\hat{J}_{ac}\left(S_{slot}-2S_{dc}\right)}{S_{slot}}\sin\left(\omega_e t\right)\right]^2 d\left(\omega_e t\right) \\ &= \frac{24 J_{dc}^2 S_{dc} L_{sk}}{k_f}\frac{2S_{dc}}{S_{slot}} + \frac{6\hat{J}_{ac}^2\left(S_{slot}-2S_{dc}\right)L_{sk}}{k_f}\frac{\left(S_{slot}-2S_{dc}\right)}{S_{slot}}. \end{aligned} \tag{6.10}$$

The value of $P_{cu,int}$ is smaller than the value of $P_{cu,sep}$ since $2S_{dc}/S_{slot} < 1$ and $(S_{slot} - 2S_{dc})/S_{slot} < 1$.

This gives the fact that by using the integrated-coil topology, the copper loss is always smaller than using the separate-coil topology. An example is given for the VFRM operating at 16 Nm, where the copper losses of coils are shown in Fig. 6.15(a) and (b) assuming a filling factor of 0.6 for both topologies. The total copper loss for the separate-coil topology is 830 W, while is 480 W for the integrated-coil topology, such that a reduction of 40% is reached.

Although the integrated-coil topology brings a lot of benefit from the efficiency point of view, it may bring the challenges into the power electronic circuit due to the biased dc current and increased peak current, which must be taken into account in implementation. The feasibility of using this method for the specific 48 V mild hybrid application is analyzed.

In the separate-coil topology, coil A_1 (or A_3) and coil A_2 (or A_4) are wound together with dc coils that have different polarities as shown in Fig. 6.16(a), hence, if coil A_1 (or A_3) and the according dc coil are integrated, the new current is expressed as

$$i'_{a1} = \hat{I}_{ac}\cos(\theta_e + \gamma) + i_f, \tag{6.11}$$

while the integrated current of coil A_2 (or A_4) and the according dc coil is expressed as,

$$i'_{a2} = \hat{I}_{ac}\cos(\theta_e + \gamma) - i_f. \tag{6.12}$$

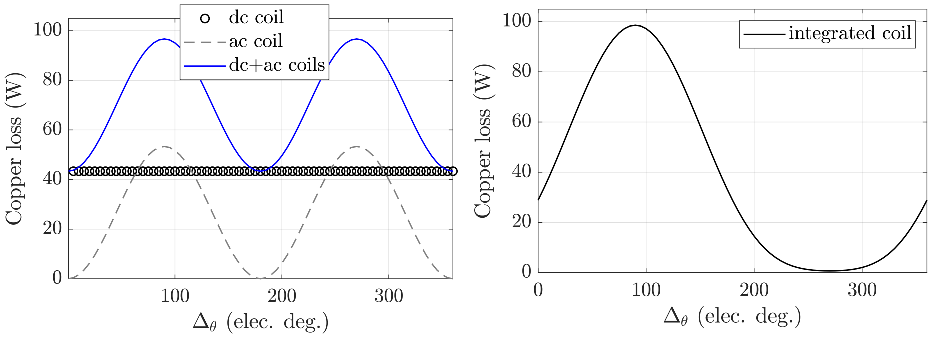

(a) (b)

Figure 6.15: (a) Copper losses of a single dc coil, a single ac coil, and the sum of the two in the separate-coil topology, and (b) copper loss of a single coil in the integrated-coil topology.

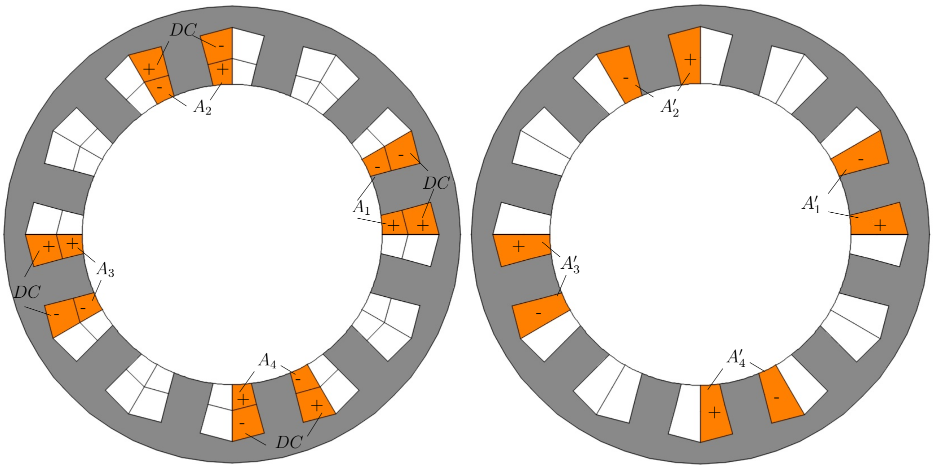

(a) (b)

Figure 6.16: Coils of phase A in (a) the separate-coil topology, and (b) the integrated-coil topology.

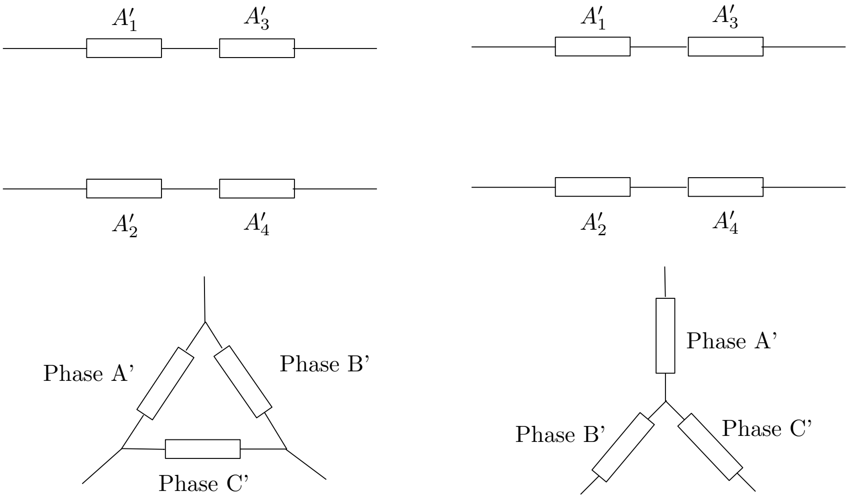

(a) (b)

Figure 6.17: Phase coil connection topologies: (a) delta connection, and (b) star connection.

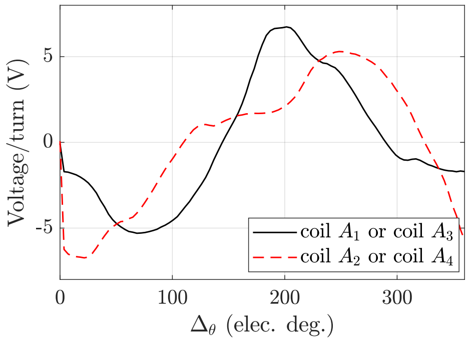

Figure 6.18: Coil voltage of a single turn for the integrated-coil topology.

Consequently, coil A'_1 and coil A'_2 (or coil A'_3 and coil A'_4) in the integrated-coil topology shown in Fig. 6.16(b) cannot be connected in series, since their currents are different. The possible coil connection topologies are shown in Fig. 6.17.

The peak line current for these two coil connections are checked. The number of turns has to be determined first. For this, the voltage per turn is calculated, as shown in Fig. 6.18. Different from the separate-coil topology in which the even harmonics are eliminated by connecting coil A_1 and coil A_2 in series, large even harmonics are observed in the voltage waveform of the integrated-coil topology. The maximum voltage for the sum of coil A'_1 and coil A'_3 (or the sum of coil A'_2 and coil A'_4) is around 6.7 V/turn at the working point 16 Nm 3000 rpm. Therefore, the number of turns should not exceed 7 and 4 for delta connection and star connection, respectively.

The peak line current for the integrated-coil topology, is calculated as,

$$\hat{I}_l' = \frac{\mathcal{F}_{dc,peak} + \hat{\mathcal{F}}_{ac,peak}}{7} \times \sqrt{3} \times 2, \quad \text{delta connection} \tag{6.13}$$

$$\hat{I}_l' = \frac{\mathcal{F}_{dc,peak} + \hat{\mathcal{F}}_{ac,peak}}{4} \times 2, \quad \text{star connection} \tag{6.14}$$

where $\mathcal{F}_{dc,peak}$ and $\hat{\mathcal{F}}_{ac,peak}$ in the equation are the mmfs at the peak torque derived for the separate-coil topology. The value of $\hat{I}_l'$ exceeds 1000 A for both connection topologies, because:

- dc-biased current intrinsically increases the peak current level;
- dc-biased voltage leads to a lower number of turns.

As a result, the integrated-coil topology is not suitable for this application.

6.7 Final design

The obtained design is evaluated with the benchmark examples that are also designed for automotive 48 V systems. Two different types of electrical machines are selected as the benchmarks, one is a rare-earth PMSM in literature and the other one is an SRM in market. The machine characteristics are listed in Table 6.7. As can be seen, without the usage of the permanent magnet, the VFRM achieves a lower power level and efficiency compared to the PMSM. While compared to the commercial SRM, the VFRM achieves a 11% higher continuous power and a 12.5% higher peak power with a roughly equal system size and a comparable efficiency.

The design obtained in sections 6.5 and 6.6 is based on the assumption of using rectangular wires with Grade 1 insulation (thickness is 0.085 mm). However, during the manufacturing process, the bondable Grade 1 wires were not available, hence, it is considered to use Grade 2 insulation (thickness is 0.145 mm) for the prototype. Consequently, the area of the stator slot has to be slightly increased to fit new coil dimensions. The final design for the prototype is listed in Table 6.8.

Table 6.7: The comparison between the designed VFRM and the benchmark electrical machines.

Machine type	VFRM	Rare-earth PMSM in Literature [45]	SRM CPT SpeedStart [34]
[3]Machine Dimension	140 × 87.5	144 × 60	-
[1]System Dimension	[4]165 × 175	-	170 × 185
Cooling	Water	Water ethylene glycol	Engine coolant
[2]Continuous power	5 kW	-	4.5 kW
[2]Peak power	10 kW 10 second	14 kW 5 second	8 kW
Efficiency	Maximum 90% Rated 83%	Maximum > 90%	[1]Rated 85%

Notes:
[1] includes integrated electronics;
[2] in motoring mode.
[3] outer diameter (mm) × axial length (mm)
[4] from the design requirement in section 6.2

Table 6.8: Final prototype dimensions and parameters.

Symbol	Description	Value	Unit
D_{so}	Stator outer diameter	140	mm
L_{sk}	Stack length	87.5	mm
D_{ro}	Rotor outer diameter	90.8	mm
D_{sh}	Shaft diameter	21	mm
α_{si}	Stator tooth inner arc	14.6	deg.
α_{ro}	Rotor tooth outer arc	11.5	deg.
α_{ri}	Rotor tooth inner arc	27	deg.
h_{sy}	Stator yoke height	8.6	mm
h_{ry}	Rotor yoke height	20.5	mm
N_{ac}	Number of turns per ac coil	10	-
N_{dc}	Number of turns per dc coil	14	-
h_w	Height of wire	1.5	mm
w_w	Width of wire	2.24	mm
k_f	Filling factor	0.55	-

6.8 Summary and conclusions

In this chapter, the design and optimization of a variable flux reluctance machine are presented. This machine is designed for automotive 48 V mild hybrid system, which requires 5 kW continuous power, 16 Nm continuous torque, 18 krpm maximum speed, 10 kW peak power and 45 Nm peak torque.

The lamination geometry is optimized using the coordinate descent method. To determine the optimization sequence, a sensitivity analysis is performed for the relation between the torque and dimensions. The shape of the stator slot is adjusted to allow higher filling factor and better heat conduction. The winding design is performed for the selection of coil connection topology, wire dimensions and winding method. The helical-wound coil with rectangular wires is chosen due to its relatively low ac copper loss and high filling factor. The feasibility of implementing integrated-coil topology is discussed, however, due to the limitation of drive current, this is not considered for this specific application.

Chapter 7

Experimental verification

7.1 Introduction

This chapter presents the experimental verification of the variable flux reluctance machine designed in Chapter 6 for the 48 V mild hybrid system. The realization of the prototype is introduced together with the test setup. Photos of the machine itself and the setup are both presented. The resistance and inductance values are provided, and back-emf waveforms, torque and coil temperature are measured and are compared with FEM results.

7.2 Realization of the prototype

To verify the predicted results for the final design in Chapter 6, a prototype is realized. The stator lamination stack is shown in Fig. 7.1(a) and (b), the coils wound with rectangular wires are shown in Fig. 7.1(c), the stator stack with dc coils is shown in Fig. 7.1(d), and the stator stack with dc and ac coils is shown in Fig. 7.1(e), where the white cylinder in the center is part of the potting tool. The complete stator is potted with a two component epoxy for mechanical fixation of the coils and for improving the thermal conductivity from the coils to the cooling jacket via the stator lamination. Kapton insulation tape is applied to the stator lamination stack as an additional insulation layer and to protect the rectangular wire from damaging during assembly. The stator assembly after potting is shown in Fig. 7.2(a), the rotor is shown in Fig. 7.2(b) and the complete machine with the cooling jacket is shown in Fig. 7.2(c). The red cables in Fig. 7.2(a) and (c) are the outward motor cables of the field winding and armature windings, while the green wires are thermocouples, which are attached to the windings and stator stack. For ease of stator assembly, the field winding and three-phase armature windings are both separated into two sets, as illustrated in Fig. 7.3. Therefore, there are in total ten motor cables as shown in Fig. 7.2(a).

7.3 Test setup

A machine test setup, Kistler [64], is used to test the prototype. It consists of an induction machine, a three-phase inverter, voltage/current sensors, a controller and a computer, as shown in Fig. 7.4. Using the integrated software, the induction machine is able to run in motor or generator mode with a specified speed or torque. The shaft of the prototype is mechanically attached to the shaft of the induction machine. A torque sensor is installed between the two axles.

Although the Kistler setup itself provides speed readings, an extra incremental encoder is attached to the prototype to further measure the position and speed using a separate dSpace system (CP1104) and Matlab Simulink platform. Addi-

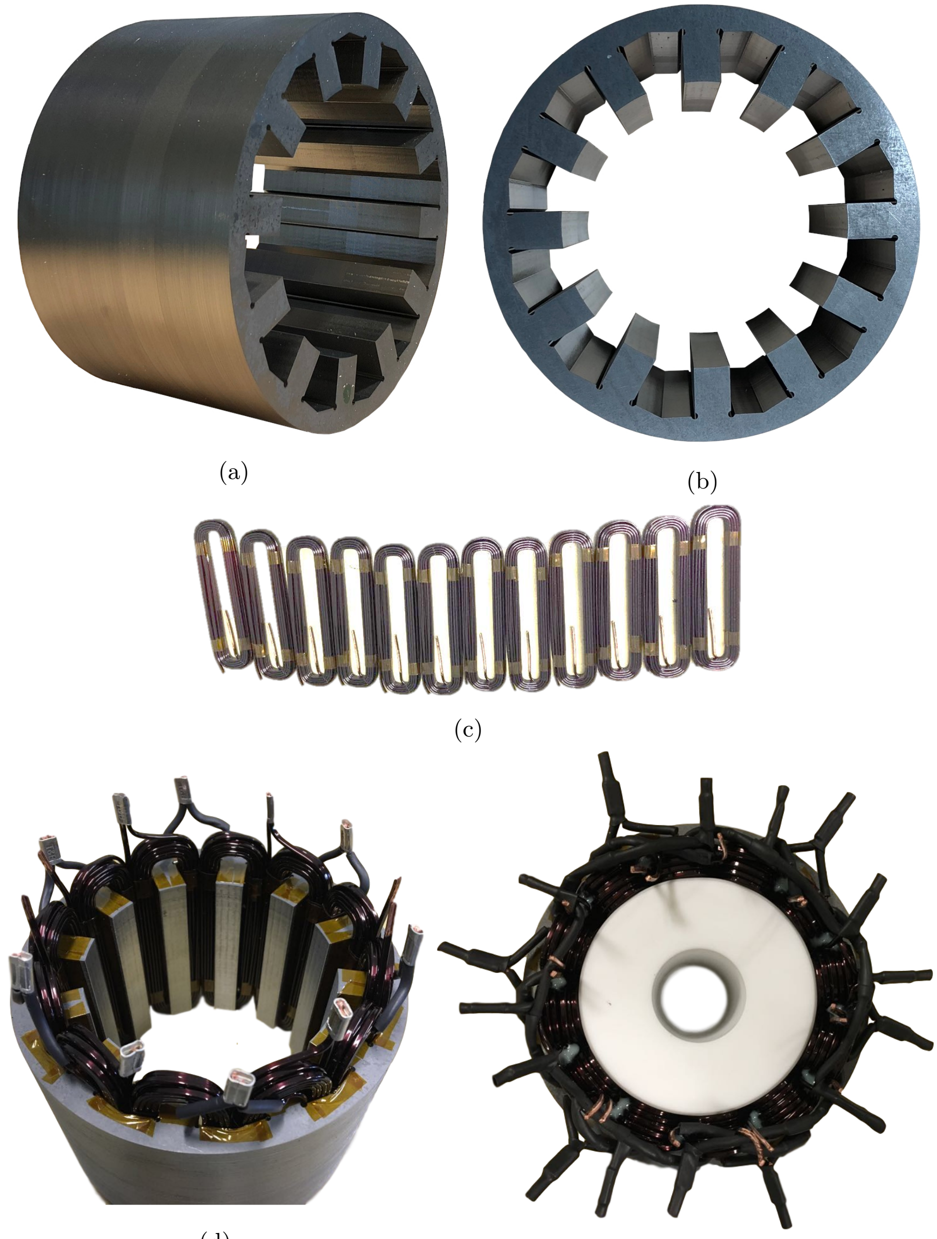

(a) (b)

(c)

(d) (e)

Figure 7.1: Variable flux reluctance machine: (a) the side view of the stator lamination stack, (b) the top view of the stator lamination stack, (c) the coils wound with rectangular wires, (d) the stator lamination stack with dc coils, and (e) the stator lamination stack with dc and ac coils.

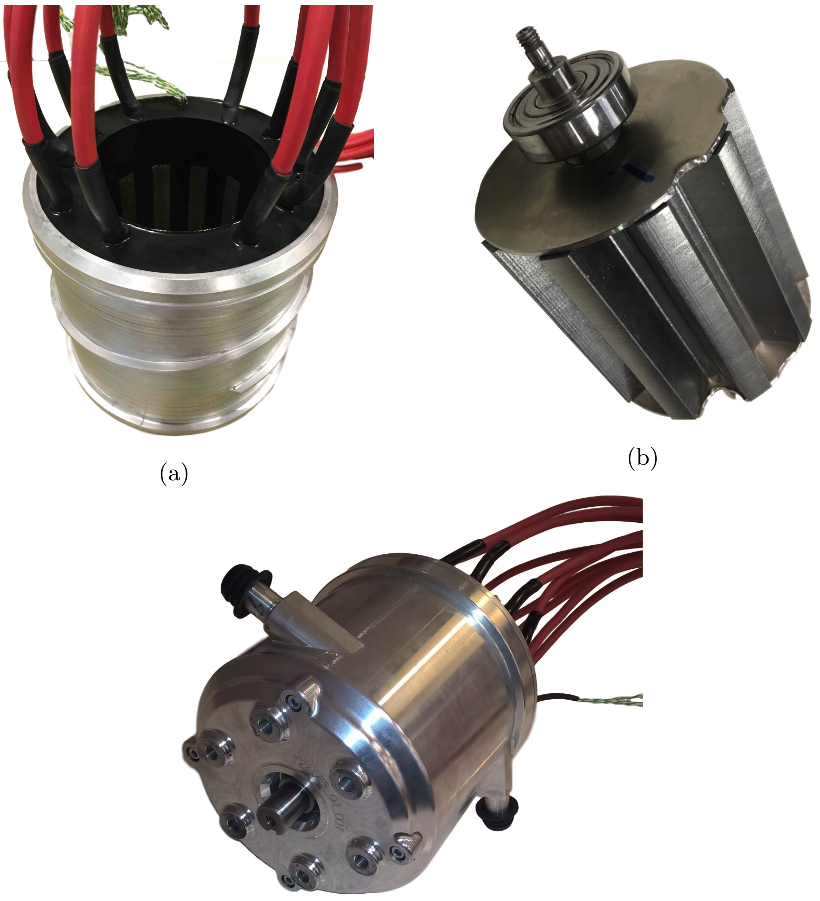

(a)

(b)

(c)

Figure 7.2: Variable flux reluctance machine: (a) the stator assembly after potting, (b) the rotor, and (c) the complete machine with the cooling jacket.

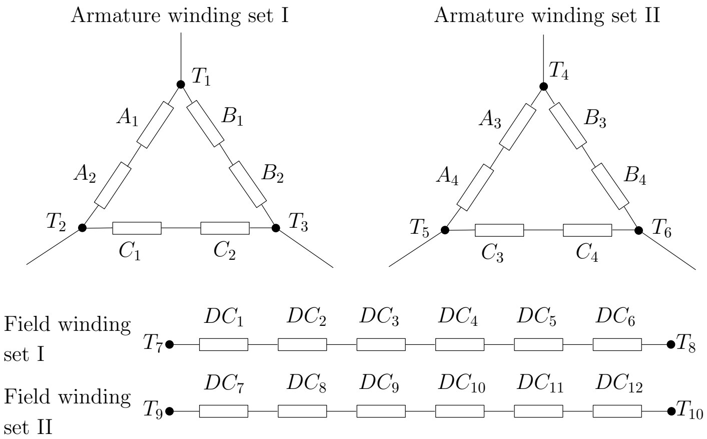
Armature winding set I
Armature winding set II
T_1
T_2
T_3
T_4
T_5
T_6
A_1
A_2
B_1
B_2
C_1
C_2
A_3
A_4
B_3
B_4
C_3
C_4
Field winding set I
T_7
T_8
DC_1
DC_2
DC_3
DC_4
DC_5
DC_6
Field winding set II
T_9
T_{10}
DC_7
DC_8
DC_9
DC_{10}
DC_{11}
DC_{12}

Figure 7.3: Two sets of the three-phase armature windings and field winding.

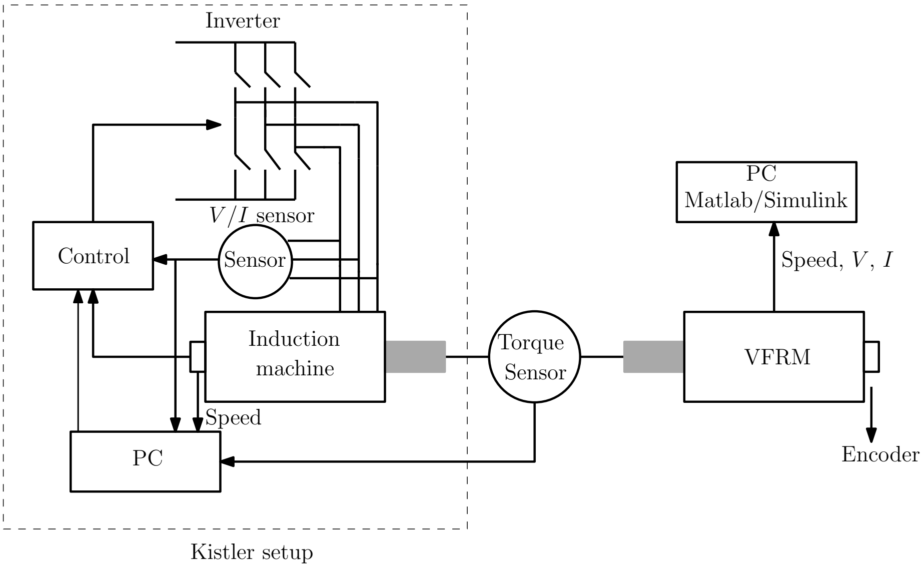
Inverter
V/I sensor
Sensor
Control
Induction machine
Speed
PC
Torque Sensor
VFRM
Encoder
PC Matlab/Simulink
Speed, V, I
Kistler setup

Figure 7.4: The schematic graph of the test setup.

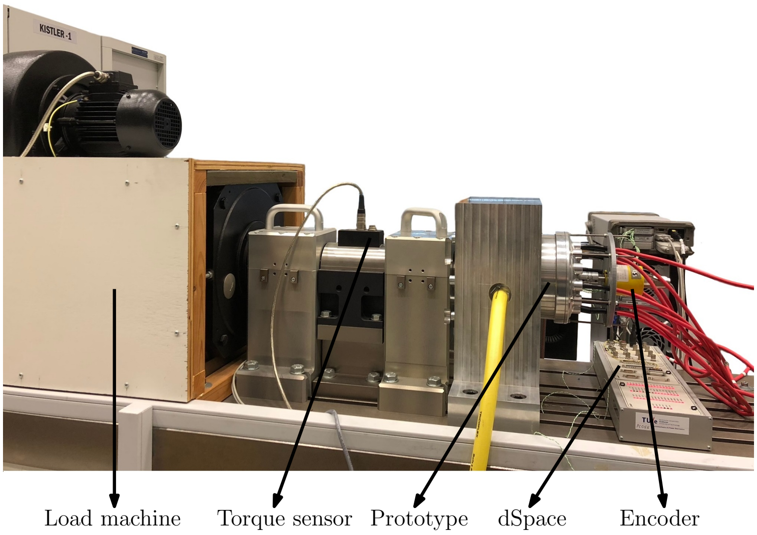

Figure 7.5: The complete Kistler setup, VFRM and dSpace system.

tionally, the voltage and current of both the field winding and armature windings are recorded simultaneously. The temperatures measured by the thermocouples are obtained using an Aligent data acquisition system and instantaneous results are recorded on the computer. A photo of the setup is shown in Fig. 7.5.

7.4 Resistances and inductances

The resistances and inductances are first measured using a four point measurement before the stator is assembled with the rotor to ensure that the realization of the stator coils and their interconnection is correct. As the phase coils are delta-connected, the resistance of each phase is respectively,

$$R_{ph,\mathrm{I}} = \frac{3}{2} R_{ll,\mathrm{I}}, \tag{7.1}$$

$$R_{ph,\mathrm{II}} = \frac{3}{2} R_{ll,\mathrm{II}}, \tag{7.2}$$

in the two sets, where $R_{ll,\mathrm{I}}$ and $R_{ll,\mathrm{II}}$ are the average line to line resistances between each two of the terminals, which are given by,

$$R_{ll,\mathrm{I}} = \sum_{\substack{i,j=1,2,3 \\ i \neq j}} \frac{R_{T_i,T_j}}{3}, \tag{7.3}$$

$$R_{ll,\mathrm{II}} = \sum_{\substack{i,j=4,5,6 \\ i \neq j}} \frac{R_{T_i,T_j}}{3}. \tag{7.4}$$

Table 7.1: Measured resistances between terminals at room temperature 20°C.

	Terminal	Measured (mΩ)
Armature winding I	T_1, T_2	19.1
	T_2, T_3	19.1
	T_3, T_1	18.8
Armature winding II	T_4, T_5	18.9
	T_5, T_6	19.4
	T_6, T_4	18.6
Field winding I	T_7, T_8	117.1
Field winding II	T_9, T_{10}	116.9

Table 7.2: Measured phase resistances and field winding resistances at room temperature 20°C.

	Symbol	Measured (mΩ)	Predicted (mΩ)	Disprepancy
Armature winding I	$R_{ph,\mathrm{I}}$	28.5	26.4	8.0%
Armature winding II	$R_{ph,\mathrm{II}}$	28.5	26.4	8.0%
Field winding I	$R_{dc,\mathrm{I}}$	117.1	112.4	4.2%
Field winding II	$R_{dc,\mathrm{II}}$	116.9	112.4	4.0%

The measured resistances between the respective terminals are listed in Table 7.1. As can be seen, the resistances are almost the same for the two sets, and are balanced for the three phases. The corresponding phase resistances and field winding resistances are listed in Table 7.2, which have a discrepancy of around 8% and 4% respectively compared to the predicted results. Taking into account the tolerances of the wire width and thickness (±0.03 mm based on IEC 60317-0-2), the predicted results can be increased up to 3.5%, and the discrepancies between the measured and predicted resistances become approximately 4.3% and 0.7%, respectively, under this circumstance.

The inductances are measured using an LCR meter which supplies 1 V at 100 Hz. The measured inductance values between each two of the terminals are provided in Table 7.3. Again, the phase inductance is calculated as,

$$L_{ph,\mathrm{I}} = \frac{3}{2} L_{ll,\mathrm{I}}, \tag{7.5}$$

$$L_{ph,\mathrm{II}} = \frac{3}{2} L_{ll,\mathrm{II}}, \tag{7.6}$$

for the two sets, respectively, where $L_{ll,\mathrm{I}}$ and $L_{ll,\mathrm{II}}$ are the average inductances

Table 7.3: Measured inductances between terminals.

	Terminal	Measured (μH)
Armature winding I	T_1, T_2	34.7
	T_2, T_3	34.7
	T_3, T_1	34.6
Armature winding II	T_4, T_5	34.2
	T_5, T_6	34.8
	T_6, T_4	34.3
Field winding I	T_7, T_8	640.6
Field winding II	T_9, T_{10}	639.3

Table 7.4: Measured phase inductances and field winding inductances.

	Symbol	Measured (μH)	Predicted (μH)	Discrepancy
Armature winding I	$L_{ph,\mathrm{I}}$	52.1	50.8	2.6%
Armature winding II	$L_{ph,\mathrm{II}}$	51.6	50.8	1.6%
Field winding I	$L_{dc,\mathrm{I}}$	640.6	673.9	4.9%
Field winding II	$L_{dc,\mathrm{II}}$	639.3	673.9	5.1%

between each two of the terminals, which are given by,

$$L_{ll,\mathrm{I}} = \sum_{\substack{i,j=1,2,3\\ i\neq j}} \frac{L_{T_i,T_j}}{3}, \tag{7.7}$$

$$L_{ll,\mathrm{II}} = \sum_{\substack{i,j=4,5,6\\ i\neq j}} \frac{L_{T_i,T_j}}{3}. \tag{7.8}$$

The corresponding inductance values are listed in Table 7.4, and are compared with the predicted results that are obtained by 3D FEM. The error of the inductances is no larger than 5.1%.

7.5 Back-emf waveform

The phase back-emf of the prototype is measured when the prototype is driven by the induction machine at the Kistler setup. The measured waveform of each phase is shown in Fig. 7.6. As can be seen, the voltage levels between the two winding sets are similar, and each phase has a 120° phase shift as expected. The voltage waveform is compared with the predicted results obtained from 2D FEM, as shown in Fig. 7.7. The harmonic content of the waveforms is analyzed, and the result is shown in Fig. 7.8. Both the measurement and the FEM result contain a dominant 5^{th} harmonic.

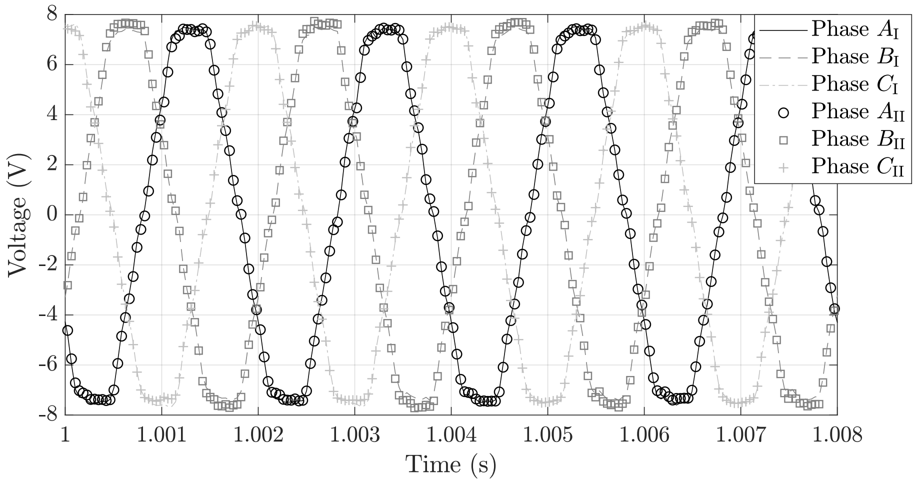

Figure 7.6: The waveforms of the back-emf at 3000 rpm with field current i_f = 10 A (nominal at 43 A aiming for 16 Nm).

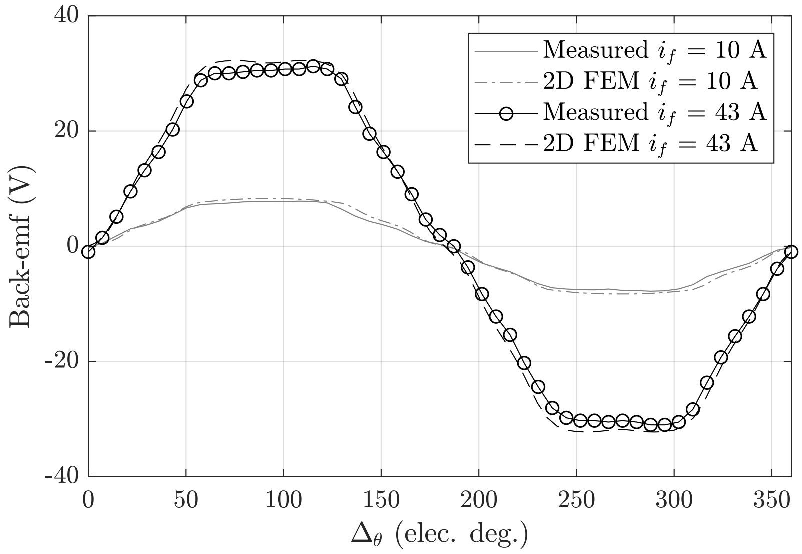

Figure 7.7: The comparison between measurement and 2D FEM result for the back-emf waveform at 3000 rpm with field current i_f = 10 A and i_f = 43 A (nominal i_f = 43 A).

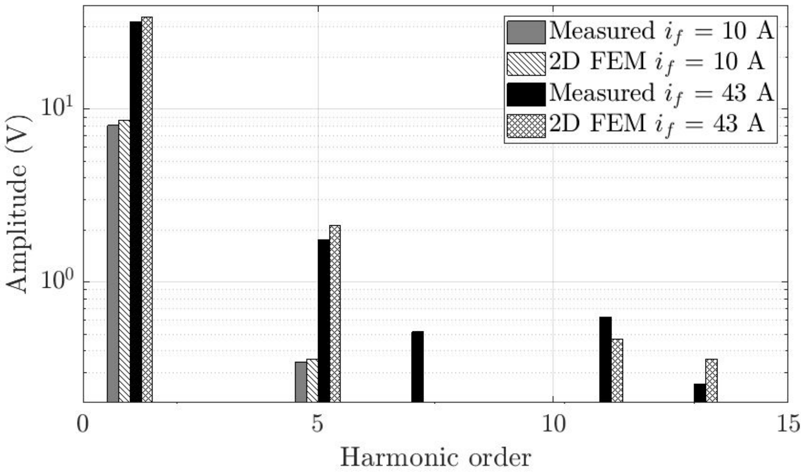

Figure 7.8: The comparison between measurement and 2D FEM result for the harmonic contents in the back-emf at 3000 rpm with field current $i_f = 10$ A and $i_f = 43$ A (nominal $i_f = 43$ A).

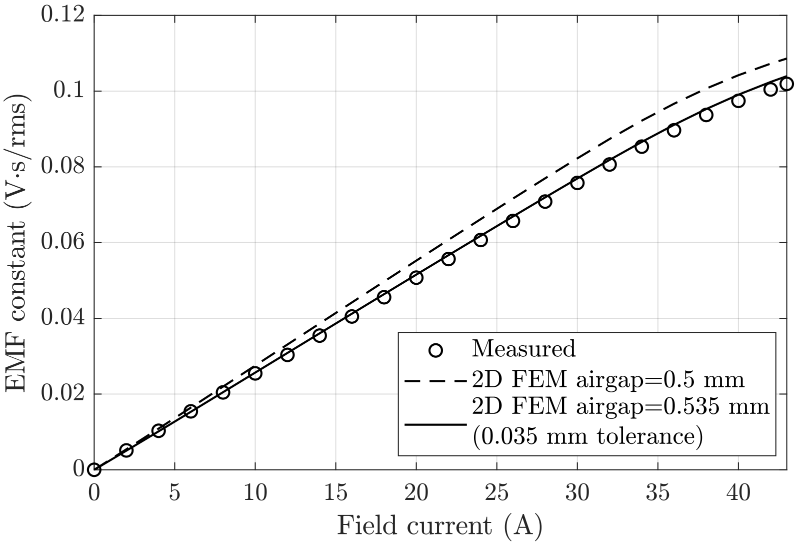

Figure 7.9: The EMF constant at various field currents.

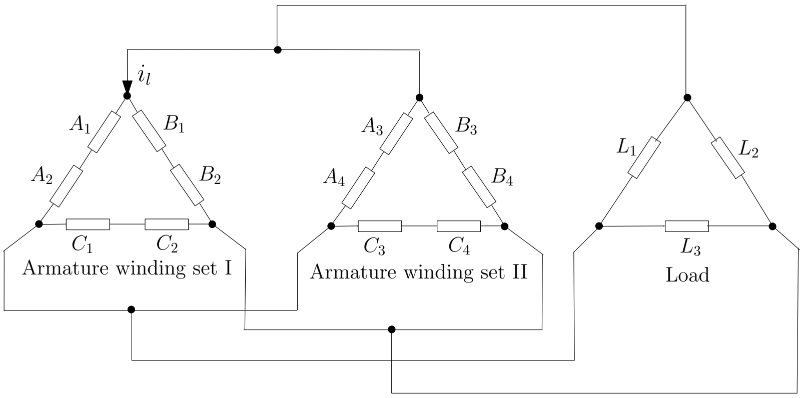

Figure 7.10: The circuit for torque measurements, where the prototype is connected with a three-phase delta-connected load.

Additionally, the back-emf is measured at different speeds and different field current levels. The EMF constant is calculated, and the result is shown in Fig. 7.9 along with the comparison with FEM. Taking into account the stacking factor of 96% provided by the manufacturer, the discrepancy between the measurement and FEM result is 6.2% with the nominal field current of 43 A.

Such difference can be caused by the mechanical tolerances and magnetic material property. The back-emf is sensitive to the dimensions. The tolerances of the stator inner diameter and rotor outer diameter are (+0.035mm, 0) and (0, -0.035 mm), respectively. If both the tolerances are at their extremes, the airgap length is increased by 0.035 mm. With such tolerances, the corresponding predicted EMF constant is shown in Fig. 7.9 with the solid line, where the discrepancy with the measurement result is 2% at the nominal current. Moreover, if μ_r is overestimated in the prediction, the EMF constant in reality is lower than expected. As an example, assuming the *B*-*H* curve of NO27 shown in Fig. 6.2(d) is replaced by the *B*-*H* curve shown in Fig. 2.19, the predicted EMF constant is reduced by 5.6%.

7.6 Torque-current performance

Since machine control is not implemented for the prototype, the VFRM is operated in generating mode during the test of torque performance, while the load machine at the Kister setup is operated in motoring mode at fixed rotor speeds. The prototype is connected to a balanced three-phase delta-connected load, as presented in Fig. 7.10. In the tests, two different balanced loads are used, where the measured resistance and inductance values are listed in Table 7.5.

The torque is measured with various field currents and speeds, and the measurement results are calculated using the measured torque deducted by the friction and windage torque which is obtained in a no-load test. In 2D FEM, the same

Table 7.5: The resistance and inductance values of the two balanced loads at room temperature 20°C.

Numbering of loads	Resistance (Ω)	Inductance (μH)
I	0.89	25.81
II	0.66	34.60

Notes: The inductances in the table are the values measured at 500 Hz (which is the electric frequency of the prototype at 3000 rpm). The measured inductances vary little at low frequencies, less than 4% as the frequency changes from 300 Hz - 600 Hz.

Table 7.6: Maximum and average discrepancies between measurement and 2D FEM results (obtained by the torques shown in Fig. 7.14).

Field current, i_f, (A)	5	10	15	20	25	30	35	40	43
Maximum discrepancy (%)	71.3	8.0	5.1	4.1	4.3	3.6	4.7	3.8	3.0
Average discrepancy (%)	33.6	3.5	2.4	1.8	2.8	2.8	2.7	2.5	2.1

circuit as in Fig. 7.10 is defined. The measurement and predicted results with the two loads are presented in Fig. 7.11 and Fig. 7.12, respectively. To show the influence of mechanical tolerance on the torque performance, the predicted results with (0.5 mm + 0.035 mm) airgap length are also shown in the figures.

During the tests, the phase currents flowing in the windings are related to the induced voltage. As presented in section 7.5, the measured back-emf is slightly smaller than the predicted values, consequently, the phase currents in the measurement are smaller than the values in FEM. This can be seen in Fig. 7.13, which shows the comparison of the current waveforms.

To compare the predicted and measured torque more fairly, an FEA is performed with the fundamental phase currents that have the amplitudes calculated from measurement results. The obtained torque is presented in Fig. 7.14, which shows the dependency of the mean torque on current levels. Using the values in Fig. 7.14, the average and maximum discrepancies between the measurement and FEM results are calculated, as listed in Table 7.6. Generally, the measurement shows a good agreement with the prediction, except for the situation when the field current is 5 A. The reason is that the torque is less than 0.08 Nm for $i_f = 5$ A, and the torque measurement is not accurate enough for such a low torque level.

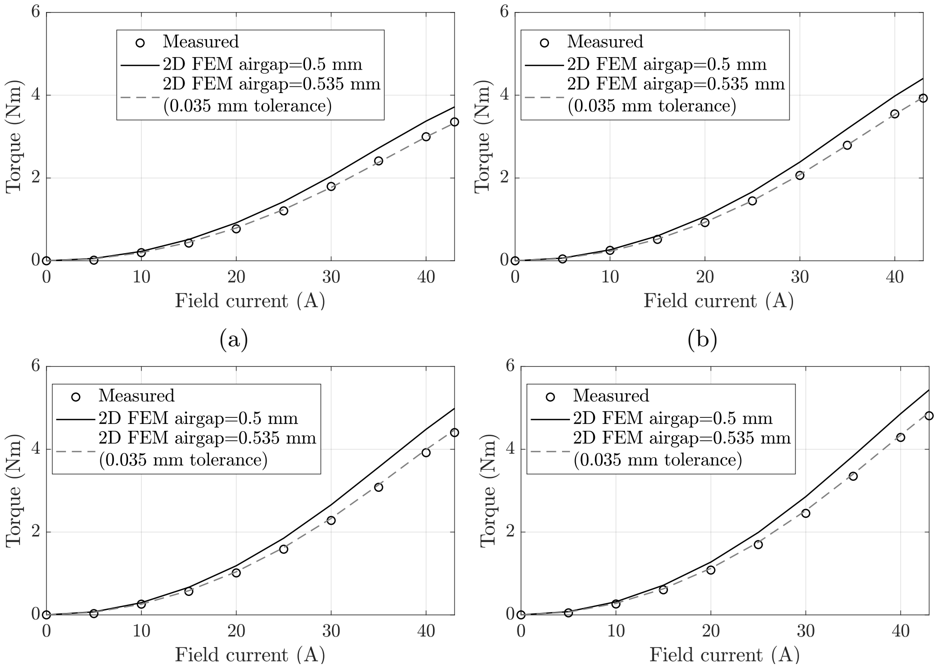

(a) (b) (c) (d)

Figure 7.11: The comparison between measurement and FEM results of the torque performance when the prototype is connected with load I: (a) at 2000 rpm, (b) at 2500 rpm, (c) at 3000 rpm, and (d) at 3500 rpm.

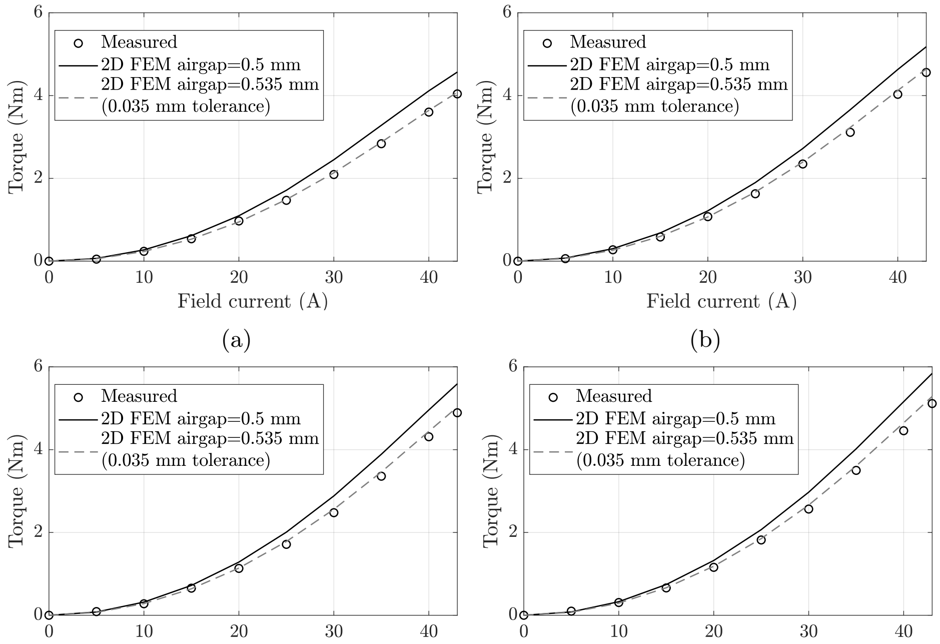

(a) (b)

(c) (d)

Figure 7.12: The comparison between measurement and FEM results of the torque performance when the prototype is connected with load II: (a) at 2000 rpm, (b) at 2500 rpm, (c) at 3000 rpm, and (d) at 3500 rpm.

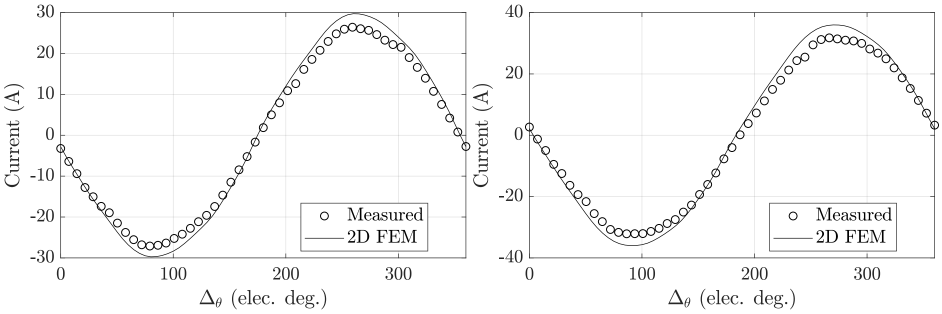

(a) (b)

Figure 7.13: The current waveforms of the line current (i_l in Fig. 7.10) obtained by measurement and 2D FEM (airgap = 0.5 mm) with a field current at 43 A and a speed of 3000 rpm, assuming: (a) the machine is connected with load I, and (b) the machine is connected with load II.

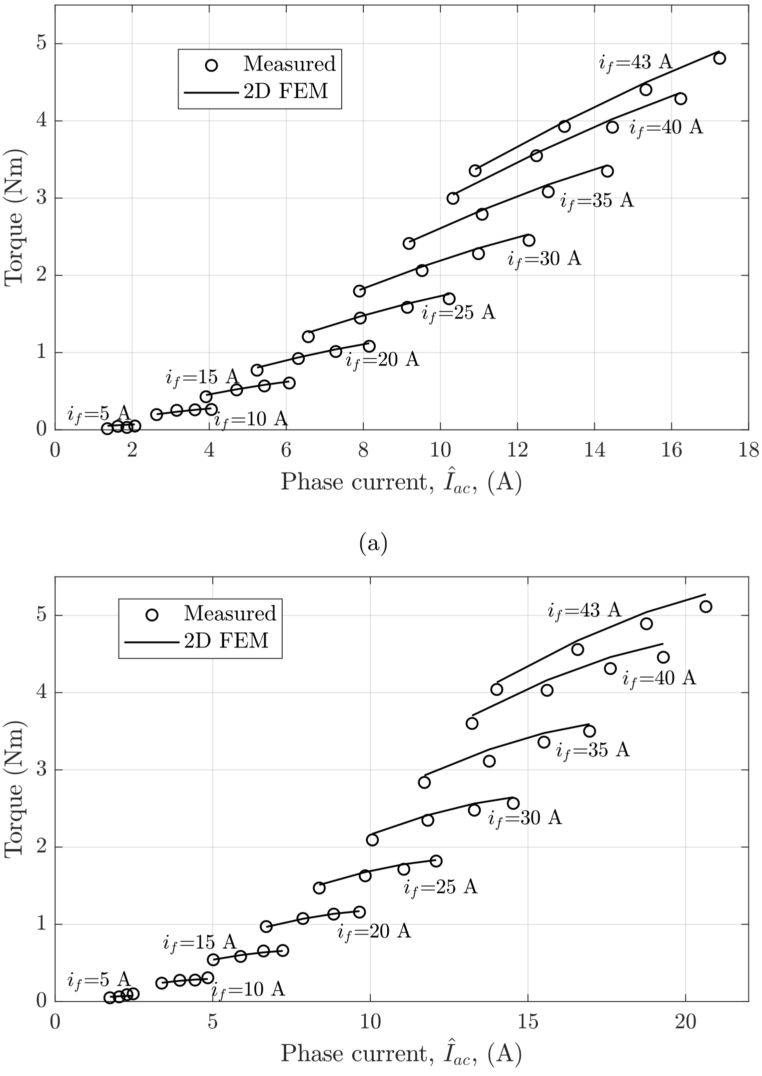

(a)

(b)

Figure 7.14: Comparison between measurement and 2D FEM results (airgap = 0.5 mm) with respect to various field currents (i_f) and phase currents ($\hat{I}_{ac}$): (a) the measured results and the predicted torque that is calculated with $\hat{I}_{ac}$ obtained in the torque measurements with load I, and (b) the measured results and the predicted torque that is calculated with $\hat{I}_{ac}$ obtained in the torque measurements with load II.

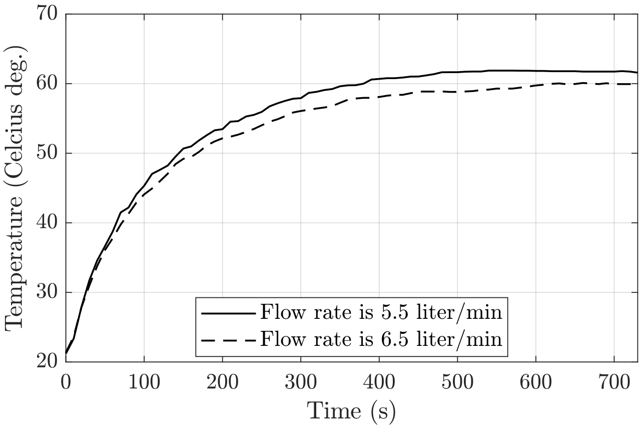

Figure 7.15: The measured coil temperature with different coolant volumetric flow rates.

7.7 Thermal evaluation

To verify the thermal model made in 2D FEM during the design process, thermal measurements are performed, and the results are discussed in this section. As mentioned in section 7.2, there are thermal couples attached to the stator lamination stack and coils. In the test setup, two additional thermal couples are used to measure the temperature of the inward and outward flow of the coolant.

A dc current is applied to the field winding during measurements, while the rotor is fixed. Hence, the heat source is only the copper loss, P_{cu}, which can be obtained by multiplying the measured voltage and current. The temperatures of the thermal couples are recorded until a steady state is reached. An example is given in Fig. 7.15, which shows the transient behavior of the coil temperature with two different coolant flow rates. As can be seen, the steady-state temperature decreases little, about 1.6°C, as the volumetric flow rate increases from 5.5 liter/minute to 6.5 liter/minute. This can be attributed to the relatively high convection caused by the large flow rate, such that the heat transfer appears to be more limited by the conduction from the inner part to the outer surface, and consequently, a further increase of flow rate does not influence significantly on the inner temperature of the machine.

In 2D FEM, the same coolant temperature and copper loss as in the measurement are applied, while the value of heat transfer coefficient is estimated by,

$$h_c = \frac{P_{cu}}{A_{out}\left(T_{st} - T_{cl}\right)}, \tag{7.9}$$

where A_{out} is the area of the outer surface, T_{st} and T_{cl} is the stator and coolant temperature, respectively. The calculated h_c is over 1300 W/Km^2.

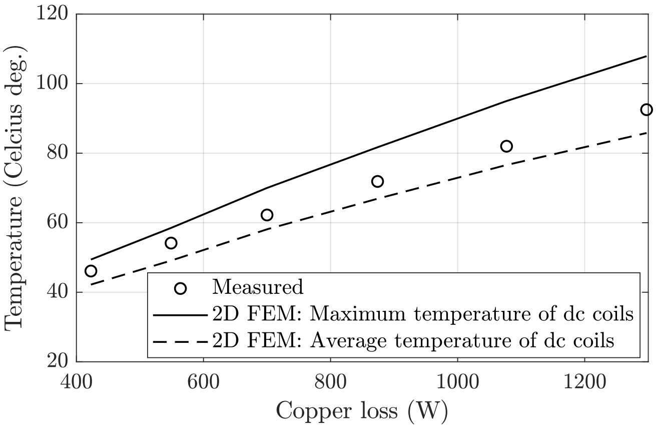

Figure 7.16: The steady-state coil temperature obtained by measurement (with the flow rate at 5.5 liter/minute) and 2D FEM.

The predicted and measured relationships between the copper loss and steady-state coil temperature are shown in Fig. 7.16. As can be seen, the measured temperature is smaller than the maximum temperature obtained in FEM, which can be attributed to the location of the thermal couple and the simplified 2D modeling:

- The thermal couple may be not positioned at the hottest spot of the coils;
- The heat generated by the end winding and the coil sections in the stator stack are accumulated, and are assumed to be distributed within the stack length in the 2D thermal model.

The above results validate the FE thermal model, that the mean discrepancy between the measured coil temperature and the maximum temperature obtained by FEM is around 10.9%.

However, the temperature shown in Fig. 7.16 is much lower than the estimated value mentioned in section 6.6.2, which is around 150°C. This is because: the slot liners are not used in the prototype, the coolant temperature is around 20°C in the measurement while is set at 65°C for the design; the heat sources are different between measurements and design, as the rotor is fixed and all the copper losses are produced by the dc coils during the tests.

7.8 Summary and conclusions

A prototype has been realized and tested. A setup is built with the Kistler setup that can drive the prototype with specified speeds. The voltage, current, temperature, position and speed are recorded instantaneously. The measured resistances and inductances of field winding and armature windings all match with the predicted results. The open-circuit back-emf waveforms are measured with different field currents, and the harmonic content and EMF constant are calculated. The torque is measured in the generating mode with various current levels. Additionally, thermal tests are performed to measure the steady-state coil temperature to validate the thermal FE model. The measured back-emf, mean torque and temperature all present a good agreement with FEM results.

Part III

Closing

Chapter 8

Conclusions and recommendations

This thesis discusses a novel hybrid analytical modeling technique for nonlinear 2D electromagnetic problems, and the design framework of the variable flux reluctance machines. The research objectives are given in two parts in section 1.5:

1. Establish a generalized 2D modeling framework and methodology that offers accurate and relatively fast prediction for nonlinear 2D electromagnetic problems;
2. Establish the design framework for the variable flux reluctance machines, and realize a design for automotive 48 V mild hybrid system.

In this chapter, the conclusions are provided regarding the fulfillment of the research objectives: In Part I, the achievement of the generalized modeling technique for nonlinear 2D electromagnetic problems is discussed. The implementation to various benchmark examples shows its broad applicability to different classes of electrical machines. In Part II, it researches, designs, optimizes, and realizes the variable flux reluctance machine as a candidate for automotive applications due to the characteristics of robust structure, wide speed range and low material cost.

8.1 Conclusions of Part I

8.1.1 Generalized hybrid analytical modeling technique

To reduce the computation effort involved in solving electromagnetic problems, a 2D hybrid analytical modeling technique is developed as an alternative to numerical methods, which allows to model nonlinear problems with combined Fourier modeling and mesh-based magnetic equivalent circuit. Fourier modeling that describes periodic electromagnetic problems by spatial harmonic expressions is fast and accurate; while magnetic equivalent circuit allows to model the variation of relative permeability and hence can incorporate nonlinear magnetic materials.

Electromagnetic problems in 2D coordinate systems are decomposed into orthogonal axes. All the regions share the same periodic boundaries in the tangential direction. In the Fourier regions, the magnetic field is derived in terms of the magnetic vector potential and is expressed by Fourier series. The MEC regions are meshed, and the magnetic field in each element is expressed by the magnetic scalar potential at the center node. Permanent magnet related and current related magnetic sources are described by magnetomotive forces, where the expression of current related sources shows the dependency on the element positions and element sizes to fulfill the Ampere's law.

The unknown coefficients in the Fourier/MEC regions are solved by a set of linear equations which satisfy the boundary conditions between the regions. Motion is integrated in the boundary conditions that allows for a free movement without re-meshing of the MEC regions. To incorporate magnetic nonlinearity, a locally linearized B-H relationship is applied that provides relative permeability and extra mmf sources for each MEC element. An iterative algorithm is performed to update the local B-H relationship until convergence is reached.

The validity of the generalized formulation is verified with 2D FEM for a benchmark problem in every coordinate system, i.e., a linear E-core actuator, a rotary switched reluctance machine and a tubular permanent magnet machine. The versatility of this HAM allows the application to a large class of electromagnetic devices, and the concept of this HAM brings a significant benefit on computation effort especially for the devices with a relatively small airgap, e.g., in doubly salient reluctance machines, permanent magnet machines, etc.

8.1.2 Modeling of variable flux reluctance machines

The developed HAM has been applied to a 12/10 variable flux reluctance machine. The generalized equation for the calculation of reluctances in meshed MEC provides the freedom of varying tooth arcs. The results of HAM have been validated against calculations obtained from 2D FEM.

The HAM provides an accurate solution of magnetic field in the airgap as well as in the iron parts. The Maxwell stress tensor is used to calculate the torque, and a very good agreement is reached for the torque profile which includes position dependency and saturation. An accuracy within 1.5% is obtained for the mean torque and is within 6% for the torque ripple. Furthermore, accurate calculation methods for the back-emf, phase voltage and inductances are provided, which give an accuracy within 3%. Finally, iron loss and ac copper loss are calculated. The obtained iron loss is within the accuracy of 1% considering the contribution of hysteresis loss, classical eddy-current loss and excess loss. The ac copper loss is calculated assuming an imposed current in the conductor. The eddy current distribution is estimated using the magnetic vector potential obtained from quasi-static Maxwell equations. The discrepancy of the ac copper loss obtained from HAM and FEM is around 12.5%, however, it increases as the speed increases, since the dynamic solution of the vector potential is not taken into account.

8.2 Conclusions of Part II

8.2.1 Topologies and configurations of variable flux reluctance machines

Operating principle

For the design of variable flux reluctance machines, which is a relatively new class of electrical machines, an insight into the physical phenomena is required. In this thesis, the torque equations are derived using the energy conversion theory and the virtual work method. The torque components induced by the self inductance of the field winding, mutual inductances between the field winding and armature windings, and the self inductances and mutual inductances of the armature windings are analyzed individually. The result shows that the mean torque is contributed by the mutual inductances between the field winding and armature windings as well as the second harmonic of the self and mutual inductances of the armature windings. A torque equation is derived which is analogous to permanent magnet synchronous machines.

Selection of preferable topologies

There are a lot of combinations of the numbers of stator poles and rotor poles for three-phase VFRMs, and the rules of feasible combinations are summarized. Considering the equal number of 'north' and 'south' poles created by the field winding and the balance of three phase armature windings, the number of stator poles, P_s, must be the multiples of 6. Further, the number of rotor poles, P_r, has to ensure that $p_s/3$ is integer (p_s is a number defined as P_s/g_{cd}, where g_{cd} is the common divisor between P_s and P_r).

To select preferable topologies, the winding factor, harmonic cancellation in back-emf, influence of the number of rotor poles on torque production, and magnetic pull are analyzed. The machine topologies of VFRMs influence significantly on the open-circuit phase flux linkages, and the winding factor, as a quantitative indication, is mathematically derived for the fundamental and higher harmonics. It has been found that when $p_s/3$ is an even number, the even harmonics of the back-emf are canceled out, which is beneficial for the torque ripple reduction, such as in the topologies of 6/5, 6/7, 12/2, 12/10, 12/14, etc. For topologies with the same winding factors, three different situations are analyzed, respectively with the conditions that, the number of rotor poles is much larger, or approximate to, or much smaller than the number of stator poles. The analysis shows that for the number of rotor poles much larger/smaller than the stator poles, the redundancy or lack of rotor poles limit the teeth widths or variation of the alignment area between stator and rotor teeth, hence lower the torque production. Consequently, it is preferred for the numbers of stator poles and rotor poles close to each other, such as the topologies of 6/5, 6/7, 12/10, etc. Finally, considering the significant unbalanced magnetic pull in the topologies with odd number of rotor poles, the 12/10 topology is selected.

8.2.2 Design considerations

Torque ripple reduction

Due to the doubly salient structure, one of the drawbacks of the VFRMs is the large torque ripple. Three methods for torque ripple reduction, i.e., rotor skewing, rotor teeth non-uniformity and harmonic injection, are proposed and investigated based upon the analysis on the sources of torque ripples. The 6^{th} harmonic dominates in the torque ripple of 12/10 VFRMs, which is mainly contributed by the 6^{th} harmonic in the self inductance of the field winding and the 5^{th} harmonic of the mutual inductances between the field winding and armature windings.

The methods of skewing or rotor teeth non-uniformity are capable to eliminate these two torque ripple sources by properly selecting the skewing angle. The effectiveness of these two methods is verified for both non-saturated and saturated machines, showing that the torque ripple is reduced by 50% with no more than 5% average torque reduction. The result of skewing is derived by analyzing a two-module structure, however, by increasing the number of modules, the torque ripple can be further reduced.

The effectiveness of harmonic current injections is analyzed individually for the field winding and armature windings, which requires a 6^{th} harmonic in the field current and a 5^{th} harmonic in the armature current, respectively. The armature current harmonic injection reduces 80% of the torque ripple in both non-saturated and saturated machines without reduction of the average torque. The field current harmonic injection creates extra 12^{th} and 18^{th} harmonics in the torque ripple in spite of the elimination of the 6^{th} harmonic. Additionally, due to the large self inductance of the field winding, harmonics in the field current significantly increase the induced voltage. As such, the armature current harmonic injection is more effective than the field current harmonic injection, hence, is more preferred.

Torque-speed characteristic

To analyze the torque-speed characteristic of VFRMs, the dq-reference frame is introduced, which defines the d-axis at the centerlines of the rotor teeth and in the middle of two rotor teeth centerlines, and the q-axis in the middle of two adjacent d-axes. The relationship among the magnetomotive forces of field and armature windings and torque-speed characteristics is analyzed. A factor K_{fw} is defined to indicate the field weakening capability, and a unity K_{fw} is desired to maximize the constant power region. It is possible to reduce the field current (for inital $K_{fw} < 1$) or armature current (for initial $K_{fw} > 1$) to adjust the value of K_{fw}. The effectiveness of such current arrangement is verified for two examples, and the speed is capable to be extended by 6 times the base speed in the constant power region based on the FEM results. Apart from the torque-speed curve, the current arrangement influences the power factor as well, i.e., a higher magnetomotive force of the field winding is beneficial to increase the power factor.

8.2.3 Design of the VFRM for 48 V mild hybrid system

A variable flux reluctance machine has been designed and optimized for the application of 48 V mild hybrid system due to its robust structure, wide speed range and low material cost. Giving the requirements of torque-speed characteristic, the optimization has been performed for efficiency maximization at the operating point of 16 Nm 3000 rpm with the specified outer dimensions, cooling capability and voltage/current limits. Several design choices are made: 1. To achieve a higher copper filling factor, the stator geometry is adjusted and rectangular wires are used; 2. The three phases are delta-connected considering the voltage and current limitations; 3. The helical-wound coils are selected considering the ac copper loss; 4. The implementation of an integrated-coil topology is not considered due to the limitation of drive current. The final design achieves a maximum efficiency of 90% in the efficiency map whilst the mechanical losses are not considered.

8.2.4 Experimental verification

To verify the working concept and machine design, a prototype has been realized and experimentally validated. A test setup has been built to drive the prototype at specified speeds, together with voltage/current/speed/position/temperature sensoring and recording. The measured back-emf waveforms show a good agreement with the FEM results. The EMF constant is measured for different current levels, and has shown a discrepancy of 6% compared to the FEM result, which can be caused by the mechanical tolerances, differences in magnetic properties, etc. The torque-current performance is measured at different current levels, the results match with the 2D FEM results. Additionally, thermal measurements are performed that validate the static FE thermal model.

8.3 Thesis contributions

The main contributions and output of the thesis are summarized as:

Part I: Hybrid modeling technique

- **The development of a generalized hybrid analytical modeling technique for nonlinear 2D electromagnetic problems.**
  A generalized framework based upon the combination of Fourier modeling and MEC is developed. This hybrid technique combines the non-meshed solution of the Fourier regions to describe the magnetic field in the airgap (or other regions with homogeneous permeability) together with the benefits of the MEC model to include nonlinear material characteristics and geometric details (such as slotting). This technique provides a fast and accurate tool for nonlinear 2D electromagnetic problems in three coordinate systems which is validated by FEM on three benchmarks problems, proving its applicability to a broad class of electromagnetic actuators and machines.
- **The application of the hybrid analytical modeling technique to the variable flux reluctance machine.**
  The developed modeling technique is applied to a variable flux reluctance machine that is generally a novel class of machine which due to the absence of permanent magnets and wide speed range, is a suitable candidate for automotive powertrains. Due to its doubly salient structure, multi-excitation, nonlinear behavior and large torque ripples, a fast and accurate modeling technique is required for design and optimization of this machine. The developed modeling technique in this thesis provides the necessary accuracy to calculate the torque profile including the torque ripple, back-emf and inductance waveforms and ac losses in both saturated and non-saturated conditions. This technique provides an alternative to finite element analysis and allows for the fast development of this new class of machine.

Part II: Variable flux reluctance machines

- **Design considerations of variable flux reluctance machines.**
  This thesis provides design considerations for variable flux reluctance machines. The working principle and different torque components due to its multi-excited topology are analyzed, and design rules are provided for the selection of pole numbers and winding configurations. Since this type of machine suffers from a relatively large torque ripple due to its salient structure, three different methods for minimization of torque ripple are analyzed and are compared on their effectiveness. The method of rotor skewing, rotor teeth non-uniformity, and harmonic current injection provide means of

minimizing the torque ripple and noise level. Additionally, the multi-excited topology provides a wide speed range by a proper control of the field current, armature current, and commutation angle.

- **The design of a variable flux reluctance machine for a 48 V automotive powertrain.**
  In this thesis, a variable flux reluctance machine is developed and optimized for a 48 V automotive powertrain. The presented machine topology has a 12/10 configuration with concentrated winding topology for both the field and armature windings. The efficiency is maximized at the operating point of 3000 rpm and 16 Nm whilst achieving a peak torque of 45 Nm and a speed extension up to 18000 rpm. By applying rectangular wire technology, the copper filling factor is maximized and by proper coil design, the ac losses are minimized. The final design achieves an efficiency of 83% at 16 Nm 3000 rpm, and a maximum efficiency of 90% in the working envelope.

- **Prototype realization and experimental verification of the developed variable flux reluctance machine.**
  A prototype of the developed design for a 48 V automotive powertrain is realized which verifies that the maximized copper filling factor can be achieved with a relatively simple manufacturing concept. Additionally, the performance of the machine is verified by static and dynamic measurements on a motor/generator test bench. The measured back-emf is within 6% accuracy compared to the predictions where the discrepancy can be attributed to tolerances in manufacturing and material properties. By means of successful realization and experimental verification, it is proven that this new class of machine can be a suitable candidate for an automotive powertrain.

8.4 Recommendations

To improve and to extend the hybrid analytical modeling technique, the following recommendations are made:

- Implementation of nonlinear 3D problems. In literature [93, 94], the implementation of HAM for 3D geometries with linear magnetic materials has been reported, showing the significant gain of calculation time for complex systems. Since the advantage of 3D HAM compared to FEM is significant, the development of this technique to solve 3D nonlinear electromagnetic problems has great research potential.

- Implementation of a dynamic solution for eddy current calculation. The eddy current in this thesis is obtained by simplifying the Maxwell equations into quasi-static problems, which results in a relatively large discrepancy of the ac copper loss calculation to the actual solution as the frequency increases. Hence, taking into account the dynamic solution of magnetic vector potential is recommended for more accurate results.

- Application of different meshing algorithms. The implementation of conformal meshing constraints the element sizes in the tangential direction, and hence limits the reduction of computation effort. On the other hand, the quadrilateral element shape is not convenient for small geometric details, e.g., tooth tips. To further reduce the number of mesh elements and to make the mesh shape more flexible, more advanced meshing algorithms have to be applied, e.g., non-conformal meshing, triangular shaped elements, etc.
- Integration of Fourier modeling with other modeling techniques. The Fourier modeling is integrated with MEC in this thesis, however, this concept is feasible for the integration with other modeling techniques, e.g., finite element method, spectral element method [15, 35] (where high order Legendre-Gauss-Lobatto polynomials are applied to increase the accuracy of the results with respect to FEM), etc.

To further implement the variable flux reluctance machine for automotive applications, the following recommendations are made:

- The development of a control algorithm for VFRMs. An inverter is designed and built for the developed VFRM, further measurement can be conducted using vector oriented control or model predictive control to measure the working envelope and efficiency. Moreover, the VFRM offers the freedom to control the magnitudes of the field current and armature current as well as the commutation angle. The development of a control algorithm for efficiency maximization in the field weakening region is recommended. In literature, a control algorithm of a dc-excited flux switching machine has been described [5], the research can be extended for VFRMs that takes the ac losses into account.
- Vibro-acoustic modeling and optimization. For automotive applications, the acoustic noise is an important factor. In literature [74], the vibration and noise of a 6/4 VFRM is investigated. Compared to the SRM with the same stator/rotor combination and load condition, the VFRM shows a reduced noise level. It is recommended to perform a comprehensive study that characterizes the vibro-acoustic response of the 12/10 VFRM for noise reduction.

Appendix A

Magnetic field solutions in Fourier regions

The source terms in Fourier regions are expressed in Fourier series, that are given by,

$$M_p(q) = M_{p0} + \sum_{n=1}^{\infty} (M_{psn} \sin(\omega_n q) + M_{pcn} \cos(\omega_n q)), \tag{A.1}$$

$$M_q(q) = M_{q0} + \sum_{n=1}^{\infty} (M_{qsn} \sin(\omega_n q) + M_{qcn} \cos(\omega_n q)), \tag{A.2}$$

where M_{p0}, M_{psn}, M_{pcn}, M_{q0}, M_{qsn} and M_{qcn} are derived by Fourier theory with the equations of,

$$M_{p0} = \frac{1}{\tau_p} \int_0^{\tau_p} M_p(q) dq, \tag{A.3}$$

$$M_{psn} = \frac{2}{\tau_p} \int_0^{\tau_p} M_p(q) \sin(\omega_n q) dq, \tag{A.4}$$

$$M_{pcn} = \frac{2}{\tau_p} \int_0^{\tau_p} M_p(q) \cos(\omega_n q) dq, \tag{A.5}$$

$$M_{q0} = \frac{1}{\tau_p} \int_0^{\tau_p} M_q(q) dq, \tag{A.6}$$

$$M_{qsn} = \frac{2}{\tau_p} \int_0^{\tau_p} M_q(q) \sin(\omega_n q) dq, \tag{A.7}$$

$$M_{qcn} = \frac{2}{\tau_p} \int_0^{\tau_p} M_q(q) \cos(\omega_n q) dq. \tag{A.8}$$

The term ω_n represents the spatial frequency and is defined as,

$$\omega_n = \frac{2n\pi}{\tau_{per}}, \tag{A.9}$$

where τ_{per} is the tangential width of the periodicity. Since the magnetization in the Poisson equation is expressed as Fourier series, the solution of magnetic vector potential is accordingly written as superposition of harmonic components,

$$A_l(p,q) = \sum_{n=1}^{\infty} A_{ln}(p,q). \tag{A.10}$$

where A_{ln} is the component of the n^{th} harmonic. Since the Poisson equation is solved by using the separation of variables, the solution of A_{ln} is given by a multiplication of two functions, one is dependent on the q-direction, and the other one is dependent on the p-direction,

$$A_{ln}(p,q) = P_n(p)Q_n(q) + S_n(x,y). \tag{A.11}$$

The first term on the right side of equation (A.11) represents the general solution of the Laplace equation, while the second term is determined by the source terms. As mentioned above, A_l is aimed to be expressed in Fourier series, $Q_n(q)$ is therefore given in a combination of sine and cosine functions, and consequently, $P_n(p)$ is defined in a way such that the Poisson equation is satisfied. As a result, the solution of magnetic vector potential is able to be written as,

$$A_l(p,q) = \sum_{n=1}^{N_h} \left(A_{lsn}(p)\sin(\omega_n q) + A_{lcn}(p)\cos(\omega_n q)\right) + A_{l0}(p), \tag{A.12}$$

where n is the harmonic counter and N_h is the total number of harmonics taken into account. Correspondingly, the expressions of flux density can be written as,

$$B_p(p,q) = \sum_{n=1}^{N_h} \left(B_{psn}(p)\sin(\omega_n q) + B_{pcn}(p)\cos(\omega_n q)\right), \tag{A.13}$$

$$B_q(p,q) = \sum_{n=1}^{N_h} \left(B_{qsn}(p)\sin(\omega_n q) + B_{qcn}(p)\cos(\omega_n q)\right) + B_{q0}(p). \tag{A.14}$$

In this thesis, the situation for a non-periodic region with an average source term of M_q is not considered, therefore, the term B_{q0} in equation (A.14) is supposed to be zero. The expressions of B_{psn}, B_{pcn}, B_{qsn} and B_{qcn} are given by sets of Fourier coefficients, denoted as a_n, b_n, c_n and d_n, written as [52],

Cartesian:

$$B_{psn} = a_n e^{\omega_n p} + b_n e^{-\omega_n p} + \mathcal{G}_{psn}, \tag{A.15}$$

$$B_{pcn} = -c_n e^{\omega_n p} - d_n e^{-\omega_n p} + \mathcal{G}_{pcn}, \tag{A.16}$$

$$B_{qsn} = c_n e^{\omega_n p} - d_n e^{-\omega_n p}, \tag{A.17}$$

$$B_{qcn} = a_n e^{\omega_n p} - b_n e^{-\omega_n p}, \tag{A.18}$$

(A.19)

where the terms $\mathcal{G}_{psn}$ and $\mathcal{G}_{pcn}$ are contributed by the magnetization and are given as,

$$\mathcal{G}_{psn} = \mu_0 M_{psn}, \tag{A.20}$$

$$\mathcal{G}_{pcn} = \mu_0 M_{pcn}. \tag{A.21}$$

Polar:

$$B_{psn} = a_n p^{\omega_n - 1} + b_n p^{-\omega_n - 1} + \mathcal{G}_{psn}, \tag{A.22}$$

$$B_{pcn} = -c_n p^{\omega_n - 1} - d_n p^{-\omega_n - 1} + \mathcal{G}_{pcn}, \tag{A.23}$$

$$B_{qsn} = c_n p^{\omega_n - 1} - d_n p^{-\omega_n - 1} + \mathcal{G}_{qsn}, \tag{A.24}$$

$$B_{qcn} = a_n p^{\omega_n - 1} - b_n p^{-\omega_n - 1} + \mathcal{G}_{qcn}, \tag{A.25}$$

where $\mathcal{G}_{psn}$and $\mathcal{G}_{pcn}$ are given as,

$$\mathcal{G}_{psn} = \begin{cases} -\mu_0 \frac{M_{psn} - M_{qcn}}{2} \ln(p), & \omega_n = 1, \\ \mu_0 \frac{4M_{psn} - 2M_{qcn}}{3}, & \omega_n = 2, \\ \mu_0 \omega_n \frac{\omega_n M_{psn} - M_{qcn}}{(\omega_n)^2 - 1}, & \text{else}, \end{cases} \tag{A.26}$$

$$\mathcal{G}_{pcn} = \begin{cases} -\mu_0 \frac{M_{pcn} + M_{qsn}}{2} \ln(p), & \omega_n = 1, \\ \mu_0 \frac{4M_{pcn} + 2M_{qsn}}{3}, & \omega_n = 2, \\ \mu_0 \omega_n \frac{\omega_n M_{pcn} + M_{qsn}}{(\omega_n)^2 - 1}, & \text{else}, \end{cases} \tag{A.27}$$

$$\mathcal{G}_{qsn} = \begin{cases} \mu_0 \frac{M_{pcn} + M_{qsn}}{2} \left[1 + \ln(p)\right], & \omega_n = 1, \\ -\mu_0 \frac{2M_{pcn} + M_{qsn}}{3}, & \omega_n = 2, \\ -\mu_0 \frac{\omega_n M_{pcn} - M_{qsn}}{(\omega_n)^2 - 1}, & \text{else}, \end{cases} \tag{A.28}$$

$$\mathcal{G}_{qsn} = \begin{cases} -\mu_0 \frac{M_{psn} - M_{qcn}}{2} \left[1 + \ln(p)\right], & \omega_n = 1, \\ \mu_0 \frac{2M_{psn} - M_{qcn}}{3}, & \omega_n = 2, \\ \mu_0 \frac{\omega_n M_{psn} - M_{qcn}}{(\omega_n)^2 - 1}, & \text{else}. \end{cases} \tag{A.29}$$

Axisymmetric:

$$B_{psn} = a_n \mathcal{I}_1(\omega_n p) + b_n \mathcal{K}_1(\omega_n p) + \mathcal{G}_{psn}, \tag{A.30}$$

$$B_{pcn} = -c_n \mathcal{I}_1(\omega_n p) - d_n \mathcal{K}_1(\omega_n p) + \mathcal{G}_{pcn}, \tag{A.31}$$

$$B_{qsn} = c_n \mathcal{I}_0(\omega_n p) - d_n \mathcal{K}_0(\omega_n p) + \mathcal{G}_{qsn}, \tag{A.32}$$

$$B_{qcn} = a_n \mathcal{I}_0(\omega_n p) - b_n \mathcal{K}_0(\omega_n p) + \mathcal{G}_{qcn}, \tag{A.33}$$

where $\mathcal{G}_{psn}$, $\mathcal{G}_{pcn}$, $\mathcal{G}_{qsn}$ and $\mathcal{G}_{qcn}$ are given as,

$$\mathcal{G}_{psn} = \mu_0 M_{psn} \mathcal{X}_{pn}(p), \tag{A.34}$$

$$\mathcal{G}_{pcn} = \mu_0 M_{pcn} \mathcal{X}_{pn}(p), \tag{A.35}$$

$$\mathcal{G}_{qsn} = \mu_0 M_{pcn} \mathcal{X}_{qn}(p), \tag{A.36}$$

$$\mathcal{G}_{qcn} = -\mu_0 M_{psn} \mathcal{X}_{qn}(p), \tag{A.37}$$

while $\mathcal{X}_{pn}$ and $\mathcal{X}_{qn}$ are defined as,

$$\mathcal{X}_{pn}(p) = \mathcal{K}_1\left(\omega_n p\right) \int_{\omega_n p_0}^{\omega_n p} p' \mathcal{I}_1(p') dp' - \mathcal{I}_1\left(\omega_n p\right) \int_{\omega_n p_0}^{\omega_n p} p' \mathcal{K}_1(p') dp', \qquad \text{(A.38)}$$

$$\mathcal{X}_{qn}(p) = \mathcal{K}_0\left(\omega_n p\right) \int_{\omega_n p_0}^{\omega_n p} p' \mathcal{I}_1(p') dp' + \mathcal{I}_0\left(\omega_n p\right) \int_{\omega_n p_0}^{\omega_n p} p' \mathcal{K}_1(p') dp', \qquad \text{(A.39)}$$

where p_0 is the inner radius of the region.

Appendix B

Distribution of magnetomotive force in *q*- or *pq*-directions

Magnetomotive force merely in q-direction

Similar concept for the mmfs in the p-direction (explained in section 2.5.5), can be used to derive the mmfs in the q-direction. Starting from a simple example, i.e., a single coil in the slot, two contours are used to derive the mmfs, as shown in Fig. B.1(a). The summation of the mmf in contour (1) should satisfy $\sum mmf_{(1)} = JS_c$ (where $S_c = w_c h_c$). Assume the mmf sources for contour (1) only distribute in the path shown in Fig. B.1(b), which is a row of elements within the width of w_c in the yoke. Consequently, the summation of mmfs in the yoke should be JS_c.

On the other hand, the mmf sources in contour (2) should satisfy $\sum mmf_{(2)} = (1-\frac{p_1}{h_c})JS_c$. Assume that the mmfs are allocated in the paths in the yoke and slot, as shown in Fig. B.1(c). With the mmfs in the yoke equal to JS_c, the summation of the mmf in the slot is accordingly $\frac{p_1}{h_c} \cdot JS_c$. Therefore, the distribution of mmf shows a linear relationship to the p-coordinate of the element before reaching the coil edges. This can also be interpreted as: the summation of mmfs on the path equals to the enclosed current in the area formed by the path itself and the slot edges. Additionally, considering the element size, the mmf in the yoke is derived as,

$$\mathcal{F}^k_{q\pm} = \frac{l^k_{q\pm}}{w_c} \cdot JS_c, \tag{B.1}$$

for the yoke, and is,

$$\mathcal{F}^k_{q\pm} = \frac{l^k_{q\pm}}{w_c} \cdot \frac{p_1}{h_c} JS_c, \tag{B.2}$$

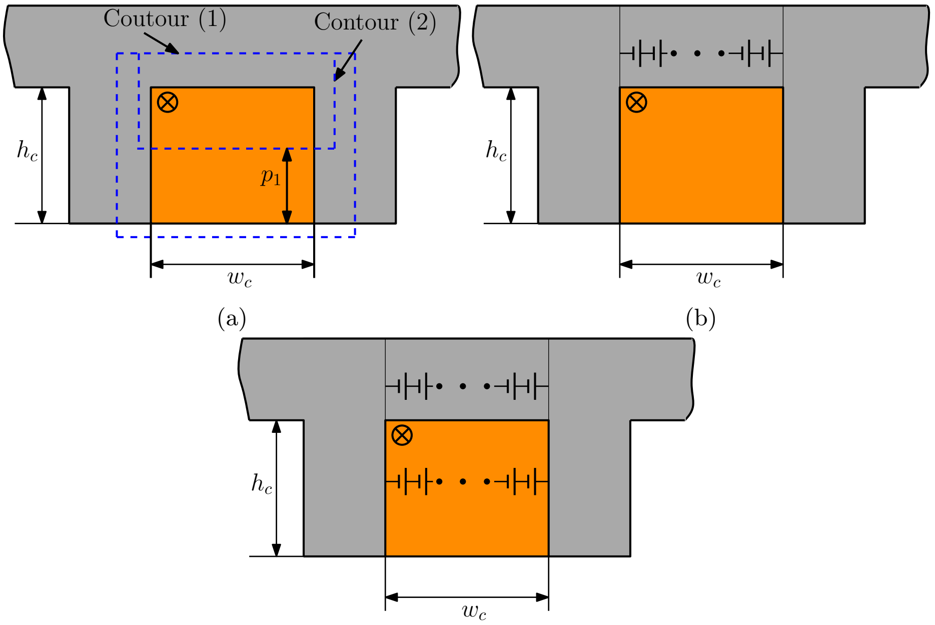
Coutour (1)
Contour (2)
h_c
p_1
w_c
h_c
w_c
h_c
w_c

(a) (b)

(c)

Figure B.1: Topology of a single coil in one slot (a) two representative contours, (b) distribution of mmfs for the path of contour (1) in the yoke, and (c) distribution of mmfs for paths of contour (2) in the yoke and slot.

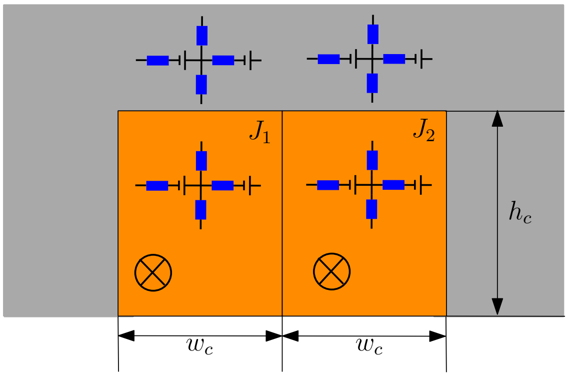

Figure B.2: Magnetomotive forces in the q-direction for the topology of two coil bundles in a single slot in the Cartesian coordinate system.

Table B.1: Distribution of current related mmf sources in the q-direction for the example in Fig. B.2.

Pos.	$\mathcal{F}^k_{p\pm}$ for J_1	$\mathcal{F}^k_{q\pm}$ for J_1	$\mathcal{F}^k_{p\pm}$ for J_2	$\mathcal{F}^k_{q\pm}$ for J_2
Yoke	0	$\frac{l^k_{q\pm}}{w_c}\mathcal{F}_{J1,p}$	0	$\frac{l^k_{q\pm}}{w_c}\mathcal{F}_{J2,p}$
Slot	0	$\frac{p^k}{h_c}\frac{l^k_{q\pm}}{w_c}\mathcal{F}_{J_1,p}$	0	$\frac{p^k}{h_c}\frac{l^k_{q\pm}}{w_c}\mathcal{F}_{J_2,p}$

Notes: $\mathcal{F}_{J_1,p} = J_1 w_c h_c$ and $\mathcal{F}_{J_2,p} = J_2 w_c h_c$.

for the slot. This concept is used to derive the mmfs for the structure shown in Fig. B.2, which has two coil bundles in a single slot, and the obtained mmfs are listed in Table B.1.

The derivation of mmfs in the axisymmetric coordinate system is similar to the Cartesian coordinate system, hence, is not repeated here. For the polar coordinate system, assume a path in q-direction passing through an element that forms an area together with the slot edges. Again, the summation of mmfs on this path should be equal to the current enclosed by the area. Since the area is quadratically linear to the p-coordinate, the expression of mmf shows a quadratic dependence on the position in p-direction. The mmfs are derived for the example shown in Fig. B.3, that has two coil bundles in a slot. The values are listed in Table B.2, where the term $(p^k)^2$ indicates the quadratic relation.

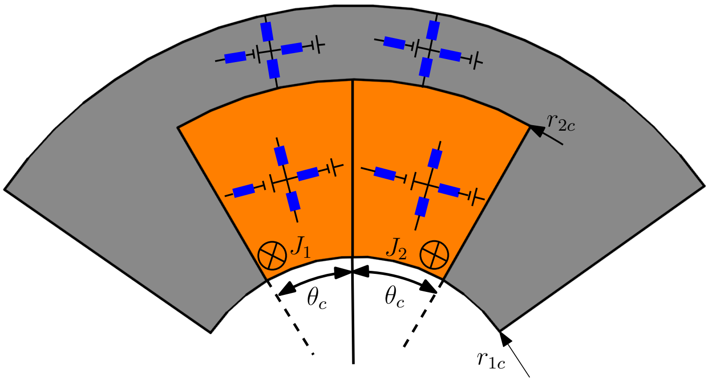

Figure B.3: Magnetomotive forces in the q-direction for the topology of two coil bundles in a single slot in the polar coordinate system.

Table B.2: Distribution of current related mmf sources in the q-direction for the example in Fig. B.3.

Pos.	$\mathcal{F}^k_{p\pm}$ for J_1	$\mathcal{F}^k_{q\pm}$ for J_1	$\mathcal{F}^k_{p\pm}$ for J_2	$\mathcal{F}^k_{q\pm}$ for J_2
Yoke	0	$\dfrac{\theta^k}{2\theta_c}\mathcal{F}_{J1,p}$	0	$\dfrac{\theta^k}{2\theta_c}\mathcal{F}_{J2,p}$
Slot	0	$\dfrac{\theta^k}{2\theta_c}\dfrac{(p^k)^2-(r^k_{1c})^2}{r^2_{2c}-r^2_{1c}}\mathcal{F}_{1,p}$	0	$\dfrac{\theta^k}{2\theta_c}\dfrac{(p^k)^2-(r^k_{1c})^2}{r^2_{2c}-r^2_{1c}}\mathcal{F}_{2,p}$

Notes: $\mathcal{F}_{1,p} = J_1\pi[(r_{2c})^2-(r_{1c})]^2\theta_c$, $\mathcal{F}_{2,p} = J_2\pi[(r_{2c})^2-(r_{1c})]^2\theta_c$, θ^k is the dimension of element k in q-direction.

Magnetomotive force in both p and q-directions

It is feasible to distribute mmfs in both p- and q-directions in the teeth, yoke and slot. However, to ensure that the total mmfs are as the same value as in the above arrangements, $\mathcal{F}^k_{p\pm}$ and $\mathcal{F}^k_{q\pm}$ should be halved compared to those values when mmfs are only arranged in p- or q directions, respectively. The mmfs in the yoke or tooth only have respectively the excitation in the q- or p-directions, while both terms are assumed in the slot. However, considering the complexity of this method compared to the other two, it is not recommended.

Appendix C

Distribution factor and pitch factor of VFRMs

Table C.1: Distribution factor of 6-stator-pole VFRMs.

	Number of rotor poles								
n	2	4	5	7	8	10	11	13	14
1	1	1	1	1	1	1	1	1	1
2	1	1	0	0	1	1	0	0	1
3	1	1	1	1	1	1	1	1	1
4	1	1	0	0	1	1	0	0	1
5	1	1	1	1	1	1	1	1	1
6	1	1	0	0	1	1	0	0	1

Notes: n is the harmonic order.

Table C.2: Distribution factor of 12-stator-pole VFRMs.

	Number of rotor poles								
n	2	4	5	7	8	10	11	13	14
1	1	1	0.966	0.966	1	1	0.966	0.966	1
2	0	1	0	0	1	0	0	0	0
3	1	1	0.707	0.707	1	1	0.707	0.707	1
4	0	1	0	0	1	0	0	0	0
5	1	1	0.259	0.259	1	1	0.259	0.259	1
6	0	1	0	0	1	0	0	0	0

Notes: n is the harmonic order.

Table C.3: Distribution factor of 18-stator-pole VFRMs.

	P_r								
n	2	4	5	7	8	10	11	13	14
1	0.96	0.96	0.96	0.96	0.96	0.96	0.96	0.96	0.96
2	0.177	0.177	0	0	0.177	0.177	0	0	0.177
3	0.667	0.667	0.667	0.667	0.667	0.667	0.667	0.667	0.667
4	-0.218	-0.218	0	0	0	-0.218	0	0	-0.218
5	0.218	0.218	0.218	0.218	0.218	0.218	0.218	0.218	0.218
6	-0.667	-0.667	0	0	-0.667	-0.667	0	0	-0.667

Notes: n is the harmonic order.

Table C.4: Pitch factor of 6-stator-pole VFRMs.

	P_r								
n	2	4	5	7	8	10	11	13	14
1	0.5	-0.5	-0.866	-0.866	-0.5	0.5	0.866	0.866	0.5
2	-0.5	-0.5	0.5	0.5	-0.5	-0.5	0.5	0.5	-0.5
3	-1	1	0	0	1	-1	0	0	-1
4	-0.5	-0.5	-0.5	-0.5	-0.5	-0.5	-0.5	-0.5	-0.5
5	0.5	-0.5	0.866	0.866	-0.5	0.5	-0.866	-0.866	0.5
6	1	1	-1	-1	1	1	-1	-1	1

Notes: n is the harmonic order.

Table C.5: Pitch factor of 12-stator-pole VFRMs.

	P_r								
n	2	4	5	7	8	10	11	13	14
1	0.866	0.5	0.259	-0.259	-0.5	-0.866	-0.966	-0.966	-0.866
2	0.5	-0.5	-0.866	-0.866	-0.5	0.5	0.866	0.866	0.5
3	0	-1	-0.707	0.707	1	0	-0.707	-0.707	0
4	-0.5	-0.5	0.5	0.5	-0.5	-0.5	0.5	0.5	-0.5
5	-0.866	0.5	0.966	-0.966	-0.5	0.866	-0.259	-0.259	0.866
6	-1	1	0	0	1	-1	0	0	-1

Notes: n is the harmonic order.

Table C.6: Pitch factor of 18-stator-pole VFRMs.

	P_r								
n	2	4	5	7	8	10	11	13	14
1	0.94	0.766	0.643	0.342	0.174	-0.174	-0.342	-0.643	-0.766
2	0.766	0.174	-0.174	-0.766	-0.94	-0.94	-0.766	-0.174	0.174
3	0.5	-0.5	-0.866	-0.866	-0.5	0.5	0.866	0.866	0.5
4	0.174	-0.94	-0.94	0.174	0.766	0.766	0.174	-0.94	-0.94
5	-0.174	-0.94	-0.342	0.985	0.766	-0.766	-0.985	0.342	0.94
6	-0.5	-0.5	0.5	0.5	-0.5	-0.5	0.5	0.5	-0.5

Notes: n is the harmonic order.

Bibliography

[1] Aleksandrov, S. R., Overboom, T. T. and Lomonova, E. A. [2018], 'Design optimization and performance comparison of two linear motor topologies with PM-less tracks', *IEEE Transactions on Magnetics* **54**(11), 1–8.

[2] Amara, Y., Reghem, P. and Barakat, G. [2010], 'Analytical prediction of eddy-current loss in armature windings of permanent magnet brushless AC machines', *IEEE Transactions on magnetics* **46**(8), 3481–3484.

[3] Amara, Y., Vido, L., Gabsi, M., Hoang, E., Ahmed, A. H. B. and Lecrivain, M. [2009], 'Hybrid excitation synchronous machines: Energy-efficient solution for vehicles propulsion', *IEEE Transactions on Vehicular Technology* **58**(5), 2137–2149.

[4] Amrhein, M. and Krein, P. [2009], '3-D magnetic equivalent circuit framework for modeling electromechanical devices', *IEEE Transactions on Energy Conversion* **24**(2), 397–405.

[5] Balyovski, T. L., Ilhan, E., Tang, Y., Paulides, J. J. H., Wijnands, C. G. E. and Lomonova, E. A. [2014], Control of DC-excited flux switching machines for traction applications, *in* 'International Conference on Ecological Vehicles and Renewable Energies', Monte-Carlo, pp. 1–5.

[6] Bao, J., Aleksandrov, S. R., Gysen, B. L. J. and Lomonova, E. A. [2018], Analysis of variable flux reluctance machines using hybrid analytical modelling, *in* 'International Conference on Ecological Vehicles and Renewable Energies (EVER)', Monte-Carlo, pp. 1–7.

[7] Bao, J., Boynov, K., Paulides, J. J. H., Wjinands, K. and Lomonova, E. A. [2016], Comparison of 48V rare-earth-free reluctance traction motor drives for mild hybrid powertrain, *in* '2016 IEEE Vehicle Power and Propulsion Conference (VPPC)', Hangzhou, pp. 1–6.

[8] Bao, J., Boynov, K., Paulides, J. J. J. and Lomonova, E. A. [2016], 'Usage of the inductive energy storage in the field winding for driving the variable reluctance motor', *IEEE Transactions on Magnetics* **52**(7), 1–4.

[9] Bao, J., Gysen, B. L. J., Boynov, K., Alexandrov, S. and Lomonova, E. A. [2017], Field weakening capability of 12-stator/10-rotor-pole variable flux reluctance machines, *in* 'International Conference on Ecological Vehicles and Renewable Energies (EVER)', Monte Carlo, pp. 1–5.

[10] Bao, J., Gysen, B. L. J., Boynov, K., Paulides, J. J. H., Bastiaens, K. and Lomonova, E. A. [2017], Analysis and minimization of torque ripple for variable flux reluctance machines, *in* 'IEEE International Electric Machines and Drives Conference (IEMDC)', Miami, FL, pp. 1–7.

[11] Bao, J., Gysen, B. L. J., Boynov, K., Paulides, J. J. H. and Lomonova, E. A. [2017], 'Torque ripple reduction for 12-stator/10-rotor-pole variable flux reluctance machines by rotor skewing or rotor teeth non-uniformity', *IEEE Transactions on Magnetics* **53**(11), 1–5.

[12] Bao, J., Gysen, B. L. J. and Lomonova, E. A. [2018], 'Hybrid analytical modeling of saturated linear and rotary electrical machines: Integration of Fourier modeling and magnetic equivalent circuits', *IEEE Transactions on Magnetics* **54**(11), 1–5.

[13] Bao, R., Avila, V. and Baxter, J. [2017], 'Effect of 48 V mild hybrid system layout on powertrain system efficiency and its potential of fuel economy improvement', *SAE Technical Paper,* pp. 1–11.

[14] Bash, M. L., Williams, J. M. and Pekarek, S. D. [2010], 'Incorporating motion in mesh-based magnetic equivalent circuits', *IEEE Transactions on Energy Conversion* **25**(2), 329–338.

[15] Bastiaens, K., Curti, M., Krop, D. C. J., Jumayev, S. and Lomonova, E. A. [2018], 'Spectral element method modeling of eddy current losses in high-frequency transformers', *Mathematical and Computational Applications* **24**(28), 1–13.

[16] Basu, D. [2000], *Dictionary of Pure and Applied Physics*, CRC Press, U.S.A.

[17] Benhama, A., Williamson, A. C. and Reece, A. B. J. [2000], 'Virtual work approach to the computation of magnetic force distribution from finite element field solutions', *IEE Proceedings - Electric Power Applications* **147**(6), 437–442.

[18] Bertotti, G. [1988], 'General properties of power losses in soft ferromagnetic materials', *IEEE Transactions on Magnetics* **24**(1), 621–630.

[19] Bertotti, G. [1991], 'An improved estimation of iron losses in rotating electrical machines', *IEEE Transactions on Magnetics* **27**(6), 5007 – 5009.

[20] Bianchi, N. [2005], *Electrical Machine Analysis Using Finite Elements*, Taylor & Francis Group, Boca Raton.

[21] Bianchi, N., Bolognani, S., Carraro, E., Castiello, M. and Fornasiero, E. [2016], 'Electric vehicle traction based on synchronous reluctance motors', *IEEE Transactions on Industry Applications* **52**(6), 4762–4769.

[22] Boldea, I. [2017], 'Electric generators and motors: An overview', *CES Transactions on Electrical Machines and Systems* **1**(1), 3–14.

[23] Boldea, I., Tutelea, L. N., Parsa, L. and Dorrell, D. [2014], 'Automotive electric propulsion systems with reduced or no permanent magnets: An overview', *IEEE Transactions on Industrial Electronics* **61**(10), 5696–5711.

[24] Bomela, X. B. and Kamper, M. J. [2002], 'Effect of stator chording and rotor skewing on performance of reluctance synchronous machine', *IEEE Transactions on Industry Applications* **38**(1), 91–100.

[25] Bostanci, E., Moallem, M., Parsapour, A. and Fahimi, B. [2017], 'Opportunities and challenges of switched reluctance motor drives for electric propulsion: A comparative study', *IEEE Transactions on Transportation Electrification* **3**(1), 58–75.

[26] Cai, H., Guan, B. and Xu, L. [2014], 'Low-cost ferrite PM-assisted synchronous reluctance machine for electric vehicles', *IEEE Transactions on Industrial Electronics* **61**(10), 5741–5748.

[27] Calverley, S. D., Jewell, G. W. and Saunders, R. J. [2000], 'Aerodynamic losses in switched reluctance machines', *IEE Proceedings - Electric Power Applications* **147**(6), 443–448.

[28] Chau, K. T., Chan, C. C. and Liu, C. [2008], 'Overview of permanent-magnet brushless drives for electric and hybrid electric vehicles', *IEEE Transactions on Industrial Electronics* **55**(6), 2246–2257.

[29] Chen, H., Dorrell, D. G. and Tsai, M. [2010], 'Design and operation of interior permanent-magnet motors with two axial segments and high rotor saliency', *IEEE Transactions on magnetics* **46**(9), 3664–3675.

[30] Chen, J. T. and Zhu, Z. Q. [2010], 'Winding configurations and optimal stator and rotor pole combination of flux-switching PM brushless AC machines', *IEEE Transactions on energy conversion* **25**(2), 293–302.

[31] Chu, W. Q., Zhu, Z. Q., Zhang, J., Liu, X., Stone, D. A. and Foster, M. P. [2015], 'Investigation on operational envelops and efficiency maps of electrically excited machines for electrical vehicle applications', *IEEE Transactions on Magnetics* **51**(4), 1–10.

[32] Cogent Power [2016], *Altogether more powerful non-oriented eletrical steel.*

[33] Cogent Power [online], https://cogent-power.com.

[34] CPT SpeedStart [online], http://www.federalmogul.com/en-US/OE/Brands/CPT/Documents/CPTSpeedStart_Final.pdf.

[35] Curti, M., Jansen, J. W. and Lomonova, E. A. [2018], 'Convergence analysis of spectral element method for magnetic devices', *International Journal of Applied Electromagnetics and Mechanics,* **57**(S1), 43–49.

[36] Custers, C. H. H. M., Overboom, T. T., Jansen, J. W. and Lomonova, E. A. [2015], '2-D semianalytical modeling of eddy currents in segmented structures', *IEEE Transactions on Magnetics,* **51**(11), 1–4.

[37] Deodhar, R. P., Staton, D. A., Jahns, T. M. and Miller, T. J. E. [1996], 'Prediction of cogging torque using the flux-mmf diagram technique', *IEEE Transactions on Industry Applications* **32**(3), 569–576.

[38] Derbas, H. W., Williams, J. M., Koenig, A. C. and Pekarek, S. D. [2009], 'A comparison of nodal- and mesh-based magnetic equivalent circuit models', *IEEE Transactions on Energy Conversion* **24**(32), 388–396.

[39] Diriye, A. A., Ouagued, S., Amara, Y., Barakat, G. and Tiegna, H. [2016], Iron loss estimation in axial field PM machines using a quasi-3D hybrid analytical model, *in* '2016 Eleventh International Conference on Ecological Vehicles and Renewable Energies (EVER)', Monte Carlo, pp. 1–6.

[40] Dlala, E. and Arkkio, A. [2008], 'Analysis of the convergence of the fixed-point method used for solving nonlinear rotational magnetic field problems', *IEEE Transactions on Magnetics* **44**(4), 473–478.

[41] Dorrell, D. G., Knight, A. M., Evans, L. and Popescu, M. [2012], 'Analysis and design techniques applied to hybrid vehicle drive machines-assessment of alternative IPM and induction motor topologies', *IEEE Transactions on Industrial Electronics* **59**(10), 3690–3699.

[42] Eggers, D., Steentjes, S. and Hameyer, K. [2012], 'Advanced iron-loss estimation for nonlinear material behavior', *IEEE Transactions on magnetics* **48**(11), 3021–3024.

[43] Ehsani, M., Gao, Y. and Miller, J. M. [2007], 'Hybrid electric vehicles: Architecture and motor drives', *Proceedings of the IEEE* **95**(4), 719–728.

[44] El-Refaie, A. M. [2013], 'Motors/generators for traction/propulsion applications: A review', *IEEE Vehicular Technology Magazine* **8**(1), 90–99.

[45] Fatemi, A., Nehl, T., Yang, X., Hao, L., Gopalakrishnan, S., Omekanda, A. and Namuduri, C. [2018], Design of an electric machine for a 48-V mild hybrid vehicle, *in* 'IEEE Energy Conversion Congress and Exposition (ECCE)', Portland, OR, pp. 2278–2285.

[46] Fei, W., Luk, P. C. and Liang, W. [2016], Comparison of torque characteristics in permanent magnet synchronous machine with conventional and herringbone rotor step skewing techniques, *in* 'IEEE Energy Conversion Congress and Exposition (ECCE)', Milwaukee, WI, pp. 1–5.

[47] Friedrich, L. A. J., Curti, M., Gysen, B. L. J. and Lomonova, E. A. [2019], 'High-order methods applied to nonlinear magnetostatic problems', *Mathematical and computational applications* **24**(1).

[48] Furlani, E. P. [2001], *Permanent Magnet and Electromechanical devices*, Academic Press, USA.

[49] G. Li, Z. Z. and Jewell, G. [2015], 'Performance investigation of hybrid excited switched flux permanent magnet machines using frozen permeability method', *IET Electric Power Applications* **9**(9), 586–594.

[50] Gioia, A. D., Brown, I. P., Nie, Y., Knippel, R., Ludois, D. C., Dai, J., Hagen, S. and Alteheld, C. [2018], 'Design and demonstration of a wound field synchronous machine for electric vehicle traction with brushless capacitive field excitation', *IEEE Transactions on Industry Applications* **54**(2), 1390–1403.

[51] Grunditz, E. A., Lundmark, S. T., Alatalo, M., Thiringer, T. and Nordelf, A. [2018], Three traction motors with different magnet materials - influence on cost, losses, vehicle performance, energy use and environmental impact, *in* '2018 Thirteenth International Conference on Ecological Vehicles and Renewable Energies (EVER)', pp. 1 – 13.

[52] Gysen, B. L. J. [2011], *Generalized Harmonic Modeling Technique for 2D Electromagnetic Problems*, Ph.D. dissertation, Eindhoven University of Technology.

[53] Gysen, B. L. J., Ilhan, E., Messen, K. J., Paulides, J. J. H. and Lomonova, E. A. [2010], 'Modeling of flux switching permanent magnet machines with fourier analysis', *IEEE Transactions on Magnetics* **46**(6), 1499–1502.

[54] Gysen, B. L. J., Meessen, K. J., Paulides, J. J. H. and Lomonova, E. A. [2010], 'General formulation of the electromagnetic field distribution in machines and devices using fourier analysis', *IEEE Transactions on Magnetics* **46**(1), 39–52.

[55] Hargreaves, P. A., Mecrow, B. C. and Hall, R. [2012], 'Calculation of iron loss in electrical generators using finite-element analysis', *IEEE Transactions on Magnetics* **48**(5), 1460–1466.

[56] Hua, W., Cheng, M., Zhu, Z. Q. and Howe, D. [2006], Design of flux-switching permanent magnet machine considering the limitation of inverter and flux-weakening capability, *in* 'Conference Record of the 2006 IEEE Industry Applications Conference Forty-First IAS Annual Meeting', Tampa, FL, pp. 2403–2410.

[57] Hwang, H., Bae, S. and Lee, C. [2016], 'Analysis and design of a hybrid rare-earth-free permanent magnet reluctance machine by frozen permeability method', *IEEE Transactions on Magnetics* **52**(7), 1–4.

[58] Ilhan, E., Kremers, M. F. J., Motoasca, E. T., Paulides, J. J. H. and Lomonova, E. A. [2012], Sensitivity analysis for phase inductances in flux-switching PM machines, *in* 'International Conference on Electrical Machines', Marseille, pp. 763–768.

[59] Jansen, J. W., Smeets, J. P. C., Overboom, T. T., Rovers, J. M. M. and Lomonova, E. A. [2014], 'Overview of analytical models for the design of linear and planar motors', *IEEE Transactions on Magnetics* **50**(11), 1–7.

[60] Jin, J. M. [2002], *The finite element method in electromagnetics*, John Wiley and Sons, USA.

[61] Jumayev, S., Merdzan, M., Boynov, K. O., Paulides, J. J. H., Pyrhnen, J. and Lomonova, E. A. [2015], 'The effect of PWM on rotor eddy-current losses in high-speed permanent magnet machines', *IEEE Transactions on Magnetics* **51**(11), 1–4.

[62] Kato, T., Mizutani, R., Matsumoto, H. and Yamamoto, K. [2015], Advanced technologies of traction motor for automobile, *in* '2013 IEEE ECCE Asia Downunder', pp. 147–152.

[63] Kim, S., Lee, G., Hong, J. and Jung, T. [2008], 'Design process of interior PM synchronous motor for 42-v electric air-conditioner system in hybrid electric vehicle', *IEEE Transactions on Magnetics* **44**(6), 1590–1593.

[64] Kistler [online], https://www.kistler.com/en/products/.

[65] Kiyota, K., Sugimoto, H. and Chiba, A. [2014], 'Comparing electric motors: An analysis using four standard driving schedules', *IEEE Industry Applications Magazine* **20**(4), 12–20.

[66] Klauz1, M. and Dorrell, D. [2006], 'Eddy current effects in a switched reluctance motor', *IEEE Transactions on Magnetics* **42**(10), 3437–3439.

[67] Krishnan, R. [2001], *Switched Reluctance Motor Drives Modeling, Simulation, Analysis, Design, and Applications*, CRC Press, U.S.A.

[68] Krishnan, R. [2010], *Permanent Magnet Synchronous and Brushless DC Motor Drives*, CRC Press, USA.

[69] Laoubi, Y., Dhifli, M., Verez, G., Amara, Y. and Barakat, G. [2015], 'Open circuit performance analysis of a permanent magnet linear machine using a new hybrid analytical model', *IEEE Transactions on Magnetics* **51**(3), 1–4.

[70] Lazari, P., Wang, J. and Sen, B. [2015], '3-D effects of rotor step-skews in permanent magnet-assisted synchronous reluctance machines', *IEEE Transactions on Magnetics* **51**(11), 1–4.

[71] Lee, B., Zhu, Z. Q. and Huang, L. R. [2017], 'Torque ripple reduction for 6-stator/4-rotor-pole variable flux reluctance machines by using harmonic field current injection', *IEEE Transactions on Industry Applications* **53**(4), 3730–3737.

[72] Lee, K., Lee, J. and Lee, H. [2015], 'Inductance calculation of flux concentrating permanent magnet motor through nonlinear magnetic equivalent circuit', *IEEE Transactions on Magnetics* **51**(11), 1–4.

[73] Lin, M., Qu, R., Li, J., Jia, S. and Lu, Y. [2016], Torque ripple reduction techniques for stator dc winding excited vernier reluctance machines, *in* 'IEEE Energy Conversion Congress and Exposition (ECCE)', Milwaukee, WI, pp. 1–8.

[74] Liu, X., Zhu, Z., Hasegawa, M., Pride, A. and Deodhar, R. [2012], Vibration and noise in novel variable flux reluctance machine with DC-field coil in stator, *in* 'International Power Electronics and Motion Control Conference', Harbin, China, pp. 1100–1107.

[75] Liu, X. and Zhu, Z. Q. [2012], Influence of rotor pole number on electromagnetic performance of novel variable flux reluctance machine with DC-field coil in stator, *in* 'Proceedings of the 7th International Power Electronics and Motion Control Conference', Harbin, pp. 1108–1115.

[76] Liu, X. and Zhu, Z. Q. [2013], 'Electromagnetic performance of novel variable flux reluctance machines with DC-field coil in stator', *IEEE Transactions on Magnetics* **49**(6), 3020–3028.

[77] Liu, X. and Zhu, Z. Q. [2014], 'Stator/rotor pole combinations and winding configurations of variable flux reluctance machines', *IEEE Transactions on Industry Applications* **50**(6), 3675–3684.

[78] Liu, X., Zhu, Z. Q. and Wu, D. [2014], Evaluation of efficiency optimized variable flux reluctance machine for EVs/HEVs by comparing with interior PM machine, *in* 'International Conference on Electrical Machines and Systems', Hangzhou, pp. 2648–2654.

[79] Liu, Z., Ivanco, A. and Filipi, Z. [2016], 'Impacts of real-world driving and driver aggressiveness on fuel consumption of 48V mild hybrid vehicle', *SAE International Journal of Alternative Powertrains* **5**(2), 249–258.

[80] Ludois, D. C., Reed, J. K. and Hanson, K. [2012], 'Capacitive power transfer for rotor field current in synchronous machines', *IEEE Transactions on power electronics* **27**(11), 4638–4645.

[81] Lundmark, S. T., Acquaviva, A. and Bergqvist, A. [2018], Coupled 3-D thermal and electromagnetic modelling of a liquid-cooled transverse flux traction motor, *in* 'International Conference on Electrical Machines (ICEM)', Alexandroupoli, pp. 2640–2646.

[82] Lundmark, S. T. and Fard, P. R. [2015], Magnet and core loss in a radial flux and a transverse flux PM traction motor, *in* 'International Conference on Ecological Vehicles and Renewable Energies (EVER)', Monte Carlo, pp. 1–9.

[83] Meessen, K. J., Gysen, B. L. J., Paulides, J. J. H. and Lomonova, E. A. [2012], 'General formulation of fringing fields in 3-D cylindrical structures using Fourier analysis', *IEEE Transactions on Magnetics* **48**(8), 2307–2323.

[84] Miller, J. M. [2006], 'Hybrid electric vehicle propulsion system architectures of the e-CVT type', *IEEE Transactions on power electronics* **21**(3), 756–767.

[85] Miller, T. [2001], *Electronic Control of Switched Reluctance Machines*, Elsevier, USA.

[86] Office for Low Emission Vehicles [2013], 'Driving the future today: a strategy for ultra low emission vehicles in the UK'.

[87] Ooi, S., Morimoto, S., Sanada, M. and Inoue, Y. [2013], 'Performance evaluation of a high-power-density PMASynRM with ferrite magnets', *IEEE Transactions on Industry Applications* **49**(3), 1308–1315.

[88] Ouagued, S., Amara, Y. and Barakat, G. [2016*a*], 'Cogging force analysis of linear permanent magnet machines using a hybrid analytical model', *IEEE Transactions on Magnetics* **52**(7), 1–4.

[89] Ouagued, S., Amara, Y. and Barakat, G. [2016*b*], 'Comparison of hybrid analytical modelling and reluctance network modelling for pre-design purposes', *Mathematics and Computers in Simulation* **130**, 3–21.

[90] Ouagueda, S., Diriye, A. A., Amara, Y. and Barakat, G. [2015], 'A general framework based on a hybrid analytical model for the analysis and design of permanent magnet machines', *IEEE Transactions on Magnetics* **51**(11), 1–4.

[91] Pellegrino, G., Vagati, A., Boazzo, B. and Guglielmi, P. [2012], 'Comparison of induction and PM synchronous motor drives for EV application including design examples', *IEEE Transactions on Industry Applications* **48**(6), 2322–2332.

[92] Pellegrino, G., Vagati, A., Guglielmi, P. and Boazzo, B. [2012], 'Performance comparison between surface-mounted and interior PM motor drives for electric vehicle application', *IEEE Transactions on Industrial Electronics* **59**(2), 803–811.

[93] Pluk, K. J. W. [2015], *Hybrid 3-D Electromagnetic Modeling: The Challenge of Magnetic Shielding of a Planar Actuator*, Ph.D. dissertation, Eindhoven University of Technology.

[94] Pluk, K. J. W., Jansen, J. W. and Lomonova, E. A. [2015*a*], '3-D hybrid analytical modeling: 3-D fourier modeling combined with mesh-based 3-D magnetic equivalent circuits', *IEEE Transactions on Magnetics* **51**(12), 1–14.

[95] Pluk, K. J. W., Jansen, J. W. and Lomonova, E. A. [2015*b*], 'Hybrid analytical modeling: Fourier modeling combined with mesh-based magnetic equivalent circuits', *IEEE Transactions on Magnetics* **51**(8), 1–10.

[96] Polinder, H., Slootweg, J. G., Hoeijmakers, M. J. and Compter, J. C. [2003], 'Modelling of a linear PM machine including magnetic saturation and end effects: maximum force to current ratio', *IEEE Transactions on Industry Applications* **39**(6), 1681–1688.

[97] Pollock, C., Pollock, H., Barron, R., Coles, J. R., Moule, D., Court, A. and Sutton, R. [2006], 'Flux-switching motors for automotive applications', *IEEE Transactions on Industry Applications* **42**(5), 1177–1184.

[98] Popescu, M. and Dorrell, D. G. [2013*a*], 'Proximity losses in the windings of high speed brushless permanent magnet AC motors with single tooth windings and parallel paths', *IEEE Transactions on Magnetics* **49**(7), 3913–3916.

[99] Popescu, M. and Dorrell, D. G. [2013*b*], Skin effect and proximity losses in high speed brushless permanent magnet motors, *in* 'IEEE Energy Conversion Congress and Exposition', Denver, CO, pp. 3520–3527.

[100] Rahman, K. M., Fahimi, B., Suresh, G., Rajarathnam, A. V. and Ehsani, M. [2000], 'Advantages of switched reluctance motor applications to EV and HEV: design and control issues', *IEEE Transactions on Industry Applications* **36**(1), 111–121.

[101] Rajashekara, K. [2013], 'Present status and future trends in electric vehicle propulsion technologies', *IEEE Journal of Emerging and Selected Topics in Power Electronics* **1**(1), 3–10.

[102] Raminosoa, T., El-Refaie, A. M., Pan, D., Huh, K., Alexander, J. P., Grace, K., Grubic, S., Galioto, S., Reddy, P. B. and Shen, X. [2015], 'Reduced rare-earth flux-switching machines for traction applications', *IEEE Transactions on Industry Applications* **51**(4), 2959–2971.

[103] Roshanfekr, P., Lundmark, S., Thiringer, T. and Alatalo, M. [2014], Torque ripple reduction methods for an interior permanent magnet synchronous generator, *in* '16th European Conference on Power Electronics and Applications', Lappeenranta, pp. 1–7.

[104] Santiago, J. d., Bernhoff, H., Ekergrd, B., Eriksson, S., Ferhatovic, S., Waters, R. and Leijon, M. [2012], 'Electrical motor drivelines in commercial all-electric vehicles: A review', *IEEE Transactions on Vehicular Technology* **61**(2), 475–484.

[105] Sheikh-Ghalavand, B., Vaez-Zadeh, S. and Isfahani, A. H. [2010], 'An improved magnetic equivalent circuit model for iron-core linear permanent-magnet synchronous motors', *IEEE Transactions on Magnetics* **46**(1), 112–120.

[106] Smeets, J. P. C., Overboom, T. T., Jansen, J. W. and Lomonova, E. A. [2012], 'Mode-matching technique applied to three-dimensional magnetic field modeling', *IEEE Transactions on Magnetics* **48**(1), 3383–3386.

[107] Sonntag, C. L. W., Lomonova, E. A., Duarte, J. L., Vandenput, A. J. A. and Pemen, A. J. M. [2006], Contactless energy transfer for office and domestic applications, *in* 'Proceedings International Conference on Electrical Machines (ICEM)', Greece, pp. 268–1/6.

[108] Soong, W. L. and Miller, T. J. E. [1994], 'Field-weakening performance of brushless synchronous AC motor drives', *IEE Proceedings - Electric Power Applications* **141**(6), 331–340.

[109] Sprangers, R. L. J. [2015], *Towards increased understanding of low-power induction and synchronous reluctance machines*, Ph.D. dissertation, Eindhoven University of Technology.

[110] Sprangers, R. L. J., Paulides, J. J. H., Gysen, B. L. J. and Lomonova, E. A. [2016], 'Magnetic saturation in semi-analytical harmonic modeling for electric machine analysis', *IEEE Transactions on Magnetics* **52**(2), 1–10.

[111] Staton, D. A., Miller, T. J. E. and Wood, S. E. [1993], 'Maximising the saliency ratio of the synchronous reluctance motor', *IEE Proceedings B - Electric Power Applications* **140**(4), 249–259.

[112] Stipetic, S., Zarko, D. and Popescu, M. [2016], 'Ultra-fast axial and radial scaling of synchronous permanent magnet machines', *IET Electric Power Applications* **10**(7), 658–666.

[113] Sudhoff, S. D., Kuhn, B. T., Corzine, K. A. and Branecky, B. T. [2007], 'Magnetic equivalent circuit modeling of induction motors', *IEEE Transactions on Energy Conversion* **22**(2), 259–270.

[114] Sulaiman, E., Kosaka, T. and Matsui, N. [2011], A new structure of 12slot-10pole field-excitation flux switching synchronous machine for hybrid electric vehicles, *in* 'Proceedings of the 2011 14th European Conference on Power Electronics and Applications', Birmingham, pp. 1–10.

[115] Sulaiman, E., Kosaka, T. and Matsui, N. [2015], 'High power density design of 6-slot-8-pole hybrid excitation flux switching machine for hybrid electric vehicles', *IEEE Transactions on Magnetics* **47**(10), 4453–4456.

[116] Sulzberger, C. [2004], 'An early road warrior: electric vehicles in the early years of the automobile', *IEEE Power and Energy Magazine* **2**(3), 66–71.

[117] Tang, Y. [2017], *Multi-excited reluctance machines: analysis, modeling and design for application in electric in-wheel traction*, Ph.D. dissertation, Eindhoven University of Technology.

[118] Tang, Y., Paulides, J. J. H. and Lomonova, E. A. [2014], 'Energy conversion in DC excited flux-switching machines', *IEEE Transactions on Magnetics* **50**(11), 1–4.

[119] Tang, Y., Paulides, J. J. H. and Lomonova, E. A. [2015], ‘Automated design of DC-excited flux-switching in-wheel motor using magnetic equivalent circuits’, *IEEE Transactions on Magnetics* **51**(4), 1–11.

[120] Tesla Roadster [Online], https://www.tesla.com/roadster.

[121] Toyota Prius [Online], https://www.toyota.nl/over-toyota/toyota-world/prius-heritage.json.

[122] U. S. Energy Department [Online], https://www.energy.gov/articles/history-electric-car.

[123] Wang, Y. and Deng, Z. [2012], ‘Comparison of hybrid excitation topologies for flux-switching machines’, *IEEE Transactions on Magnetics* **48**(9), 2518–2527.

[124] Williamson, S., Lukic, S. M. and Emadi, A. [2006], ‘Comprehensive drive train efficiency analysis of hybrid electric and fuel cell vehicles based on motor-controller efficiency modeling’, *IEEE Transactions on Power Electronics* **21**(3), 730–740.

[125] Woodsen, H. H. and Melcher, J. R. [2014], *Electromechanical Dynamics*, (Massachusetts Institute of Technology: MIT OpenCourseWare) http://ocw.mit.edu.

[126] Wright, S. J. [2015], ‘Coordinate descent algorithms’, *Mathematical Programming* **151**(1), 3–34.

[127] Wu, Z. Z. and Zhu, Z. Q. [2015], ‘Analysis of air-gap field modulation and magnetic gearing effects in switched flux permanent magnet machines’, *IEEE Transactions on Magnetics* **51**(5), 1–12.

[128] Yang, H., Lin, H. and Zhu, Z. Q. [2018], ‘Recent advances in variable flux memory machines for traction applications: A review’, *CES Transactions on Electrical Machines and Systems* **2**(1), 34–50.

[129] Yang, S., Zhang, J. and Jiang, J. [2016], ‘Modeling torque characteristics and maximum torque control of a three-phase, DC-excited flux-switching machine’, *IEEE Transactions on magnetics* **52**(7), 1–4.

[130] Zeraoulia, M., Benbouzid, M. E. H. and Diallo, D. [2006], ‘Electric motor drive selection issues for HEV propulsion systems: a comparative study’, *IEEE Transactions on Vehicular Technology* **55**(6), 1756–1764.

[131] Zhu, Z. Q., Chu, W. Q. and Guan, Y. [2017], ‘Quantitative comparison of electromagnetic performance of electrical machines for HEVs/EVs’, *CES Transactions on Electrical Machines and Systems* **1**(1), 37–47.

[132] Zhu, Z. Q., Lee, B. and Liu, X. [2016], ‘Integrated field and armature current control strategy for variable flux reluctance machine using open winding’, *IEEE Transactions on Industry Applications* **52**(2), 1519–1529.

Acknowledgements

First of all, I would like to express my sincere gratitude to prof.dr. Elena Lomonova, who provided me the opportunity as a PhD candidate. Her continuous support helped me for going this far. Her advice opened new doors of research areas to me and very importantly, led me to the correct direction that straightened my pave of pursuing the PhD.

Secondly, I wish to give my thanks to my supervisor dr. Bart Gysen. Actually not just in this four-year PhD work, but also during my master and PDEng, he gave me valuable guidance, assistance and comments with his profound knowledge, experience and structured way of thinking. His professional academic attitude inspired me to explore further and deeper. His encouragement and faith brought me more confidence.

Thirdly, I would like to thank dr. Konstantin Boynov and dr. Johan Paulides for their time and scientific inputs in different phases of this project. Additionally, my special thanks go to Marijn, who contributed his time and efforts in construction of the experimental setup, and was always willing to help me with a lot of patience.

Next, a lot of thanks go to Prodrive Technologies and Punch Powertrain. They not only sponsored this project, but were also responsible for the realization of the design. The successful manufacturing of the prototype would not have been accomplished without their professionalism in production. Particular thanks go to dr. Ruud Sprangers, who arranged a lot of discussions, delivered useful information and provided strong support.

Furthermore, I would like to thank the committee members of my PhD defense: dr. G. Pellegrino, dr. R.L.J. Sprangers, dr. S.T. Lundmark, prof. Y. Amara and prof. A.J.M. Pemen for spending time reviewing my thesis and providing valuable comments.

PhD projects are often for individuals, and a lot of time we have to face the difficulties alone. Luckily, the EPE group bonded us together, and I felt the supports from my friends and officemates. I would like to thank dr. Y. Tang in particular for the help I got from our long discussions; and additionally, to thank Leo, Marco, Mitrofan, Koen, Ya, Coen, Sam, Michael, Marko, and Jereon for all

their generous help.

At last, I want to thank my families and friends, who accompanied and supported me spiritually during this long journey. Particular gratitude goes to my husband and parents for respecting all my decisions and bringing the beautiful moments into my life.

最后，特别感谢我的父母，感谢你们的付出，包容和支持。谢谢你们给我的爱！

Curriculum Vitae

Jing Bao was born on the 21st of August 1987 in Hangzhou, China. After finishing Bachelor in 2010 at Zhejiang University in China, she studied Electrical Engineering at Eindhoven University of Technology (TU/e) in the Netherlands. In 2012 she received the Master's degree within the Electromechanics and Power Electronics (EPE) group. In 2015, she received a diploma of Professional Doctorate in Engineering (PDEng) from TU/e. Since then she has started a PhD project at EPE group of which the results are presented in this dissertation. Her research focuses on the analytical modeling for 2D nonlinear electromagnetic problems, and the establishment of the design framework for variable flux reluctance machines.